6

RELIABILITY OF NAND FLASH MEMORY

6.1 INTRODUCTION

Reliability of NAND flash memory [1] is more interesting than that of other semiconductor devices. This is because a very high electric field (>10 MV/cm) is applied to tunnel oxide during program and erase operations, in comparison with a low field (<5 MV/cm) in other devices. Program and erase of NAND flash perform by electron injection and emission to/from floating gate (FG). There are several methods of electron injection and emission. For electron injection, there are two methods. One is channel hot electron (CHE) injection. The voltages (5–12 V) are applied to drain and control gate (CG), as drain current flows. A portion of the electrons of the drain current in the channel becomes hot, and it is injected to FG over the energy barrier of gate oxide. The CHE can operate the electron injection by relatively low applied voltage (~12 V); however, large channel electron current is needed to make a required number of hot electron injections. Then program efficiency (injected electron/drain electron current) is quite low ($\sim 10^{-6}$). It is difficult to implement the parallel programming (page programming), where many cells are simultaneously programmed to achieve fast programming. The other electron injection method is the Fowler–Nordheim tunneling (FN-t) injection. A high voltage (~23 V) is applied to CG to inject electrons from channel to FG. The applied voltage is needed to be high (~23 V); however, program efficiency is high (~1). Therefore, it is possible to program many cells at the same time (parallel program or page programming).

Nand Flash Memory Technologies, First Edition. Seiichi Aritome.
© 2016 The Institute of Electrical and Electronics Engineers, Inc. Published 2016 by John Wiley & Sons, Inc.

Micron Ex. 1014, p. 214
Micron v. YMTC
IPR2025-00119

TABLE 6.1 Program and Erase Schemes of NOR and NAND Flash

Flash	Electron Injection	Electron Emission
NOR flash	CHE	FN-t @ S
NOR flash [5]	CHE	Uniform FN-t
NAND flash [1]	CHE	—
NAND flash [2,3,8]	Uniform FN-t	FN-t @ D
NAND flash [4–8]	Uniform FN-t	Uniform FN-t

CHE, channel hot electron; FN-t @ S, FN-t at source; FN-t @ D, FN-t at drain; Uniform FN-t, FN-t entire channel (tunnel oxide).

For electron emission, there are mainly two methods. One is FN-t emission at a source or drain gate overlap area. High voltage (~20 V) is applied to source or drain to eject electrons from FG. During FN-t emission at a source or drain, a large source (or drain) leakage current is caused by band-to-band tunneling (BB-t) mechanism. By BB-t, electron–hole pairs are generated in substrate. A portion of the holes is accelerated by high field at a source (or drain), and it is injected to tunnel oxide. Then some holes are trapped in tunnel oxide. These hole traps have degraded Program/Erase cycling and data retention characteristics, as described in Sections 6.2 and 6.3. The other electron emission method is the FN-t emission entire channel region (entire tunnel oxide). The BB-t does not occur due to no voltage difference between the source (or drain) and the substrate.

The possible program and erase schemes of flash memory are summarized in Table 6.1. Reliability performances are compared between these program and erase schemes in Sections 6.2 [6,7] and 6.4 [5].

It had been reported that high field FN-t during program and erase causes oxide degradation in tunnel oxide. Figure 6.1 shows one of the degradation mechanisms [9] of FN-t. Hot electron injection from cathode (FG) to anode (substrate) makes

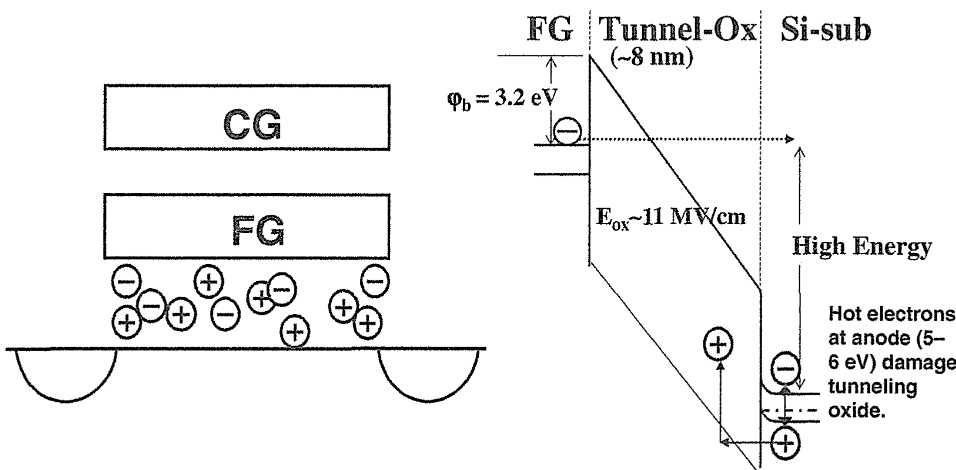

FIGURE 6.1 The degradation mechanism of Fowler–Nordheim tunneling stress on tunnel oxide.

Micron Ex. 1014, p. 215
Micron v. YMTC
IPR2025-00119

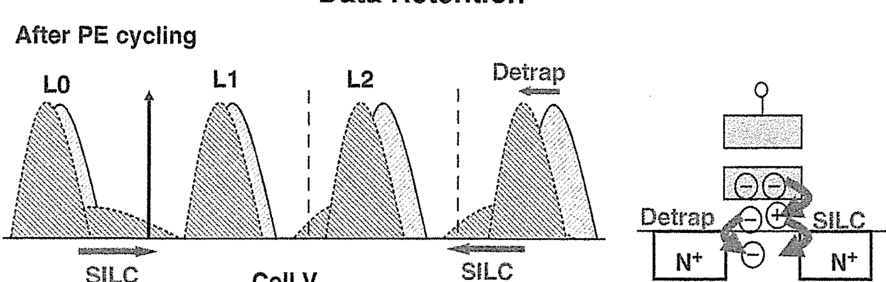

FIGURE 6.2 Data retention phenomena.

electron–hole pairs at anode. And a portion of the hot holes has been injected to tunnel oxide and trapped inside tunnel oxide. An electron trap has also occurred in tunnel oxide during FN-t stress. These hole and electron traps have caused oxide degradation in tunnel oxide and have direct impacts on program/erase cycling endurance characteristics, such as program/erase window narrowing, as described in Sections 6.2 and 6.3.

Data retention is also degraded by electron and hole traps in tunnel oxide, as shown in Fig. 6.2. Detrapping of trapped charges in tunnel oxide is a major root cause of V_t shift during the data retention test, as described in Sections 6.2 and 6.3. And trapped holes would make a stress-induced leakage current (SILC) for tunnel oxide, because the potential barrier of tunnel oxide may locally decrease by hole traps. SILC makes tail bits in the V_t distribution, as shown in Fig. 6.2.

Figure 6.3 shows the read disturb phenomena. Read disturb failure is mainly caused in the erase state after program/erase cycling stress. The stress-induced leakage current (SILC), which is generated by program/erase cycling stress, is major root cause, as described in Section 6.4.

The program disturb issue is becoming serious as scaling memory cells. A low self-boosting voltage was the major root cause of the program disturb issue for <90-nm generation memory cells. However, below 70-nm generation, several new program disturb phenomena by the hot carrier injection mechanism were reported, as described in Section 6.5.

The erratic over-program is presented in Section 6.6. The mechanism of erratic over program is considered to be an excess electron injection at hole trap sites in tunnel oxide. The number of failure bits by erratic over program is increased by scaling memory cells. There is no good way to mitigate erratic over-program, except for slower programming operations. The strong ECC can actually save erratic over-program failure bits.

Micron Ex. 1014, p. 216
Micron v. YMTC
IPR2025-00119

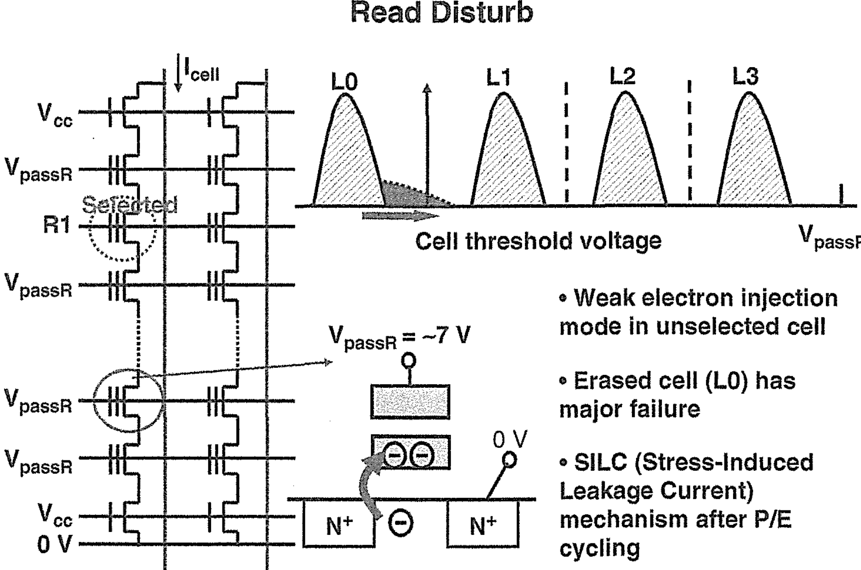

FIGURE 6.3 Read disturb phenomena.

In the NAND flash program and erase operation, a high voltage is applied to CG or substrate. This high program and erase voltage cannot be effectively decreased by the scaling feature size of the memory cell. Therefore, the high-field stress problem has been caused in memory cells [10]. One of the problems is "the negative V_t shift" during programming, as described in Section 6.7 [11].

6.2 PROGRAM/ERASE CYCLING ENDURANCE AND DATA RETENTION

6.2.1 Program and Erase Scheme

The program/erase cycling endurance and the data retention are key characteristics of floating-gate memories such as EEPROMs (electrically erasable and programmable read-only memories) and flash memories [1, 8, 12–17]. An essential requirement for the memory cell is sufficient data retention even after a large number of program/erase cycles. However, the data retention is degraded by the high-field stress in the thin tunnel oxide during the program and erase operations.

The degradation mechanisms of the flash memory cell had been studied [5–8, 18–21] to improve the reliability of the memory cell. The degradation behavior is related to the charge-trapping process in the thin tunnel oxide during both the program and erase operations [5–8, 18–21], which are performed by the Fowler–Nordheim tunneling of electrons through the thin tunnel oxide. The generation of traps in the thin tunnel oxide is strongly dependent on the program and erase conditions [5–8, 14, 20, 21]. Therefore, the program/erase cycling endurance and the data retention characteristics had been studied in several program/erase schemes [5–8], to decide a proper program/erase scheme.

Micron Ex. 1014, p. 217
Micron v. YMTC
IPR2025-00119

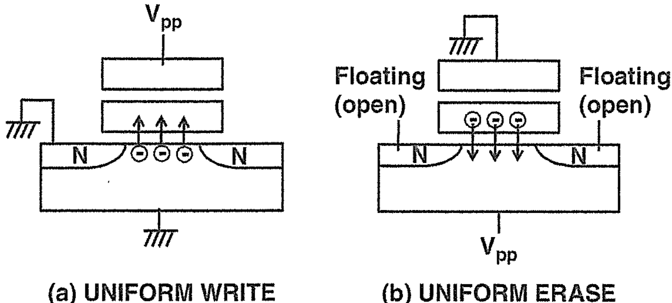

FIGURE 6.4 Operation of the uniform program (write) and uniform erase scheme. (a) Uniform program (write). A positive high voltage is applied to the control gate with the drain and substrate grounded. Electrons are injected to the floating gate over the whole channel area. (b) Uniform erase. A positive high voltage is applied to the substrate with the control gate grounded. Electrons in the floating gate are emitted uniformly over the whole channel area. Copyright © 1994 IEICE.

The endurance and data retention characteristics of the flash memory cell programmed by two different program and erase schemes are compared [6, 7, 20]. One is a uniform program (write) and uniform erase scheme (Fig. 6.4), using uniform Fowler–Nordheim tunneling over the whole channel area both during the program and erase operation. The other is a uniform program (write) and nonuniform erase scheme (Fig. 6.5), using uniform tunneling over the whole channel area during the program operation (Fig. 6.5a) and local nonuniform tunneling at the drain during the erase operation (Fig. 6.5b). A uniform program and nonuniform erase scheme could also be applied to NOR-type cells, such as the Di-NOR cell [16]. However, a uniform program and uniform erase scheme could be applied to only NAND-type cells because it was not possible to implement a selective program (program inhibit) operation in a NOR-type cell.

In experiments of program/erase cycling endurance, the programming voltages (V_{pp}) for cells of various tunnel oxide thickness were determined by the V_{pp} when the

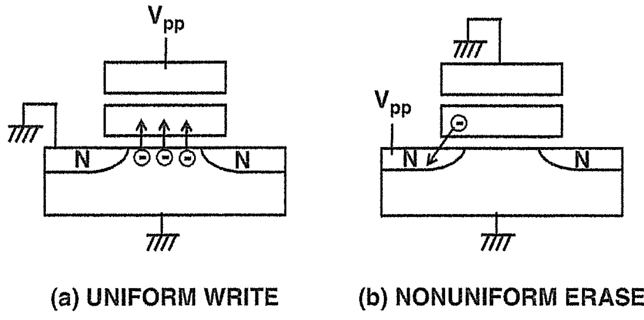

FIGURE 6.5 Operation of the uniform program (write) and nonuniform erase scheme. (a) Uniform program (write). A positive high voltage is applied to the control gate with drain and substrate grounded. (b) Nonuniform erase. A positive high voltage is applied to the drain with the control gate grounded. Copyright © 1994 IEICE.

Micron Ex. 1014, p. 218
Micron v. YMTC
IPR2025-00119

threshold voltage reached 2.5 V in a program operation after 10 cycles, and −3.0 V in an erase operation after 10 cycles. The programming time was fixed at 1 ms. This method of V_{pp} determination is suitable for the comparison of these two schemes, because an initial window widening during the first 10 program/erase cycles occurs in the uniform program and nonuniform erase scheme. The threshold voltage of the flash memory cell is measured with a drain voltage of 1 V. The accelerated data retention tests were done at a temperature of 150–300°C after different numbers of program/erase cycles from 10 to 1 million had been applied to the devices.

A conventional n-channel floating gate transistor with a tunnel oxide over the entire channel region was used for experiments. The gate length is 1.0 μm. The thin gate oxide of 5.6–12.1 nm is thermally grown at 800°C. The effective oxide thickness of the oxide–nitride–oxide (ONO) inter-poly dielectric is 25 nm [22].

6.2.2 Program and Erase Cycling Endurance

The program/erase cycling endurance characteristics of the two different schemes are shown in Fig. 6.6. The uniform program and uniform erase scheme guarantees a wide cell threshold voltage (V_t) window of upto 4 V, even after 1 million program (write) and erase cycles (Fig. 6.6a). However, the threshold window obtained by the uniform program and nonuniform erase scheme begins to close rapidly after around 100 program (write) and erase cycles, and it fails after 100K program and erase cycles (Fig. 6.6b).

In the case of the uniform program and nonuniform erase scheme (Fig. 6.6b), holes are generated near the drain of the memory cell by the band-to-band tunneling mechanism [23–25] due to the presence of a high voltage over the drain junction during the erase. A part of these holes is injected into the thin gate oxide after being accelerated in the depletion region. The injection of hot holes results in hole trapping

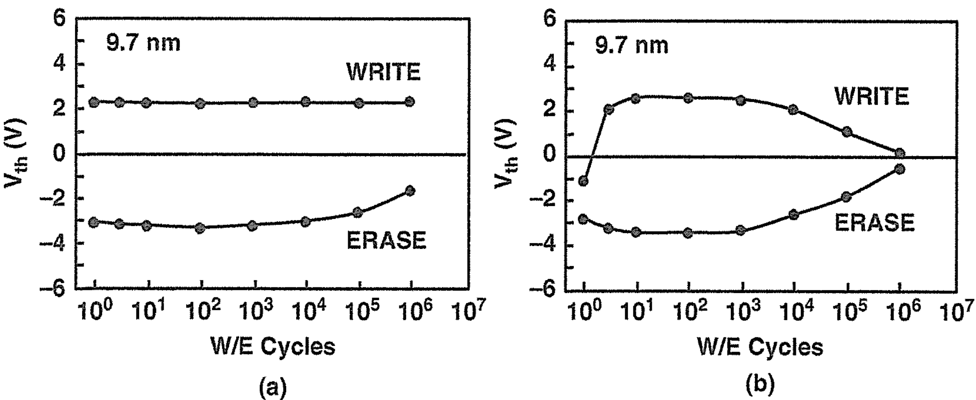

FIGURE 6.6 Program/erase cycling endurance characteristics. (a) Uniform program and uniform erase scheme, using uniform injection and uniform emission over the whole channel area. (b) Uniform program and nonuniform erase scheme, using uniform injection over the whole channel area and local nonuniform emission at the drain, respectively. Copyright © 1994 IEICE.

Micron Ex. 1014, p. 219
Micron v. YMTC
IPR2025-00119

in gate oxide near the drain. As a result, field enhancement occurs, resulting in an initial threshold window widening, which is observed in the first 10 program/erase cycles. During the first cycle, the threshold window is small (about 1.5 V), because field enhancement has not yet occurred. After a few cycles, holes are trapped locally in the gate oxide near the drain, and the Fowler–Nordheim tunneling during both the nonuniform erase and the uniform program could be confined to a small region near the drain. Therefore, the electron trapping in the gate oxide near the drain area is enhanced, subsequently, these trapped electrons impede the tunneling of electrons between the floating gate and the substrate. As a result, window narrowing rapidly occurs.

On the other hand, in the uniform program and uniform erase scheme, the program and erase operation is performed without hot-hole generation by band-to-band tunneling mechanism; therefore, the initial window widening and rapid window narrowing do not occur.

In the uniform program and uniform erase scheme, the threshold voltage (V_{th}) of the erased cell is dependent on the number of program/erase cycles, namely V_{th} slightly shift down by 1K cycles and shift up after 1K cycles. However, the V_{th} of the programmed cell is not dependent on the number of program/erase cycles. This can be explained as follows. The oxide traps and interface traps are generated uniformly over the entire channel area because the Fowler–Nordheim tunneling of electrons is performed uniformly during uniform program and erase operations. The uniformly trapped oxide charges over the channel area affect not only the electron tunneling current through the oxide, but also the flat-band voltage. The V_{th} of the erased cell decreases slightly by 1K cycles (Fig. 6.6a) due to the hole trap generated in the oxide during the Fowler–Nordheim tunneling. The hole traps result in an increase of electron tunneling current (V_{th} decrease) as well as a decrease of the flat-band voltage (V_{th} decrease). After about 1K cycles, the V_{th} of the erased cell increases due to electron trapping. The electron traps result in a decrease of electron tunneling current (V_{th} increase) as well as an increase of the flat-band voltage (V_{th} increase).

On the other hand, the V_{th} of the programmed cell remains almost constant up to 1 million cycles in spite of the positive and negative charge trapping in the oxide. For programmed V_{th}, by 1K cycles, the hole traps result in an increase of electron tunneling current (V_{th} increase) as well as a decrease of the flat-band voltage (V_{th} decrease). After about 1K cycles, the electron traps result in a decrease of electron tunneling current (V_{th} decrease) as well as an increase of the flat-band voltage (V_{th} increase) [6, 7, 20]. Therefore V_{th} movement in programmed and erased cells in uniform program/erase scheme can be explained by the trap effect on both electron FN-t tunneling current and the flat-band voltage [6, 7, 20].

The influence of the trapped oxide charges on the flat-band voltage is confirmed by measuring the flat-band voltage shift during equivalent program and erase stress cycles of the test devices in which the floating gates are connected with the control gates, as shown in Fig. 6.7. Using the uniform program (write) and uniform erase scheme, the threshold voltage shift is negative at the beginning but becomes positive with an increasing number of stress cycles, because hole trapping mainly occurs up to the first 1K cycles while electron trapping becomes dominant after 1K cycles. The

Micron Ex. 1014, p. 220
Micron v. YMTC
IPR2025-00119

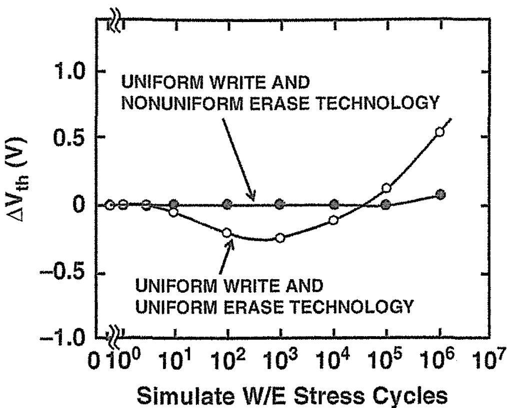

FIGURE 6.7 Threshold voltage shift of the test device in which the floating gate is connected with the control gate, during equivalent program and erase stress on tunnel-oxide. The equivqlent program/erase stress condition: In the case of uniform program and uniform erase scheme, high-voltage pulses of 12.0 V, 0.1 ms, and 13.5 V, 0.1 ms are applied to the gate and substrate, respectively. In the case of the uniform program and nonuniform erase scheme, high-voltage pulses of 10.4 V, 0.1 ms and 13.0 V, 0.1 ms are applied to the gate and drain, respectively. In the uniform program and uniform erase scheme, the trapped oxide charges are directly affecting the threshold voltage. However, in uniform program and nonuniform erase scheme, the trapped oxide charges are not directly affecting the threshold voltage. Copyright © 1994 IEICE.

influence of the trapped oxide charges on the flat-band voltage is confirmed; thus the mechanism of threshold voltage compensation with flat-band voltage and FN-t current is also confirmed [6,7,20].

Figure 6.8 shows the dependence of the endurance characteristics on the tunnel-oxide thickness [7]. In the case of the uniform program and uniform erase scheme, the window narrowing of the thicker tunnel oxides is larger than that of the thinner

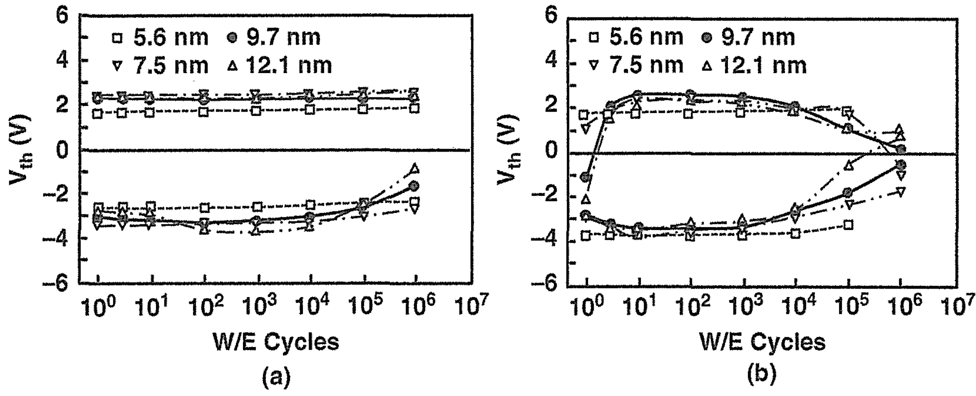

FIGURE 6.8 Dependence of the program/erase cycling endurance characteristics on the tunnel-oxide thickness. (a) Uniform program and uniform erase scheme. (b) Uniform program and nonuniform erase scheme. Copyright © 1994 IEICE.

Micron Ex. 1014, p. 221
Micron v. YMTC
IPR2025-00119

oxides. The window widening around 1K cycles is also larger in thicker tunnel oxides, as compared with the thinner oxides. The increased hole trapping is caused by an increased hole generation in thicker oxides. Consequently, since holes are involved in the generation of traps, the electron trapping will also be enhanced for thicker oxides. In the case of the uniform program and nonuniform erase scheme, the window widening and narrowing is almost independent of the oxide thickness over the 7.5 to 12.1-nm thickness range. However, for a 5.6-nm oxide thickness, the window narrowing is strongly reduced for both program and erase operations. However, the breakdown of the 5.6-nm oxide occurs very early, before 1 million cycles, in the case of uniform program and nonuniform erase scheme.

6.2.3 Data Retention Characteristics

A. Program and Erase Scheme Dependence Figure 6.9 shows the data retention characteristics of erased cells, which are subjected to several program/erase cycles from 10 to 1 million by two program/erase schemes [6–8]. In the case of the uniform program and nonuniform erase scheme (Fig. 6.9b), the stored positive charge gradually decays as the baking time increases, so the threshold voltage window decreases. However, in the case of the uniform program and uniform erase scheme (Fig. 6.9a), the stored positive charge effectively increases up to a 100-minute baking time due to the detrapping of electrons from the gate oxide to the substrate during the retention bake, as shown in Fig. 6.10. This effective increase of the stored positive charge becomes

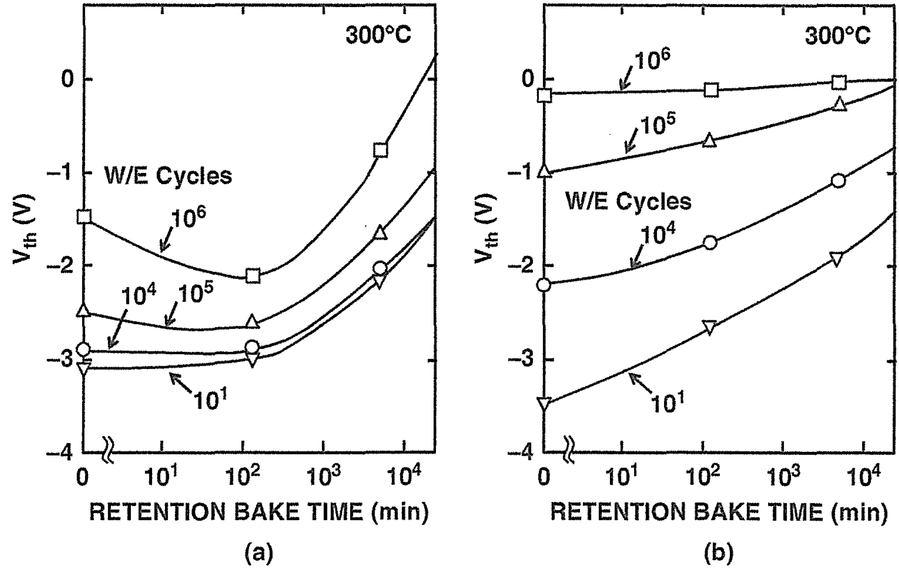

FIGURE 6.9 Data retention characteristics of the erased cell, which stores positive charges in the floating gate, as a function of retention bake time at 300°C in (a) uniform program (write) and uniform erase scheme and (b) uniform program (write) and nonuniform erase scheme, subjected to 10, 10K, 100K, 1 million program and erase cycles (P/E cycles). Copyright © 1994 IEICE.

Micron Ex. 1014, p. 222
Micron v. YMTC
IPR2025-00119

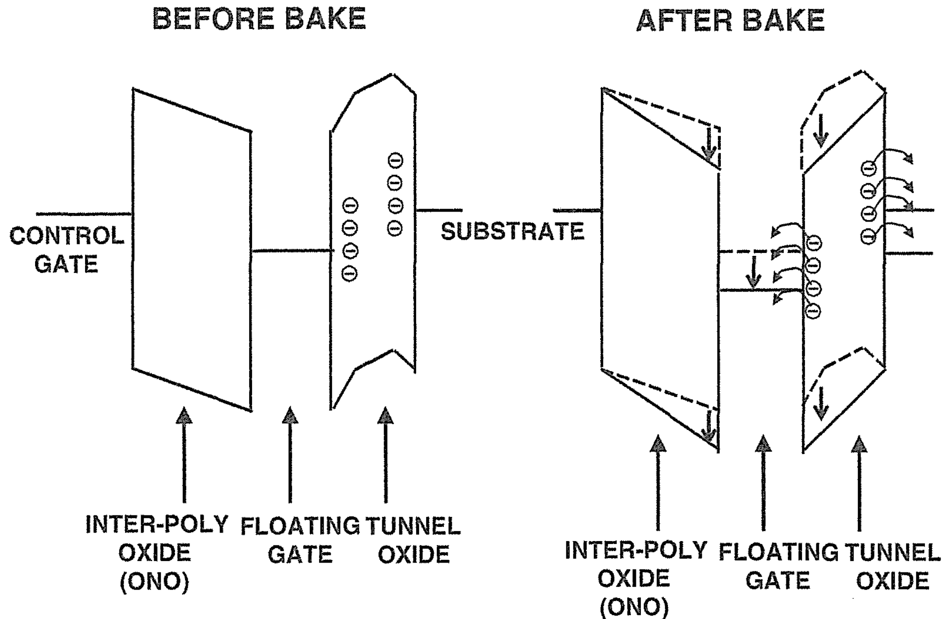

FIGURE 6.10 Band diagram before and after baking. The effect of detrapping electrons from the gate oxide to the substrate is equivalent to the effect of trapping holes in the gate oxide. Copyright © 1994 IEICE.

larger with an increasing number of program/erase cycles because the amount of trapped negative charge in the thin oxide increases. The effect of detrapping electrons is equivalent to the effect of trapping holes in the gate oxide. As a result, the detrapping of the electrons suppresses the data loss of the positively charged cell because the stored positive charge is effectively increasing at the beginning of the bake. This effect extends the data retention time of an erased cell, which is programmed by the uniform program and uniform erase scheme. Figure 6.11 shows the data retention time as a function of the number of program/erase cycles. The data retention time of an erased cell can be extended by using the uniform program and uniform erase scheme, especially beyond 100K program and erase cycles.

Figure 6.12 shows the data retention characteristics of both a programmed and an erased cell after various P/E (program/erase) cycles for two program and erase schemes [7]. In a uniform program (write) and uniform erase scheme, a large threshold voltage (V_{th}) shift in a programmed cell can be observed after a 20-min bake in a cell subjected to 1 million program/erase cycles. This is also due to the detrapping of electrons from the tunnel oxide. This V_{th} shift was observed in a 1.0-μm design rule cell, but it became worse as scaling memory cell size. In a <30-nm cell, same initial V_{th} shift can be observed even after several thousand program/erase cycles. This issue is further discussed in the next section.

B. Temperature Dependence In order to estimate the data retention lifetime of the memory cell under the operation temperature (<85°C) in the case of the uniform

Micron Ex. 1014, p. 223
Micron v. YMTC
IPR2025-00119

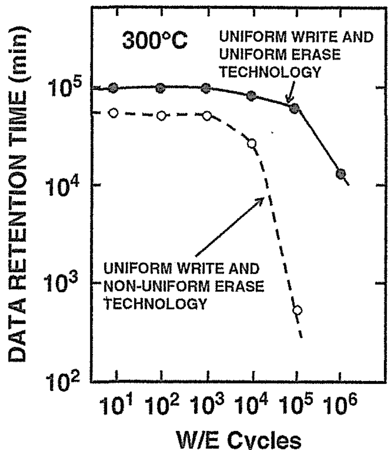

FIGURE 6.11 Data retention time of the erased memory cell after program and erase cycling. The data retention time is defined by the time that the threshold voltage reaches −0.5 V during the retention bake at 300°C. Copyright © 1994 IEICE.

program and uniform erase scheme, the data retention characteristics at different temperatures (150–300°C) had been measured, as shown in Fig. 6.13 [7]. The 1.0-μm design rule memory cells with a 9.7-nm tunnel oxide are subjected to 1 million program/erase cycles. For the programmed cell, the V_{th} monotonically shifts negative toward the neutral V_{th} (0.7 V), as baking time increases. The negative V_{th} shift after 20 min of baking increases with the number of program(write)/erase cycles, as shown in Fig. 6.14a. This is because both the charge loss from the floating gate and the electron detrapping from the tunnel oxide to the substrate are enhanced at high

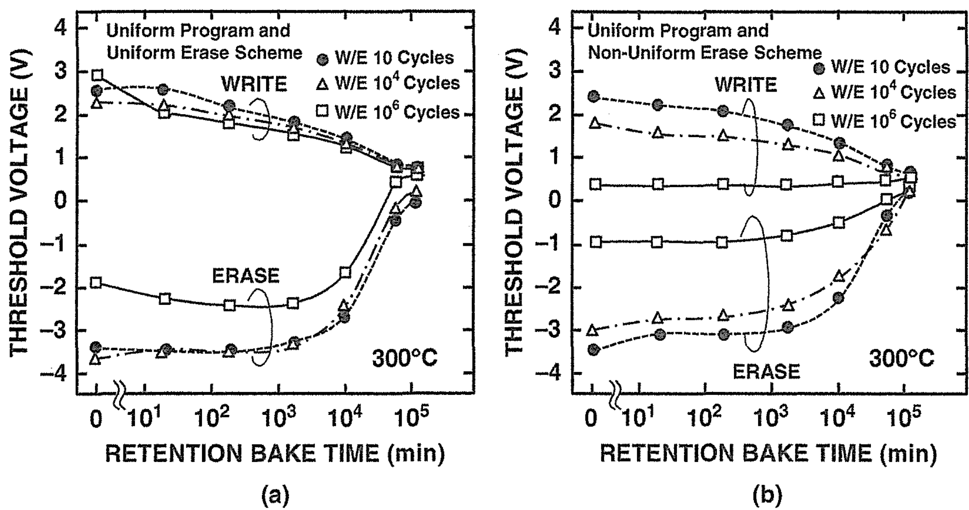

FIGURE 6.12 Data retention characteristics after different program/erase cycle. (a) Uniform program and uniform erase scheme. (b) Uniform program and nonuniform erase scheme. Copyright © 1994 IEICE.

Micron Ex. 1014, p. 224
Micron v. YMTC
IPR2025-00119

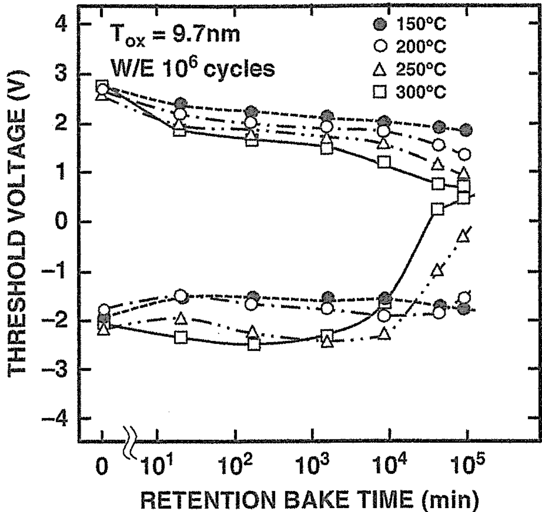

FIGURE 6.13 Dependence of the data retention characteristics on the baking temperature in the uniform program and uniform erase scheme. Copyright © 1994 IEICE.

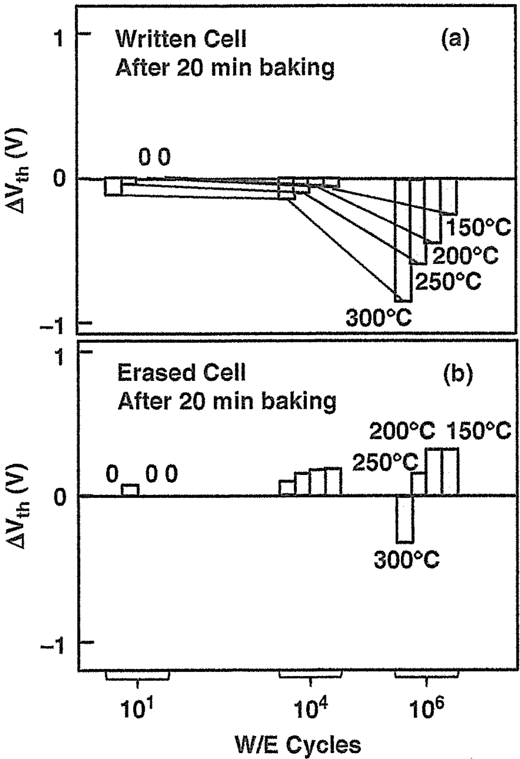

FIGURE 6.14 Threshold voltage shift after a 20-min bake at 150–300°C. (a) Programmed ce11 (b) Erased cell. Copyright © 1994 IEICE.

Micron Ex. 1014, p. 225
Micron v. YMTC
IPR2025-00119

temperatures. For practical applications of the NAND flash memory, the negative V_{th} shift of the programmed cell at 100°C is estimated to be less than 0.2 V. So the V_{th} margin of the programmed cell should be determined with more than 0.2 V in this cell.

For the erased cell, the phenomenon of the effective increase of the stored positive charge can be observed at all test temperatures from 150°C to 300°C, as shown in Fig. 6.13. However, the threshold shift is strongly dependent on the temperature. For a bake of 300°C, the threshold voltage shows a negative shift until 200 min; after that, the V_{th} shows a positive shift toward the neutral V_{th} (0.7 V). However, for 150–250°C baking, the initial V_{th} shift is positive (about 0.3 V) after 20 min of baking; after that the V_{th} shift is negative for 1000 min and becomes positive again with V_{th} shifting toward the neutral V_{th}. The first positive V_{th} shift after about 20 min of baking can be explained by the charge loss from the floating gate due to the high-field-stress-induced leakage current in the tunnel oxide [5, 26, 27]. The negative shift of the V_{th} can be explained by the effect of electron detrapping from the tunnel oxide to the substrate.

Because of the lower detrapping rate of electrons at lower temperatures, the time at which the minimum V_{th} is reached during the bake is longer at lower temperature—for example, 1000 min at 250°C and 10,000 min at 200°C. Therefore, at the operation temperature (<100°C), the maximum negative V_{th} shift will occur after more than 1,000,000 min.

Figure 6.15 shows the estimation of the data retention time using the temperature dependence of the data retention of the memory cell for different numbers of program/erase cycles. Due to the program/erase cycling, the data retention time is shortened. However, 10 years of data retention time for an operation temperature of less than 100°C can be guaranteed even after 1 million cycles in the case of the

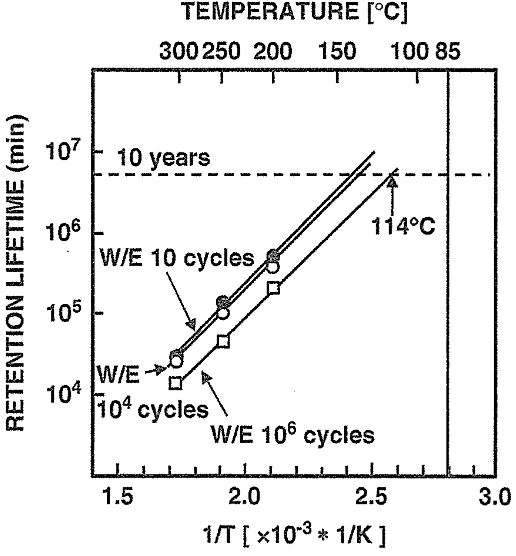

FIGURE 6.15 Estimation of the data retention time at the operation temperature. Copyright © 1994 IEICE.

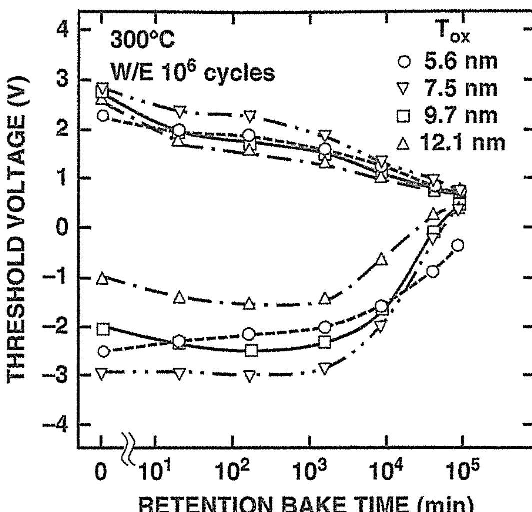

FIGURE 6.16 Dependence of the data retention characteristics on the tunnel oxide thickness in the uniform program and uniform erase scheme. Copyright © 1994 IEICE.

uniform program and uniform erase scheme. The activation energy (slope in Fig. 6.15) of data retention time is almost the same in the range of 10–10^6 program/erase cycling in the case of this experiment of a 1.0-μm rule cell. This is because data retention time is mainly determined by the mechanism of charge loss from floating gates; however; data retention time is not determined by detrapping mechanism, as shown in Fig. 6.12 and Fig. 6.13.

C. Tunnel-Oxide Thickness Dependence In order to clarify the scaling limit of the tunnel-oxide thickness with respect to the data retention, the data retention characteristics of cells with various tunnel-oxide thicknesses had been measured, as shown in Fig. 6.16 [7]. The negative V_{th} shift of a programmed cell after a 20-min bake decreases with decreasing oxide thickness, as shown in Fig. 6.17a, because the amount of electron detrap is smaller in thinner tunnel oxide. For an erased cell, the negative V_{th} shift can be observed in cells having a 7.5- to 12.1-nm tunnel oxide; however, the negative V_{th} shift cannot be observed for cells with a tunnel oxide of 5.6 nm. The V_{th} shift is positive for those cells. This is because the stress leakage current increases as the tunnel oxide becomes thinner, so in the 5.6-nm tunnel-oxide case, the charge loss from the floating gate is larger than the influence of the detrapping of electrons.

Figure 6.18 shows the dependence of the data retention time on both the tunnel-oxide thickness and the number of program/erase cycles [7]. For the thinner tunnel oxides, the data retention time is shortened in case of 10–10K program/erase cycles; however, in the case of 1 million cycles, the data retention time is extended because of the reduced window narrowing due to the reduced electron detrapping. Therefore, the scaling of the tunnel oxide is not limited by the degradation of the data retention due to the thinning of the tunnel oxide up to a thickness of 5.6 nm.

Micron Ex. 1014, p. 227
Micron v. YMTC
IPR2025-00119

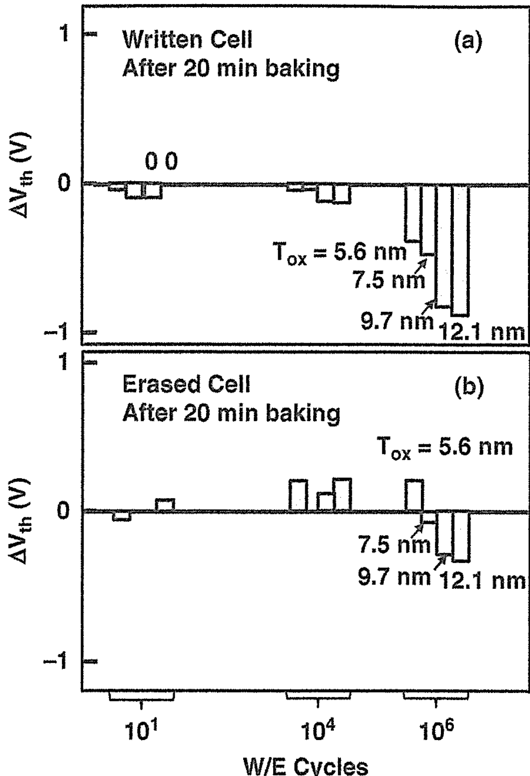

FIGURE 6.17 Threshold voltage shift after a 20-min bake at 300°C. The memory cell has a 5.6- to 12.1-nm tunnel oxide. (a) Programmed cell, (b) Erased cell. Copyright © 1994 IEICE.

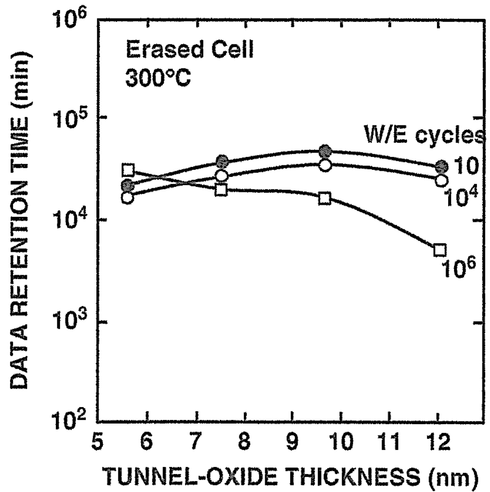

FIGURE 6.18 Data retention time at 300°C depending on the tunnel-oxide thickness and the number of program/erase cycles. Copyright © 1994 IEICE.

Micron Ex. 1014, p. 228
Micron v. YMTC
IPR2025-00119

The program/erase cycling endurance and data retention characteristics were described in two program/erase schemes. In a uniform program and uniform erase scheme, the wide cell threshold voltage window was guaranteed even after 1 million program/erase cycles. And the data retention characteristics was improved by applying a uniform program and uniform erase scheme, which uses uniform Fowler–Nordheim tunneling over the whole channel area during both program (write) and erase. It was clarified experimentally that the detrapping of electrons from the gate oxide to the substrate results in an extended retention time of erase state. The uniform program and uniform erase scheme results in a highly reliable flash memory with an extended data retention time.

6.3 ANALYSIS OF PROGRAM/ERASE CYCLING ENDURANCE AND DATA RETENTION

6.3.1 Program/Erase Cycling Degradation

The performance and reliabilities of flash memory cells are degraded by repeating the program and erase cycling. The degradation is mainly related with the tunnel oxide degradation by Fowler–Nordheim (FN) tunneling electron injection stress during program and erase operations. Many degradation phenomena of the thin tunnel oxide had been reported.

First, the cell V_{th} shift dependence on the program and erase pulse is discussed [28]. In the program/erase scheme of the NAND cell, the V_{th} shift during program/erase cycling mainly appears on the erased V_{th}, because the erased V_{th} is very sensitive to charge trapping in the tunnel oxide, as described in Section 6.2.2. For example, if electrons are trapped in the tunnel oxide, the V_{th} of the memory cell will shift in the positive direction. Furthermore, since the electric field strength in the tunnel oxide is reduced due to the trapped electrons, the FN tunneling current during the erase will be reduced, resulting also in a V_{th} shift in the positive direction.

To investigate the program and erase pulse effect, erase V_{th} degradation was compared in program and erase pulse shape [28]. Four different program/erase pulse shapes had been used, as shown in Fig. 6.19. For the pulses A and B, the stress during erase is very low but the stress during program (write) is high for pulse A and relatively low for pulse B. For the pulses C and D, the program (write) stress is low while the erase stress for pulse C is high and relatively low for pulse D. Figure 6.19a,b shows the V_{th} shift in the erased state during program/erase cycling. During the first few hundred cycles, the V_{th} of the cells is lower than initially, this is because of hole trapping in the tunnel oxide which results in both a decrease of the V_{th} and an increase of the FN tunneling current density. After about 1000 cycles, the V_{th} increases because of electron trapping in the tunnel oxide. For the high stress pulse A and C, since more holes are generated [29], the hole trapping is about 10 times higher than for the low stress pulse B and D. Furthermore, from the differences in the slope of the V_{th} shift curves at 100K program/erase cycles, it can be concluded that the electron trap generation rate is higher for the high stress pulse A and C in comparison

Micron Ex. 1014, p. 229
Micron v. YMTC
IPR2025-00119

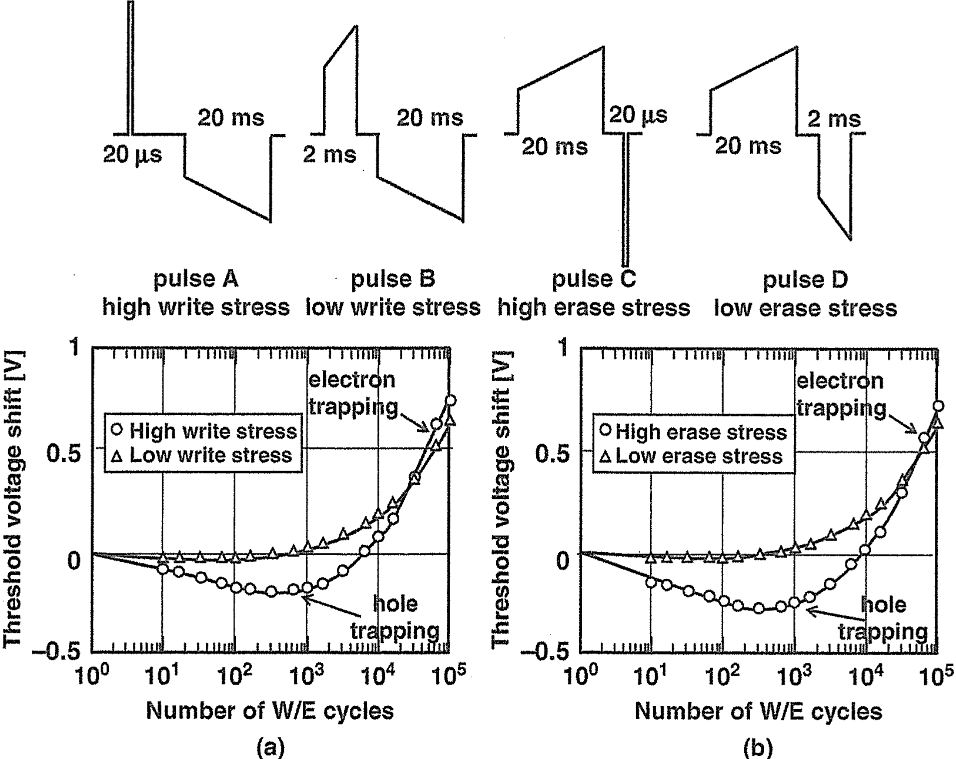

FIGURE 6.19 Program(write)/Erase pulses applied to the control gates of the memory cells. For pulses A and B the erase pulse is long (20 ms) and has a trapezoidal shape to obtain a low erase stress. For pulse A the program pulse is very short (20 µs); resulting in a high program stress. For pulse B the program (write) pulse is long (2 ms) and has a trapezoidal shape to reduce the write stress. For pulses C and D the program (write) pulse is long to obtain a low program stress. For pulse C the erase pulse is very short, resulting in a high erase stress, while for pulse D the erase stress is reduced by using a longer trapezoidal pulse. (a, b) Average erased threshold voltage shift of 96 memory cells relative to the initial erased threshold voltage during W/E cycling for (a) the high and low program (write) stress pulses A and B and (b) for the high and low erase stress pulses C and D. For the high-stress pulses A and C, hole trapping is significantly larger than for the low-stress pulses B and D. Electron trapping occurs for both the high- and low-stress pulses.

with the low stress pulse B and D. The hole trapping for high erase stress pulse C seems to be slightly larger than for the high program stress pulse A. This indicates that hole injection is increased for high erase stress pulse C; however, a more likely explanation is that for the high erase stress pulse C, the holes are trapped closer to the Si/SiO_2 interface (~10–20 Å), where they originated since the Si/SiO_2 interface corresponds with the anode during the high stress erase pulse. The hole traps near the Si/SiO_2 interface have much impact on the read disturb characteristics (Sections 6.4 and 6.5), the program disturb (Section 6.6), and the erratic over-program (Section 6.7) because the potential barrier for electron injection to the floating gate is reduced. Therefore the erase condition has to be carefully controlled to be better reliabilities.

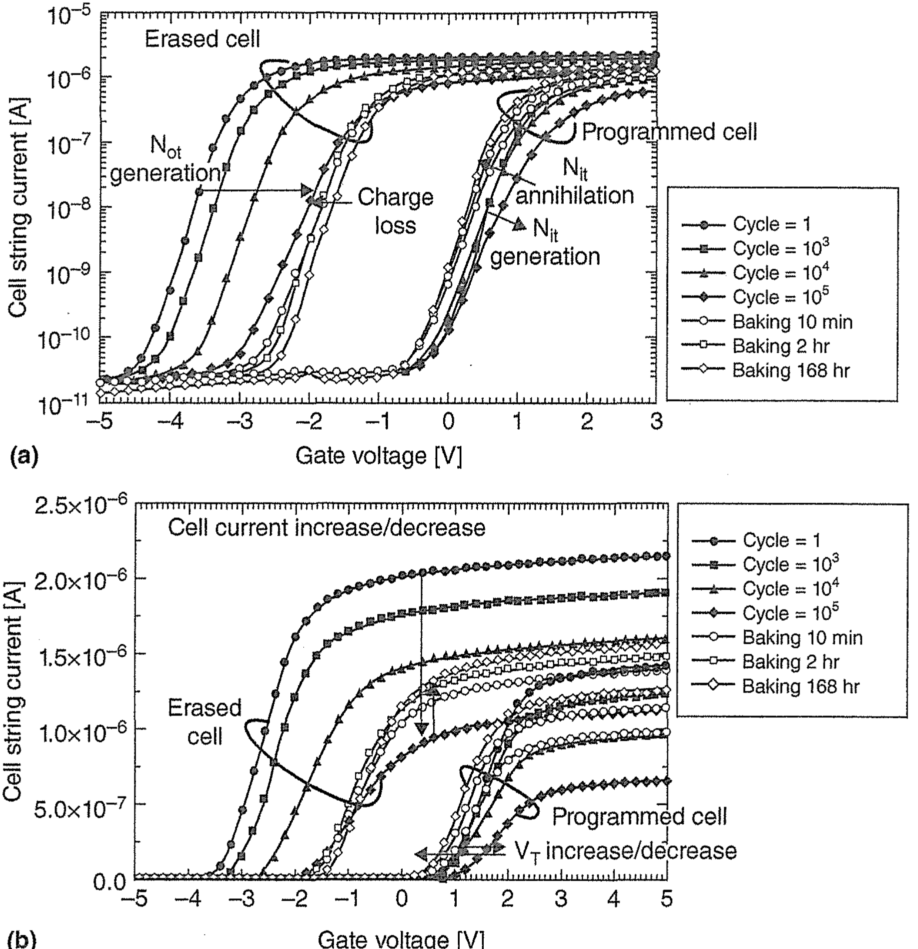

FIGURE 6.20 Drain-current–gate-voltage (I_d–V_g) curves of a cell transistor during endurance cycling and data retention test, with y-axis in (a) logarithmic scale and (b) linear scale. Programming pulses are 17 V–100 μs and erasing pulses are 17 V–1 ms in the cycling mode. The baking temperature was 250°C in the retention mode. Cell current and mobility are degraded by P/E cycling due to the interface trap generation and recovered by 250°C bake.

Next, memory cell degradation phenomena are discussed. As discussed above, the program/erase cycling has an impact on interface state and interface trap generation at the interface of tunnel oxide and substrate [30–32]. Figure 6.20 shows the cell current and mobility degradation by program/erase cycling. The origin of degradation mechanism is investigated by I_d–V_g curves of the cell transistor during the 100K program/erase cycling and 250°C 168H baking test. The oxide trap (N_{ot}) generation and charge loss can be monitored by the midgap voltage (V_{mg}) shift, and the interface trap density (N_{it}) can be monitored by the subthreshold slope of the transistor.

During program/erase cycling, oxide traps are generated in the tunnel oxide and electrons are captured at the trap sites, therefore, midgap voltage V_{mg} shifting

Micron Ex. 1014, p. 231
Micron v. YMTC
IPR2025-00119

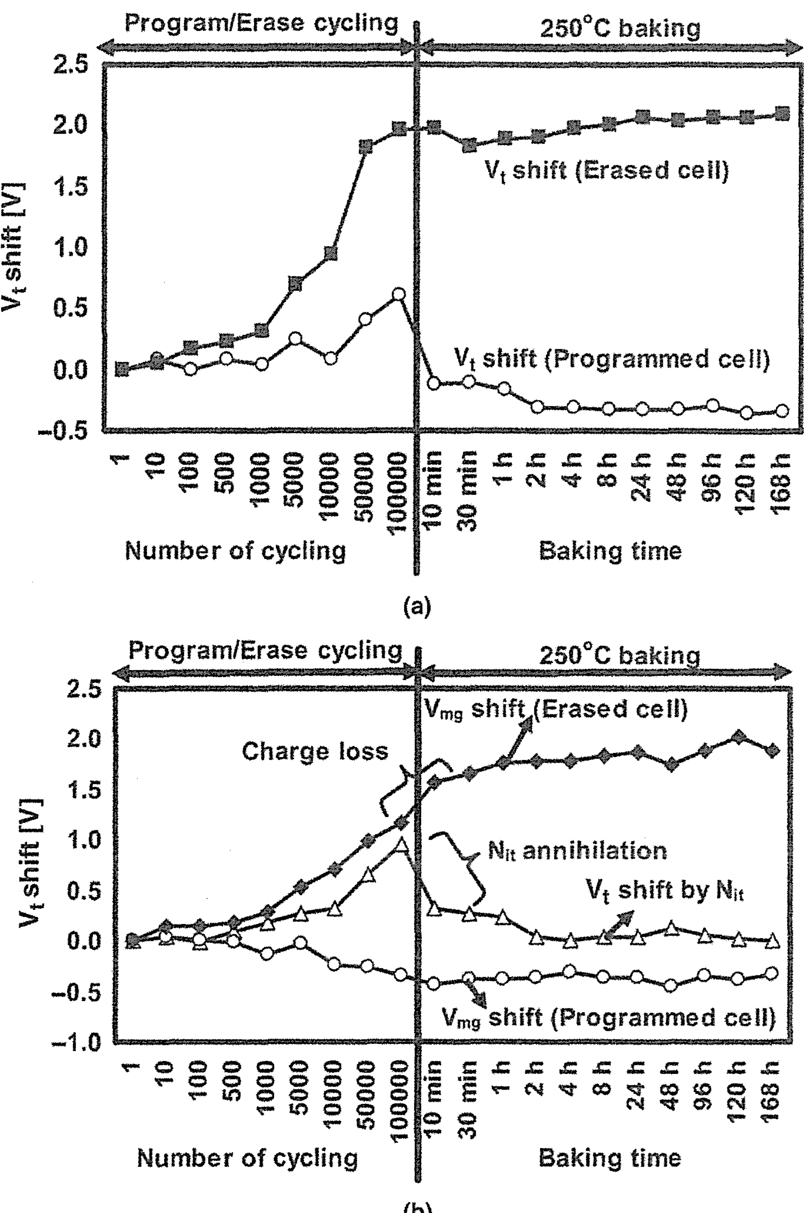

FIGURE 6.21 Analysis of threshold voltage shift in Fig. 6.20 during cycling and retention test. (a) Threshold voltage shift of the programmed cell and the erased cell. (b) Classification of threshold voltage shift by midgap voltage (V_{mg}) shift and by N_{it} generation/annihilation. V_t shift by interface trap (N_{it}) is the same both for the programmed cell and the erased cell.

toward the positive direction can be observed in the erased cells from 10^3 cycles to 10^5 cycles, as shown in Fig. 6.20. However, this phenomenon cannot be monitored in the program cell because the electron trap effects of reducing both FN current and positive V_t shift are canceled out, as described in Section 6.2.2. The threshold voltage shift in the cycling and the retention mode is shown in Fig. 6.21a. The threshold

Micron Ex. 1014, p. 232
Micron v. YMTC
IPR2025-00119

voltage shift can be classified by the midgap voltage V_{mg} shift and by the subthreshold slope change (V_t shift by N_{it}), as shown in Fig. 6.21b. The midgap voltage V_{mg} shift indicates oxide trap generation in the endurance cycling mode and charge loss in the retention mode. The subthreshold slope degradation and saturation current reduction (see Fig. 6.20b) indicate the interface trap generation in the endurance mode. And the recovery of subthreshold slope and saturation current indicates the interface trap annihilation in the retention mode of 250°C bake due to detrapping. In the endurance mode, oxide traps and interface traps are generated, however, in the retention mode, charge loss and interface trap annihilation occurs. The threshold voltage shift by interface trap annihilation is somewhat larger than the charge loss component (Fig. 6.21b). Thus, it can be concluded that the effect of interface traps in the degradation and data retention characteristics are very important in NAND flash cells.

The program/erase cycling degradation mechanism had been also reported in the scaled memory cell of 51- to 32-nm design rule [33]. The degradation phenomenon was explained by nonuniform trap distribution in tunnel oxide along a channel length (L) direction as well as channel width (W) direction.

The cycling degradation was compared between a 90-nm cell with a long shallow trench isolation (STI) edge cell structure (LSE) (see structure in Fig. 6.22a) and a 51-nm cell with short STI edge structure (SSE) (see structure in Fig. 6.22c), as shown in Fig. 6.22. The threshold voltage change after cycles (ΔV_t) in a program state of LSE (Fig. 6.22a,b) is mainly due to ΔSS (subthreshold slope degradation) resulting from generation of interface states [32]. In LSE, V_{MG} (midgap voltage) in a program state remains almost constant during cycling. However, in the case of SSE (Fig. 6.22c,d), V_{MG} in the program state shifts to the higher gate voltage during cycling along with subthreshold slope degradation (ΔSS). This is explained by the fact that a narrow FG width of SSE devices leads to high-field crowding near FG edges during the erase operation [33]. Accordingly, erase FN current density increases under FG edges. The increased erase current density at the FG edges together with the effects of the etch damage can lead to nonuniform generation of the oxide trap charges over channel area with maximum charge concentration near floating gate edges (nonuniform trap distribution of channel width (W) direction). This trapped charge affects mainly the erase tunneling current, but does not affect the program tunneling current because the program current flows at the FG center area. Therefore, V_{MG} in the program state shifts to the higher gate voltage in SEE because program FN tunneling current does not get reduced by oxide trapped charge.

This nonuniform charge distribution model was extended to the direction of gate length (L direction). It is known that oxide charges located near source/drain (S/D) junctions influence not only V_{MG} but also SS [34]. ΔSS (subthreshold slope degradation) due to the nonuniform oxide charges was simulated using negative charge clusters placed in a tunnel oxide under FG edges [33]. Simulation results reveal that the charge clusters can either increase or decrease SS depending on S/D overlap. This phenomenon can be explained by three-dimensional current flux distortion at a low current level in the presence of negative charge over the S/D region. If the S/D overlap is large, the oxide charges under FG edges are located over S/D region. Thus, the oxide charges effectively impede S/D electrons current and confine the electrons

Micron Ex. 1014, p. 233
Micron v. YMTC
IPR2025-00119

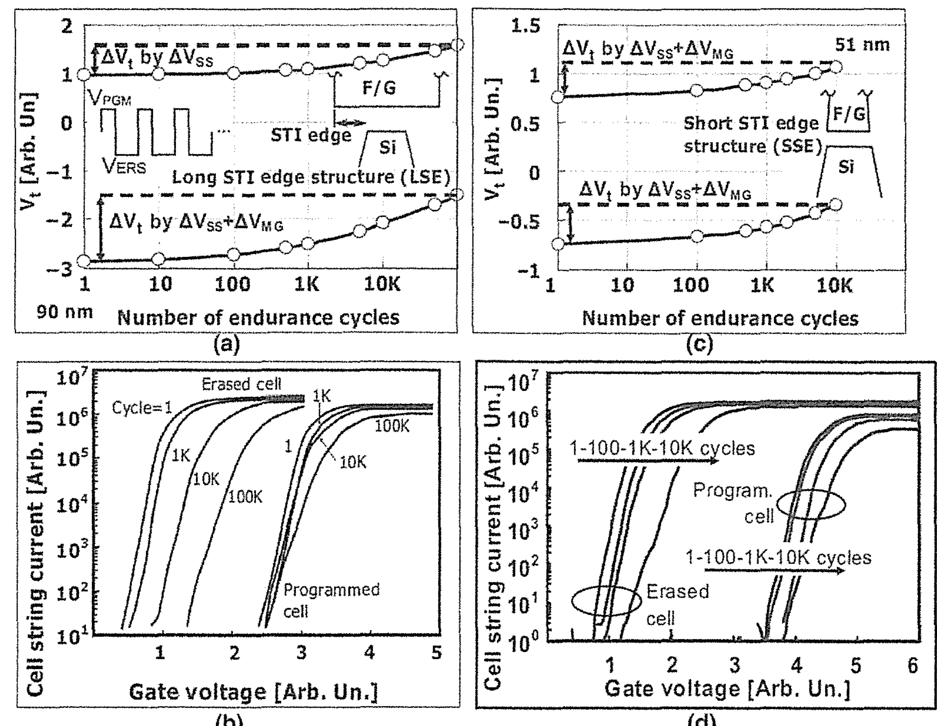

FIGURE 6.22 (a) Typical P/E cycling characteristics of LSE devices (90-nm cell). Erase state V_t degradation is caused by V_{MG} and SS change. Program state V_t is determined only by SS increase. Inset shows feature of LSE structure (bitline cross-section view). (b) I_d–V_g characteristics for various cycle amounts indicate combined V_{MG} and SS degradation in the erase state and SS degradation without V_{MG} change in the program state. (c) Typical P/E cycling characteristics of SSE structure (see inset: 51-nm cell). Erase state V_t degradation is caused by V_{MG} and SS shifts. Contrary to LSE, V_t in the program state is also determined by SS and V_{MG} change. (d) I_d–V_g characteristics for various cycle amounts indicate combined V_{MG} and SS degradation in the program and erase states.

contributing to subthreshold currents to a channel surface region. This effect leads to the improved SS. On the other hand, in the cell with a relatively small S/D overlap, the oxide charges impede both channel and S/D electrons current. Consequently, subthreshold currents arise far from the channel surface. This results in degradation of gate controllability and the deteriorated SS.

The nonuniform charge trapping model can well explain measurement results proving the dependence of ΔSS (subthreshold slope degradation) on an initial SS after cycling. For the higher initial SS value (a larger S/D overlap), SS reduces (SS improves) after cycling. However, for lower initial SS value (a smaller S/D overlap), SS increases (SS is degraded) after cycling [33].

Therefore, the model of nonuniform distribution of negative oxide charges, which are located near the floating gate edge, can explain the program/erase degradation mechanism in the scaled memory cell below the 50-nm design rule. It is shown that the nonuniformly distributed negative charges reduce erase FN current while they do

Micron Ex. 1014, p. 234
Micron v. YMTC
IPR2025-00119

not change program FN currents, leading to a positive midgap voltage shift in the program state. The localized oxide charge near the gate edges significantly influences source/drain junction potential, resulting in observed degradation of subthreshold swing value.

6.3.2 SILC (Stress-Induced Leakage Current)

Figure 6.23 shows the typical V_t distribution of SILC (stress induced leakage current) characteristics of a NOR-type flash memory cell in room temperature [35]. The cells in Fig. 6.23a were cycled 10 times, and the number of tail bits (SILC bits) is small even after about 7 years' retention time. SILC bits are less than 0.1%. However, after 100K cycles in Fig. 6.23b, 20% of cells are showing a large V_t shift of SILC. There is a relatively large number of cells exhibiting very large V_t variation. In this experiment, the impact of cycling is enhanced by the thin tunnel oxide of about 8 nm thickness. The tails in the distributions are due to cells with an electron leakage current through the tunnel oxide much higher than that of cells in the main distribution.

The program/erase (P/E) cycling dependence of the SILC cell in 16-Mbit NAND flash memory was also presented [36]. Figure 6.24 shows the memory cell V_t distribution of a 1000-hr bake at room temperature after 100K and 1 million program/erase cycles. The initial V_t before baking is over 3.9 V. A small number of cells appear a large charge loss, and they make a distribution of "tail bits." The tail bits increases as P/E cycling increases over 10^5. And the cell of large charge loss (SILC bit) has strong V_t dependence (electric field dependence). Higher V_t (higher electric field) produces a worse V_t shift of SILC. The leakage current was calculated from V_t shift of SILC bit, shown in Fig. 6.25. J/S is leakage current density. J is calculated by

$$J = C_{\text{cg-fg}} * \Delta V_t / \Delta t$$

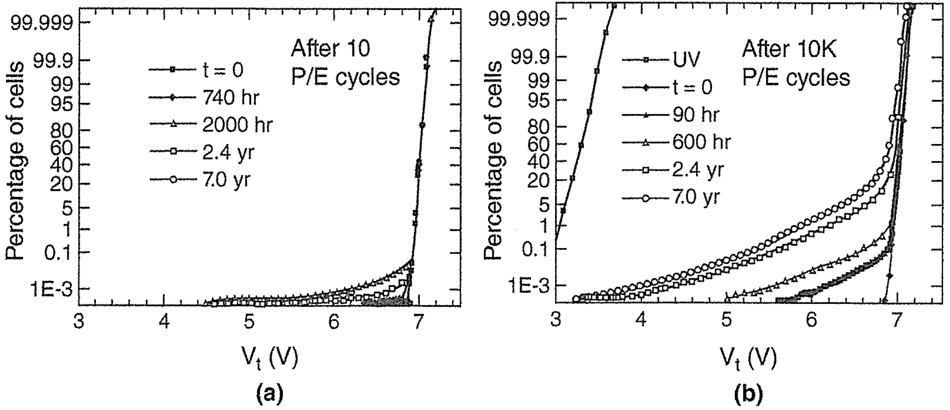

FIGURE 6.23 Data retention of SILC in the NOR flash cell. V_t distribution at different room-temperature storage times for an 8-nm-thick oxide after (a) 10 and (b) 10K cycles. Cell V_t shift-related SILC is much larger than detrapping, but a smaller percentage of cells has SILC. Strong dependence on number of cycles is observed. SILC cells disappear in high-temperature bake (250°C). Trap-assisted tunneling would be the root cause of SILC.

Micron Ex. 1014, p. 235
Micron v. YMTC
IPR2025-00119

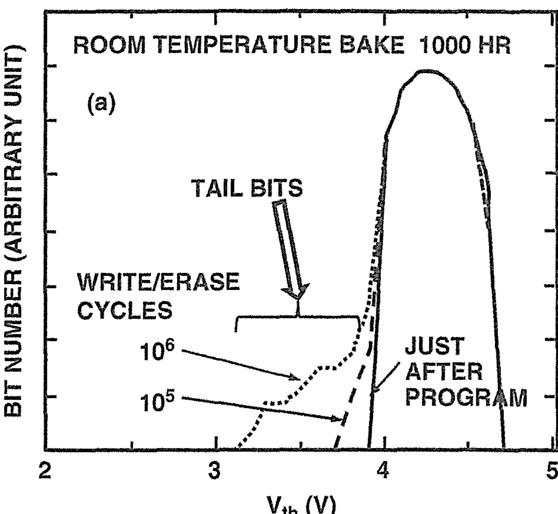

FIGURE 6.24 Data retention of SILC in NAND flash cells. V_t distribution. Solid line indicates V_t just after programming. Dotted line and dashed line are the V_t distributions after a 1000-hr bake. In programming, V_t is controlled to be more than 4.0 V.

where $C_{\text{cg-fg}}$ is the capacitance between a control gate and a floating gate. The charge loss is very small when the electric field E_{ox} is less than 1.2 MV/cm, where it corresponds to $V_t = 2.0$ V. However, it rises sharply near $E_{\text{ox}} = 1.4$ MV/cm, and it increases exponentially with increasing E_{ox}.

Repeatability of SILC bits had been also investigated [36], as shown in Fig. 6.26. Two times data retention test of first and second MEAS was performed for the same cells with recording address of bits. Tail bits behavior is categorized into two groups.

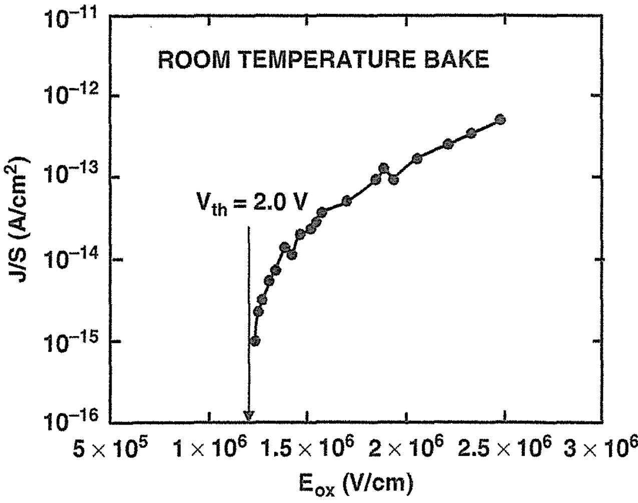

FIGURE 6.25 Charge loss rate of a typical tail bit as a function of the electric field E_{ox} in tunnel oxide.

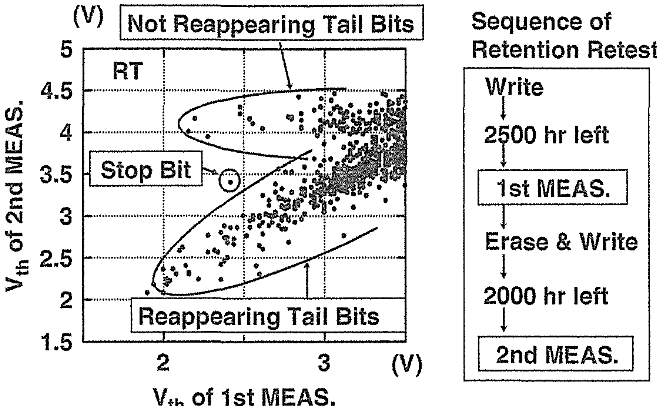

FIGURE 6.26 Reappearence of the anomalous cells when retention characteristics are measured again. After 1 million program (write)/erase cycles, memory cells were baked for 2500 hr at room temperature. After that, all cells are erased, programmed, and baked for 2000 hr again.

One group is transformed from tail bits to normal cells during reprogramming and it appears as normal cells (see "Not Reappearing Tail Bits"). The other is continuously kept as anomalous tail bit cells, which show almost the same charge loss characteristics in two measurements (see "Reappearing Tail Bits"). Many bits (~90%) appeared as the tail bits again after reprogramming and one more retention bake. After one more program/erase operation, about 10% of tail bits are transformed into normal cells. This fact indicates that tail bits are easily transformed from tail bit to normal bit. In Fig. 6.27, an exceptional cell named "stop bit" is identified. By tracking the

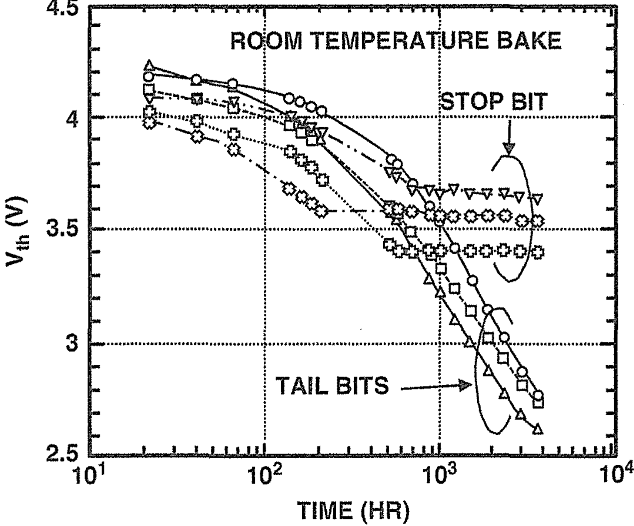

FIGURE 6.27 Charge loss characteristics of the anomalous cells of "stop bit." There are three bits whose rapid charge loss is suddenly and randomly stopped.

Micron Ex. 1014, p. 237
Micron v. YMTC
IPR2025-00119

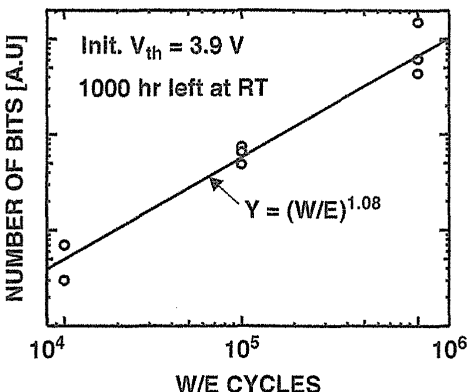

FIGURE 6.28 Program/erase cycle dependence of tail bits. The initial V_t before baking exceeds 3.9 V. Tail bits are defined as the cells whose V_t become less than 3.7 V during baking. The number of SILC bits is strongly depended on number of P/E cycles. The fail bits are almost proportional to P/E cycles. The degradation of tunnel oxide becomes worse proportional to P/E cycles.

stop bits individually, the stop bits are suddenly transformed from tail bit to normal bit during retention baking at room temperature, as shown in Fig. 6.27. Existence of stop bits strongly supports the easy transformation between the tail bit and normal bit.

This experiment result suggests that SILC is caused by electron current through trap-assisted tunneling. And trap and detrap would make reappearance and no reappearance phenomena. Also, these facts indicate that the anomalous leakage current of the tail bits flows only through one or a few spots. This leakage path can be easily transferred from inactivated to activated, or from activated to inactivated. A model of the leakage path is that electrons can easily flow from the floating gate to the substrates through the leakage path. Leakage paths are generated with a constant probability per power law of program/erase cycles, as shown in Fig. 6.28.

6.3.3 Data Retention in NAND Flash Product

Data retention performance was compared between several NAND flash products of different suppliers [37]. Figure 6.29a shows RBER (raw bit error rate) during a room-temperature bake after 10K program/erase cycles. RBER at time = 0 is due to program errors induced by program/erase cycling. RBER increases with retention time because of data retention errors.

Retention errors are mostly due to charge loss. A cell is losing charge and thus moves from one V_t level (e.g., L3, L2) to the one below. Two dominant mechanisms cause this retention error. The first one is a loss of FG charge via stress-induced leakage current (SILC) through the tunnel oxide [5, 27]. The second one is a detrapping of the tunnel-oxide charge that had been trapped during cycling [6–8, 38–40]. The effect on the V_t distributions is sketched in Fig. 6.29b. Detrapping causes the distributions

Micron Ex. 1014, p. 238
Micron v. YMTC
IPR2025-00119

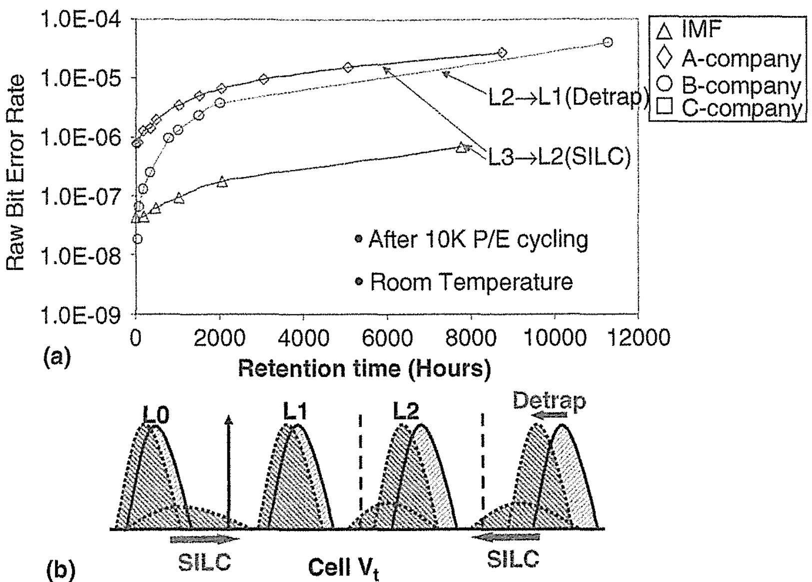

FIGURE 6.29 RBER versus room-temperature retention time following 10K P/E cycles. RBER increases as retention time.

to intrinsically broaden and shift lower. SILC causes a small number of cells to lose charge, forming tail bits in the distribution (see Section 6.3.2), as shown in Fig. 6.29b. Because SILC is more strongly field-dependent than detrapping [36, 41, 42], SILC tends to dominate the RBER of L3 cells, as shown in Fig. 6.29, which have the largest electric field in the tunnel oxide because they have the most stored electrons. Detrapping tends to dominate the RBER of L1 and L2 cells in the product of the B-company. This seems that errors are caused due to insufficient margin between L2 and below read voltage in this product. Interestingly, the same detrapping that generates retention errors also causes some program errors (from the final cycles) to recover with time because some of the tail cells that were above their intended read level drop below that read level due to charge loss. These program error bits are considered to be caused by "erratic over-program," as described in Section 6.7. Over the retention period of Fig. 6.29, about one-third of the program error recovered.

RBER of both retention mechanisms are greatly dependent on products from several suppliers. The errors were mostly L3→L2 type in two supplier's product, L2→L1 type in the third supplier's product, and both these types are available for other products. The characteristics of the retention errors can be more clearly seen by plotting only the charge-loss error, with excluding program errors, as shown in Fig. 6.30. Curve (△) in Fig. 6.30b shows that RBER scales as a power law in cycles, which is consistent with what is known for SILC [42]. Curve (○) has a much steeper dependence on cycling count, which is what is seen for the detrapping mechanism because of its intrinsic nature. Although curve (◇) is dominated by L3→L2, the increasing cycling slope suggests that the physical mechanism may be a mix of both SILC and detrapping. From data of several suppliers, it seems that each supplier has

Micron Ex. 1014, p. 239
Micron v. YMTC
IPR2025-00119

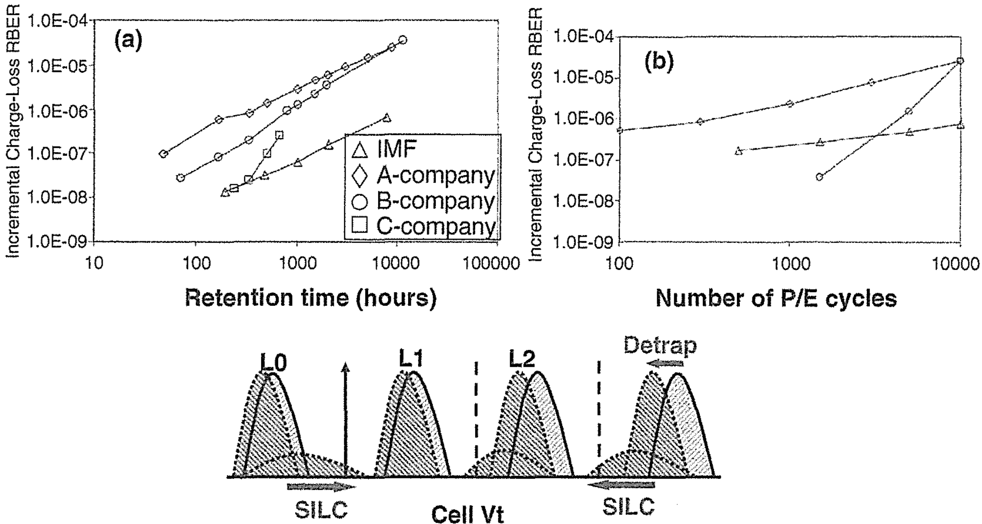

FIGURE 6.30 Charge-loss RBER as a function of (left) retention bake time after 10K P/E cycles and (right) number of P/E cycles followed by 1 year of bake. The bake was at room temperature. Data are available over only a short retention time (672 hr) for product.

a different strategy of V_t level setting. B-company of curve (○) has much less RBER in <1K cycling than other suppliers. However, at 10K cycling, L2→L1 type error is dominant as detrapping. The margin between L2 and below read voltage would not be enough. This product might have strategy to be a priority on minimizing RBER in <1K cycling, compromising L2 read margin. And other suppliers would have a priority on minimizing RBER at 10K cycling.

The relative contributions of the mechanisms also depend on the cycling and bake conditions. These devices were cycled at room temperature over several days and then baked at room temperature. If the cycling had been done at high temperature or over a longer time, then the detrapping contribution would have been reduced because some traps would have annealed in the delays between cycles [41,43]. On the other hand, if the retention bake had been done at high temperature, then the detrapping would have been larger and the SILC smaller. This is because detrapping is strongly temperature-accelerated [41,43] as shown in Section 6.3.2, whereas SILC anneals out at high temperature [41,44]. In fact, it is often thought that the detrapping mechanism is significant only at high temperature, but this discussion shows that some products under some conditions may be dominant by detrapping even at room temperature. The products dominated by detrapping charge-loss might have had substantially better retention over a more realistic time, such as year.

In order to minimize RBER in applications, it is very important to define the actual usage of NAND flash, such as temperature range, dominant temperature, number of cycles, cycling distribution, number of read, and so on. Based on this usage condition, the supplier has to optimize process and operations setting, such as V_t setting, to minimize RBER. And as applications are wide spread, product lines would be separated to satisfy criteria for each application.

Micron Ex. 1014, p. 240
Micron v. YMTC
IPR2025-00119

6.3.4 Distributed Cycling Test

It had been reported the distributed cycling results. Compagnoni et al. [45] presented a detailed experimental investigation of the cycling-induced threshold voltage instability of NAND flash memory cells, focusing on its dependence on cycling time and temperature. This investigation was a trial to obtain a reasonable and universal test condition for guarantee quality of NAND flash products, with mechanism of SILC and detrapping described in Section 6.3.3.

When the cells are in a programmed state after cycling, the cell V_t instability mainly shows up as a negative shift of its threshold voltage cumulative distribution, increasing with time and resulting from partial recovery of cell damage created in the previous cycling period. The threshold voltage loss shows a strong dependence not only on the tunnel-oxide electric field during retention, but also on the cycling conditions. In particular, the threshold voltage transient is delayed by cycling over a longer time interval or at higher temperatures on the logarithmic time axis. The delay factor is studied as a function of the cycling duration and temperature on 60- and 41-nm technologies, extracting the parameter values required for a universal damage-recovery metric for NAND.

Figure 6.31 schematically shows the experimental procedure most commonly adopted to test V_t instabilities after cycling on multilevel NAND flash memory devices. (1) A certain number N of P/E cycles is performed in a time $t_{cyc} = N^* t_{wait}$ (t_{wait} is a constant delay time between cycles). (2) A program-and-verify (PV) algorithm is performed on the cells to a certain programmed V_t level. (3) V_t is monitored (Read) at logarithmically spaced interval times t_B since the first read operation, performed

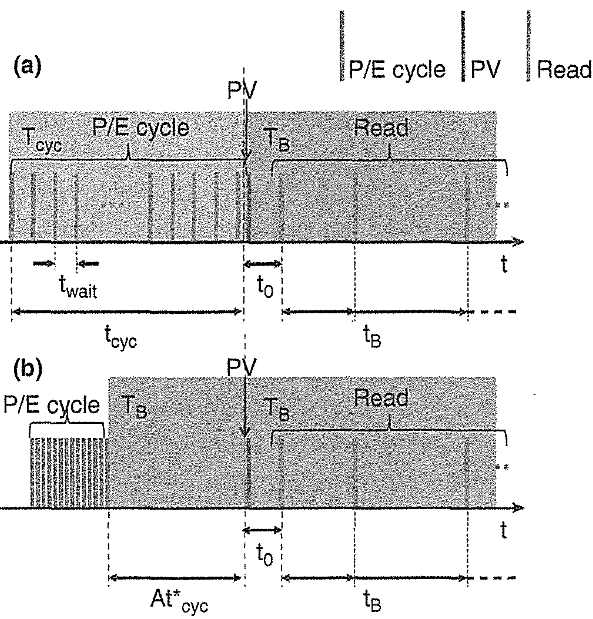

FIGURE 6.31 Schematics for the experimental procedure to investigate (a) cycling–induced V_t instabilities and (b) equivalent model for distributed cycling.

Micron Ex. 1014, p. 241
Micron v. YMTC
IPR2025-00119

after a delay since the end of cycling. Note that the V_t monitoring (Read) phase corresponds to a data retention experiment at temperature T_B, which may be room temperature (RT) or, more generally, a selected bake temperature. In the latter case, bakes are periodically interrupted and the device cooled to room temperature for V_t reading.

The amount of cell damage present at the end of cycling in the experimental test of Fig. 6.31a is the result of damage creation by P/E cycles and damage recovery during the time elapsing in between the cycles. Assuming that damage creation by P/E cycles depends neither on t_{wait} nor on T_{cyc} and that damage recovery during cycling can be reproduced by a bake period of duration proportional to t_{cyc} at temperature T_{cyc} after damage has been created [41, 43], the testing procedure of Fig. 6.31a is equivalent to that of Fig. 6.31b; that is, the test procedure of Fig. 6.31b can be used as the shorter time evaluation procedure. In this latter experimental test, the same cell damage existing in Fig. 6.31a prior to the PV operation is obtained by a fast cycling at RT and a subsequent damage recovery period of duration At^*_{cyc}, where A is a constant to be determined from experiments. In order to deal with damage recovery at a single temperature, the time t^*_{cyc} was introduced, corresponding to the time at T_B that is required to have the same damage recovery taking place in a time t_{cyc} at T_{cyc}:

$$t^*_{\text{cyc}} = t_{\text{cyc}} \cdot \exp(E_A(1/kT_B - 1/kT_{\text{cyc}})) \tag{6.1}$$

where an Arrhenius law of activation energy E_A was used for the time conversion. Assuming now that V_t has a logarithmic decrease due to damage recovery since the end of the damage creation period, the following formula holds for the V_t variation (ΔV_t) resulting in a time t_B since the first read operation in the experimental test of Fig. 6.31b and, in turn, of Fig. 6.31a [43]:

$$|\Delta V_t| = \alpha \ \ln(1 + t_B/(t_0 + At^*_{\text{cyc}})) = \alpha \ \ln(1 + t_B/t^*_B) \tag{6.2}$$

where α gives the magnitude of the logarithmic decrease of V_t due to partial damage recovery and $t^*_B = t_0 + At^*_{\text{cyc}}$. From the t^*_B definition, lower V_t-loss transients should result from longer t_{cyc} and and higher T_{cyc}.

Measurement and calculation results are shown in Fig. 6.32 as a function of $1/kT_{\text{cyc}}$, referring to cell distribution probability $p = 5 \times 10^{-5}$ of lower tail of distribution. This graph is defined as the Arrhenius plot for cycling, showing a characteristic time for the data retention ΔV_t transients as a function of the reciprocal of the cycling temperature and not of the retention temperature, which is always equal to RT. Experimental data can reasonably be reproduced by the theoretical definition of $t_B{}^*$ given in lines in Fig. 6.32, allowing the extraction of $E_A = 0.52$ eV, $t_0 = 0.8$ h, and $A = 0.022$ independently of the PV level and p. Note that the extracted value of t_0 well matches the experimental delay between the end of cycling and the first read operation on 60-nm NAND test-chip.

Experimental data and extracted theoretical trends in Fig. 6.32 show that for fixed t_{cyc}, $t_{\text{B}}{}^*$ grows with T_{cyc} in the large T_{cyc} regime, where the slope of the $t_B{}^*$ curve is

Micron Ex. 1014, p. 242
Micron v. YMTC
IPR2025-00119

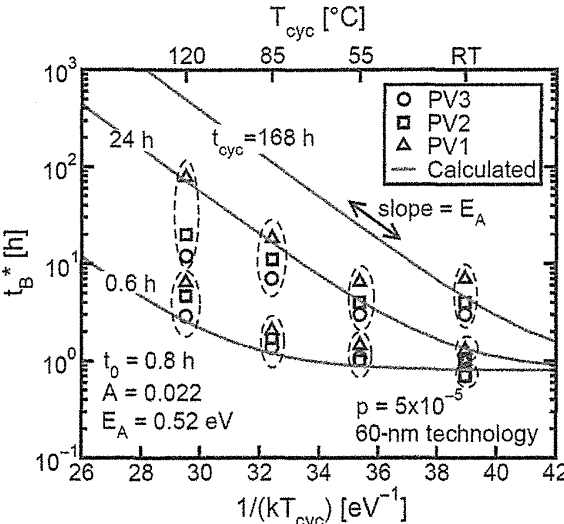

FIGURE 6.32 Arrhenius plot for cycling for the 60-nm test-chip.

given by E_A while reaching a constant value equal to t_0 for low T_{cyc}. The transition from the high to the low T_{cyc} regime depends on the t_{cyc} value, with longer cycling times allowing reaching the T_{cyc} sensitive regime at lower temperatures.

6.4 READ DISTURB

6.4.1 Program/Erase Scheme Dependence

It had been reported that the thin-oxide leakage currents, which are induced by the program and erase cycling stress, degrade the data retention and read disturb characteristics of memory cell [27]. Figure 6.33 shows the oxide current density

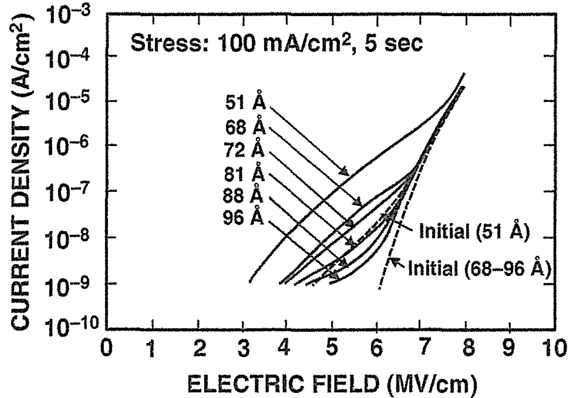

FIGURE 6.33 J–E characteristics (SILC) measured by capacitors having 51- to 96-Å oxide thickness before and after charge injection stress.

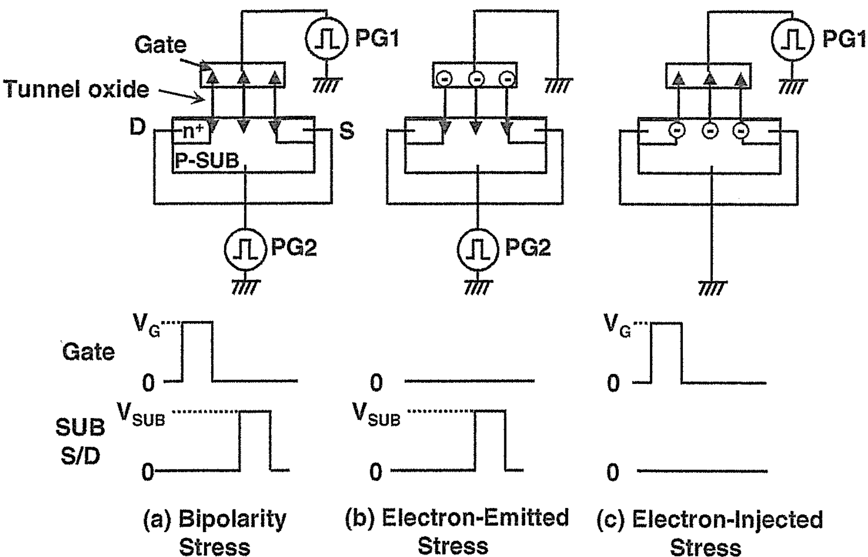

FIGURE 6.34 Setup and stressing waveform for (a) Bipolarity stress. (b) Electron-emitted stress and (c) Electron-injected stress. Stress conditions are shown in Table 6.2.

versus electric field before and after stress of electron injection from the substrate under positive gate polarity, where measurements are performed on the capacitors having 5.1- to 9.6-nm thickness oxide [27]. It can be seen that the stress induced leakage current (SILC) at low electric field is induced by the charge injection stress, and also SILC increases with decreasing the oxide thickness. The origin of the SILC was not well understood; however, it seems to be well fit by a Frenkel–Poole-type conduction. Due to SILC, it is very difficult to scale down the tunnel-oxide thickness of the memory cell [27]. An impact of SILC on NAND flash reliability was also investigated [5].

The stress-induced leakage currents (SILC) which are subjected to three types of simulated program/erase (P/E) stressing are compared. Figure 6.34 shows the stressing waveform for simulated P/E stress. Table 6.2 shows the stress conditions which correspond to program/erase conditions in NAND flash memory cells. A high voltage is applied to gate or substrate (SUB) and source/drain (S/D). The SILCs are

TABLE 6.2 Stress Conditions

T_{ox}	Gate	Sub, S/D
5.6 nm	6.79 V	8.0 V
	0.2 ms	0.2 ms
7.5 nm	7.91 V	9.15 V
	0.2 ms	0.2 ms

[a]High-voltage pulses are applied to the gate and substrate. Stress voltage V_g and V_{sub} are determined by the voltage that the opposite tunneling currents are approximately the same.

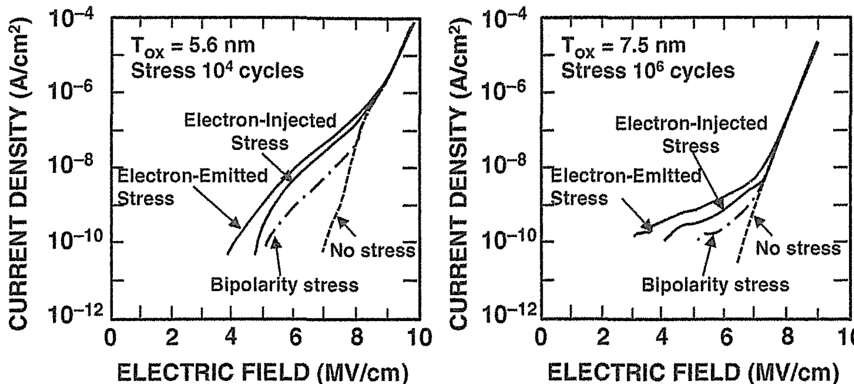

FIGURE 6.35 Stress-Induced Leakage currents (SILC) of tunnel oxide at low voltages for 5.6- and 7.5-nm oxide thickness after bipolarity stress, electron-emitted stress, and electron-injected stress. In the case of bipolarity stress, oxide leakage current is small as compared with the others.

induced by the electron injection and emission between the gate and substrate, as shown in Fig. 6.35. It was observed that the SILC induced by (a) bipolarity dynamic stressing is about one order smaller than that induced by both (b) the electron-emitted stress and (c) the electron-injected stress. This result shows that the origin of the SILC can be removed by reverse Fowler–Nordheim tunneling (FN-t) stress, and it would be the directional defect or strain or trapped holes in the tunnel oxide. This reduction of the SILC by bipolarity stress can extend the read disturb and data retention time in NAND flash memory cell.

Read disturb characteristics of the flash memory cell are compared in two program/erase (P/E) schemes. One is a bipolarity FN-t W/E technology, performed by uniform injection and uniform emission over the whole channel area of a flash memory cell (Fig. 6.36a). The other is a conventional channel-hot-electron (CHE) write and FN-t erase technology for NOR-type flash, performed by CHE injection at drain and uniform emission over the whole channel area (Fig. 6.36b). In erasing, a high voltage is applied to the substrate [6] as well as source/drain in order to prevent from causing the degradation of the thin-gate oxide due to band-to-band tunneling stress [21]. Flash memory cells which are used in this experiment have 5- to 10-nm-thick tunnel oxide, 25-nm-thick ONO inter-poly dielectric (IPD) [22], and 0.8-μm gate length.

Figure 6.37 shows the program(write)/erase endurance characteristics of two P/E schemes. The closure of the cell threshold window has not been found up to 100,000 program/erase cycles in both two schemes.

Read disturb characteristics were measured at applied various gate voltage conditions, which were the accelerated electric field test, as shown in Fig. 6.38 [5]. In the case of a CHE write and FN-t erase scheme (technology), the stored positive charges rapidly decay as stress time (retention time) increases, so the threshold window decreases. However, in the case of a bipolarity FN-t W/E scheme (technology), data loss of the stored positive charges is greatly improved. So, data retention time

Micron Ex. 1014, p. 245
Micron v. YMTC
IPR2025-00119

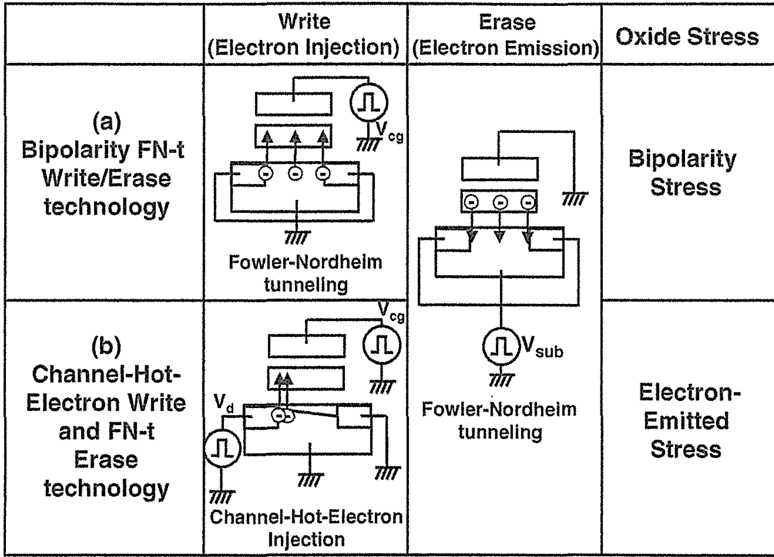

FIGURE 6.36 Comparison between (a) bipolarity FN tunneling write/erase technology, corresponding to bipolarity stress of tunnel oxide and (b) channel hot electron(CHE) write and FN tunneling erase technology, corresponding to electron-emitted stress of tunnel oxide, because of no leakage current induced by CHE injection.

of a bipolarity FN-t W/E scheme is extended about 10 times as long as that of conventional scheme. This phenomenon can be explained by the fact that the SILC is reduced by the bipolarity FN tunneling stress.

Figure 6.39 shows the data retention time under the read-disturb condition after program and erase cycling as a function of the tunnel-oxide thickness. The improvement in data retention is more effective with decreasing oxide thickness. Therefore, in the bipolarity FN-t W/E scheme, the tunnel-oxide thickness can be reduced by scaling

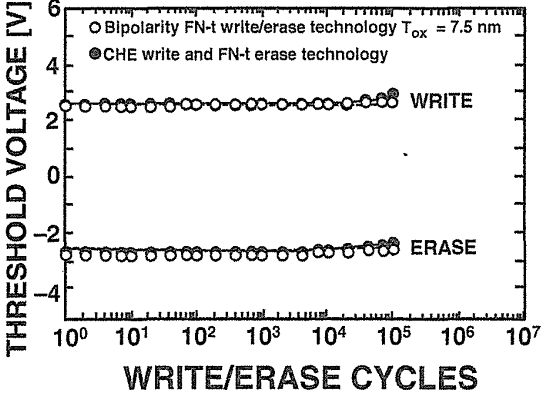

FIGURE 6.37 Endurance characteristics of flash memory cell with 7.5-nm tunnel oxide. In bipolarity FN tunneling W/E technology, write: $V_{cg} = 18$ V, 1 ms, erase: $V_{sub} = 20$ V, 1 ms. In conventional technology, write: $V_{cg} = 7$ V, $V_d = 8.5$ V, 1 ms. Erase: $V_{sub} = 20$ V, 1 ms.

Micron Ex. 1014, p. 246
Micron v. YMTC
IPR2025-00119

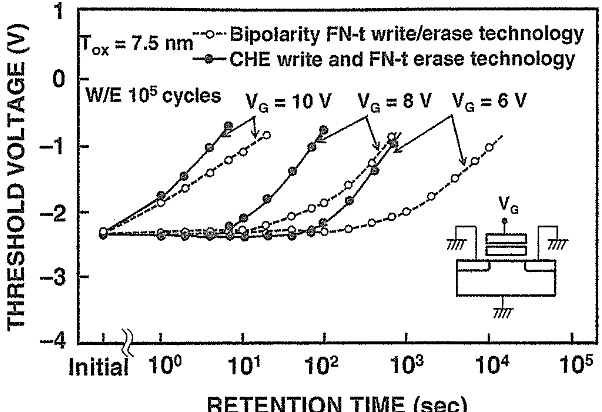

FIGURE 6.38 Read disturb characteristics at the applied various gate voltage stress. Flash memory cell having 7.5-nm-thick oxide are subjected to 100,000 program (write)/erase cycles. In bipolarity FN tunneling W/E scheme, data loss of stored positive charge is improved as compared with conventional scheme; it corresponding to results of oxide leakage currents.

down the flash memory cell. Then, it gives advantages of low-voltage program and erase operations.

Initial data loss is measured at 300°C, as shown in Fig. 6.40. It is confirmed that the initial data loss of bipolarity FN-t W/E scheme is smaller than that of the CHE write and FN-t erase scheme due to reduction of stress-induced oxide leakage current.

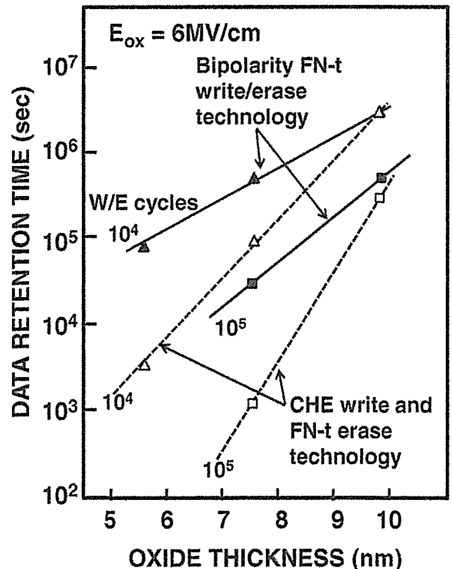

FIGURE 6.39 Data retention time of the flash memory cell after program and erase cycling as a function of tunnel-oxide thickness. Data retention time is defined by the time that V_{th} reaches −1.0 V during the applied gate voltage stress (accelerated read disturb condition). In bipolarity FN tunneling write/erase scheme, the tunnel-oxide thickness can be reduced with scaling down the flash memory cell.

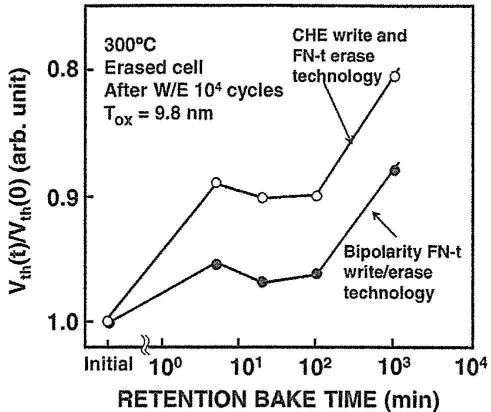

FIGURE 6.40 Initial data loss of the erased cell which stores positive charges in floating gate as a function of retention bake time at 300°C in a bipolarity FN tunneling write/erase scheme and CHE write and F–N tunneling erase scheme, subjected to 10,000 program and erase cycles.

Read disturb and data retention characteristics have been described in two different program/erase schemes on flash memories. It is clarified experimentally that flash memory cell, which is programmed and erased by bipolarity uniform Fowler–Nordheim tunneling (FN-t), has 10 times as long retention time as the conventional one, which is programmed by channel-hot-electron (CHE) injection and erased by unipolarity FN-t. This difference of data retentivity between these two W/E schemes is due to decreasing the stress-induced leakage current (SILC) in thin tunnel oxide by bipolarity FN-t stress. Also, this improvement in data retention is more remarkable, in accordance with decreases in the tunnel-oxide thickness.

6.4.2 Detrapping and SILC

The read disturb characteristics become worse after program/erase cycling due to generation of SILC (stress-induced leakage current) in tunnel oxide during program/erase cycling. The SILC mechanism had been reported by several papers [44, 46–58]. And an impact of SILC on NAND memory cell characteristics had been also reported[38–40].

Figure 6.41 shows typical read disturb characteristics with an accelerated gate voltage, after 1 million program/erase cycles at room temperature (30°C) [38, 39]. The threshold voltage V_t is increased with read disturb stress time. The stress-induced leakage current (SILC) can be directly calculated from the threshold voltage shift (ΔV_{th}) of the flash memory cell during read stress. The stress-induced leakage current can be expressed by

$$I_{leak} = C_{ono} * \Delta V_{th} / \Delta t \tag{6.3}$$

where I_{leak} is the stress-induced leakage current (SILC), C_{ono} is the capacitance of inter-poly dielectric ONO between the control gate and the floating gate, and the read disturb time (t) is read stress time.

Micron Ex. 1014, p. 248
Micron v. YMTC
IPR2025-00119

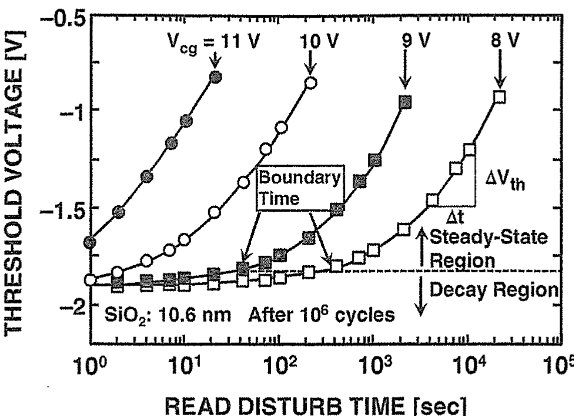

FIGURE 6.41 Read disturb characteristics with accelerated control gate voltage (V_{cg}). The threshold voltage V_t has a positive shift due to the electron injection to floating gate by SILC and the electron detrapping.

The threshold voltage of a memory cell is determined by both the floating-gate charge (Q_{fg}) and the oxide trapped charge (Q_{ot}) which consists of trapped electrons or holes in tunnel oxide. During the read disturb measurements, the Q_{fg} change is caused by the electron injection from the inversion layer and the electron trap states to the floating gate, which results in the stress-induced leakage current. And the Q_{ot} change is caused by the trapping or detrapping of carriers in the tunnel oxide. Therefore, the stress-induced leakage current calculated by the read disturb characteristics has two terms. One is the differential of the Q_{fg}, which is described as the steady-state leakage current. The other is the differential of the Q_{ot}, which is described as the decay region leakage current. As a result, the stress-induced leakage current can be written as

$$I_{leak} = -dQ_{fg}/dt + ((C_{ono} + C_{ox})/C_{ox}) * (dQ_{ot}/dt) \tag{6.4}$$

where C_{ox} is the capacitance of the tunnel oxide. It is assumed in (6.4) that Q_{ot} is localized near the Si/SiO$_2$ interface. The electric field over the tunnel oxide (E_{ox}) is a function of the floating-gate voltage and is given by

$$E_{ox} = (V_{fg} + \phi_f - \phi_s)/T_{ox} \tag{6.5}$$

where ϕ_f is the Fermi potential of the floating gate, ϕ_s the surface potential of the p-well, and T_{ox} the tunnel-oxide thickness. The floating-gate voltage is given by

$$V_{fg} = (C_{ono}/(C_{ono} + C_{ox})) * (V_{cg} - V_{th}) + V_{fgth} \tag{6.6}$$

where V_{cg} is the control gate voltage during the read disturb condition, and V_{fgth} is the threshold voltage as measured on the floating gate of the memory cell. The stress-induced leakage current is calculated from (6.3), (6.5), and (6.6).

Micron Ex. 1014, p. 249
Micron v. YMTC
IPR2025-00119

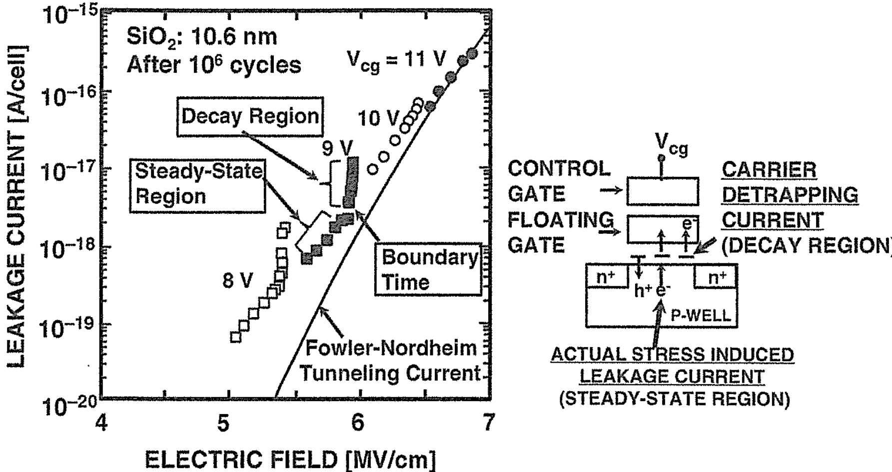

FIGURE 6.42 The calculation of the stress-induced leakage current derived from the threshold voltage shift of the flash memory cell during the read disturb condition. Quick V_t shift is caused by detrapping, and longer and large V_t shift is caused by SILC.

Figure 6.42 shows the calculated stress-induced leakage current (I_{leak}) as a function of the electric field over the tunnel oxide (E_{ox}). This leakage current is derived from the differential (dV_{th}/dt) of the threshold voltage during the read disturb condition, as shown in (6.3). It is observed that the leakage current quickly decays at the beginning of the read disturb stress (decay region). After the decay region, the leakage current reaches a certain steady value where dV_{th}/dt gradually decreases with the read disturb time (steady-state region). Two regions could be clearly confirmed by the plot of logarithmic read disturb time, as shown in Fig. 6.43. In the decay region, the decay of dV_{th}/dt is considered to be caused by both the fast decay of the stress-induced leakage current and the decay of the number of trapped carriers in the tunnel oxide, which

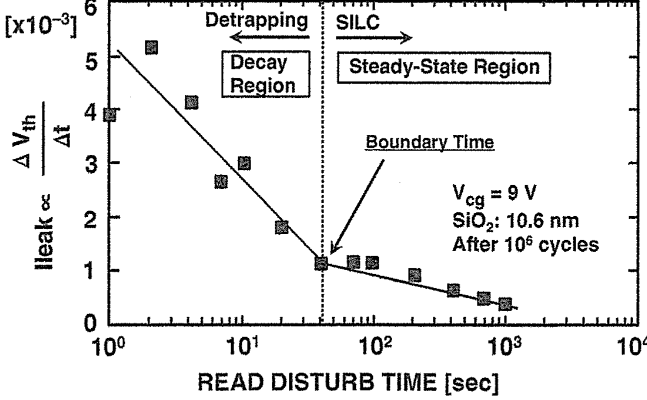

FIGURE 6.43 The differential of the threshold voltage versus read disturb time. Read disturb mechanism is explained by the detrapping and SILC mechanism. The detrapping means that a trapped carrier in tunnel oxide is detrapped in a short time. SILC (stress-induced leakage current) is dominant in a longer read disturb time.

Micron Ex. 1014, p. 250
Micron v. YMTC
IPR2025-00119

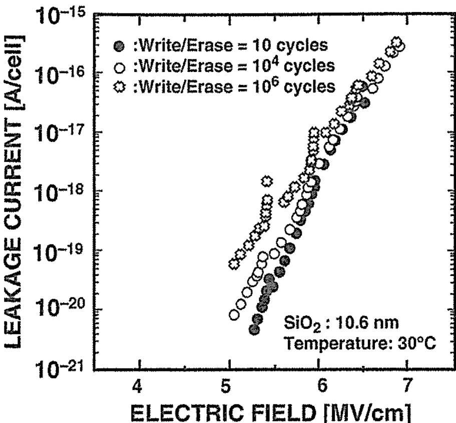

FIGURE 6.44 The stress-induced leakage current (SILC) after various write/erase cycling.

is generated during program/erase cycling. In the steady-state region, the threshold voltage shift is mainly caused by the stress-induced leakage current, which follows the same leakage current regardless of the control gate voltage of V_{cg} (the same electric field dependence in tunnel oxide), as shown in Fig. 6.42. The boundary between the decay region and the steady-state region is called "the boundary time" (see Fig. 6.43).

In this method of the leakage current derived from cell V_t shift, very low-level leakage current ($\sim 10^{-20}$ A) can be evaluated. On the other hand, in the conventional method of using capacitors as a test device, it is not possible to evaluate extremely low-level stress-induced leakage current. Therefore, using a memory cell is more practical and reliable than using a capacitor, when the stress-induced leakage current needs to be investigated.

Figure 6.44 shows the stress-induced leakage current after a number of program (write) /erase cycles (10–10^6 cycles). It was observed that the stress-induced leakage current increases with increasing the number of program/erase cycles. Also, in the decay region, the leakage current (emerging as an initial threshold voltage shift) increases with increasing the number of program/erase cycles. This result indicates that the charge traps in the tunnel oxide, which cause both stress-induced leakage current and the initial threshold voltage shift in the decay region, increase with increasing the number of program/erase cycles.

Figure 6.45 shows the stress-induced leakage current after 10^6 program/erase cycles for an oxide thickness range from 5.7 nm to 10.6 nm. The stress-induced leakage current increases greatly as the tunnel-oxide thickness decreases. The threshold voltage shift of the decay region after 10^6 program/erase cycles is independent of both the control gate voltage (V_{cg}) during the read disturb condition and the tunnel-oxide thickness for the range of 5.7–10.6 nm. Since the initial threshold voltage shift is only about 0.1 V after 10^6 program/erase cycles, the read disturb lifetime is not determined by the decay region but mainly by the steady region. Therefore, with respect to the read disturb lifetime, it is important to reduce the saturated leakage current (steady-state region) rather than the time-dependent leakage current (decay region).

Micron Ex. 1014, p. 251
Micron v. YMTC
IPR2025-00119

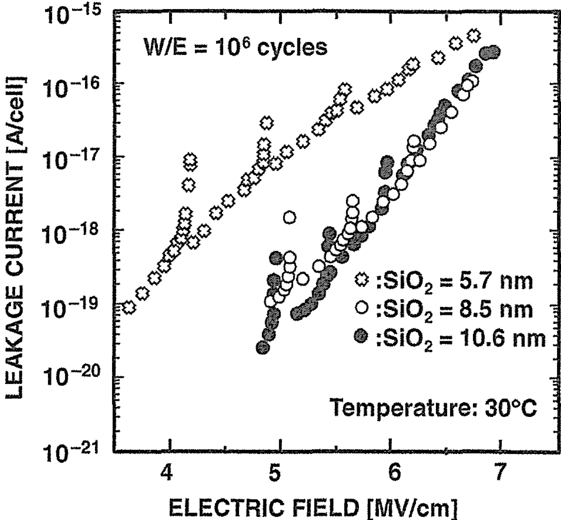

FIGURE 6.45 The stress-induced leakage current in the tunnel oxide with a thickness from 5.7 nm to 10.6 nm.

The high-temperature (125°C) operation (the temperature during program/erase operation equals the temperature during read disturb operation) degrades the read disturb characteristics in comparison with room temperature operation, as shown in Fig. 6.46. The steady-state leakage current after 125°C operation increases about three times in comparison with that at room temperature. Therefore, in the case of an accelerated test of read disturb, the high-temperature operation of the flash memory cell should be used. On the other hand, the boundary time decreases during high-temperature operation, while the initial threshold voltage shift is nearly constant

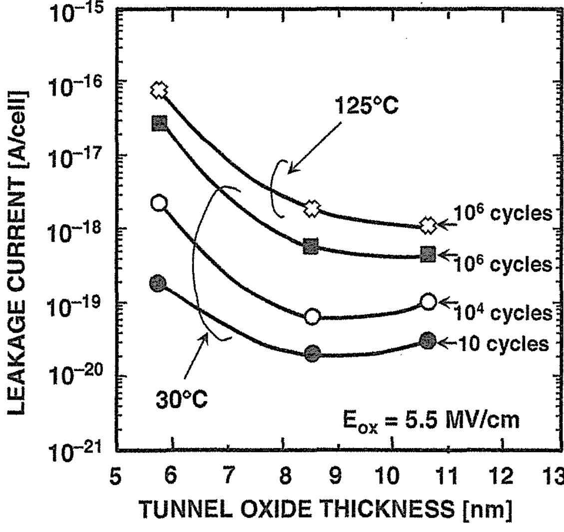

FIGURE 6.46 The stress-induced leakage current as a function of tunnel-oxide thickness.

Micron Ex. 1014, p. 252
Micron v. YMTC
IPR2025-00119

(0.1 V). This indicates that, in the decay region, the trapping or detrapping of carriers in the oxide is accelerated by higher temperatures, while the amount of the charge depends very little on the operation temperature.

6.4.3 Read Disturb in NAND Flash Product

Raw bit error rate (RBER) of read disturb was reported for several company's NAND flash product [37].

Figure 6.47a [37] shows RBER as a function of the number of reads per page performed on devices, which have cycled program/erase 10K times. When a NAND cell is in read operation, a voltage of V_{passR} is applied to all unselected word lines in the block. V_{passR} must be higher than the highest V_t of the programmed cells so that the unselected cells do not block the current from the cell being read. The V_{passR} bias tends to disturb bits at high values of V_t either through SILC [5,8,27,38–40,44], which allows electrons to reach the floating gate, or through the filling of traps in the tunnel oxide.

Failure bit is mainly caused from L0 (erase state) due to higher electric field in tunnel oxide, as shown in Fig. 6.47b. This is as expected for the SILC mechanism, which is strongly field-dependent, because the lowest V_t state has the highest electric field in the tunnel oxide under read bias V_{passR}. The characteristics of the read disturb failures were studied by excluding the program errors and plotting only the incremental read-disturb errors, as shown in Fig. 6.48. The RBER increases as a power law in the number of reads (Fig. 6.48a) and in the number of P/E cycles (Fig. 6.48b), consistent again with SILC [38–40,59]. Failure rate is degraded about 2 orders of magnitude with increasing program/erase cycling from 1000 to 10,000. Failure rate of read disturb should be saved by ECC.

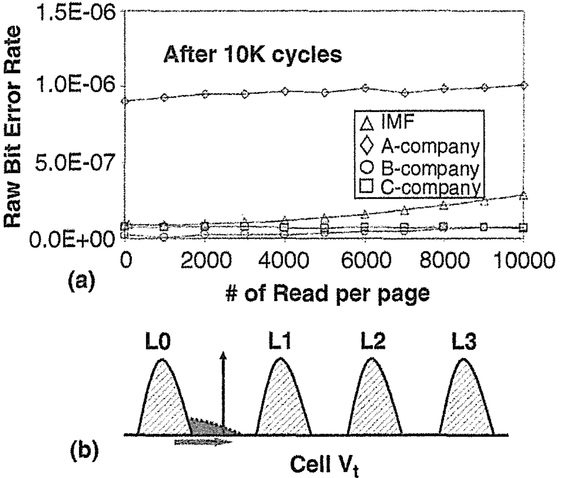

FIGURE 6.47 Read disturb characteristics in NAND flash product. (a) RBER versus number of read per page after 10K program/erase cycles. Failure is mainly caused in L0 failure. Bit failure rate increase as increasing number of read cycles. (b) SILC mechanism after P/E cycling.

Micron Ex. 1014, p. 253
Micron v. YMTC
IPR2025-00119

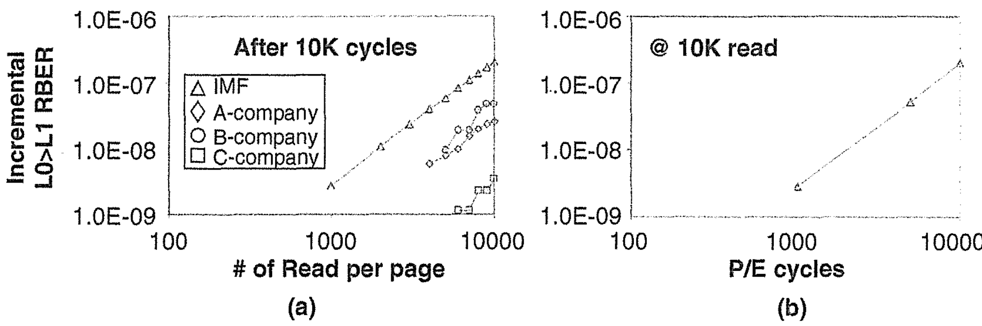

FIGURE 6.48 Incremental RBER in read disturb as measured by L0 bit failures, as a function of (a) number of reads per page for 10K-cycled blocks and (b) number of program/erase cycles before the 10K reads per page. Bit failure rate increases as an increasing number of read, and bit failure rate also increases as an increasing number of P/E cycling precondition.

6.4.4 Hot Carrier Injection Mechanism in Read Disturb

The other read disturb mechanism was reported [60]. It is called the "boosting hot-carrier injection effect." The hot carrier injection is occurred by unexpected boosting voltage induced by V_{pass_read} in unselected cells in a NAND string.

In order to investigate the read disturb mechanisms of "boosting hot-carrier injection effect," three different read voltages and four different cell data states (S0, S1, S2, and S3) were applied on the selected cell. Figure 6.49 shows (a) the operation condition and (b) waveform of SGS/SGD rising time shift scheme [61] for read-disturb evaluation. In the evaluation, the selected WLn was performed with more than 100K read cycles.

During the read operation, the channel potential in part of string (WL2–31 area) is boosting up by V_{pass_read} (V_{passR}) in unselected word lines, as shown in Fig. 6.50 bottom. This boosting potential generates hot electrons at a selected cell which has a large potential difference between source and drain (see Fig. 6.50a,b). Due to a large potential difference, some of the hot electrons are injected to the floating gate in a cell adjacent to the selected cell, as illustrated in Fig. 6.51.

Figure 6.50, upper portion, shows the measured results of WL2 V_{th} shift (i.e., read disturb failure) during select WL1 read disturb cycles with different WL1 voltages (V_{WL1}) and cell data states (WL1 = S0–S3; see Fig. 6.49a). From these data, a serious WL2 V_{th} shift can be observed in $V_{WL1} = 0.5$ V and $V_{WL1} = 1.8$ V after 1K read cycles. In Fig. 6.50a, upper portion, the magnitude of the V_{th} shift with the WL1 = S2 state is larger than that with WL1 = S3 state. However, obviously WL2 V_{th} shift can be found only when WL1 is at S3 state in Fig. 6.50b, upper portion. In Fig. 6.50c, upper portion, WL2 V_{th} is unchanged while V_{WL1} is set to 3.6 V.

To precisely analyze the phenomenon, TCAD simulation and analysis were carried out to clarify the mechanism of the read disturb failure. Based on simulation results of Fig. 6.50, the channel potential difference between selected WL*n* (e.g., WL1) and unselected WL*n*+1 (e.g., WL2) is related to cell data states (S0–S3) and the read voltage of the selected WL (V_{WL1}). Figure 6.50a, bottom portion, shows that the

Micron Ex. 1014, p. 254
Micron v. YMTC
IPR2025-00119

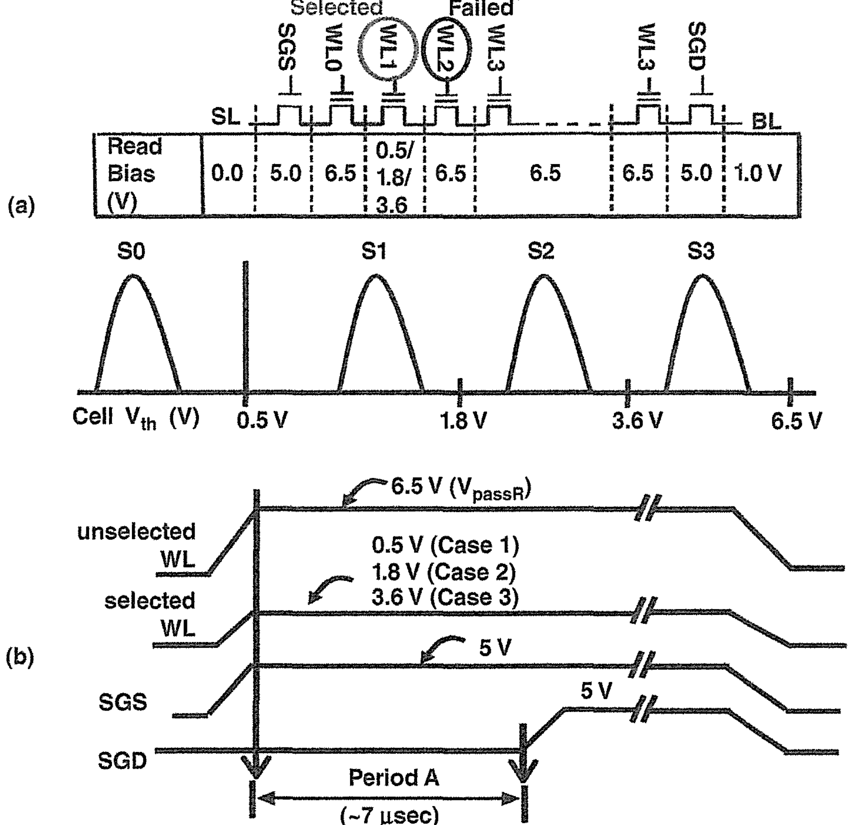

FIGURE 6.49 (a) Schematic diagram of read condition. The read cycling on WL1 was performed more than 100K. Four different cell data states (S0–3) are assigned for MLC NAND flash memory operation. (b) Waveform of read operation. There are three different voltages applied on the selected WL; these are represented as case 1 to case 3. In order to avoid SG–WL coupling noise, an SGS/SGD rising time shift scheme is used.

selected WL1 channel is tuned off and the channel potential of unselected WL2~31 is boosted to a high level when the WL1 cell data state is S2 or S3. Therefore, a sufficient potential difference between WL*n* and WL*n*+1 causes a high transverse electric field. When V_{WL1} is increased to 1.8 V as in Fig. 6.50b, bottom, a high programming cell state (S3) is required to support the potential boosting of unselected WL2–31. In addition, from Fig. 6.50c, bottom portion, and the case of WL1 = S2 in Fig. 6.50b, bottom portion, the large potential difference cannot be observed since the WL1 channel is turned on by high WL1 voltage. Therefore, the potential difference can be reduced by the turn-on effect of the selected cell. These simulation results are well corresponding with read disturb results of Fig. 6.50, top portion.

Electron current density is another factor to cause the V_{th} shift of WL*n*+1. From Fig. 6.49a, the current density of WL1 = S2 should be higher than that of WL = S3 since its V_{th} is lower. Consequently, the probability of impact ionization can be increased due to the high current density in the case of WL1 = S2. According to the

Micron Ex. 1014, p. 255
Micron v. YMTC
IPR2025-00119

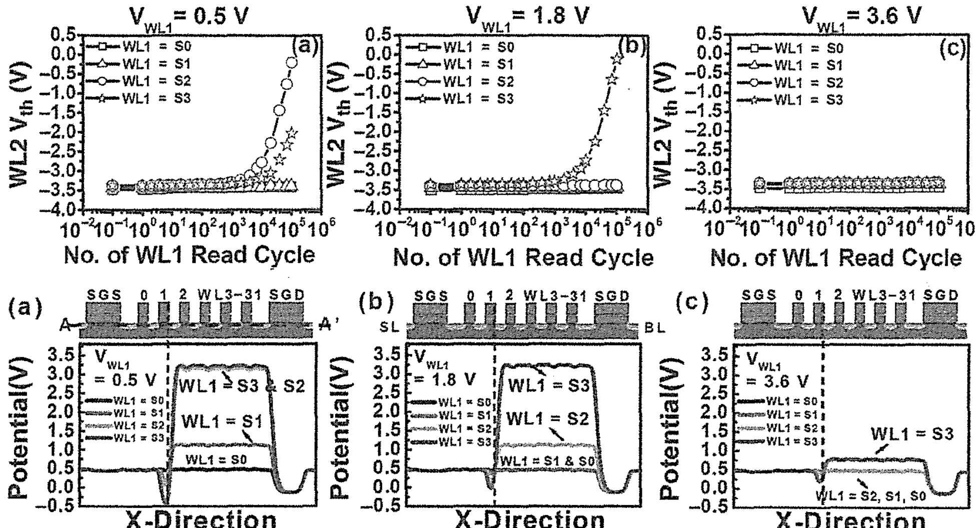

FIGURE 6.50 Measured results of WL2 V_{th} shift during WL1 read cycles. (a) WL1 voltage (V_{WL1}) is 0.5 V (case 1). The data shows serious WL2 V_{th} shift if WL1 cell was programmed (S2 and S3). (b) WL1 voltage (V_{WL1}) is 1.8 V (case 2). The data shows that the WL2 V_{th} shift occurred only with S3 state. (c) WL1 voltage (V_{WL1}) is 3.6 V (case 3). There is no obvious WL2 V_{th} shift in this condition.

model, the phenomenon of the serious WL2 V_{th} shift in the condition of WL1 = S2 rather than WL1 = S3 can be clearly explained.

Figure 6.51 shows the schematic diagram of the mechanism of boosting hot-carrier injection in MLC NAND flash memories. The transverse *E*-field can be enhanced by the channel potential difference and consequently make a high probability of impact ionization. As a result, electron–hole pairs are generated, and then electrons are injected into the adjacent cell (WL2) since the higher vertical field of V_{WL2}. Thus, the V_{th} of an adjacent cell is changed after 1K cycles with the repeating injecting of the hot electrons.

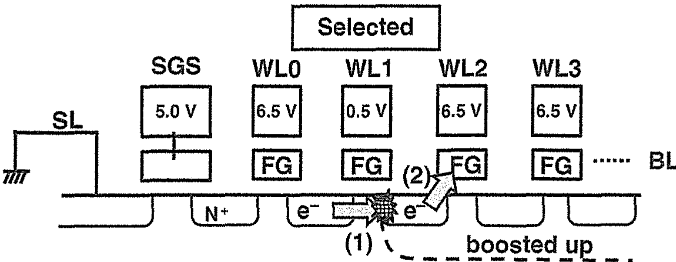

FIGURE 6.51 The schematic diagram of the mechanism of boosting hot-carrier injection (HCI) on read disturb in NAND flash memories. The probability of HCI could be enhanced by (1) high transverse E-field, and then (2) electrons injected into the floating gate due to the high vertical *E*-field.

Micron Ex. 1014, p. 256
Micron v. YMTC
IPR2025-00119

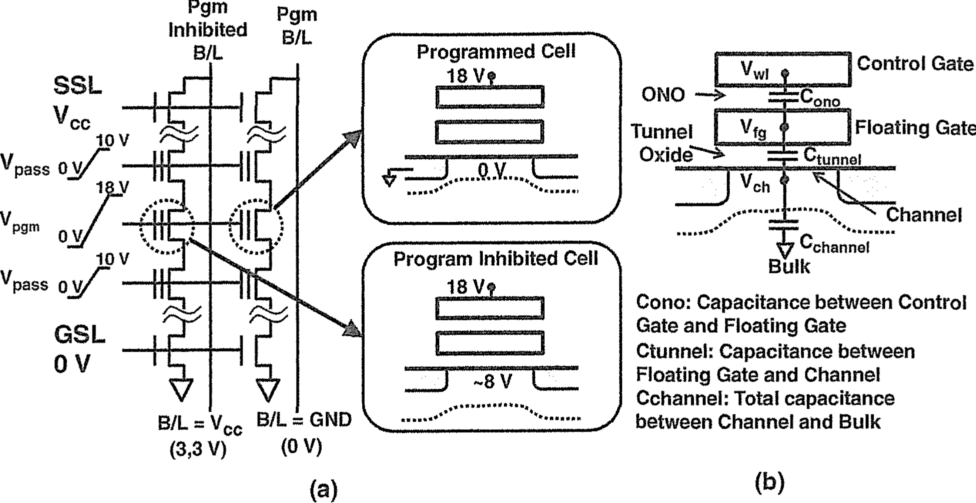

FIGURE 6.52 Self-boosted program inhibit voltage generation. (a) Bias conditions for self-boosting. (b) Capacitance model for coupling ratio calculation.

6.5 PROGRAM DISTURB

6.5.1 Model of Self-Boosting

The program self-boosting operation is used in an inhibit cell string of NAND flash memory cells, as shown in Section 2.2.4. The channel potential in inhibit strings are boosted up mainly by inhibit WL voltage (V_{pass}). The bias conditions for generating program inhibit boosting voltages to the channel of the inhibit NAND string is shown in Fig. 6.52a [62]. With the SSL transistors (drain side select transistor) turned on and the GSL transistors (source side select transistor) turned off, the bit-line voltages for cells to be programmed are set to 0 V, while the bit-line voltages for cells to be program inhibited are set to V_{cc}. In program-inhibited cells, the V_{cc} bit-line initially precharges the associated channel, which is normally V_{cc}-V_{tssl} (V_t of SSL transistor). When the word lines of the NAND string rise (selected word line to the program voltage of V_{pgm} and unselected word lines to the pass voltage of V_{pass}), the series capacitances through the control gate, floating gate, channel, and bulk are coupled and the channel potential is boosted automatically. Assuming a single boosted pass cell and using the model of Fig. 6.52b, the boosted channel voltage, V_{ch}, can be estimated as follows:

$$V_{ch} = V_{wl} * C_{ins}/(C_{ins} + C_{channel}) \tag{6.7}$$

where C_{ins} is the total capacitance between control gate and channel (C_{ono} in series connection with C_{tunnel})

$$C_{ins} = C_{ono} * C_{tunnel}/(C_{ono} + C_{tunnel})$$

Micron Ex. 1014, p. 257
Micron v. YMTC
IPR2025-00119

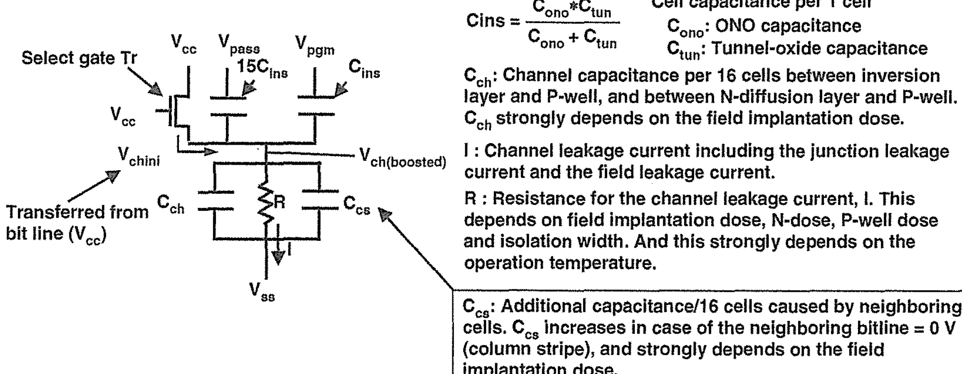

FIGURE 6.53 The equivalent circuit for self-boosting model, including an additional capacitor, C_{cs}. In the column stripe pattern, C_{cs} becomes large and decreases the channel voltage, V_{ch}. As a result, the number of programmable cycles (NOP) is limited by the column stripe pattern.

In a program inhibit string, the coupled channel voltage rises from V_{cc}-V_{tssl}, to V_{ch} when the word-lines voltages rise. The SSL transistor shuts off under the conditions of the drain BL in V_{cc} and the source in V_{ch}, due to the body effect of the SSL transistor. The GSL transistor also shuts off by applying 0 V to the gate and applying V_{cc} to the source line (SL). Then the channel becomes a floating node. By calculating (6.7), it is determined that the floating channel voltage rises to approximately 80% of the gate voltage. Thus, channel voltages of program inhibited cells are boosted to approximately 8 V when program (15.5–20 V) and pass (~10 V) voltages are applied to the control gates. This high-boosted channel voltage prevents the FN tunneling current from being initiated in the program-inhibited cells.

The program-boosting mechanism and limitation had been investigated in detail [63] in the LOCOS cell. Figure 6.53 shows the equivalent circuit for the channel-boosting mechanism. For the "1" data program (program inhibit), which keeps the negative threshold voltage (V_{th}), the program inhibit channel voltage (V_{ch}) is raised by the capacitive coupling with the pass voltages (V_{pass}) and the program voltage (V_{pgm}). V_{ch} must be raised enough to reduce the tunnel-oxide electric field, because the difference between V_{pgm} and V_{ch} is an effective program voltage for program inhibit cells.

In measurement data, program inhibit performance has a neighbor string data dependence. In the case of the column stripe pattern (channel of neighbor string is 0 V during programming "0" data), the number of allowable programmable cycles (NOP) is decreased to about 2/3 of that in the case of the all "1" pattern (channel of neighbor string is boosting voltage V_{ch} for programming "1" data). This means that the program inhibit performance is degraded in the column stripe pattern. Therefore, NOP is limited by the column stripe pattern.

In a conventional model, the program disturbance in the column stripe pattern is explained by the field leakage current from the program inhibit channel voltage V_{ch}.

Micron Ex. 1014, p. 258
Micron v. YMTC
IPR2025-00119

$$V_{ch} = V_{chini} + C_r(V_{pass}-V_t-V_{chini}) + C_r'(V_{pgm} - V_{th} - V_{chini}) - \frac{T_{pw}}{C_{tot}} I$$

$[V_{pgm}-V_{ch}]$ is a potential difference between CG and the channel for "1" data programming cells.
Vchnin is the initial voltage, which is transferred by SGD from bitline (V_{cc})

$C_{tot} = 16C_{ins}+C_{ch}+C_{cs}$: **Total channel capacitance**

$C_r = \frac{15C_{ins}}{C_{tot}}$: **Channel boost ratio for un-selected cells**

$C_r' = \frac{C_{ins}}{C_{tot}}$: **Channel boost ratio for selected cell**

FIGURE 6.54 Channel voltage equation used in the simulation. V_{th} is the threshold voltage of un-selected cell (if D-type cells then $V_{th} = 0$ V). Cr, Cr' is the-channel boost ratio. T_{pw} is the pulse width of V_{pass} and V_{pgm}.

On the other hand, in the new model the program disturbance is extended mainly by the additional capacitance (C_{cs}) between the active area and the neighboring cells, as shown in Fig. 6.53. The C_{cs} increases when the depletion area under LOCOS isolation is widened in column stripe pattern. As shown in Fig. 6.54, an increasing C_{cs} (increasing C_{tot}) decreases the channel boost ratio (C_r), and then decreases the V_{ch} in the column stripe pattern. Figure 6.55 shows the measured and simulated program disturbance characteristics. The C_{cs} is a fitting parameter. The simulated result is well matched with the measured result.

V_{pass} and V_{pgm} waveforms dependence on the program disturbance was also investigated for analysis of the channel leakage current, as shown in Fig. 6.56. The various pulse widths of T_{pw} are used, as shown in Fig. 6.56a. Figure 6.56b shows the V_{th} of the "1" program cell (program inhibit cell), as a function of T_{pw}. In a conventional model, V_{th} difference between the all "1" pattern and the column stripe pattern at $T_{pw} = 30$ μs

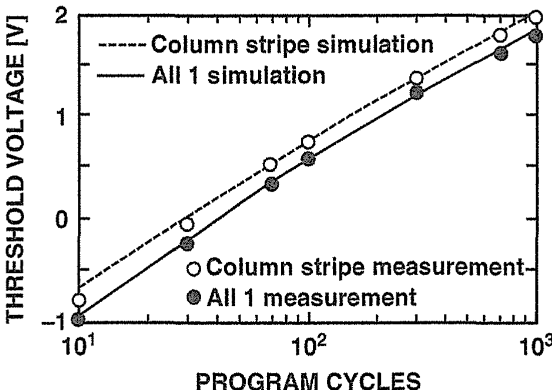

FIGURE 6.55 Simulated and measured program inhibit (self-boosting) characteristics for "1" data program cell. C_{cs} is a fitting parameter. Operation temperature is 85°C. Field implantation dose is 1 E14/cm^2. $V_{pass} = 10$ V, $V_{pgm} = 17$ V, $C_{cs} = 5$ E-16 farad/16 cells.

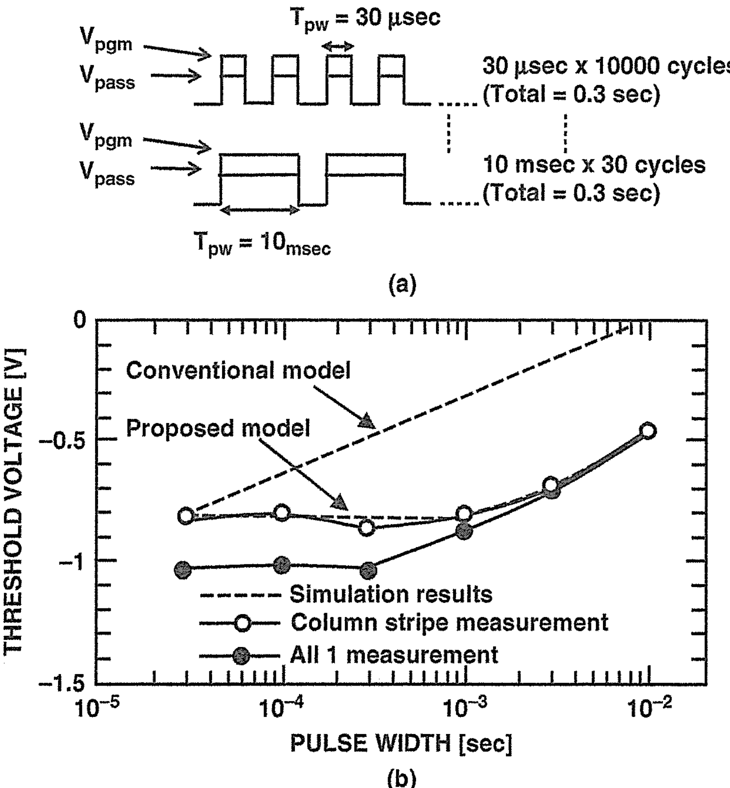

FIGURE 6.56 (a) V_{pgm} and V_{pass} waveform for analysis of the channel leakage current, "1". (b) Threshold voltage as a function of V_{pass} and V_{pgm} pulse width. The model well reproduces the measurement data. On the other hand, the conventional field leakage current model deviates from the measurement data. The threshold voltage shift at long T_{pw} (>1 ms) is caused by the junction leakage current.

is considered to be due to the field leakage current. However, the measurement data deviates from the simulation result as pulse width increases. On the other hand, in the proposed model, the simulation result can well reproduce the measurement data, where the V_{th} difference is calculated by the enlarged C_{cs} with C_{cs} = 5E-16 (farad/16 cells) derived from Fig. 6.55. The increase of V_{th} when the T_{pw} is longer than 1 ms is caused by the junction leakage current in the boosted channel.

A quantitative NAND string boosting model was investigated in a sub-30-nm NAND cell [64] to clarify the impacts of the channel capacitance, the channel leakage current, and the cell scaling on the program disturb. The model is including the channel boosting ratio (CBR) from capacitances network of 3-D technology computer-aided design (TCAD) simulations, the transient channel potential with the junction leakage (J/L) current, the band-to-band tunneling (BTBT) current, and the Fowler–Nordheim (FN) tunneling current of cells.

Figure 6.57a illustrates a schematic of NAND strings during programming, along with the various mechanisms that impact the program disturb. Typical program and

Micron Ex. 1014, p. 260
Micron v. YMTC
IPR2025-00119

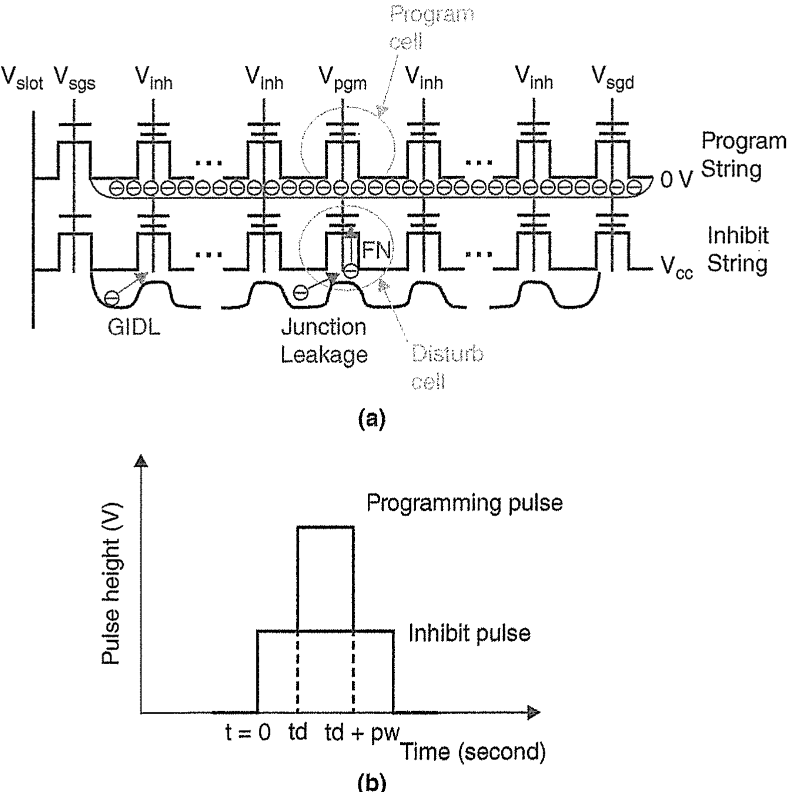

FIGURE 6.57 (a) Bias conditions of NAND strings during programming, along with the different program disturb mechanisms. (b) Program and inhibit-pulse waveforms. A td is a ramp-up delay between inhibit pulse (V_{inh}) and programming pulse (V_{pgm}).

inhibit-pulse waveforms are shown in Fig. 6.57b. Here, td is the time delay between ramp-up of the inhibit-pulse V_{inh} and ramp-up of the program-pulse V_{pgm}, and pw is the programming pulse width.

Figures 6.58a and 6.58b show the V_t of disturbed cell as a function of the inhibit voltage (V_{inh}, i.e., V_{pass}) for three different delay times td of 5, 100, and 500 μs. Simulation results and experimental data show a good fit over a series of the inhibit voltage V_{inh}. The model also shows the overall trend in both low and high channel boron concentration cases. In the case of the low channel boron concentration of Na (see Fig. 6.58a), the cell program disturb continues to improve with higher V_{inh} voltage values. This indicates that the channel potential is mainly determined by the channel boosting ratio (CBR). On the other hand, the cell with a higher channel boron concentration shows a different behavior. In the case of the higher boron dose (see Fig. 6.58b), the V_t of the disturbed cell starts to saturate at a V_{inh} value of around 7 V, which indicates that the channel boosting potential is limited by the channel leakage current. The difference between the delay times of 5 and 100 μs is almost the same as that between 100 and 500 μs, which suggests a much higher channel leakage current at the high channel boosting voltage. In Fig. 6.58b, the V_t of the disturbed

Micron Ex. 1014, p. 261
Micron v. YMTC
IPR2025-00119

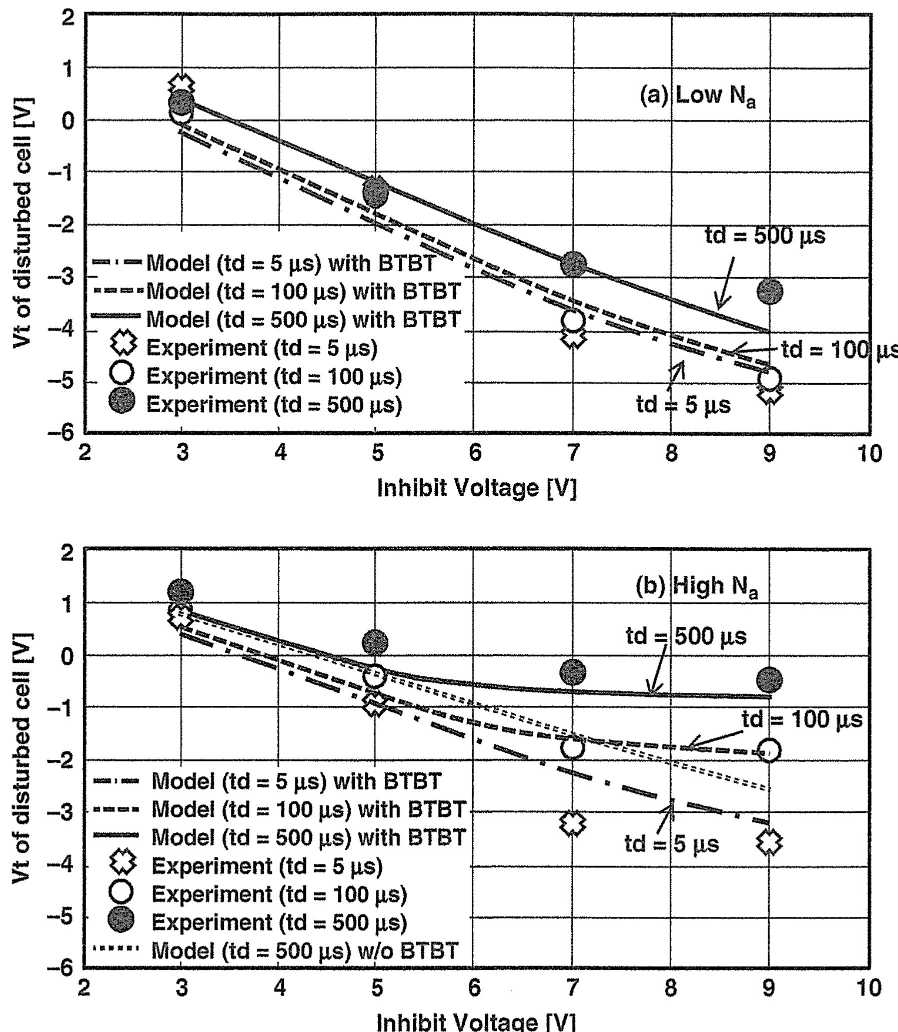

FIGURE 6.58 Disturbed cell V_t as a function of the inhibit voltage in the case of (a) low and (b) high channel boron concentrations of Na. $V_{seed} = 1$ V. Initial erased V_t is below −7 V.

cell without the BTBT current in model is also shown. Without the BTBT current, the simulation results do not match the experimental data. This result indicates that the dominant leakage mechanism for the program disturb is the BTBT current when the boron concentration is high.

As the NAND cell scales down further, a higher channel boron concentration is required to mitigate the short-channel effect. The leakage current of channel boosting node is increased. Figure 6.59 illustrates the boron concentration requirement (closed circles) and the resultant channel leakage current (open circles) during the boosting across generations [64]. The boron concentration is determined to maintain a charge neutral V_t across technology nodes. The BTBT current is expected to be a dominant program disturb mechanism for cells beyond 20 nm.

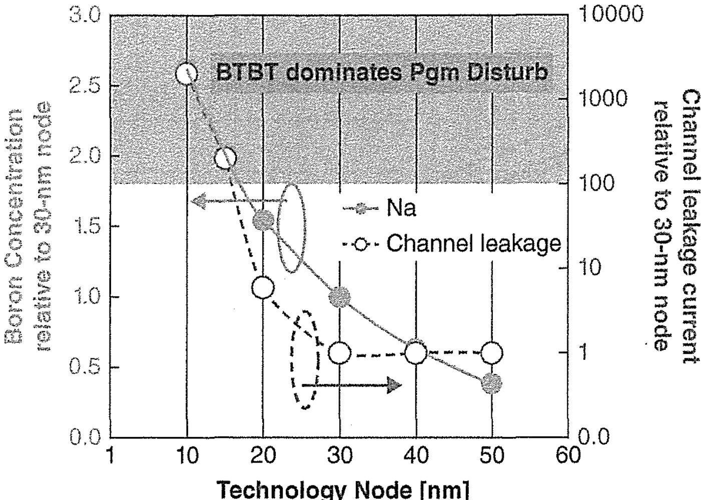

FIGURE 6.59 Technology scaling trend. Channel boron concentration is determined to maintain a charge-neutral V_t across technology nodes. At the sub-20-nm node, BTBT current becomes the dominant mechanism for NAND-cell program disturb.

6.5.2 Hot Carrier Injection Mechanism

Two program disturb mechanisms of the boosting mode and V_{pass} mode were described in Fig. 2.21 (Section 2.2.4). Except for these two conventional program-disturb modes, several program disturb mechanisms have been reported.

Figure 6.60 shows "source/drain hot-carrier injection disturbance" [65], so-called "SGS GIDL (gate-induced drain leakage) disturb." Before measurement, all the cells were erased to $V_{th} = -3$ V, and then a selected cell was programmed to $V_{th} = +1$ V followed by V_{th} monitoring. Thus, V_{th} difference from -3 V corresponds to the disturbance amount. For characterization of multiple NOP operations, the same

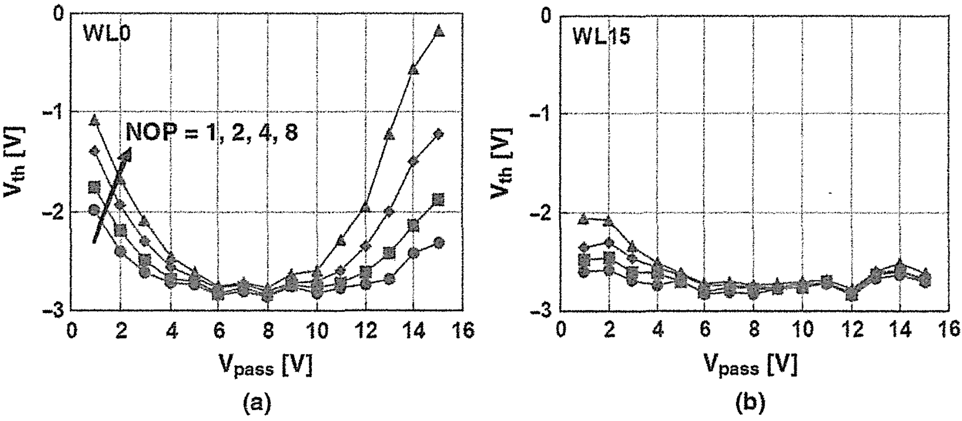

FIGURE 6.60 Programming disturbance characteristics of a NAND cell array measured at WL0 and WL15 during programming operation.

Micron Ex. 1014, p. 263
Micron v. YMTC
IPR2025-00119

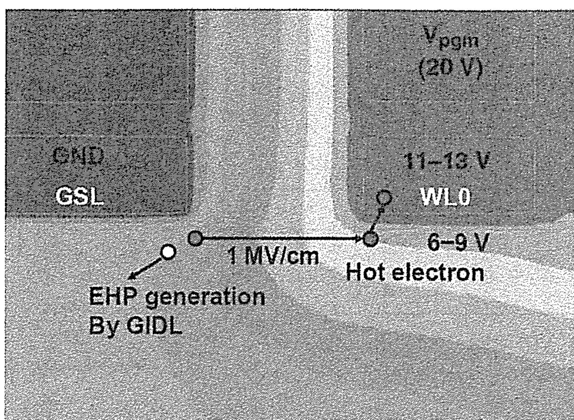

FIGURE 6.61 Simulation of the "hot-carrier disturbance" phenomenon, illustration of the "hot-carrier disturbance" model at WL0 cell.

programming operation cycles were repeated in the same word line with a repetition number of NOP. In Fig. 6.60, conventional V_{pgm} disturbance can be observed at low V_{pass} voltages ($V_{pass} < 6$ V) and the V_{pgm} disturbance is logarithmically proportional to NOP. The program disturbance characteristic at WL15 (Fig. 6.60b) is typical, which occurs only at low V_{pass} voltages. However, the program disturbance characteristic at WL0 (Fig. 6.60a) shows that another disturbance phenomenon can be observed at high V_{pass} voltages, and it is more severe at higher V_{pass} voltages. In contrast to typical V_{pgm} disturbance, the disturbance at high V_{pass} voltages is linearly proportional to NOP. As shown in Fig. 6.60, the new programming disturbance is worst at WL0, while negligible at other WLs.

The model is verified by device simulation of a NAND cell string. Figure 6.61 shows the potential profile across the simulation structure at GSL/WL0 during programming operation. The channel potential is raised to 8 V, and the lateral electric field at the GSL-WL0 space is around 1 MV/cm. The large hole current is generated at the GSL (SGS) edge due to the GIDL mechanism. Also, the large electron current is generated, and a part of the generated electron is injected to the floating gate of WL0 by accelerating with lateral electric field. The GIDL situation also occurred at the SSL (SGD; drain side select gate) edge; however, comparing with GSL bias conditions, the V_{gs} (voltage different between gate and source) at the SSL transistor is lowered as much as the applied voltage at the SSL gate. In addition, the lateral electric field at the SSL-WL31 space is lowered by the same amount with the same reason. Therefore, although the same phenomenon happens at the WL31 cell, the situation is even better than the WL0 cell.

By using simulation tools, a method to minimize the disturbance problem was obtained. This disturb phenomenon is strongly depended on WL0-SGS(GSL) space length, as shown in Fig. 6.62. The narrower space of less than 110 nm makes this program disturb worse. This suggests that "SGS GIDL disturb" becomes worse as a memory cell scaling (WL0-SGS (DSL) space scaling).

Micron Ex. 1014, p. 264
Micron v. YMTC
IPR2025-00119

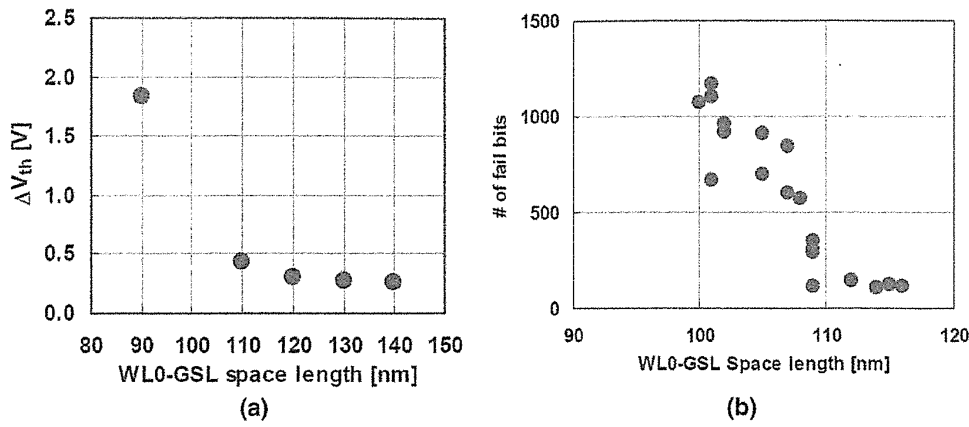

FIGURE 6.62 (a) Simulation result of the number of electrons injected to the WL0 cell for various WL0-GSL space. (b) Number of failure bits measured with 1-Mb block array at $V_{pass} = 10$ V.

The other mechanism was also reported for the same disturb phenomenon [66]. It was concluded that this program disturb is caused by hot electrons which are generated due to the generation-recombination center (GR-center) at the oxide–silicon interface of SSL, not generated by GIDL. The high electric field in space from SSL transistor to cell (WL0) accelerates generated electrons, and then hot electrons are injected to FG of WL0.

Another program disturb mechanism had been reported as a "DIBL-generated hot-electron injection" mechanism in 51-nm memory cell [67, 68], as described in Figs. 6.63–6.65. Due to DIBL (drain-induced barrier lowering) by the channel boosting voltage, punch-through between source and drain occurred at cut-off cells

BL
GSL
WL31
WL16
WL15
WL14
WL00
GND
CSL

▪Erase(E)/Program(P) Pattern

Pattern	WL00–WL13	WL14	WL15	WL16–WL31
EP1	E	E	P1	E
EP3		E	P3	
PP1		P1	P1	
PP3		P3	P3	

▪BVdss Meas. condition

Pattern	V_{csl} (source)	SSL Tr. & WL0–13	WL14	WL15	WL16–WL31 & GSL Tr.	V_{bl} (drain)
EP1	0 V	V_{pass}	V_{pass}	0V	V_{pass}	0 – 8 V sweep
EP3			V_{pass}	0V		
PP1			0V	0V		
PP3			0V	0V		

FIGURE 6.63 Erase(E)/program(P) patterns and BV_{dss} measurement conditions. E: $V_{th} = -3.0$ V; P1: $V_{th} = +1.0$ V; and P3: $V_{th} = +3.0$ V.

Micron Ex. 1014, p. 265
Micron v. YMTC
IPR2025-00119

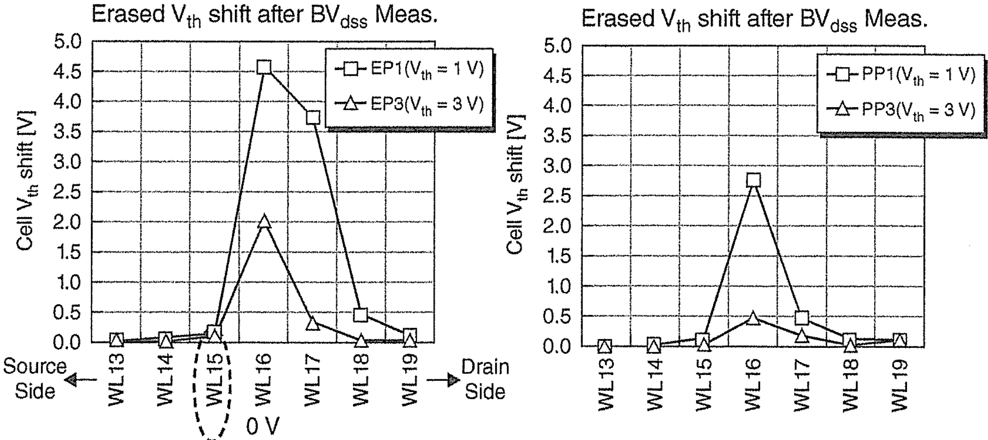

FIGURE 6.64 Erased cell V_{th} shifts from initial erased state after BV_{dss} measurements of EP1, EP3, PP1, PP3 patterns, respectively. EP1(WL14: erased E, WL15: programmed P1), EP3(E, P3), PP1(P1, P1), and PP3(P3, P3).

in the program self-boosting scheme. This punch-through generates the hot electrons, and a portion of hot electrons is injected near the floating gate, as shown in Fig. 6.65. The punch-through has a strong dependence of cell V_t. The lower V_t makes punch-through and this DIBL disturb worse.

To investigate a new program disturb induced by DIBL leakage, BV_{dss} curves of the selected cell in various erase/program data patterns are measured by sweeping bit-line voltage V_{bl} to 8 V. Before BV_{dss} measurements, all the cells were erased to $V_{th} = E(-3.0\text{ V})$, and then one (WL15) or two (WL14, 15) selected cells in each array were programmed to $V_{th} = \text{P1}(+1.0\text{ V})$ or P3(+3.0 V), followed by monitoring the

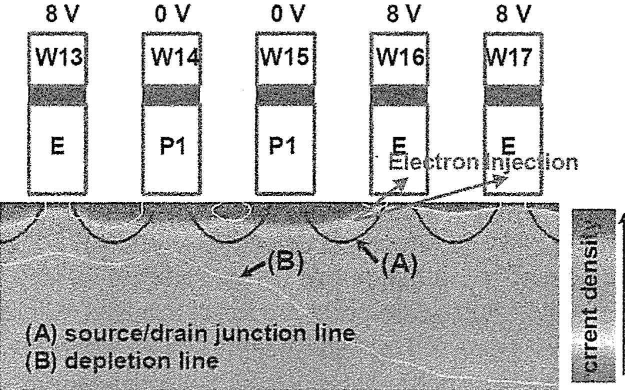

FIGURE 6.65 Device simulation is performed on the BV_{dss} measurement condition at PP1 pattern. Current density shows the punch-through of WL15 off-cell at $V_{bl} = 4$ V. DIBL (drain-induced barrier lowering) generates punch-through between source and drain in unselected cell. Electrons generated by punch-through are injected at nearby cells (disturb happens). Lower V_t cell shows larger DIBL.

Micron Ex. 1014, p. 266
Micron v. YMTC
IPR2025-00119

entire cell V_{th} shifts from its initial erased states. Detailed measurement conditions are summarized in Fig. 6.63.

As seen in Fig. 6.64, cell V_{th} shifts of WL16 and WL17 were observed at EP and PP patterns after BV_{dss} measurements of sweeping bit-line voltage V_{bl} to 8 V. In the order of EP1 → PP1 → EP3 → PP3 patterns, cell V_{th} shifts of WL16 and WL17 are smaller. This pattern dependency of V_{th} shifts can be explained as follows. EP1(WL15 $V_{th} = +1.0$ V) → EP3(WL15 $V_{th} = +3.0$ V) pattern implies that increasing cell V_{th} leads to the high electron energy barrier of the WL15 cell. Also, EP → PP pattern means that effective channel length of WL15 cell becomes longer with combined WL14. Therefore, the DIBL leakage current is reduced so that hot carrier injection into erased cells is suppressed.

In addition, it was found that the erased cell V_{th} shift of PP3 is smaller compared to the PP1 pattern. In view of the GIDL current generation mechanism in a normal NMOS transistor, the greater the number of electrons that are stored in the floating-gate poly-Si (referred to as high programmed state in MLC flash operation), the greater the amount of GIDL-current that is generated. According to this assumption, PP1 should have a good immunity against a GIDL-induced hot carrier program disturb compared to EP3 pattern. However, the cell V_{th} shift of PP1 was larger cell V_t shift than PP3, as shown in Fig. 6.64. This indicates that hot carrier program disturb is mainly caused by DIBL, not by GIDL current in a 51-nm device. Therefore the short channel effect by DIBL should be controlled for an MLC NAND flash device beyond 51 nm. The simulation result also supports that the leakage source for a hot carrier is mainly originated by DIBL as seen in Fig. 6.65.

6.5.3 Channel Coupling

Channel boosting potential is decreasing as the cell dimension is scaled down. The boosted potential has a dependency on the neighboring string potential pattern. In the V_{cc}–V_{cc}–V_{cc} mode (condition of bit-line voltage order; see Fig. 6.66a), two adjacent active lines are under program-inhibit conditions when the center active line is in the program-inhibited condition. In the 0 V–V_{cc}–0 V mode, two adjacent active lines are under program operation. The 0 V–V_{cc}–V_{cc} mode means that only one adjacent active line is under program operation, and the other is under program inhibition.

Figure 6.66b shows the program disturbance characteristics of neighbor string potential pattern dependence [69]. The threshold voltage shifts of the program cell and program-inhibited cells in three neighbor data pattern modes are concurrently measured as selected cells are programmed by the incremental step pulse programming (ISPP). The boosted channel potential is derived from the difference of program voltage between the program cell and the inhibit cell to reach the same program threshold voltage (see Fig. 6.66b). The boosted channel potential appeared to be worst in the case of the 0 V–V_{cc}–0 V mode. From the measurement, adjacent channel potentials have a large impact on a boosted channel potential under program inhibit conditions.

To reveal a physical mechanism of neighbor data pattern dependence, TCAD simulation was performed [69]. In the 0 V–V_{cc}–0 V mode, the virtual sidewall transistor

Micron Ex. 1014, p. 267
Micron v. YMTC
IPR2025-00119

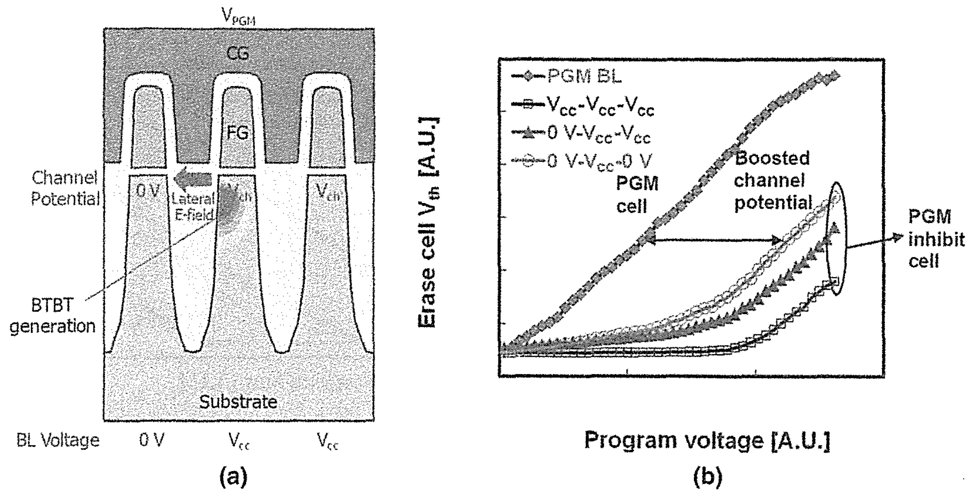

FIGURE 6.66 (a) Schematic illustration of the BTBT generation phenomenon by the lateral electric field. Channel boosting potential drops by BTBT generation at the side wall of the channel. (b) Program characteristics of the selected cell in program bit line, along with program disturbance characteristics of the unselected cell in program-inhibit bit line. For the V_{cc}–V_{cc}–V_{cc} mode, all the adjacent active lines are under program inhibition. For the 0 V–V_{cc}–V_{cc} mode, one of the adjacent active lines is under program operation, and the other is under program inhibition. For the 0 V–V_{cc}–0 V mode, all the adjacent active lines are under program operation.

is built up. When the neighboring channel is under the program by applying 0 V to the bit line, the channel potential is set to GND. The channel acts as a virtual gate of 0 V, and trench isolation dielectrics acts as a gate oxide; thus, program-inhibited channel potential is controlled by the neighboring channel virtual gate. The program-inhibited boosted channel near the Si surface below a tunnel oxide acts as the drain side of the virtual sidewall transistor. In the condition of the 0 V–V_{cc}–0 V mode, a large "gate-induced drain leakage" (GIDL) is generated in a booting channel. The GIDL current appears in the form of band-to-band tunneling (BTBT) leakage, and the BTBT leakage is source of losing boosting channel potential. The BTBT increases very abruptly over critical electric field, and thus the boosted channel potential has become saturated in spite of increasing pass voltage.

The BTBT generation mechanism at the sidewall of the channel is illustrated in Fig. 6.66a [69–71]. At the sidewall of the boosted channel facing a channel of GND, a large lateral electric field is built, thus BTBT electron–hole pair generation occurs at the sidewall. The generated electrons drop the boosted potential sooner than expected considering only the capacitive coupling effects.

To overcome the program disturb at 1X-nm node cell, the active air gap was developed to reduce the active channel coupling effect [69, 72]. Figure 6.67a shows a schematic active air gap [72]. And Fig. 5.25 (in Section 5.3.4) shows a SEM photograph of active air gap. The active air gap can improve program disturb in 0 V–V_{cc}–0 V (0 F inhibit cell), as shown in Fig 6.67b.

Micron Ex. 1014, p. 268
Micron v. YMTC
IPR2025-00119

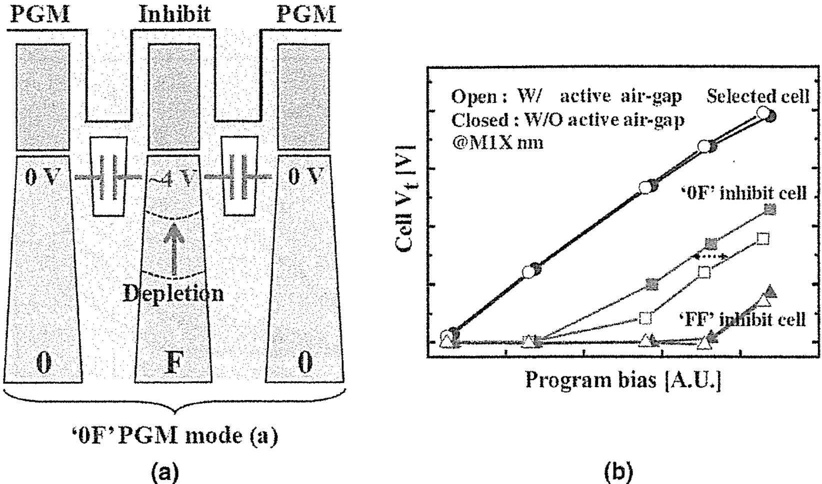

FIGURE 6.67 (a) The schematic of "0 F" disturbance mode. Boosted channel potential of inhibit BL is severely affected by grounded adjacent BL. (b) The improvement of "0 F" boosting level with active air gap.

6.6 ERRATIC OVER-PROGRAM

The erratic over-program is the phenomenon of unexpected large V_t shift during programming. Erratic over-program cells make the tail of V_t distribution in upper side distribution, as shown in Fig. 6.68. If the V_t of tail bit exceeds over read voltage in the case of L0, L1, and L2, it produces a single bit failure. However, in case of L3, if the V_t of tail bit exceeds (or closed to) V_{passR}, all cells of L0/L1/L2 in the NAND string become failure bits because the over-programmed cell is always OFF during read due to high V_t. Then the over-program in L3 makes a failure rate much worse than in other states.

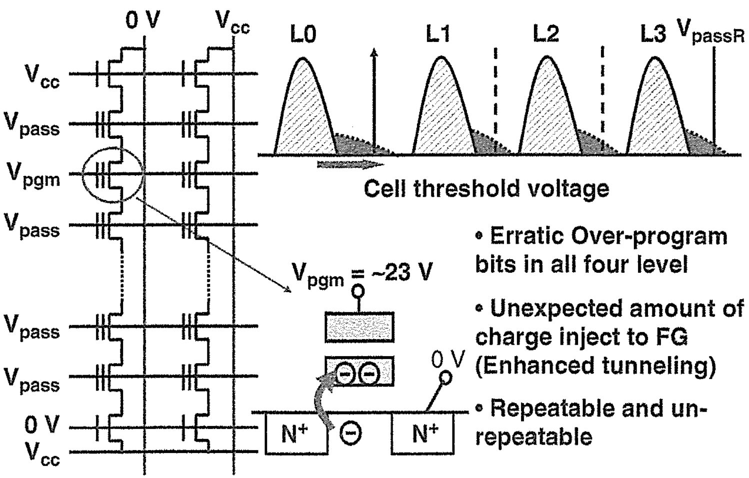

FIGURE 6.68 Erratic over-programming.

Micron Ex. 1014, p. 269
Micron v. YMTC
IPR2025-00119

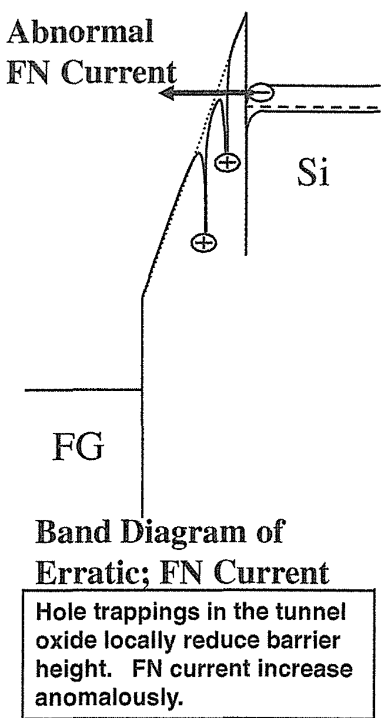

FIGURE 6.69 Schematic model of erratic over-program. Two hole traps in tunnel oxide induce an abnormal FN current.

The root cause of the erratic over-program is explained by an enhanced tunneling at two or more hole traps at close location in tunnel oxide. Figure 6.69 shows an image of an enhanced tunneling at a two-hole trap site. Hole traps locally reduce the barrier height of the tunnel oxide.

As another model of the erratic over-program, the neutral electron-assisted two-step tunneling is considered. It was observed as an anomalous increase of tunneling current of the stress-induced leakage current in the tunnel oxide at low electric field. Figure 6.70a shows an example of the stress-induced leakage current that suddenly increases during the gate stressing [63]. The increased stress-induced leakage current can fit with the FN tunneling current line, and the estimated barrier height is 0.57 eV. During the gate stressing, there is no hole generation, and hole capturing into the tunnel oxide could not happen because of the lower electric field. As a model for the stress-induced leakage current of the typical cell, neutral electron-assisted two-step tunneling is supported by several works [55–58]. Figure 6.70b shows a schematic model to explain the anomalous current increase phenomenon. Before the increase of the stress-induced leakage current, the two-step tunneling through a neutral electron trap located at the trap depth level Φ_{t1} occurs. Due to hole movement in the tunnel oxide by the electric field during the gate stress, another electron trap site which has the shallow barrier height Φ_{t2} is leveled down to the position where the electron in the conduction band of the substrate can tunnel. As a result, local

Micron Ex. 1014, p. 270
Micron v. YMTC
IPR2025-00119

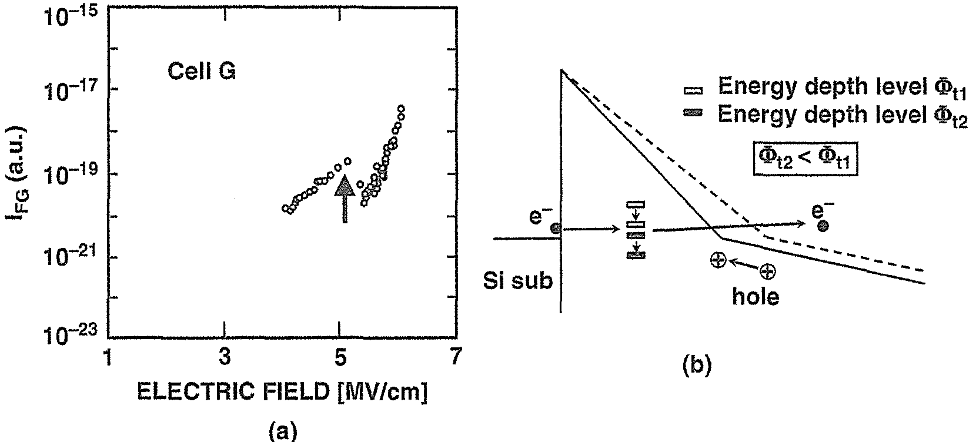

FIGURE 6.70 (a) Increase of the stress-induced leakage current during the gate stress. (b) Energy band diagram to explain increase of stress-induced leakage current during the gate stressing.

two-step tunneling of electron becomes possible, and the stress-induced leakage current increases.

Erratic over-program failure rate was investigated in several NAND flash products from different suppliers [37], as shown in Fig. 6.71. Bit failure rate is increased with P/E cycling increased. And the percentage of failure bits for each level is dependent on the product (suppliers). It would be dependent on program condition setting, read condition setting, and process difference.

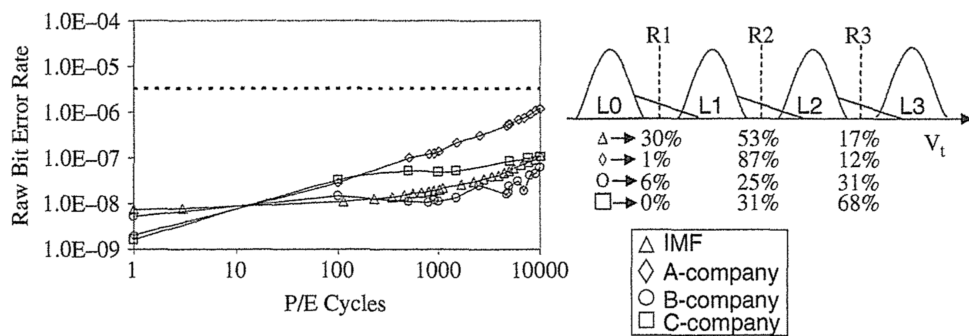

FIGURE 6.71 Erratic over-programming. RBER after programming data, as a function of prior program/erase cycles. Errors were logged at the cycle points noted by the symbols. The dashed line is the RBER where the instantaneous UBER (Uncorrectable Bit Error Rate) reaches 10^{-15}. Nonmonotonic curves result from small sample sizes and erratic RBER behavior. Schematic illustration of the dominant types of program errors and the percentage weighting of each type for each product. The RBER was dominated by cells with higher V_t's than intended; exceptions exist to some degree and result in percentages sometimes adding to less than 100%. RBER is gradually increased with P/E cycling increasing. The percentage of fail bits for each level is dependent on product (provider). Oxide trap-assisted tunneling is a major root cause.

Micron Ex. 1014, p. 271
Micron v. YMTC
IPR2025-00119

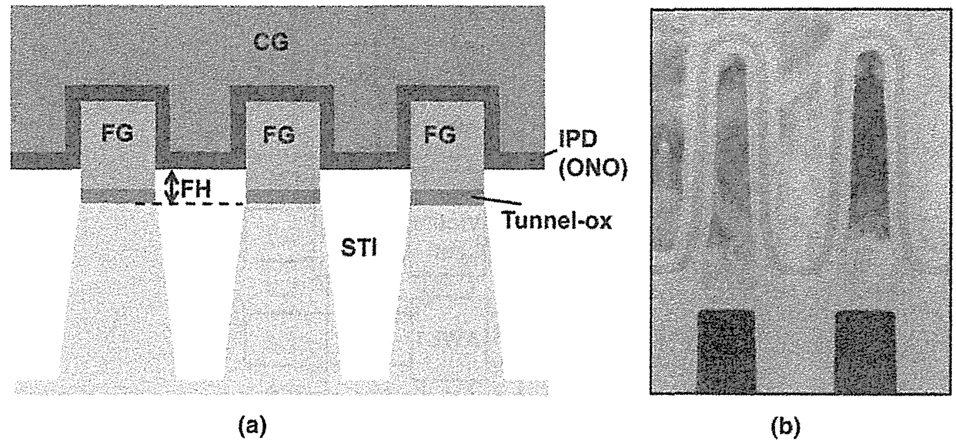

FIGURE 6.72 (a) The self-aligned shallow trench isolation cell (SA-STI cell) structure along word line (WL). (b) TEM micrograph of a 26-nm SA-STI cell [74]. A field oxide height (FH) is the distance between a channel Si and the top of an STI field oxide.

6.7 NEGATIVE V_t SHIFT PHENOMENA

6.7.1 Background and Experiment

The self-aligned shallow trench isolation cell (SA-STI cell) [10, 73] has been used for NAND flash memory products for a long time from 0.2-μm generation [74–76] to present middle-1X-nm generation [72, 77]. The structure of the SA-STI cell along word line (WL) is shown in Fig. 6.72. A floating gate (FG) is self-aligned patterned with STI to avoid overlap of FG on STI edge corner. In the SA-STI cell, the sidewall of FG is used for increasing a capacitance between FG and CG, to increase a coupling ratio. Then the field oxide height (FH), which is the distance between the channel Si and the top of the STI field oxide, has to be decreased as small as possible to increase a coupling ratio, as shown in Fig. 6.72a. The decreasing FH can also obtain a small FG–FG coupling interference [78] along the WL direction. However, in a small FH, high voltage (~20 V) is applied directly between substrate (channel) and CG during program and erase. This high electric field is a concern that could have an impact on reliability and performance of NAND flash memory.

Section 6.7 describes the "negative" V_t shift phenomena in program inhibit conditions of a 2X- to 3X-nm SA-STI NAND flash cell [11, 79]. The negative V_t shift occurs in the small FH case, thus it is one of the high field effects during programming. The negative V_t shift phenomena makes the V_t read window margin (RWM) worse for MLC/TLC due to widening V_t distribution width. Therefore, the negative shift phenomena could become a new potential obstacle of scaling NAND flash cells in the scaled 2X-nm NAND flash.

A 2X- and 3X-nm rule SA-STI cells with various FH were used for this experiment. The range of FH small/middle/large in experiments are 10–20 nm. And thickness of IPD (ONO) is around 12 nm. The cross-sectional TEM micrograph of 26-nm SA-STI cell [80] is shown in Fig. 6.72b.

Micron Ex. 1014, p. 272
Micron v. YMTC
IPR2025-00119

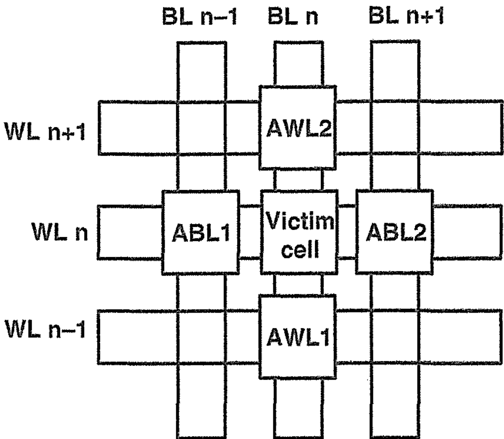

FIGURE 6.73 The cell arrangement for program-inhibited test. Attack cells of ABL1&2 are the adjacent cells along WL direction, and attack cells of AWL1&2 are adjacent cells along BL direction.

Figure 6.73 shows the cell arrangement for the program-inhibited test. Attack cells of ABL1&2 are adjacent cells along the WL direction, and attack cells of AWL1&2 are adjacent cells along the BL direction. The V_t of inhibit victim cells are monitored before and after programming the attack cells.

For an analysis of current flow in an SA-STI structure in the program condition in Section 6.7.4, a cell-structured capacitor is used. Terminals of CG, FG, source/drain junction, and substrate are independently connected to monitor the current.

6.7.2 Negative V_t Shift

Figure 6.74 shows the victim cell V_t shift during the programming of the attack cell. In the case of attack AWL2, the V_t of the victim cell monotonously increases with attack AWL2 cell V_t increased due to conventional FG–FG coupling interference [78] (see Section 5.3). However, in the case of ABL1&2, the V_t of the victim cell initially increases and then decreases as the attack ABL1&2 are programmed. V_t shift caused by programming a neighbor cell should be positive if it is caused by conventional FG–FG coupling interference. However, the V_t shift is showing a negative direction as attack cell V_t increases over $V_t > 7$. This phenomenon is called the "negative V_t shift."

Figure 6.75 shows the dependence of the negative V_t shift on FH. The negative V_t shift has a strong FH dependence. The negative V_t shift is larger when FH is small. In the region of attack cell $V_t < 6$, the slope of (victim cell V_t)/(attack cell V_t) is showing the conventional FG–FG coupling interference. In the case of FH low, the slope is smaller than the case of FH middle and large. This means that the FH low case has small FG–FG coupling interference due to the CG shield effect between FGs.

Figure 6.76 shows the victim cell V_t dependence on (a) attack cell: program and (b) attack cell: inhibit condition, which are illustrated in the right-hand side of Fig. 6.76.

Micron Ex. 1014, p. 273
Micron v. YMTC
IPR2025-00119

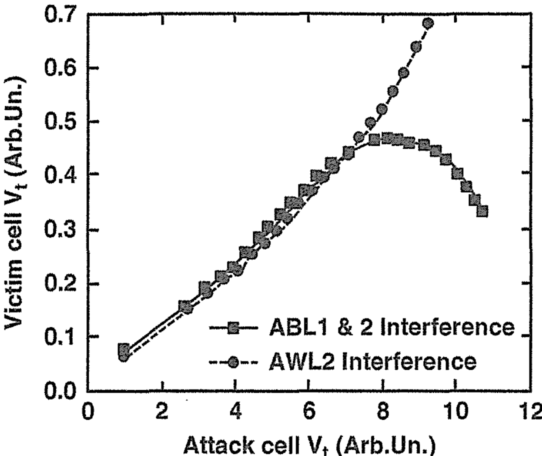

FIGURE 6.74 Victim cell V_t shift versus attack cell programmed V_t. Negative V_t shift phenomena are observed in the case of attack ABL1 and ABL2. Victim cell V_t is corresponding to L1 for MLC.

In (a) attack cell: program, attack cell V_t is monotonously increased. Victim cell V_t initially increases and then decreases as attack cell V_t increases. This V_t movement is the same as that in Fig. 6.74 and Fig. 6.75. However, in the case of (b) attack cell: inhibit, attack cell V_t initially increases, and when the attack cell V_t has reached to around 4 or 7, attack cell V_t stops increasing by changing channel voltage from 0 V to V_{boosting} (inhibit mode) during program pulse. This operation corresponds to the program verify operation [81] in product, such that when V_t has reached a certain V_t, programming is stopped by changing to the inhibit mode during next program pulse (channel voltage changes from 0 V to V_{boosting}). For victim cell V_t in (b) attack cell

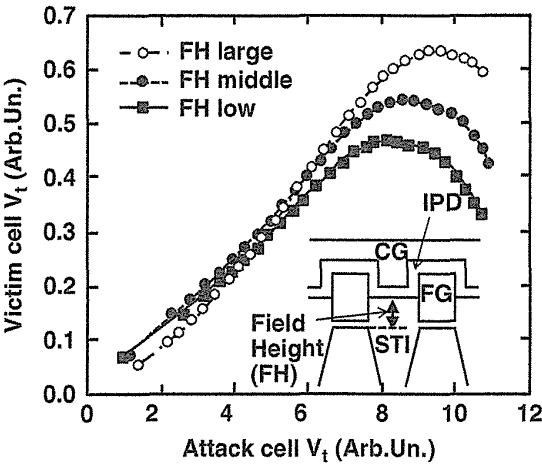

FIGURE 6.75 Field height (FH) dependence of "negative" V_t shift. Small FH has the larger "negative" shift. Victim cell V_t corresponds to L1 for MLC.

Micron Ex. 1014, p. 274
Micron v. YMTC
IPR2025-00119

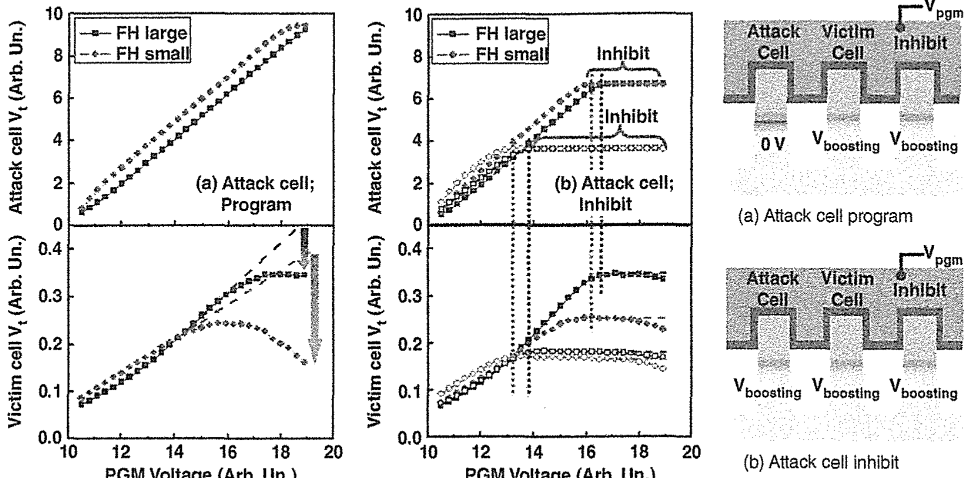

FIGURE 6.76 Victim cell V_t shift in (a) attack cell: program and (b) attack cell: Inhibit. In the case of (a) attack cell program, a large negative shift of victim cell is observed, however, in the case of (b) attack cell: inhibit, negative V_t shift is much smaller. Difference of bias conditions between (a) and (b) is a channel voltage of 0 V for program or V_{boost} (~8 V) for inhibit. Victim cell V_t corresponds to L1 for MLC.

inhibit, a negative shift is much smaller than case (a) attack cell: program, when attack cells are in the inhibit mode, even high program voltage (V_{pgm}) is applied. Because the same high V_{pgm} pulses are applied in both cases (a) and (b), the difference of bias condition between (a) attack cell: program and (b) attack cell: inhibit is only the channel voltage in attack cell, which are 0 V for program or $V_{boosting}$ for inhibit, as shown on the right-hand side of Fig. 6.76. Thus, the channel voltage of 0 V in attack cell produces a negative V_t shift in inhibit victim cell, especially in the case of small FH.

$V_{boosting}$ (~8 V) is generated mainly by V_{pass} for an unselected WL with capacitive coupling between the unselected WL and the cell channel which is isolated by a select transistor in the NAND string in the self-boosting program inhibit scheme [63, 82] (see Section 6.5.1).

6.7.3 Program Speed and Victim Cell V_t Dependence

The program speed dependence of an attack cell is measured in actual page program sequence of MLC NAND product with incremental step pulse program (ISPP) [82] and bit-by-bit verify operation [81]. Figure 6.77 shows the victim cell delta V_t versus attack cell program speed for a 16-Kbit (2-KByte) page. The horizontal axis shows the V_t distribution of a page after applying one program-voltage pulse (V_{pgm}), which means that the left-side cells have slower programming speed, and the right-side cells have faster programming speed. In the case of (a) attack cell ABL1 = L1 & ABL2 = L1 (programming to L1 (lower V_t); Erase → L1), victim cell delta V_t is larger in a slow attack cell and the smaller in a fast attack cell, due to conventional FG–FG

Micron Ex. 1014, p. 275
Micron v. YMTC
IPR2025-00119

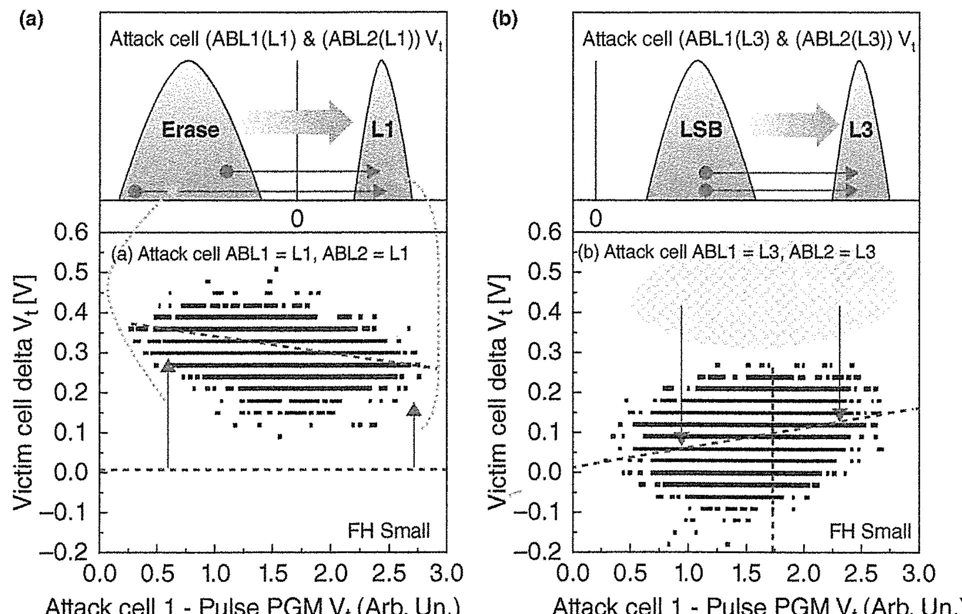

FIGURE 6.77 Victim cell delta V_t distribution of a 16-Kbit cell versus attack cell program speed (attack cell V_t distribution of a page after applying one program-voltage pulse). In the case of (a) attack cell ABL1 = L1 & ABL2 = L1, victim cell delta V_t shows dependence of conventional FG–FG coupling interference. However, in the case of (b) attack cell ABL1 = L3 & ABL2 = L3, victim cell delta V_t shows the larger negative V_t shift for slow attack cell. Victim cell V_t corresponds to L3 for MLC.

interference. The slower attack cells have the larger victim cell delta V_t, because an attack cell V_t change during programming (Erase → L1) is larger in a slow attack cell, as shown in Fig. 6.77a, upper portion.

In order to ensure the larger V_t change in a slow attack cell, the bit-by-bit V_t distribution after program and erase are measured. Figure 6.78 shows the bit-by-bit correspondence of program and erase V_t distributions after one program pulse and one erase pulse. We can see that the program cells on the left-hand side of programmed V_t distribution are also on the left-hand side of erased V_t distribution, and similarly the program cells on the right-hand side of the programmed V_t distribution are also on the right-hand side of the erased V_t distribution. Therefore, it is confirmed that the slow program cells are on the left-hand side of erased V_t distribution, as shown in Fig. 6.77a, upper portion.

On the other hand, in case of (b) attack cell ABL1 = L3 and ABL2 = L3 (programming to L3 (higher V_t); LSB →L3) in Fig. 6.77b, the victim cell delta V_t is smaller in a slow attack cell and larger in a fast attack cell, even if the V_t shift by a conventional FG–FG coupling should be the same between slow and fast cells due to the same attack cell V_t change during programming (LSB → L3), as shown in Fig. 6.77b, upper portion. This means the negative V_t shift is much larger (−0.2 to −0.4 V) in the case of a slow attack cell, compared with a fast attack cell.

Micron Ex. 1014, p. 276
Micron v. YMTC
IPR2025-00119

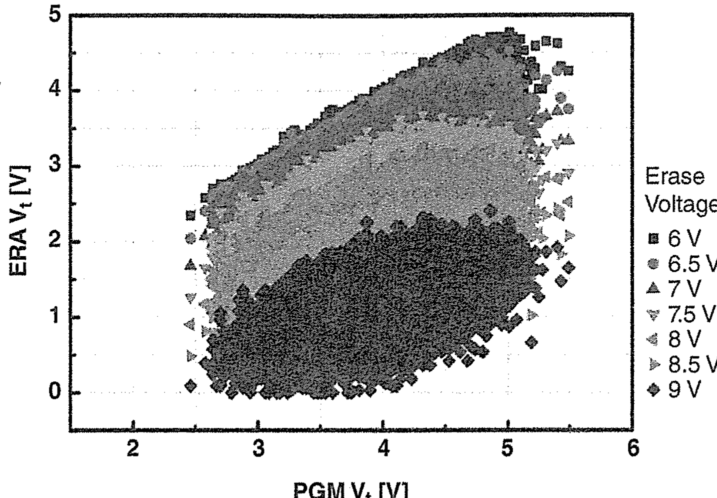

FIGURE 6.78 The bit-by-bit correspondence of program and erase V_t after one program pulse and one erase pulse. Several erase voltages are used (6–9 V). The erased V_t has a parallel shift as erase voltage increases. Then it is supposed that erased V_t distribution in more negative V_t has the same correspondence, so that it is confirmed that the slow program cells are on the left side of the erased V_t distribution.

The reason is supposed that in a slow attack cell, the larger number and higher voltage (V_{pgm}) of program pulses are subjected to the condition of channel voltage = 0 V (see Fig. 6.76a attack cell program). Then the negative shift becomes larger in a slow attack cell. Conversely, in a fast attack cell, the larger number and higher voltage of program pulse are shortly subjected to the condition of channel voltage = 0 V, because a fast attack cell becomes inhibit mode (channel voltage = $V_{boosting}$) earlier than a slow attack cell.

Furthermore, this new negative V_t shift results in wider placement V_t distribution. In the case of (a) attack cell ABL1 = L1 & ABL2 = L1, the victim cell delta V_t distribution width is 0.36 V; however, in the case of (b) attack cell ABL1 = L3 & ABL2 = L3, the victim cell delta V_t distribution width is 0.48 V. These V_t distribution widths have an impact on the read window margin of the MLC/TLC NAND flash product.

Figure 6.79 shows the victim cells dependence on the program state: (a) L1, (b) L2, and (c) L3. The victim cell delta V_t of L3 is smaller than that of L1 and L2, especially in the case of the attack cell ABL1 = L3 & ABL2 = L3. It means the negative V_t shift is larger in victim cell L3. This is considering the fact that if the FG of L3 is negatively charged, then it could gather more positive charge during attack cell programming.

Summarizing the results of the negative V_t shifts phenomena (Sections 6.7.2 and 6.7.3), the negative V_t shift is enhanced in the case of (1) neighbor cell along WL (ABL1,2) in programming (channel voltage = 0 V), (2) small FH, (3) higher V_{PGM}, (4) attack cell: L3, (5) attack cell: slow programming, and (6) victim cell: higher V_t (L3).

Micron Ex. 1014, p. 277
Micron v. YMTC
IPR2025-00119

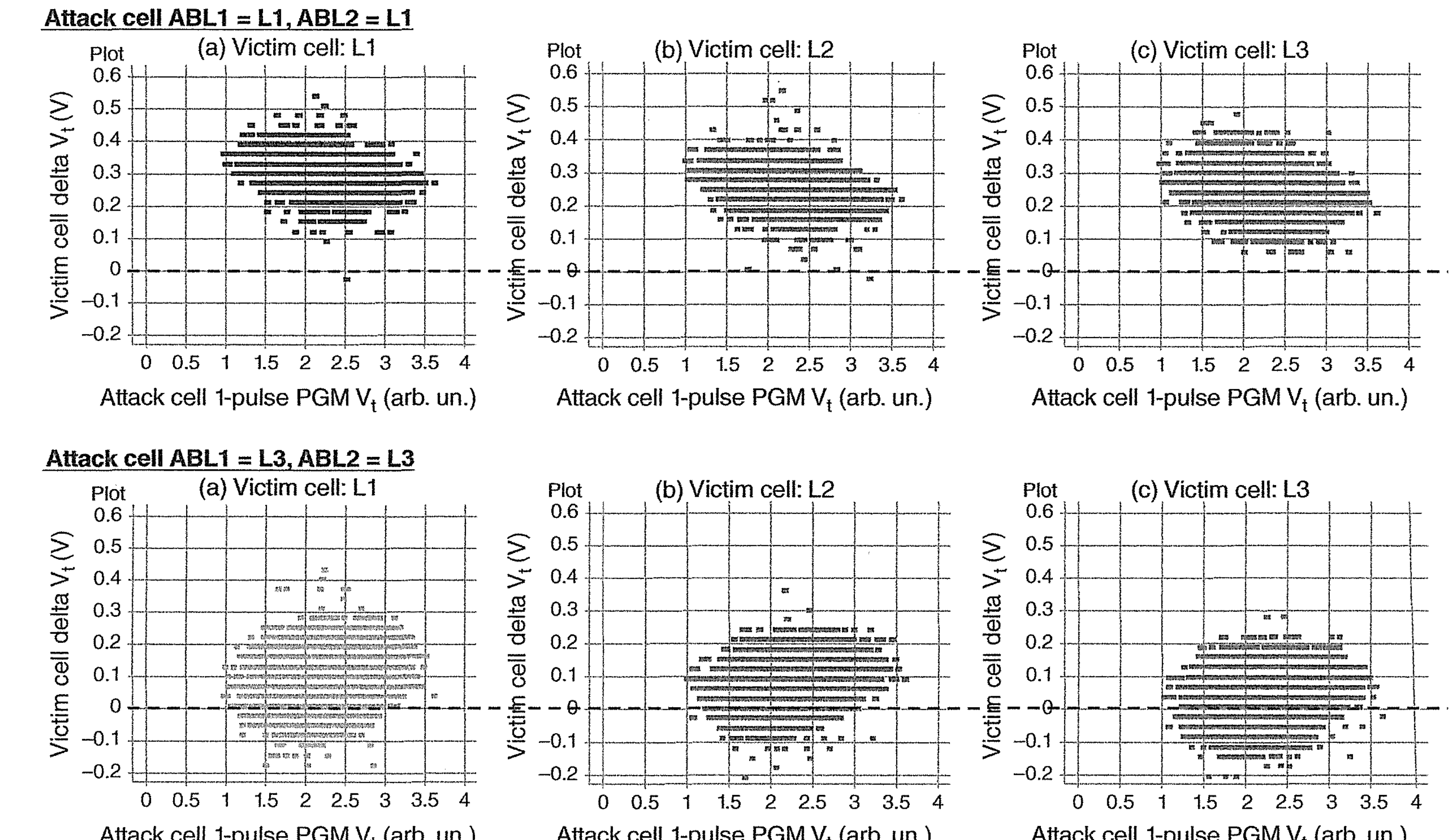

FIGURE 6.79 The dependence of victim cell delta V_t on program states (L1, L2, L3), in attack cell ABL1 = L1 & ABL2 = L1 and Attack cell ABL1 = L3 & ABL2 = L3. Victim cell delta V_t of (c) L3 has the larger negative shift than that of (a) L1 and (b) L2.

Micron Ex. 1014, p. 278
Micron v. YMTC
IPR2025-00119

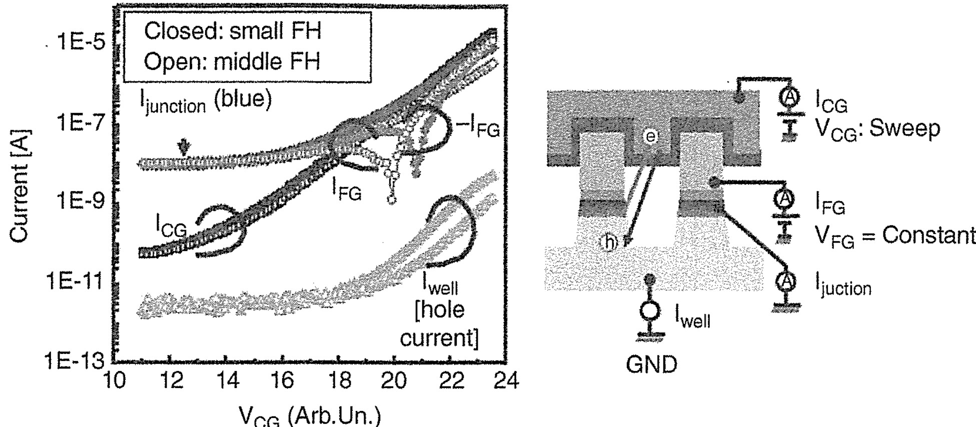

FIGURE 6.80 Current analysis of cell structured capacitor by carrier separation technique. Hole currents (I_{Well}) are observed, and they are increased as V_{CG} is increased. A large hole current is generated due to large I_{junction} in the case of small FH.

6.7.4 Carrier Separation in Programming Conditions

In order to clarify the mechanism of a negative V_t shift, a cell-structured test capacitor was measured by using a carrier separation technique [29, 83–86], as shown in Fig. 6.80 [11, 79]. A cell-structured test capacitor has a stripe patterned active area/STI and flat CG pattern, with source and drain. A measurement condition of Fig. 6.80 is that a control gate voltage (V_{CG}) sweeps while keeping V_{FG} = constant (8 V) and $V_{\mathrm{well}} = V_{\mathrm{juction}} = 0$ V. The image of electron flow is illustrated in Fig. 6.81. Measured current of I_{CG}, I_{FG}, and I_{junction} in Fig. 6.80 can be expressed by using electron flow as shown in Fig. 6.81.

$$I_{\mathrm{CG}} = -I_{\mathrm{CG_Juction}} - I_{\mathrm{CG_FG}} \tag{6.8}$$

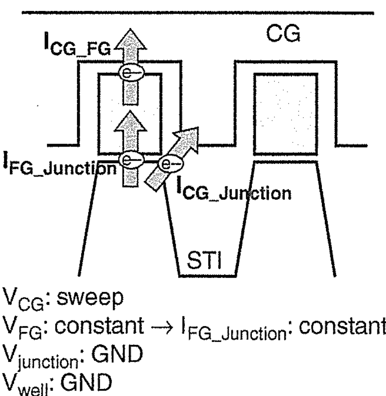

FIGURE 6.81 Electron flow in condition of Fig. 6.80. I_{junction} (in Fig. 6.80) = $I_{\mathrm{CG_Junction}} + I_{\mathrm{FG_Junction}}$. Hole current ($I_{\mathrm{well}}$) at region of $V_{\mathrm{CG}} > 18$ (Fig. 6.80) is generated by $I_{\mathrm{CG_Junction}}$.

$$I_{FG} = -I_{FG_Junction} + I_{CG_FG} \tag{6.9}$$

$$I_{Junction} = I_{CG_Junction} + I_{FG_Junction} \tag{6.10}$$

$$I_{FG_Junction} = \text{constant}$$

It was observed in Fig. 6.80 that the hole current (I_{well}) was increased as V_{CG} increased in a high $V_{CG} > 18$ region. In the region of $V_{CG} > 18$, $I_{CG_Junction}$ and I_{CG_FG} are increased as V_{CG} increased, while $I_{FG_Junction}$ are basically constant because of constant V_{FG}. At $V_{CG} > 18$ in Fig. 6.80, $I_{junction}$ of small FH is larger than $I_{junction}$ of middle FH, and also I_{well} of small FH is larger than I_{well} of middle FH. From these observations of $I_{Junction}$ and I_{well} in Fig. 6.80, I_{well} (hole current) is considered to be generated by $I_{CG_Junction}$, not by I_{CG_FG}, as shown in Fig. 6.81. $I_{CG_Junction}$ is the electron flow of FN injection from channel/junction to CG. $I_{CG_Junction}$ may generate I_{well} (hole current) based on the anode hole injection model [29, 83, 89].

For I_{FG}, I_{FG} is almost constant at $V_{CG} < 20$ because $I_{FG_Junction}$ = constant while I_{CG_FG} is small due to small $V_{CG} - V_{FG}$. As increased V_{CG} to $V_{CG} > 20$, I_{FG} polarity is changed, because I_{CG_FG} is increased by increasing ($V_{CG} - V_{FG}$) and become the dominant current of I_{FG}.

Figure 6.82 shows a current flow in constant V_{CG}. Even if a voltage between channel/junction and CG is constant, I_{CG} is increased as V_{FG} is increased. This means that I_{CG}, which is mainly a direct electron injection from channel/junction to CG, is strongly enhanced by V_{FG}, even if constant V_{CG} is applied. As a scaling down of memory cell size, a FG–FG space becomes narrow. Then I_{CG} will increase because V_{FG} could enhance I_{CG} intensively. It suggests that the negative V_t shift phenomena may be enhanced by scaling down of a memory cell.

The ratio of (substrate hole current) / (gate electron current) [= $I_{well}/I_{junction}$] in Fig. 6.82 is in the range of 10^{-3} over V_{FG} = 3–5. The substrate hole current (I_{well}) is

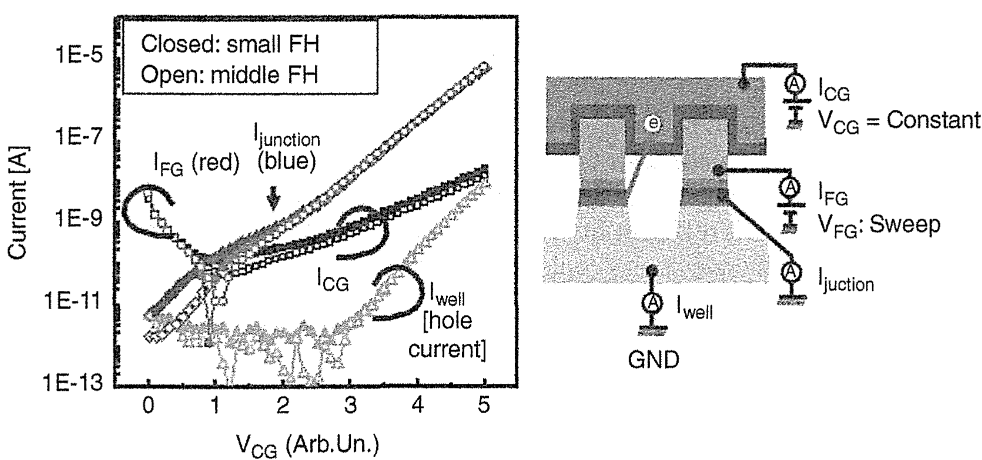

FIGURE 6.82 Current analysis of cell structured capacitance. Even if V_{CG} is constant, I_{CG} (direct electron injection from channel/junction to CG) is increased as V_{FG} is increased. This means I_{CG} is enhanced by FG potential.

Micron Ex. 1014, p. 280
Micron v. YMTC
IPR2025-00119

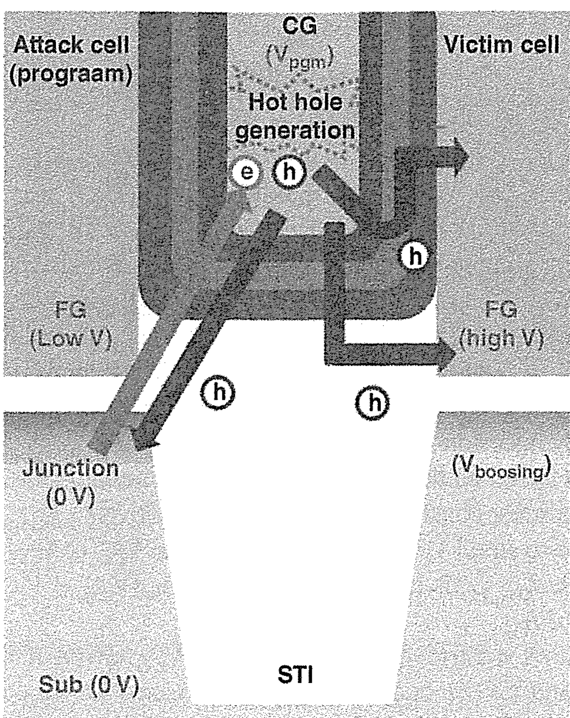

FIGURE 6.83 Suggested mechanism of negative V_t shift in victim cell. Electron injection from channel/Junction (0 V) to CG (V_{PGM}) could generate hot hole at CG, and parts of hot holes are injected to FG of victim cell through field dielectric and IPD. This hot hole injection causes a "negative V_t shift."

mainly generated by FN current through tunnel oxide ($I_{FG_Junction}$). The value is in the same range as previously reported [29,83,84,86,89] for the same oxide thickness and electric field. However, in Fig. 6.80, the ratio of (substrate hole current)/(gate electron current) [$=I_{well}/I_{CG}$], in which the substrate hole current (I_{well}) is mainly generated by FN current from channel to CG, is in the range of 10^{-4}. It is one or two orders of magnitude smaller than the previously reported value of 10^{-3}–10^{-2} [83]. The reason for smaller substrate hole current is not clear; however, it would be that the large number of the generated holes does not flow to the substrate due to cell structure, which is different from the flat capacitor in the previous report [83]. It suggests that the generated holes could flow to any directions, including the direction of FG.

6.7.5 Model

From the results of current flow in cell structured capacitor, the mechanism of negative V_t shift is considered as illustrated in Fig. 6.83. During programming, electrons are injected from channel/junction (0 V) to CG (V_{PGM}) directly. Electron injection generates hot holes by impact ionization, and hot holes are injected to IPD on STI.

Micron Ex. 1014, p. 281
Micron v. YMTC
IPR2025-00119

Parts of hot holes are injected into the FG of the victim cell through the field-oxide dielectric or IPD. Consequently, the V_t of the victim cell has shifted negatively.

This phenomenon would be accelerated with memory cell scaling since I_{CG} increases due to narrow FG–FG space field effect. Then the negative V_t shift phenomenon will be worse in future scaled memory cells. Then the negative V_t shift will be one of new scaling limitation factors to manage the V_t read window margin of 2 bits/cell and 3 bits/cell in 2X nm and beyond the NAND flash memory cell.

A novel program inhibit phenomenon of "negative" cell V_t shift had been presented in 2X- to 3X-nm self-aligned STI NAND flash memory cells. The negative V_t shift is caused in an inhibit cell when an along-WL adjacent cell is programming. The magnitude of the negative shift becomes larger in the case of higher program voltage (V_{PGM}), lower field oxide height (FH), slower program speed of the adjacent cell, and high V_t of the victim cell. The experimental results suggest that the mechanism of negative V_t shift is attributed to hot holes that are generated by FN electrons injection from channel/junction to the control gate (CG). Many reports had previously described the substrate hole current (I_{well}) in an MOS capacitor. However, this negative V_t shift phenomenon was a very rare case where a generated hole current could be directly observed in the device of flash memory cells as V_t shift.

6.8 SUMMARY

In Chapter 6, the phenomena of NAND flash memory reliability have been described.

In Section 6.2, the program/erase (P/E) cycling degradation and data retention characteristics were described. A uniform program and erase scheme, which uses uniform Fowler–Nordheim tunneling over the whole channel area both program and erase, guarantees a wide cell threshold voltage window even after 1 million program/erase cycles. The data retention characteristics could be also guaranteed by applying a uniform program and erase scheme. This uniform program/erase scheme has been used in NAND flash as de facto standard.

Several reliability aspects related to P/E cycling endurance and data retention are discussed in Section 6.3. The degradation by P/E cycling stress are mainly caused by electron/hole traps, stress-induced leakage current (SILC), and interface state generation. And by scaling memory cells, these degradation phenomena are becoming more severe.

In Section 6.4, read disturb characteristics were described. It was clarified experimentally that flash memory cell programmed and erased by Fowler–Nordheim tunneling (FN-t) has 10 times longer retention time than the conventional one, which is programmed by channel-hot-electron (CHE) injection and erased by FN-t. This difference of data retentivity between these two P/E schemes is due to decreasing the stress–induced leakage current (SILC) of thin gate oxide by bipolarity FN-t stress. Also, this improvement in data retention is more remarkable as the gate oxide thickness decreases. Therefore, a bipolarity FN-t P/E scheme, which enables a flash memory cell to scale down its oxide thickness, promisingly becomes the key technology to realize reliable flash memory.

Micron Ex. 1014, p. 282
Micron v. YMTC
IPR2025-00119

Several analysis results of read disturb were also presented. The V_t shift of read disturb can be separated into two regions. Initially, the electron detrapping from tunnel oxide causes V_t shift in read disturb; after that, SILC causes a V_t shift. Also, the hot carrier injection phenomenon was presented in Section 6.4.4. During read operation, a hot carrier is generated by locally boosted node in NAND string and then is injected to a cell floating gate.

Program disturb was described in Section 6.5. By scaling down memory cells, it is becoming difficult to manage a program disturb failure because of the unexpected degradation mechanism of hot carrier injection and channel coupling. The hot carrier injection is caused in the high-field location between the self-boosting voltage (~8 V) and other (0 V), as described in Section 6.5.2. The channel coupling effect during programming was also described in Section 6.5.3. The neighbor channel voltage of 0 V has an impact on self-boosted inhibit channel voltage not only by capacitive coupling but also by band-to-band leakage in boosting node.

The erratic over program are described in Section 6.6. The erratic over-program is caused by excess electron injection through tunnel oxide during programming. Strong ECC can manage the erratic over-programming failure.

In Section 6.7, a novel program inhibit phenomena of "negative" cell V_t shift had been presented. The negative V_t shift is caused in an inhibit cell when an along-WL adjacent cell is programming. The magnitude of the negative shift becomes larger in the case of higher program voltage (V_{PGM}), lower field oxide height (FH), slower program speed of the adjacent cell, and high V_t of the victim cell. The experimental results suggest that the mechanism of negative V_t shift is attributed to hot holes that are generated by FN electrons injection from channel/junction to the control gate (CG).

Flash memory reliability and physical phenomena are summarized in Fig. 6.84 [90]. It is clarified that carrier traps in tunnel oxide, detrapping, SILC (stress–induced leakage current) are the major root causes of degradation of flash memory reliability.

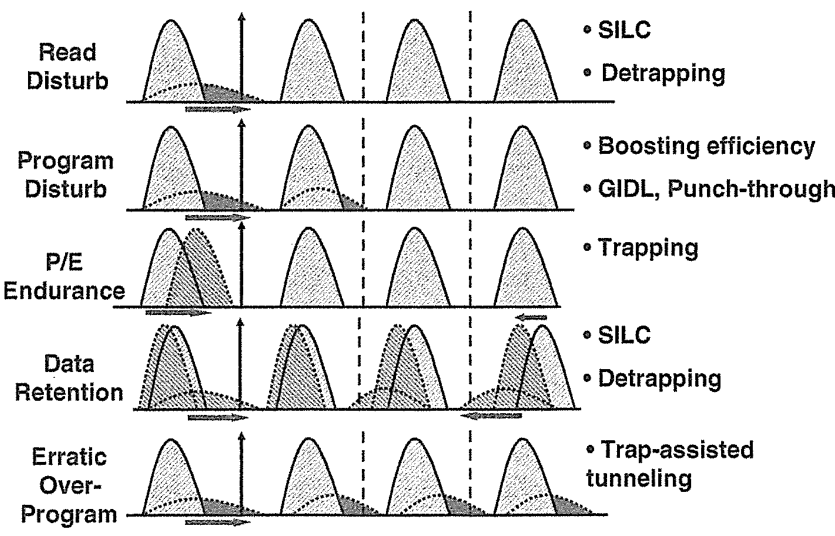

FIGURE 6.84 Summary of reliability and physical mechanism.

Micron Ex. 1014, p. 283
Micron v. YMTC
IPR2025-00119

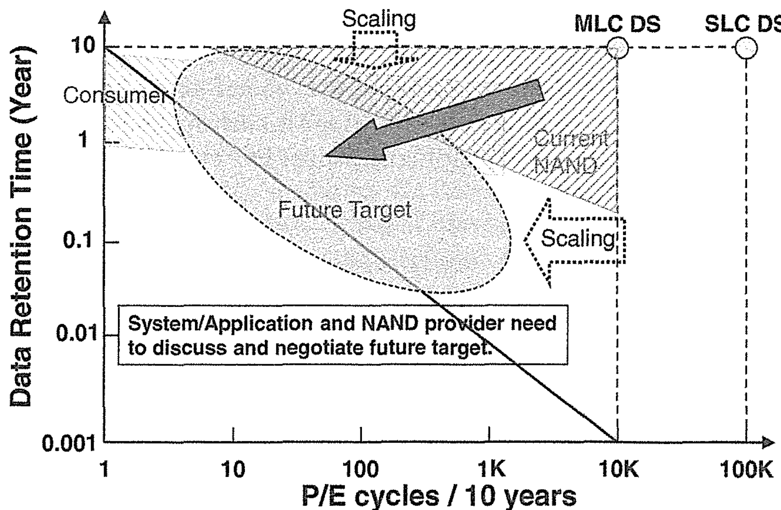

FIGURE 6.85 Prospect of data retention versus program/erase cycling. Due to encountering physical limitation, reliability in a future scaling device will be worse than that in the current device. System management would be essential.

The important reliability aspects of program/erase cycling endurance and data retention are trade-off relationship, as shown in Fig. 6.85 [90]. The future target of P/E cycling and data retention will be compromised as <1K P/E cycling and <1 year data retention even with system solutions.

Performance and reliability are also trade-off relationship [90], as shown in Fig. 6.86. If high-speed programming is required, the reliability (such as P/E cycling) will be degraded because the higher electrical field is applied to tunnel oxide in the

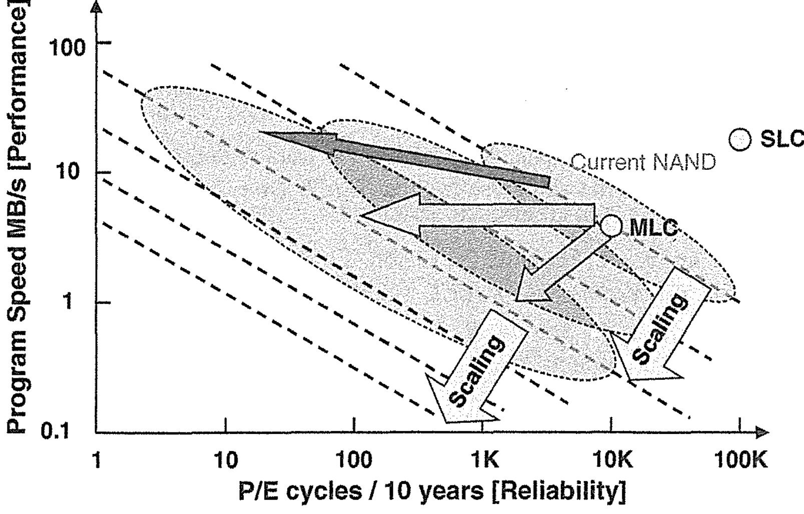

FIGURE 6.86 Prospect of performance versus reliability. Performance and reliability are "trade-off." As device scaling, both performance and reliability will be degraded naturally. By efforts of increasing page size, performance could be kept or be improved.

Micron Ex. 1014, p. 284
Micron v. YMTC
IPR2025-00119

memory cell during program. On the other hand, if some application requires high reliability, such as >10K P/E cycling, >3 years retention, the performance of such high-speed programming should be compromised. Therefore, target specification of NAND flash reliability would be greatly subdivided to each application, such as memory cards, consumer application (smartphone, tablet PC, etc), high-end applications (enterprise server SSD), and so on.

REFERENCES

[1] Masuoka, F.; Momodomi, M.; Iwata, Y.; Shirota, R. New ultra high density EPROM and flash EEPROM with NAND structure cell, *Electron Devices Meeting, 1987 International*, vol. 33, pp. 552–555, 1987.

[2] Shirota, R.; Itoh, Y.; Nakayama, R.; Momodomi, M.; Inoue, S.; Kirisawa, R.; Iwata, Y.; Chiba, M.; Masuoka, F. New NAND cell for ultra high density 5v-only EEPROMs, *Digest of Technical Papers—Symposium on VLSI Technology*, 1988, pp. 33–34.

[3] Momodomi, M.; Kirisawa, R.; Nakayama, R.; Aritome, S.; Endoh, T.; Itoh, Y.; Iwata, Y.; Oodaira, H.; Tanaka, T.; Chiba, M.; Shirota, R.; Masuoka, F. New device technologies for 5 V-only 4 Mb EEPROM with NAND structure cell, *Electron Devices Meeting, 1988. IEDM '88. Technical Digest, International*, pp. 412–415, 1988.

[4] Kirisawa, R.; Aritome, S.; Nakayama, R.; Endoh, T.; Shirota, R.; Masuoka, F. A NAND structured cell with a new programming technology for highly reliable 5 V-only flash EEPROM, *1990 Symposium on VLSI Technology. Digest of Technical Papers*, pp. 129–130, 1990.

[5] Aritome, S.; Shirota, R.; Kirisawa, R.; Endoh, T.; Nakayama, R.; Sakui, K.; Masuoka, F. A reliable bi-polarity write/erase technology in flash EEPROMs, *International Electron Devices Meeting, 1990. IEDM '90. Technical Digest*, pp. 111–114, 1990.

[6] Aritome, S.; Kirisawa, R.; Endoh, T.; Nakayama, R.; Shirota, R.; Sakui, K.; Ohuchi, K.; Masuoka, F. Extended data retention characteristics after more than 10^4 write and erase cycles in EEPROMs, *International Reliability Physics Symposium, 1990. 28th Annual Proceedings*, pp. 259–264, 1990.

[7] Aritome, S.; Shirota, R.; Sakui, K.; Masuoka, F. Data retention characteristics of flash memory cells after write and erase cycling, *IEICE Trans. Electron*, vol. E77-C, no. 8, pp. 1287–1295, Aug. 1994.

[8] Aritome, S.; Shirota, R.; Hemink, G.; Endoh, T.; Masuoka, F. Reliability issues of flash memory cells, *Proceedings of the IEEE*, vol. 81, no. 5, pp. 776–788, 1993.

[9] Hemink, G.; Endoh, T.; Shirota, R. Modeling of the hole current caused by fowler–nordheim tunneling through thin oxides, *Japanese Journal of Applied Physics*, vol. 33, pp. 546–549, 1994.

[10] Aritome, S.; Satoh, S.; Maruyama, T.; Watanabe, H.; Shuto, S.; Hemink, G. J.; Shirota, R.; Watanabe, S.; Masuoka, F. A 0.67 μm^2 self-aligned shallow trench isolation cell (SA-STI cell) for 3 V-only 256 Mbit NAND EEPROMs, *Electron Devices Meeting, 1994. IEDM '94. Technical Digest, International*, pp. 61–64, 11–14 Dec. 1994.

[11] Aritome, S.; Seo, S.; Kim, H.-S.; Park, S.-K.; Lee, S.-K.; Hong, S. Novel negative V_t shift phenomenon of program–inhibit cell in 2X–3X nm self-aligned STI NAND flash

Micron Ex. 1014, p. 285
Micron v. YMTC
IPR2025-00119

memory, *Electron Devices, IEEE Transactions on*, vol. 59, no. 11, pp. 2950–2955, Nov. 2012.

[12] Masuoka, F.; Asano, M.; Iwahashi, H.; Komuro, T.; Tanaka, S. A new flash E^2PROM cell using triple polysilicon technology, *Electron Devices Meeting, 1984 International*, vol. 30, pp. 464–467, 1984.

[13] Tam, S.; Sachdev, S.; Chi, M.; Verma, G.; Ziller, J.; Tsau, G.; Lai, S.; Dham, V. *1988 Symposium on VLSI Technology, Technical Papers*, pp. 31–32, 1988.

[14] Kume, H.; Yamamoto, H.; Adachi, T.; Hagiwara, T.; Komori, K.; Nishimoto, T.; Koike, A.; Meguro, S.; Hayashida, T.; Tsukada, T. A flash-erase EEPROM cell with an asymmetric source and drain structure, *Electron Devices Meeting, 1987 International*, vol. 33, pp. 560–563, 1987.

[15] Ajika, N.; Ohi, M.; Arima, H.; Matsukawa, T.; Tsubouchi, N. A 5 volt only 16M bit flash EEPROM cell with a simple stacked gate structure, *Electron Devices Meeting, 1990. IEDM '90. Technical Digest, International*, pp. 115–118, 9–12 Dec. 1990.

[16] Onoda, H.; Kunori, Y.; Kobayashi, S.; Ohi, M.; Fukumoto, A.; Ajika, N.; Miyoshi, H. A novel cell structure suitable for a 3 volt operation, sector erase flash memory, *Electron Devices Meeting, 1992. IEDM '92. Technical Digest, International*, pp. 599–602, 13–16 Dec. 1992.

[17] Kodama, N.; Saitoh, K.; Shirai, H.; Okazawa, T.; Hokari, Y. A 5V only 16 Mbit flash EEPROM cell using highly reliable write/erase technologies, *VLSI Technology, 1991. Digest of Technical Papers, 1991 Symposium on*, pp. 75–76, 28–30 May 1991.

[18] Verma, G.; Mielke, N. Reliability performance of ETOX based flash memories, *Reliability Physics Symposium 1988. 26th Annual Proceedings, International*, pp. 158–166, 12–14 April 1988.

[19] Baglee, D. A.; Smayling, M. C. The effects of write/erase cycling on data loss in EEPROMs, *Electron Devices Meeting, 1985 International*, vol. 31, pp. 624–626, 1985.

[20] Witters, J. S.; Groeseneken, G.; Maes, H. E. Degradation of tunnel-oxide floating-gate EEPROM devices and the correlation with high field-current-induced degradation of thin gate oxides, *IEEE Transactions on Electron Devices*, vol. 36, no. 9, part 2, pp. 1663–1682, 1989.

[21] Haddad, S.; Chang, C.; Swaminathan, B.; Lien, J. Degradations due to hole trapping in flash memory cells, *Electron Device Letters, IEEE*, vol. 10, no. 3, pp. 117–119, March 1989.

[22] Mori, S.; Kaneko, Y.; Arai, N.; Ohshima, Y.; Araki, H.; Narita, K.; Sakagami, E.; Yoshikawa, K. Reliability study of thin inter-poly dielectrics for non-volatile memory application, *Reliability Physics Symposium, 1990. 28th Annual Proceedings, International*, pp. 132–144, 27–29 March 1990.

[23] Chen, J.; Chan, T.-Y.; Chen, I.-C.; Ko, P.-K.; Chenming, Hu. Subbreakdown drain leakage current in MOSFET, *Electron Device Letters, IEEE*, vol. 8, no. 11, pp. 515, 517, Nov. 1987.

[24] Chan, T.-Y.; Chen, J.; Ko, P.-K.; Hu, C. The impact of gate-induced drain leakage current on MOSFET scaling, *Electron Devices Meeting, 1987 International*, vol. 33, pp. 718, 721, 1987.

[25] Shirota, R.; Endoh, T.; Momodomi, M.; Nakayama, R.; Inoue, S.; Kirisawa, R.; Masuoka, F. An accurate model of subbreakdown due to band-to-band tunneling and its application,

Micron Ex. 1014, p. 286
Micron v. YMTC
IPR2025-00119

Electron Devices Meeting, 1988. IEDM '88. Technical Digest, International, pp. 26, 29, 11–14 Dec. 1988.

[26] Olivo, P.; Nguyen, T.N.; Ricco, B. High-field-induced degradation in ultra-thin SiO_2 films, *Electron Devices, IEEE Transactions on*, vol. 35, no. 12, pp. 2259–2267, Dec. 1988.

[27] Naruke, K.; Taguchi, S.; Wada, M. Stress induced leakage current limiting to scale down EEPROM tunnel oxide thickness, *IEDM Technical Digest*, pp. 424–427, Dec. 1988.

[28] Hemink, G. J.; Shimizu, K.; Aritome, S.; Shirota, R. Trapped hole enhanced stress induced leakage currents in NAND EEPROM tunnel oxides, *IEEE International Reliability Physics Symposium*, 1996. *34th Annual Proceedings*, pp. 117–121, 1996.

[29] Weinberg, Z. A.; Fischetti, M. V.; Nissan-Cohen, Y. SiO_2 induced substrate current and its relation to positive charge in field effect transistor, *Journal of Applied Physics*, vol. 59, no. 3, pp. 824–832, 1 Feb. 1986.

[30] Lee, J.-D.; Choi, J.-H.; Park, D.; Kim, K. Data retention characteristics of sub-100 nm NAND flash memory cells, *IEEE Electron Device Letters*, vol. 24, no. 12, pp. 748–750, 2003.

[31] Lee, J.-D.; Choi, J.-H.; Park, D.; Kim, K. Degradation of tunnel oxide by FN current stress and its effects on data retention characteristics of 90 nm NAND flash memory cells, *41st Annual. 2003 IEEE International Reliability Physics Symposium Proceedings*, pp. 497–501, 2003.

[32] Lee, J.-D.; Choi, J.-H.; Park, D.; Kim, K. Effects of interface trap generation and annihilation on the data retention characteristics of flash memory cells, *IEEE Transactions on Device and Materials Reliability*, vol. 4, no. 1, pp. 110–117, 2004.

[33] Fayrushin, A.; Seol, K.S.; Na, J.H.; Hur, S.H.; Choi, J.D.; Kim, K. The new program/erase cycling degradation mechanism of NAND flash memory devices, *2009 IEEE International Electron Devices Meeting (IEDM)*, pp. 822–826, 2009.

[34] Perniola, L.; Bernardini, S.; Iannaccone, G.; Masson, P.; De Salvo, B.; Ghibaudo, G.; Gerardi, C. Analytical model of the effects of a nonuniform distribution of stored charge on the electrical characteristics of discrete-trap nonvolatile memories, *Nanotechnology, IEEE Transactions on*, vol. 4, no. 3, pp. 360, 368, May 2005.

[35] Cappelletti, P.; Bez, R.; Modelli, A.; Visconti, A. What we have learned on flash memory reliability in the last ten years, IEEE International Electron Devices Meeting, 2004. IEDM Technical Digest. 2004, pp. 489–492.

[36] Arai, F.; Maruyama, T.; Shirota, R. Extended data retention process technology for highly reliable flash EEPROMs of 10^6 to 10^7 W/E cycles, *36th Annual 1998 IEEE International Reliability Physics Symposium Proceedings, 1998*. pp. 378–382, 1998.

[37] Mielke, N.; Marquart, T.; Ning, Wu; Kessenich, J.; Belgal, H.; Schares, E.; Trivedi, F.; Goodness, E.; Nevill, L.R. Bit error rate in NAND flash memories, *IEEE International Reliability Physics Symposium, 2008. IRPS 2008*. pp. 9–19, 2008.

[38] Satoh, S.; Hemink, G.; Hatakeyama, K.; Aritome, S. Stress-induced leakage current of tunnel oxide derived from flash memory read-disturb characteristics, *IEEE Transactions on Electron Devices*, vol. 45, no. 2, pp. 482–486, 1998.

[39] Satoh, S.; Hemink, G. J.; Hatakeyama, F.; Aritome, S. Stress induced leakage current of tunnel oxide derived from flash memory read-disturb characteristics, *Microelectronic Test Structures, 1995. ICMTS 1995. Proceedings of the 1995 International Conference on*, pp. 97–101, 22–25 March 1995.

Micron Ex. 1014, p. 287
Micron v. YMTC
IPR2025-00119

[40] Kato, M.; Miyamoto, N.; Kume, H.; Satoh, A.; Adachi, T.; Ushiyama, M.; Kimura, K. Read-disturb degradation mechanism due to electron trapping in the tunnel oxide for low-voltage flash memories, *Technical Digest., International Electron Devices Meeting, 1994. IEDM '94*. pp. 45–48, 1994.

[41] Mielke, N.; Belgal, H.; Kalastirsky, I.; Kalavade, P.; Kurtz, A.; Meng, Q.; Righos, N.; Wu, J. Flash EEPROM threshold instabilities due to charge trapping during program/erase cycling, *IEEE Transactions on Device and Materials Reliability*, vol. 4, no. 3, pp. 335–344, 2004.

[42] Belgal, H. P.; Righos, N.; Kalastirsky, I.; Peterson, J. J.; Shiner, R.; Mielke, N. A new reliability model for post-cycling charge retention of flash memories, *Reliability Physics Symposium Proceedings, 2002. 40th Annual*, pp. 7–20, 2002.

[43] Mielke, N.; Belgal, H.P.; Fazio, A.; Meng, Q.; Righos, N. Recovery effects in the distributed cycling of flash memories, *IEEE International Reliability Physics Symposium Proceedings, 2006. 44th Annual*, pp. 29–35, 2006.

[44] Modelli, A.; Gilardoni, F.; Ielmini, D.; Spinelli, A. S. A new conduction mechanism for the anomalous cells in thin oxide flash EEPROMs, *Proceedings. 39th Annual. 2001 IEEE International Reliability Physics Symposium, 2001*. pp. 61–66, 2001.

[45] Compagnoni, C. M.; Miccoli, C.; Mottadelli, R.; Beltrami, S.; Ghidotti, M.; Lacaita, A. L.; Spinelli, A. S.; Visconti, A. Investigation of the threshold voltage instability after disturbuted cycling in nanoscale NAND flash memory array, *IEEE International Reliability Physics Symposium, 2010, IRPS 2010*, pp. 604–610, 2010.

[46] Ielmini, D.; Spinelli, A. S.; Lacaita, A. L.; Modelli, A. Equivalent cell approach for extraction of the SILC distribution in flash EEPROM cells, *IEEE Electron Device Letters*, vol. 23, no. 1, pp. 40–42, 2002.

[47] Ielmini, D.; Spinelli, A. S.; Lacaita, A. L.; Leone, R.; Visconti, A. Localization of SILC in flash memories after program/erase cycling, *40th Annual Reliability Physics Symposium Proceedings*, pp. 1–6, 2002.

[48] Ielmini, D.; Spinelli, A. S.; Lacaita, A. L.; van Duuren, M. J. Correlated defect generation in thin oxides and its impact on flash reliability, *Digest International Electron Devices Meeting, 2002. IEDM '02*, pp. 143–146, 2002.

[49] Ielmini, D.; Spinelli, A. S.; Lacaita, A. L.; Modelli, A. A statistical model for SILC in flash memories, *IEEE Transactions on Electron Devices*, vol. 49, no. 11, pp. 1955–1961, 2002.

[50] Ielmini, D.; Spinelli, A. S.; Lacaita, A. L.; Visconti, A. Statistical profiling of SILC spot in flash memories, *Electron Devices, IEEE Transactions* on, vol. 49, no. 10, pp. 1723–1728, 2002.

[51] Ghidini, G.; Sebastiani, A.; Brazzelli, D. Stress induced leakage current and bulk oxide trapping: Temperature evolution, *40th Annual Reliability Physics Symposium Proceedings*, pp. 415–416, 2002.

[52] Scott, R. S.; Dumin, N. A.; Hughes, T. W.; Dumin, D. J.; Moore, B. T. Properties of high-voltage stress generated traps in thin silicon oxide, *IEEE Transactions on Electron Devices*, vol. 43, no. 7, pp. 1133–1143, 1996.

[53] Kurata, H.; Otsuga, K.; Kotabe, A.; Kajiyama, S.; Osabe, T.; Sasago, Y.; Narumi, S.; Tokami, K.; Kamohara, S.; Tsuchiya, O. The impact of random telegraph signals on the scaling of multilevel flash memories, *VLSI Circuits, 2006. Digest of Technical Papers. 2006 Symposium on*, pp. 112–113.

Micron Ex. 1014, p. 288
Micron v. YMTC
IPR2025-00119

[54] Yamada, S.; Amemiya, K.; Yamane, T.; Hazama, H.; Hashimoto, K. Non-uniform current flow through thin oxide after Fowler–Nordheim current stress, *Reliability Physics Symposium, 1996. 34th Annual Proceedings, IEEE International*, pp. 108–112, 30 Apr–2 May 1996.

[55] Kimura, M.; Koyama, H. Stress-induced low-level leakage mechanism in ultrathin silicon dioxide films caused by neutral oxide trap generation, *Reliability Physics Symposium, 1994. 32nd Annual Proceedings, IEEE International,* pp. 167–172, 11–14 April 1994.

[56] Dumin, D. J.; Maddux, J. R. Correlation of stress-induced leakage current in thin oxides with trap generation inside the oxides, *Electron Devices, IEEE Transactions on*, vol. 40, no. 5, pp. 986–993, May 1993.

[57] Rofan, R.; Hu, C. Stress-induced oxide leakage, *Electron Device Letters, IEEE*, vol. 12, no. 11, pp. 632–634, Nov. 1991.

[58] Takagi, S.; Yasuda, N.; Toriumi, A. A new I–V model for stress-induced leakage current including inelastic tunneling, *Electron Devices, IEEE Transactions on*, vol. 46, no. 2, pp. 348–354, Feb. 1999.

[59] Belgal, H.P.; Righos, N.; Kalastirsky, I.; Peterson, J.J.; Shiner, R.; Mielke, N. A new reliability model for post-cycling charge retention of flash memories, *Reliability Physics Symposium Proceedings, 2002. 40th Annual*, pp. 7–20, 2002.

[60] Wang, H.-H.; Shieh, P.-S.; Huang, C.-T.; Tokami, K.; Kuo, R.; Chen, Shin-Hsien.; Wei, Houng-Chi.; Pittikoun, S.; Aritome, S. A new read-disturb failure mechanism caused by boosting hot-carrier injection effect in MLC NAND flash memory, *Memory Workshop, 2009. IMW '09. IEEE International*, pp. 1–2, 10–14 May 2009.

[61] Takeuchi, K.; Kameda, Y.; Fujimura, S.; Otake, H.; Hosono, K.; Shiga, H.; Watanabe, Y.; Futatsuyama, T.; Shindo, Y.; Kojima, M.; Iwai, M.; Shirakawa, M.; Ichige, M.; Hatakeyama, K.; Tanaka, S.; Kamei, T.; Fu, J.Y.; Cernea, A.; Li, Y.; Higashitani, M.; Hemink, G.; Sato, S.; Oowada, K.; Shih-Chung Lee; Hayashida, N.; Wan, J.; Lutze, J.; Tsao, S.; Mofidi, M.; Sakurai, K.; Tokiwa, N.; Waki, H.; Nozawa, Y.; Kanazawa, K.; Ohshima, S. A 56 nm CMOS 99 mm^2 8 Gb Multi-level NAND flash memory with 10 MB/s Program Throughput, *Solid-State Circuits Conference, 2006. ISSCC 2006. Digest of Technical Papers. IEEE International*, pp. 507–516, 6–9 Feb. 2006.

[62] Suh, K.-D.; Suh, B.-H.; Lim, Y.-H.; Kim, J.-K.; Choi, Y.-J.; Koh, Y.-N.; Lee, S.-S.; Kwon, S.-C.; Choi, B.-S.; Yum, J.-S.; Choi, J.-H.; Kim, J.-R.; Lim, H.-K. A 3.3 V 32 Mb NAND flash memory with incremental step pulse programming scheme, *Solid-State Circuits, IEEE Journal of*, vol. 30, no. 11, pp. 1149–1156, Nov. 1995.

[63] Satoh, S.; Hagiwara, H.; Tanzawa, T.; Takeuchi, K.; Shirota, R. A novel isolation-scaling technology for NAND EEPROMs with the minimized program disturbance, *Electron Devices Meeting, 1997. IEDM '97. Technical Digest, International*, pp. 291–294, 7–10 Dec. 1997.

[64] Torsi, A.; Yijie Zhao; Haitao Liu; Tanzawa, T.; Goda, A.; Kalavade, P.; Parat, K. A program disturb model and channel leakage current study for sub-20 nm NAND flash cells, *Electron Devices, IEEE Transactions on*, vol. 58, no. 1, pp. 11,16, Jan. 2011.

[65] Lee, J. D.; Lee, C. K.; Lee, M. W.; Kim, H.S.; Park, K. C.; Lee, W. S. A new programming disturbance phenomenon in NAND flash memory by source/drain Hot-electrons generated by GIDL current, *NVSMW*, pp. 31–33, 2006.

[66] Joo, S. J.; Yang, H. J.; Noh, K. H.; Lee, H. G.; Woo, W. S.; Lee, J. Y.; Lee, M. K.; Choi, W. Y.; Hwang, K. P.; Kim, H. S.; Sim, S. Y.; Kim, S. K.; Chang, H. H.; Bae,

Micron Ex. 1014, p. 289
Micron v. YMTC
IPR2025-00119

G. H. Abnormal disturbance mechanism of Sub-100 nm NAND flash memory, *Japanese Journal of Applied Physics*, 45, pp. 6210–6215, 2006.

[67] Oh, D.; Lee, S.; Lee, C.; Song, J.; Lee, W.; Choi, J. Program disturb phenomenon by DIBL in MLC NAND Flash Device, *NVSMW*, pp. 5–7, 2008.

[68] Oh, D.; Lee, C.; Lee, S.; Kim, T. K.; Song, J.; Choi, J. New self-boosting phenomenon by source/drain depletion cut-off in NAND flash memory, *NVSMW*, pp. 39–41, 2007.

[69] Lee, C.; Hwang, J.; Fayrushin, A.; Kim, H.; Son, B.; Park, Y.; Jin, G.; Jung, E. S. Channel coupling phenomenon as scaling barrier of NAND flash memory beyond 20 nm node, *Memory Workshop (IMW), 2013 5th IEEE International*, pp. 72,75, 26–29 May 2013.

[70] Park, Y.; Lee, J. Device considerations of planar NAND flash memory for extending towards sub-20 nm regime, *Memory Workshop (IMW), 2013 5th IEEE International*, pp. 1,4, 26–29 May 2013.

[71] Park, Y.; Lee, J.; Cho, S. S.; Jin, G.; Jung, EunSeung. Scaling and reliability of NAND flash devices, *Reliability Physics Symposium, 2014 IEEE International*, pp. 2E.1.1, 2E.1.4, 1–5 June 2014.

[72] Seo, J.; Han, K.; Youn, T.; Heo, H.-E.; Jang, S.; Kim, J.; Yoo, H.; Hwang, J.; Yang, C.; Lee, H.; Kim, B.; Choi, E.; Noh, K.; Lee, B.; Lee, B.; Chang, H.; Park, S.; Ahn, K.; Lee, S.; Kim, J.; Lee, S. Highly reliable M1X MLC NAND flash memory cell with novel active air-gap and p+ poly process integration technologies, *Electron Devices Meeting (IEDM), 2013 IEEE International*, pp. 3.6.1, 3.6.4, 9–11 Dec. 2013.

[73] Aritome, S. Advanced flash memory technology and trends for file storage application, *Electron Devices Meeting, 2000. IEDM Technical Digest. International*, pp. 763–766, 2000.

[74] Shimizu, K.; Narita, K.; Watanabe, H.; Kamiya, E.; Takeuchi, Y.; Yaegashi, T.; Aritome, S.; Watanabe, T. A novel high-density $5F^2$ NAND STI cell technology suitable for 256 Mbit and 1 Gbit flash memories, *Electron Devices Meeting, 1997. IEDM '97. Technical Digest, International*, pp. 271–274, 7–10 Dec. 1997.

[75] Takeuchi, Y.; Shimizu, K.; Narita, K.; Kamiya, E.; Yaegashi, T.; Amemiya, K.; Aritome, S. A self-aligned STI process integration for low cost and highly reliable 1 Gbit flash memories, *VLSI Technology, 1998. Digest of Technical Papers. 1998 Symposium on*, pp. 102–103, 9–11 June 1998.

[76] Imamiya, K.; Sugiura, Y.; Nakamura, H.; Himeno, T.; Takeuchi, K.; Ikehashi, T.; Kanda, K.; Hosono, K.; Shirota, R.; Aritome, S.; Shimizu, K.; Hatakeyama, K.; Sakui, K. A 130 mm^2 256 Mb NAND flash with shallow trench isolation technology, *Solid-State Circuits Conference, 1999. Digest of Technical Papers. ISSCC. 1999 IEEE International*, pp. 112–113, 1999.

[77] Hwang, J.; Seo, J.; Lee, Y.; Park, S.; Leem, J.; Kim, J.; Hong, T.; Jeong, S.; Lee, K.; Heo, H.; Lee, H.; Jang, P.; Park, K.; Lee, M.; Baik, S.; Kim, J.; Kkang, H.; Jang, M.; Lee, J.; Cho, G.; Lee, J.; Lee, B.; Jang, H.; Park, S.; Kim, J.; Lee, S.; Aritome, S.; Hong, S.; Park, S. A middle-1X nm NAND flash memory cell (M1X-NAND) with highly manufacturable integration technologies, *Electron Devices Meeting (IEDM), 2011 IEEE International*, pp. 199–202, Dec. 2011.

[78] Lee, J.-D.; Hur, S.-H.; Choi, J.-D. Effects of floating-gate interference on NAND flash memory cell operation, *Electron Device Letters, IEEE*, vol. 23, no. 5, pp. 264–266, May 2002.

Micron Ex. 1014, p. 290
Micron v. YMTC
IPR2025-00119

[79] Seo, S.; Kim, H.; Park, S.; Lee, S.; Aritome, S.; Hong, S. Novel negative V_t shift program disturb phenomena in 2X–3X nm NAND flash memory cells, *Reliability Physics Symposium (IRPS), 2011 IEEE International*, pp. 6B.2.1–6B.2.4, 10–14 April 2011.

[80] Shim, H.; Lee, S.-S.; Kim, B.; Lee, N.; Kim, D.; Kim, H.; Ahn, B.; Hwang, Y.; Lee, H.; Kim, J.; Lee, Y.; Lee, H.; Lee, J.; Chang, S.; Yang, J.; Park, S.; Aritome, S.; Lee, S.; Ahn, K.-O.; Bae, G.; Yang, Y. Highly reliable 26 nm 64 Gb MLC E2NAND (embedded-ECC & enhanced-efficiency) flash memory with MSP (Memory Signal Processing) controller, *VLSI Technology (VLSIT), 2011 Symposium on*, pp. 216–217, 14–16 June 2011.

[81] Tanaka, T.; Tanaka, Y.; Nakamura, H.; Oodaira, H.; Aritome, S.; Shirota, R.; Masuoka, F. A quick intelligent program architecture for 3 V-only NAND-EEPROMs, *VLSI Circuits, 1992. Digest of Technical Papers, 1992 Symposium on*, pp. 20–21, 4–6 June 1992.

[82] Suh, K.-D.; Suh, B.-H.; Lim, Y.-H.; Kim, J.-K.; Choi, Y.-J.; Koh, Y.-N.; Lee, Sung-Soo; Kwon, Suk-Chon.; Choi, B.-S.; Yum, J.-S.; Choi, J.-H.; Kim, J.-R.; Lim, H.-K. A 3.3 V 32 Mb NAND flash memory with incremental step pulse programming scheme, *Solid-State Circuits, IEEE Journal of*, vol. 30, no. 11, pp. 1149–1156, Nov. 1995.

[83] Chen, I. C.; Holland, S.; Hu, C. Oxide breakdown dependence on thickness and hole current—enhanced reliability of ultra thin oxides, *Electron Devices Meeting, 1986 International*, vol. 32, pp. 660–663, 1986.

[84] Schuegraf, K. F.; Hu, C. Hole injection SiO breakdown model for very low voltage lifetime extrapolation, *IEEE Trans. Electron Devices*, pp. 761–767, April 1994.

[85] Esseni, D.; Bude, J. D.; Selmi, L. On interface and oxide degradation in VLSI MOSFETs. II. Fowler–Nordheim stress regime, *Electron Devices, IEEE Transactions on*, vol. 49, no. 2, pp. 254–263, Feb. 2002.

[86] Chang, C.; Hu, C.; Robert, W. Brodersen. Quantum yield of electron impact ionization in silicon, *Journal of Applied Physics*, vol. 57, p. 302, 1985.

[87] Fischetti, M. V.; Weinberg, Z. A.; Calise, J. A. The effect of gate metal and SiO_2 thickness on the generation of donor states at the Si–SiO_2 interface, *Journal of Applied Physics*, vol. 57, no. 2, pp. 418–425, 1985.

[88] DiMaria, D. J.; Cartier, E. Mechanism for stress-induced leakage currents in thin silicon dioxide films, *Journal of Applied Physics*, vol. 78, pp. 3883–3894, 1995.

[89] Hemink, G.; Endoh, T.; Shirota, R. Modeling of the hole current caused by Fowler–Nordheim tunneling through thin oxides, *Japanese Journal of Applied Physics*, 33 pp. 546–549, 1994.

[90] Aritome, S. NAND flash memory reliability, in *International Solid-State Circuits Conference 2009 (ISSCC 2009)*, at Forum "SSD Memory Subsystem Innovation."

Micron Ex. 1014, p. 291
Micron v. YMTC
IPR2025-00119

7

THREE-DIMENSIONAL NAND FLASH CELL

7.1 BACKGROUND OF THREE-DIMENSIONAL NAND CELLS

The demand of NAND flash memory [1] greatly increases with expanding applications, such as solid-state drive (SSD), because a bit cost greatly decreases by aggressive scaling of two-dimensional (2D) NAND flash memory cell, as shown in Fig. 3.1 [2] in Chapter 3. However, beyond the 20-nm technology node, the scaling of 2D NAND flash memory cell is facing several serious physical limitations, such as floating-gate capacitive (FG–FG) coupling interference, random telegraph signal noise (RTN), and so on, as described in Chapter 5.

In order to further scale down the memory cell size of NAND flash memory, several three-dimensional (3D) NAND flash cells had been proposed before 2006 [3–9], as shown in Fig. 7.1 [2]. One is the stacked NAND cell [3–5], as shown in Fig. 7.2. The NAND strings are fabricated on each stacked silicon layers in vertical and are connected to common bit line and source line. The channel Si-layers and gates have to be fabricated for each duplicated layer. Then a fabrication cost is increased due to increasing process steps. The other is the stacked-surrounding gate transistor cell (S-SGT cell) [7–9], as shown in Fig. 7.3. The surrounding gate transistor cells with a floating gate are vertically connected in series to fabricate the NAND cell strings. However, a fabrication process was very complicate, and also the cell size was very large due to the step structure of silicon substrate for each cell, as shown in Fig. 7.3. Therefore, before 2006, these 3D cells could not effectively decrease a

Nand Flash Memory Technologies, First Edition. Seiichi Aritome.
© 2016 The Institute of Electrical and Electronics Engineers, Inc. Published 2016 by John Wiley & Sons, Inc.

Micron Ex. 1014, p. 292
Micron v. YMTC
IPR2025-00119

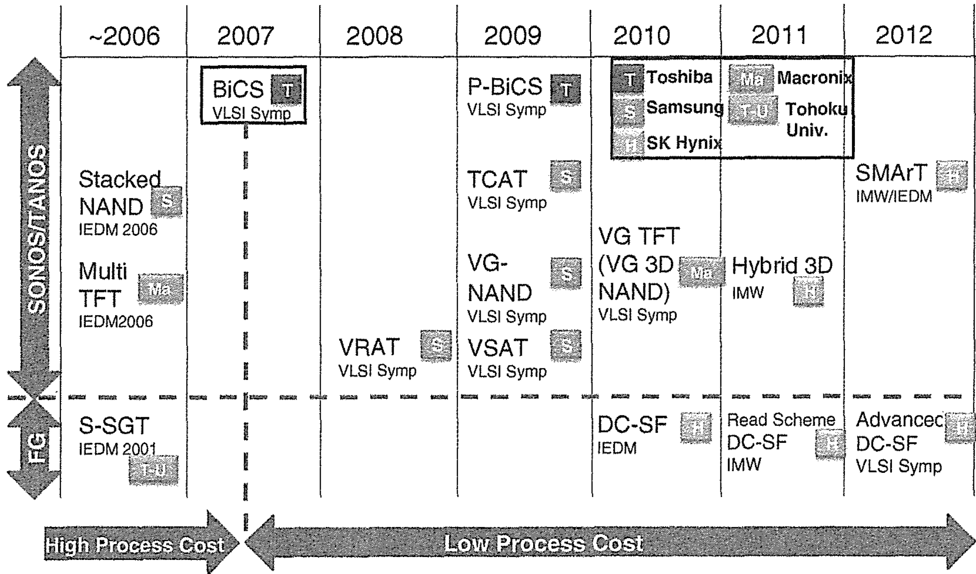

FIGURE 7.1 History of three-dimensional NAND flash.

- **Stacked Si-layer for NAND strings**
- **TANOS charge trap cell**
- **Increased process cost due to increasing number of process steps for each duplicated layers.**

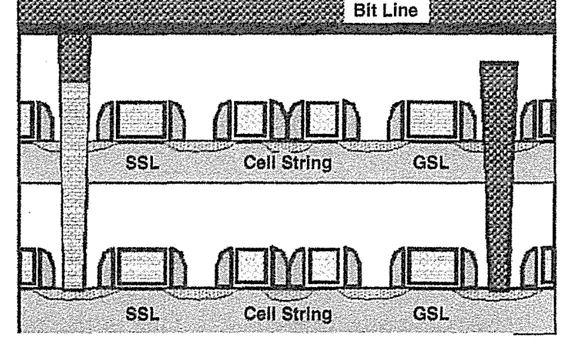

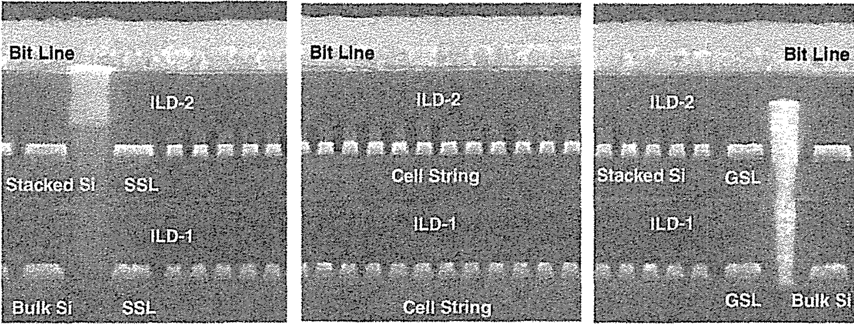

FIGURE 7.2 Stacked NAND cell.

Micron Ex. 1014, p. 293
Micron v. YMTC
IPR2025-00119

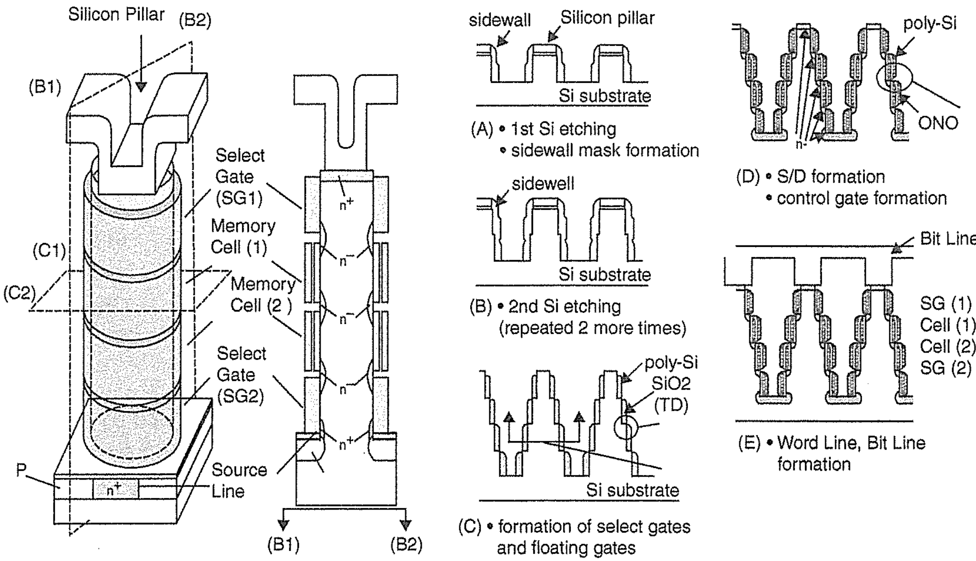

FIGURE 7.3 Stacked-surrounding gate transistor cell (S-SGT cell).

bit cost because of a complicate fabrication process, an increased process steps, and large unit cell size.

In 2007, the BiCS cell (bit cost scalable cell) technology had been proposed [10], as shown in Fig. 7.1. The BiCS cell has a new structure of the stacked control gate layers and vertical poly-Si channel, as described in detail in Section 7.2. The new process concept is shown in Fig. 7.4 [11,12]. The multi-stacked layers of gate (plate) and dielectric are deposited ("Stack"), and then the through-hole is fabricated through

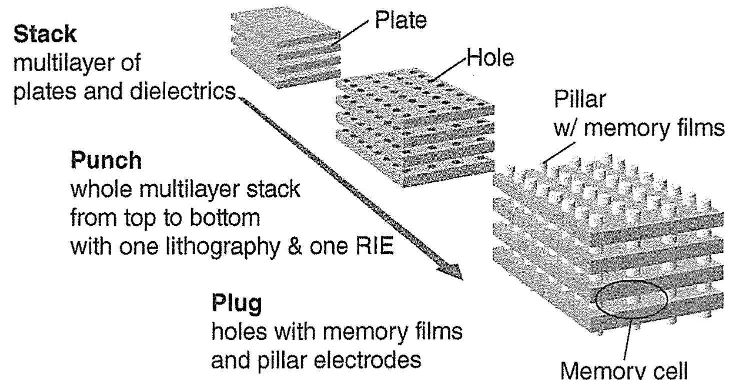

FIGURE 7.4 Basic concept of BiCS (bit cost scalable) technology.

Micron Ex. 1014, p. 294
Micron v. YMTC
IPR2025-00119

TABLE 7.1 Comparison of major 3D NAND cells.

	BICS/ P-BiCS	TCAT (V-NAND)	SMArT	VG-NAND	DC-SF
Channel	Vertical	Vertical	Vertical	Horizontal	Vertical
Gate structure	Surrounding (GAA)	Surrounding (GAA)	Surrounding (GAA)	Dual	Surrounding (GAA)
Charge storage	SONOS	SONOS (TANOS)	SONOS (TANOS)	SONOS (TANOS)	FG
Gate process	Gate first	Gate last	Gate last	Gate last	Gate last

the multi-stacked layers ("Punch"). After that, the through-holes are filled by memory film (ONO) and channel poly-Si (pillar electrodes) ("Plug"). Due to this new process concept, the fabrication process became very simple and low cost, and also it was expected that very small effective cell size could be achieved.

After introducing BiCS cell in 2007 [10], several 3D NAND cells were proposed, such as an advanced BiCS [13, 14], P-BiCS [15–17], VRAT [18], TCAT [19], VG-NAND [20], VSAT [21], VG-TFT [22,23], DC-SF [24–28], SMArT [29], and so on, as shown in Fig. 7.1.

Table 7.1 shows the comparison of major 3D cells. 3D cells are categorized by channel structure (vertical or horizontal), gate structure (surrounding gate (GAA) or dual gate), charge storage (SONOS/TANOS or FG), and gate process (gate first or gate last). Each 3D cell has both advantage and disadvantage of structure, process, operation, and so on. In Chapter 7, major 3D cells are introduced and discussed.

7.2 BiCS (BIT COST SCALABLE TECHNOLOGY) / P-BiCS (PIPE-SHAPE BiCS)

7.2.1 Concept of BiCS

Concept of BiCS (bit cost scalable technology) is described in Figs. 7.5–7.7. All of the stacked electrode plates (control gates) are punched through and plugged with poly-silicon channel at one time, forming a series of vertical FETs which act as a NAND string of SONOS-type memories [10, 13], as shown in Fig. 7.5. The single memory cell has a vertical poly-silicon channel surrounding by both the ONO dielectrics (silicon dioxide/SiN of charge storage layer/silicon dioxide) and the surrounding gate electrode (GAA; gate all around). The memory cells work in depletion mode with the body poly-silicon, which is undoped or lightly n-doped uniformly without source/drain n-type diffusion within plug. Each electrode plate acts as a control gate except the lowest plate, functioning as the lower select gate (lower SG). A single bit is located in the intersection of a control gate plate and plugged poly-silicon. The control gates and lower SG are commonly connected in each layer in block, as shown in Fig. 7.7. The string is selected by a bit line and an upper select gate (upper SG), as shown in Fig. 7.7. As shown in Fig. 7.6, the control gates and upper/lower SG

Micron Ex. 1014, p. 295
Micron v. YMTC
IPR2025-00119

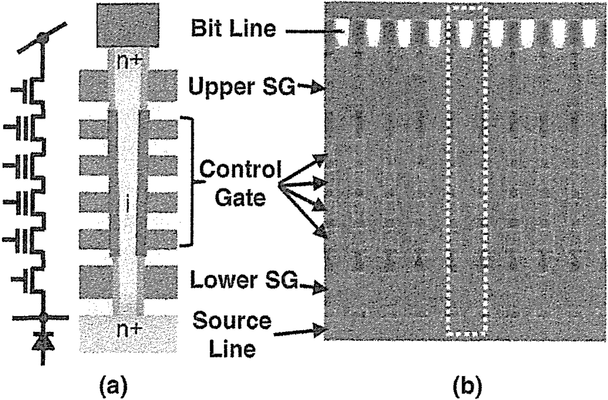

FIGURE 7.5 BiCS (bit cost scalable) flash memory. (a) The memory string. (b) Cross-sectional SEM image of BiCS flash memory array.

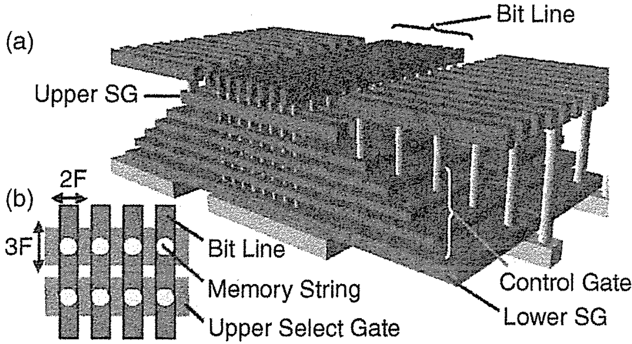

FIGURE 7.6 (a) Bird's-eye view of BiCS flash memory. (b) Top-down view of BiCS flash memory array.

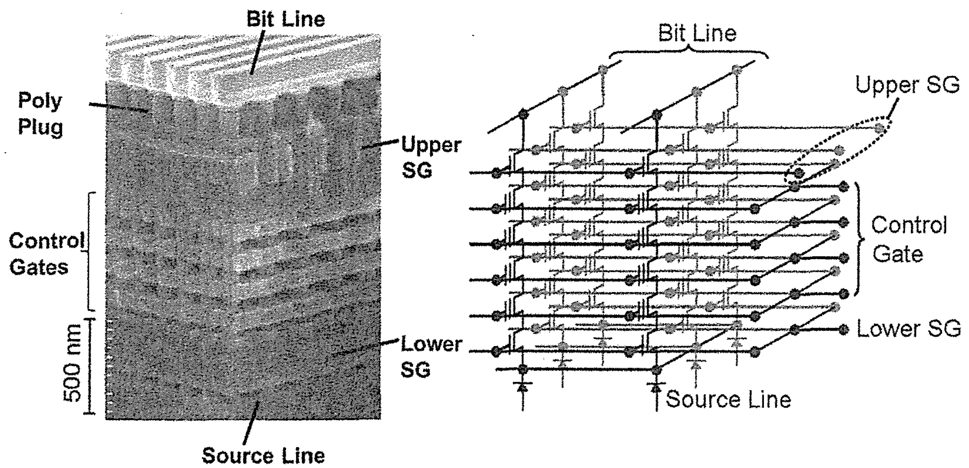

FIGURE 7.7 BiCS cell cross-sectional SEM photo and equivalent circuit.

Micron Ex. 1014, p. 296
Micron v. YMTC
IPR2025-00119

are connected to the metal layers at stair-like gate structure, which is fabricated by resist slimming process, described in Section 7.2.2. The bottom of memory string is connected to the common source diffusion formed on the silicon substrate.

The surrounding gate transistor (SGT), which is used in BiCS, had been previously proposed for logic CMOS in IEDM 1988 because of an excellent current drivability and body effect [30]. The vertical channel SGT EPROM cell was proposed in 1993 [31–33]. Also, the stacked-SGT cell for NAND flash was proposed in 2001 [7]. Therefore, the special feature of BiCS technology is a low-cost process to fabricate many stacked cells all at one process sequence.

7.2.2 Fabrication Process of BiCS

Figure 7.8 shows the fabrication sequence of BiCS flash memory cell [10]. Lower select gate transistors ((2) and (3) in Fig. 7.8), series-connected memory cells ((4)–(7) in Fig. 7.8), and upper select gate transistors ((8) and (9) in Fig. 7.8) are fabricated sequentially. Stacked gate materials and dielectric films are P+ poly-Si and Si dioxide

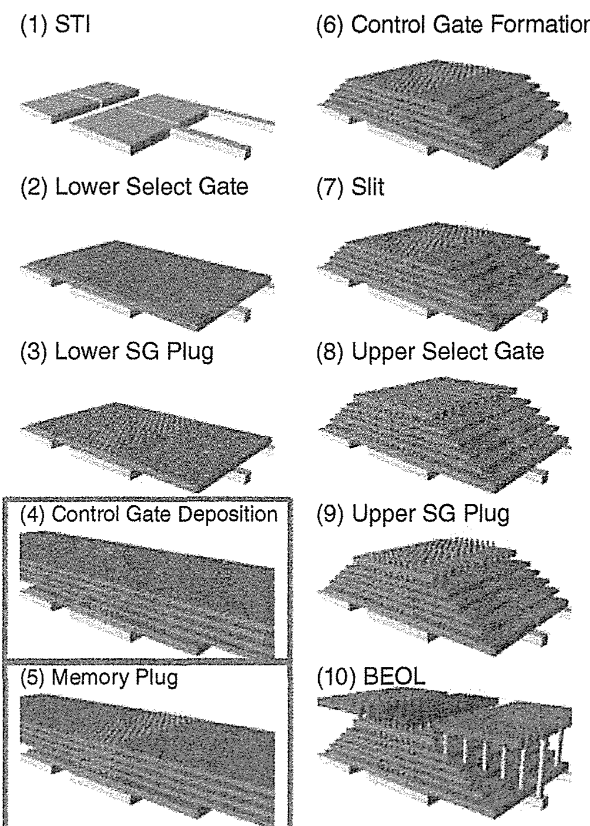

FIGURE 7.8 Fabrication sequence of BiCS flash memory. The key to obtain low process cost is a one-time process of multi-stacked control gates, channel hole open, and poly-channel plug.

Micron Ex. 1014, p. 297
Micron v. YMTC
IPR2025-00119

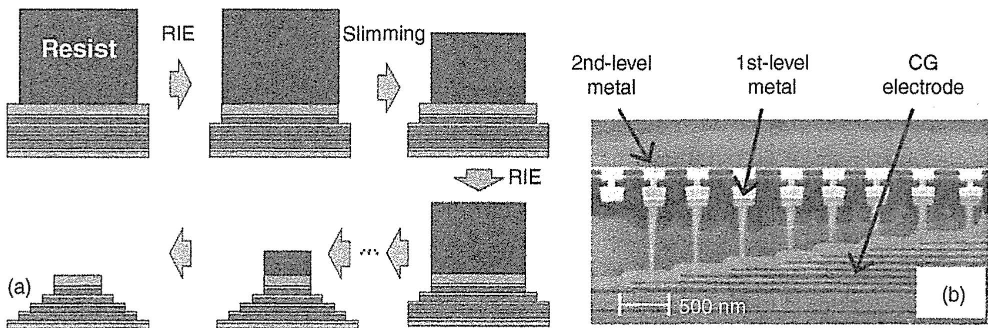

FIGURE 7.9 (a) Fabrication sequence of edge of control gates (control gate pick-up area) into stair-like structure. (b) Cross-sectional SEM image of edge of control gates.

(SiO_2), respectively. Holes for transistor channel or memory plug are punched through by RIE. And then LPCVD TEOS film or ONO films are deposited for lower/upper SG and for memory cells, respectively. The bottom of dielectric films are removed by RIE and plugged by amorphous Si to connect Si substrate. Arsenic is implanted and activated for drain and also source of the upper device. ONO films are deposited in the opposite order as compared to the conventional SONOS device—that is, from LPCVD TEOS film as top block oxide (5 nm), LPCVD SiN film (11 nm), and LPCVD TEOS film as tunnel oxide (2.5 nm).

Edges of control gate are processed into stair-like structure by repeating of RIE and resist sliming, as shown in Fig. 7.9a. Figure 7.9b shows the cross-sectional SEM image of control gates stair-like structure and contact area in the edge of control gates. The control gates and SGs can be connected to metal layer by the control gates stair-like structure and the contacts.

For minimizing program disturb and read disturb, all stacked control gates and lower select lines have to be separated by a slit which separates a block of memory plugs from each other, as shown in (7) of Fig. 7.8. Only upper select gate is cut into line pattern to work as row address selector, as shown in (8) of Fig. 7.8 and Fig. 7.7. Via contact hole and BL metal layer are fabricated on the array and peripheral circuit simultaneously, as shown in (10) of Fig. 7.8.

7.2.3 Electrical Characteristics

Figure 7.10 shows the I_d–V_g characteristics of (a) the SONOS memory cell [10] and (b) the select gate transistor [13] of BiCS technology. In the SONOS memory cell, a good I_{on}/I_{off} ratio of more than 6 orders of magnitude is obtained in both erase and program states, as shown in Fig. 7.10a. For the select transistor, the gate dielectric is 7 nm SiN which is deposited by LPCVD. A good subthreshold slope of ~190 m V/dec is obtained. The program/erase characteristics are shown in Fig. 7.11a [13]. Low-voltage program and erase operations are confirmed with surrounding gate transistors. The channel hole diameter dependence of the program and erase (P/E) window is measured on the test structure of cylindrical capacitors in Fig. 7.11b [15].

Micron Ex. 1014, p. 298
Micron v. YMTC
IPR2025-00119

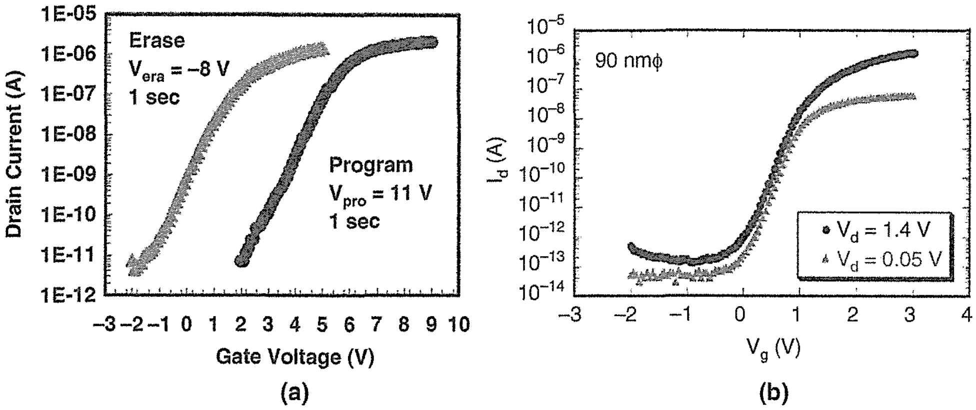

FIGURE 7.10 I_d–V_g characteristics of (a) the SONOS memory cell and (b) the select gate vertical transistor with SiN-gate in BiCS technology.

The P/E window can be enlarged by the smaller channel hole diameter, because the electric field strength of the tunnel film is enhanced by the curvature effect.

The field enhancement effect of channel hole curvature plays a significant role in programming/erasing, since the BiCS cell is a surrounding gate device. When channel radius (R1) is decreased and comparable to the ONO thickness, the field enhancement effect become very large, as shown in Fig. 7.12 [22, 34]. The field in tunnel oxide (bottom oxide) is enhanced as the radius of the channel is decreased. Meanwhile, the field in the blocking oxide (top oxide) of ONO is simultaneously decreased.

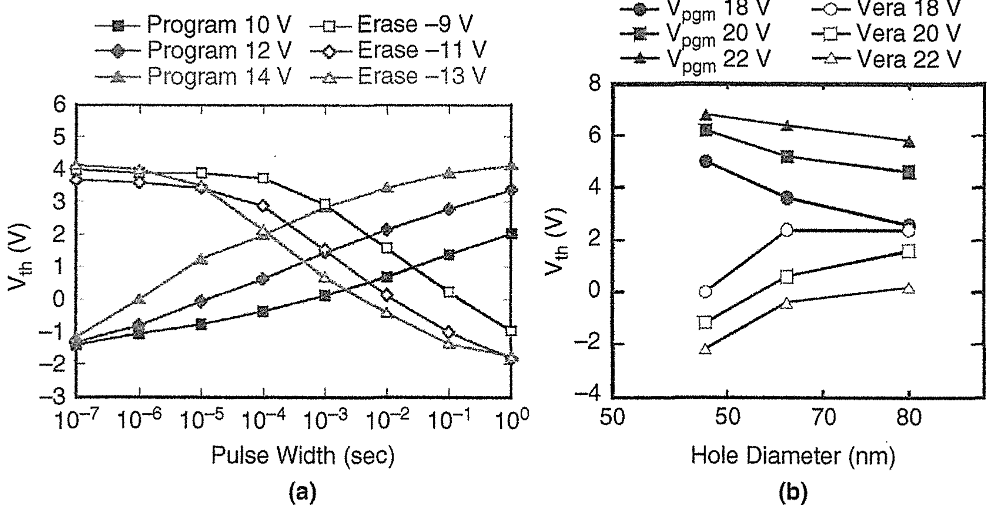

FIGURE 7.11 (a) Program/erase (P/E) characteristics of vertical SONS memory in BiCS technology. (b) Hole-diameter dependence of P/E characteristics in BiCS technology. The P/E window is enhanced by a smaller hole.

Micron Ex. 1014, p. 299
Micron v. YMTC
IPR2025-00119

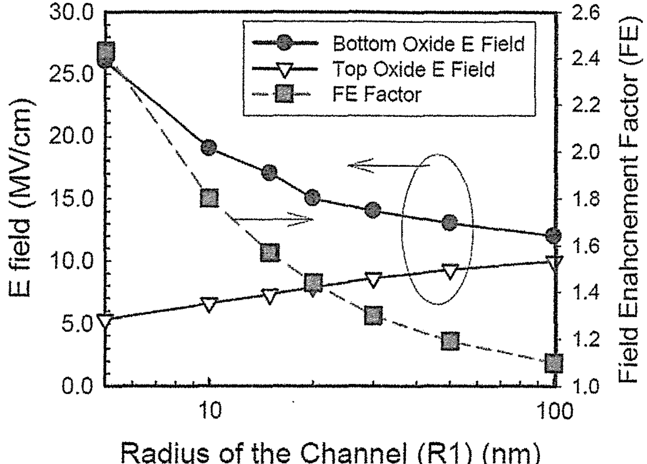

FIGURE 7.12 Calculated bottom oxide and top oxide electrical field for the surrounding gate (gate all around; GAA) nano wire SONOS device. ONO = 5/8/7 nm. The radius R1 is half of the poly diameter. The applied voltage is +18 V in this calculation. Field enhancement factor is shown in the right axis. The FE factor is defined as the ratio of the bottom oxide field (with radius $R1$) over the capacitor (with $R1 \to \infty$).

Conventional erase operation in two-dimensional NAND flash cell with applying erase voltage to substrate (*p*-well) cannot be used in BiCS cell because erase *p*-well voltage cannot be directly transferred to channel plug poly-silicon. Then, erase operation is executed by raising the potential of channel poly-Si pillars of NAND string with injection of holes which are generated by GIDL (gate-induced drain leakage) at the junction side edge of the select gate, as shown in Fig. 7.13 [13, 14].

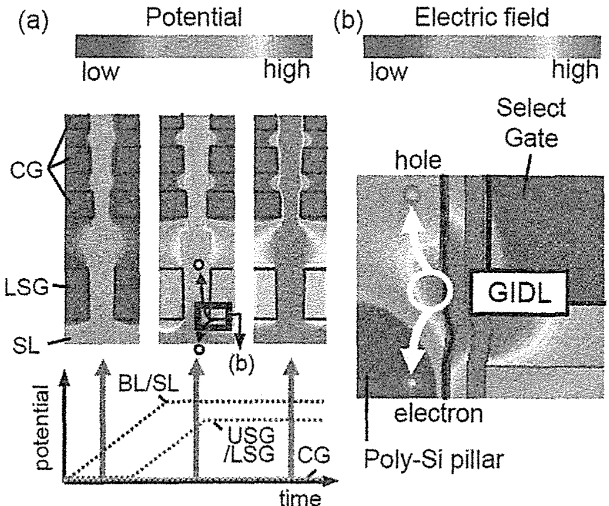

FIGURE 7.13 BiCS erase operation.

Micron Ex. 1014, p. 300
Micron v. YMTC
IPR2025-00119

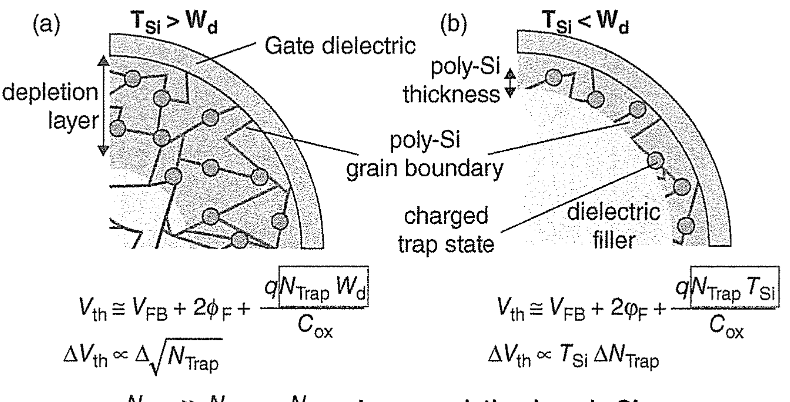

FIGURE 7.14 Schematics of V_{th} dependence on trap density at poly-silicon grain boundaries when (a) $T_{Si} > W_d$, and (b) $T_{Si} < W_d$ (T_{Si}, poly-Si thickness; W_d, width of depletion layer). If poly-Si thickness (T_{Si}) is thinner than depletion layer width (W_d), ΔV_{th} becomes dependent on the total number of traps, and thus ΔV_{th} becomes smaller with thinner body thickness.

There are many traps in grain boundary of channel poly silicon in BiCS cell, as described detail in Section 8.6. Then, subthreshold characteristics of poly-silicon channel transistors have quite a large variation, and it is difficult to control to ensure a tight distribution. Based on the model described in Fig. 7.14 [13], the approach to achieve better controllability of the V_t distribution is making the body silicon much thinner than the depletion width (W_d), in order to reduce the volume of poly-silicon and total number of traps and to make threshold voltage less sensitive to the trap density fluctuation. The concept of the "macaroni" body vertical transistor is illustrated in Fig. 7.15 [13]. Very thin poly-silicon is deposited on the gate dielectric to form a macaroni-shaped body. The center of the body is filled with dielectric film to make process integration easier. Thinner body thickness makes channel potential better controlled by gate electrode.

Figure 7.16a shows I_d–V_g characteristics of the "macaroni" body vertical transistor [13]. The macaroni body vertical transistor shows the much better subthreshold

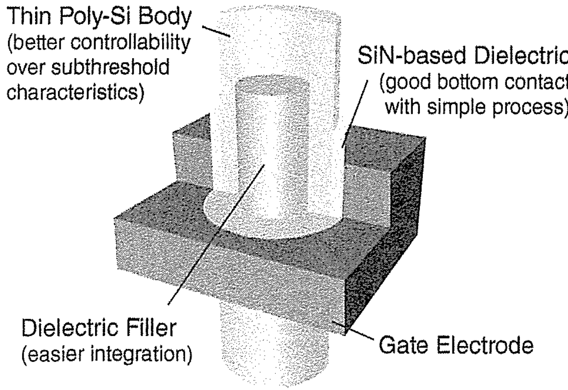

FIGURE 7.15 Concept of 'macaroni' body vertical transistor.

Micron Ex. 1014, p. 301
Micron v. YMTC
IPR2025-00119

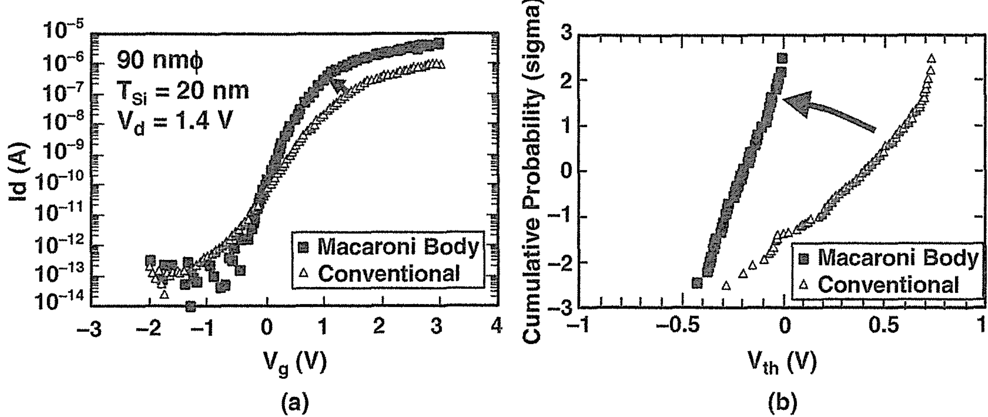

FIGURE 7.16 (a) Typical I_d–V_g characteristics of conventional vertical transistor and "macaroni" body vertical transistor. (b) V_{th} distribution of conventional and macaroni body vertical transistor.

characteristics as well as the better drive current as compared with a conventional channel transistor. V_{th} variation can be well reduced by the macaroni body vertical transistor, as shown in Fig. 7.16b [13].

The macaroni channel transistor was compared with the full channel transistor in detail [35]. Figure 7.17 compares the statistical distributions of threshold voltage V_{th} (Fig. 7.17a) and subthreshold swing (STS) (Fig. 7.17b) of full channel and macaroni channel devices (Si channel thickness d_{Si} of 7, 10, and 13 nm). From both plots, it is clarified that the distributions of both V_{th} and STS are tighter in the case of macaroni.

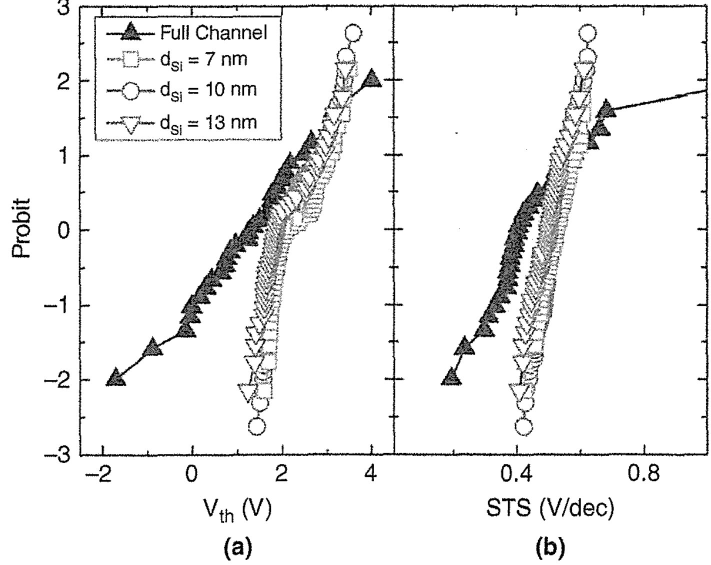

FIGURE 7.17 (a) Threshold voltage and (b) subthreshold swing distributions of full channel and macaroni devices with different channel thicknesses; the memory hole diameter is $\varphi = 80$ nm.

Micron Ex. 1014, p. 302
Micron v. YMTC
IPR2025-00119

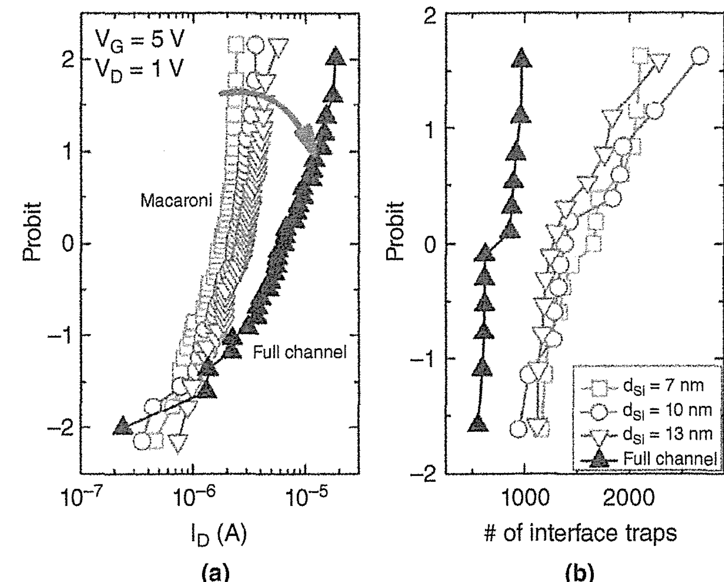

FIGURE 7.18 (a) Statistical distributions of drain current at read condition and (b) distribution of number of interface traps for macaroni (different d_{Si}) and full channel devices.

This is because the macaroni channel can achieve a better control of the conduction by reducing the volume of the poly-Si channel. The thinner poly-Si channel can obtain the easier electrostatic control performed by the gate electrode over the thinner body and the smaller poly-Si grains which reduce the impact on the channel current of statistical variation of smaller grain size configuration [36]. Furthermore, no relevant difference is observed between devices with different channel thickness in this range of thickness.

Figure 7.18a compares the statistical distributions of the drain current (I_D) for macaroni channel devices with different channel poly-Si thicknesses and for the full channel device. The drain current is measured by biasing the gate at 5 V and the drain voltage V_D at 1 V. It can be observed that the full channel device have higher average I_D than macaroni channel device; however, the full channel device has a larger variation. Especially in lower I_D tail, a very small I_D device can be observed, contrast to no tail I_D in Macaroni channel device. And the drain current in macaroni channel increases consistently with increasing the channel poly-Si thickness.

Figure 7.18b reports the number of interface traps measured by the charge pumping method. The number of interface defects is twofold higher in macaroni channel than in full channel devices. And it is independent on channel poly-Si thickness. It suggests that the macaroni channel device has an interface trap at both interfaces of gate oxide side and the filler side, thus resulting in the much higher number of defects. These results, combined with the I_D trend of Fig. 7.18a, are a clear indication that the conduction is not confined to the tunnel oxide/channel interface, but involves the full channel thickness of macaroni channel. Interface traps at the filler side interface are also responsible for the higher V_{th} values observed in Fig. 7.17a.

Micron Ex. 1014, p. 303
Micron v. YMTC
IPR2025-00119

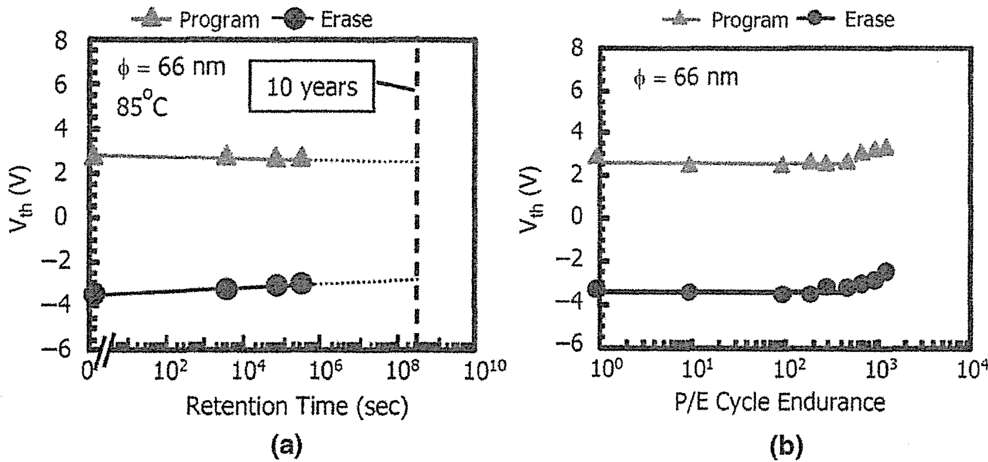

FIGURE 7.19 (a) Data retention characteristics of P-BiCS cells. It has no obvious degradation for 10-year-long data retention. (b) Program/erase endurance characteristics.

Figure 7.19 shows (a) data retention characteristics and (b) program/erase cycling endurance characteristics of the BiCS cell [17]. They show good enough characteristics to implement a NAND flash product. Figure 7.20 shows V_{th} distribution of three programmed levels of storage data for MLC [17]. Tight V_t distribution widths of MLC cells were obtained.

7.2.4 Pipe-Shaped BiCS

BiCS technology evolved to the pipe-shape BiCS (P-BiCS). Figure 7.21 shows the schematic of pipe-shaped BiCS flash memory [15]–[17]. Two adjacent NAND strings are connected at the bottoms by pipe-connection (PC) which is gated by the bottom electrode (pipe gate). One of the terminals for the U-shaped pipe is connected to the bit line (BL), and the other is connected to the source line (SL). The SL consists

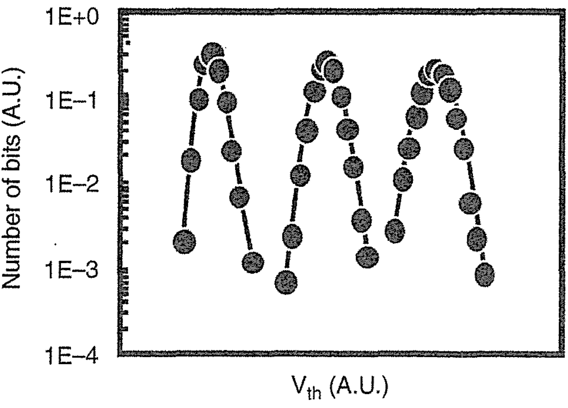

FIGURE 7.20 V_{th} distribution of a fabricated test chip of a BiCS cell.

Micron Ex. 1014, p. 304
Micron v. YMTC
IPR2025-00119

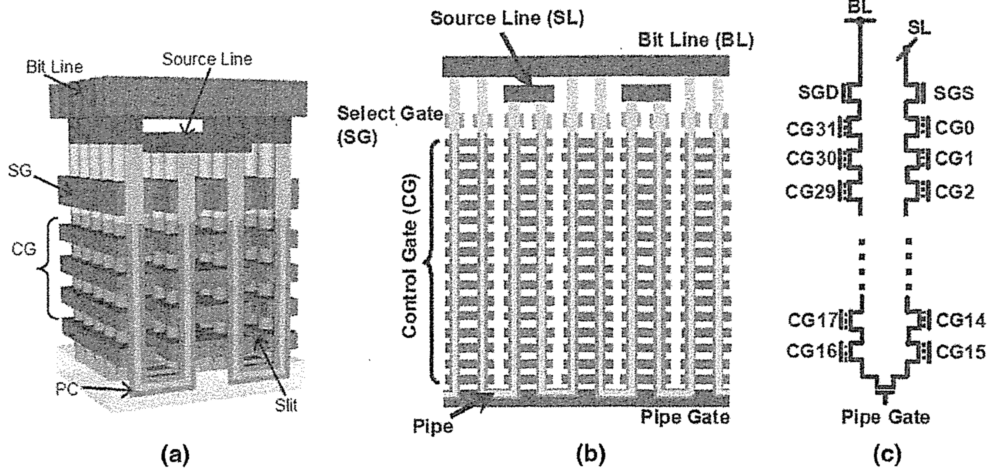

FIGURE 7.21 (a) Schematic of pipe-shaped-BiCS (P-BiCS) flash memory. (b) Cross-sectional view of the P-BiCS. (c) An equivalent circuit of P-BiCS.

of the meshed wiring of the third level metal (not shown in Fig) and accessed by the first and the second level metal like a conventional planar (2D) NAND flash cell technology. Therefore the resistance of the SL is sufficiently low. The both of the SG transistors are placed on the stacked control gates (CG). The control gate (CG) is isolated by the slits and faces to each other as a couple of combs pattern.

The fabrication process of the P-BiCS NAND strings is described in Fig. 7.22 [15]. The pipe connection (PC) is filled by a sacrificial-film and connected to a sacrificial film in the stacked control gates after the memory hole formation. And the sacrificial films are removed after SG-hole formation. Then, the gate dielectric ONO (memory films) and the channel poly-silicon film (silicon-body) can be sequentially deposited, because the gate dielectric etching process is not required before channel poly silicon deposition, compared that the gate dielectric etching is required before channel poly silicon deposition in conventional straight-shaped BiCS process to connect channel poly-Si with substrate. Therefore, P-BiCS flash could improve some critical problems on BiCS flash, such as high resistance of source line, cut-off characteristics of the lower select gate, and poor reliability of memory cells. Three advantages are compared with straight-shaped BiCS, as summarized in the table in Fig. 7.23. P-BiCS realizes (1) Low resistance of source line by introducing metal wiring and (2) tightly controlled cut-off characteristics of select gate enable good functionality of memory array. And also, (3) good data retention and wide V_{th} window can be realized because of less process damage on tunnel oxide in the fabrication process. P-BiCS is easily fabricated by adding pipe connection process to straight- shaped BiCS.

By using the pipe-shaped bit-cost scalable (P-BiCS) flash memory cell, a 16-Gb flash memory test chip had been developed with 60 nm technology [16]. The three-dimensional 16 stacked control gates could realize the small effective 1-bit cell size of 0.00082 μm^2.

In the original BiCS flash memory, the control gates are shared by several neighboring NAND cell strings to minimize cell size. In P-BiCS flash memory cell, the

Micron Ex. 1014, p. 305
Micron v. YMTC
IPR2025-00119

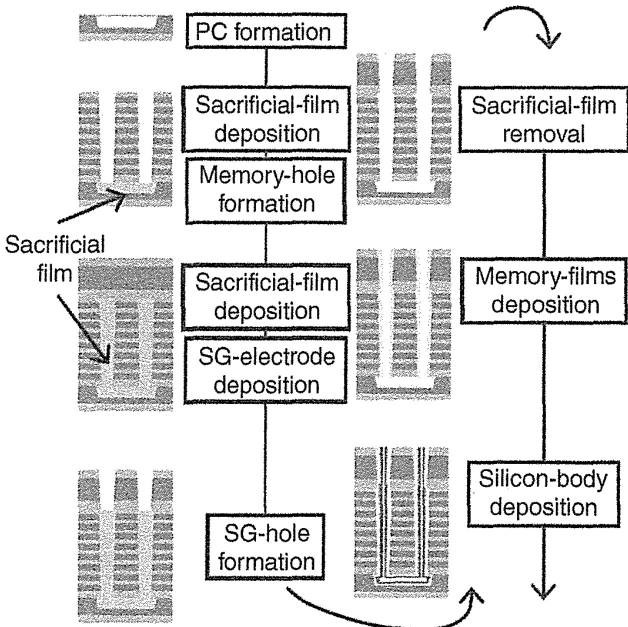

FIGURE 7.22 Fabrication process of P-BiCS flash memory. PC is formed on the first-level gate-conductor, which is also used for the support devices.

branched control gate configuration was adopted. Control gates are shared and connected by fork-shaped plates with four branches, as shown in Fig. 7.24. Each branch controls cells of two pages. The block in P-BiCS is formed by vertically stacked 16 pairs of control gates. Each pair of control gate plates is arranged in a staggered layout. (See CG0 and CG31 in Fig. 7.24 as an example.) Thanks to the high boost efficiency cell, program disturbances are not a serious concern in BiCS [14] and P-BiCS.

Unlike control gates, select gates are individually separated for the selectivity of cell strings. Figure 7.25 shows a schematic of row decoders. Two row decoders are placed on both sides of the cell array, one side for CG0 to CG15 and the other side

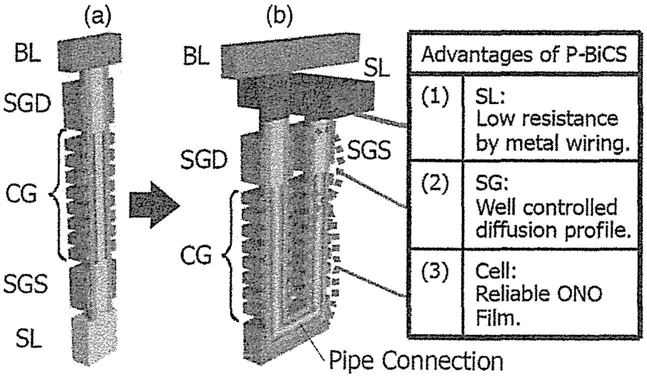

FIGURE 7.23 Advantages of pipe-shaped-BiCS.

Micron Ex. 1014, p. 306
Micron v. YMTC
IPR2025-00119

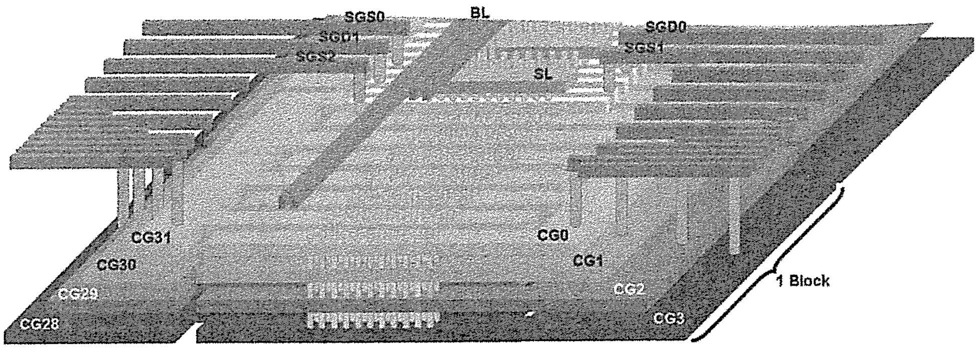

FIGURE 7.24 Branched control gate structure (showing upper four gate layers) of 16-Gb pipe-shaped BiCS test chip.

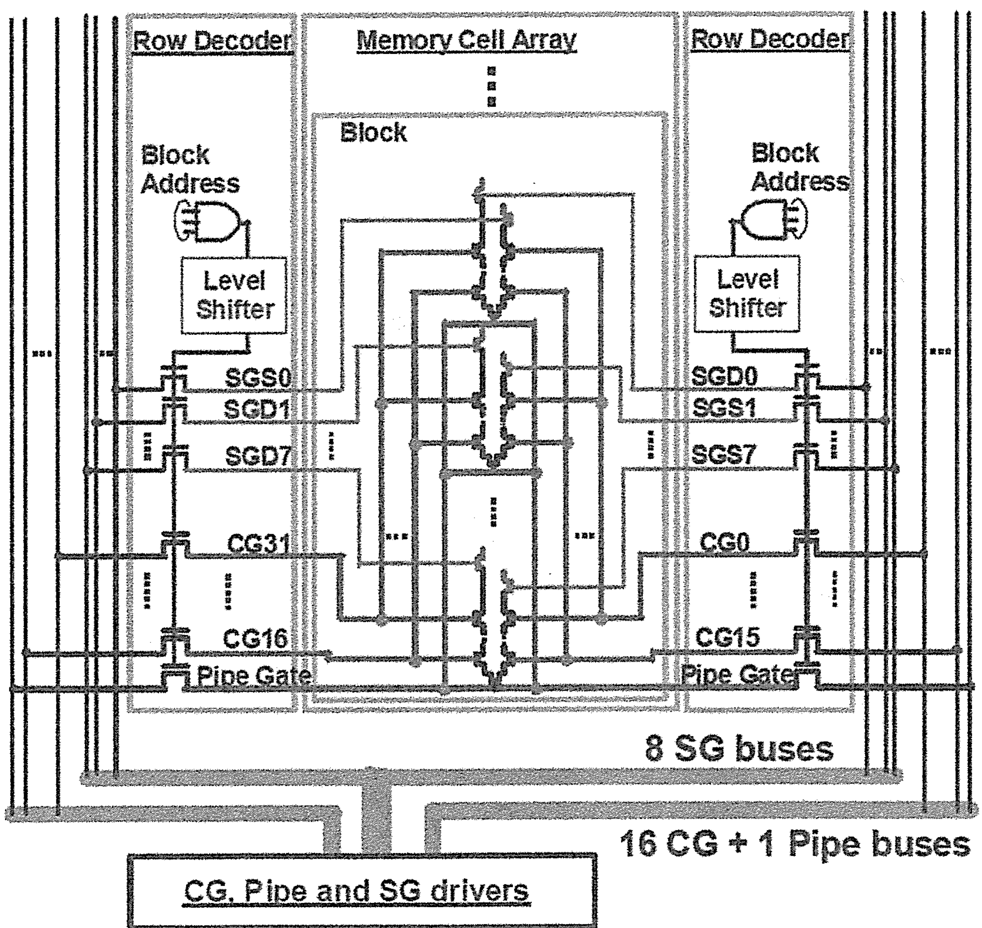

FIGURE 7.25 Row decoder configuration of 16-Gb test chip of pipe-shaped-BiCS cell.

Micron Ex. 1014, p. 307
Micron v. YMTC
IPR2025-00119

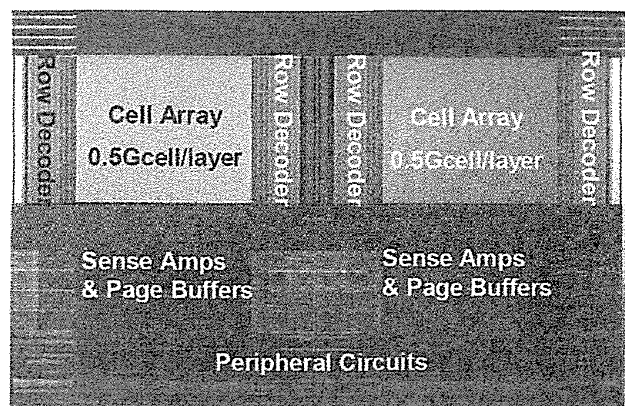

Density	1Gcell/layer
Cell Size	0.00082 μm²
Number of Layers	16 layers
Block Size	2M Byte(SLC) 4M Byte(MLC)
Page Size	8K Byte
Die Size	10.11x15.52 mm²

FIGURE 7.26 Image of 16-Gb pipe-shaped BiCS test chip.

for CG16 to CG31. Row decoders only decode the block address. The selectivity of eight select gates in a block is ensured by eight buses and drivers of select gates. Since the pipe connection (PC) forms a transistor, the pipe gate driver is needed.

Figure 7.26 shows a micrograph of the 16-Gb test chip. The number of cells in one string is 32 in 16 stacked control gate layers. Every layer has 1G memory cells. The chip contains 1K blocks with a page size of 8K byte. A commercial 64-Gb P-BiCS MLC NAND flash memory die size is estimated to be 10.5 mm × 12.3 mm by using the same configurations.

7.3 TCAT (TERABIT CELL ARRAY TRANSISTOR)/V-NAND (VERTICAL-NAND)

7.3.1 Structure and Fabrication Process of TCAT

The schematic structure of TCAT (terabit cell array transistor) is shown in Fig. 7.27 [19]. TCAT has a similar structure of BiCS, with a vertical poly-silicon channel, stacked word lines, and a silicon nitride (SiN) charge storage layer of the surrounding gate SONOS cell.

Figure 7.28 shows a process sequence of a TCAT flash memory cell. The points of process and structural differences with BiCS flash are (i) oxide(SiO_2)/nitride(SiN) multilayer stack for both memory cells and select gates, (ii) line-type "word line (W/L) cut" etched through the whole stack between the each row array of channel poly plug (see Fig. 7.28d), (iii) line-type CSL formed by an implant through the "W/L cut," (iv) replaced metal gate lines from SiN to tungsten (W), and (v) select transistors of GSL/SSL fabricated simultaneously with memory cell process. The most unique process is "gate replacement" to achieve the metal gate SONOS structure and low-resistance word line. Figure 7.29 shows the detail process of gate replacement from SiN to tungsten W [19]. After "W/L cut" dry etch and wet removal of sacrificial nitride layer (see Fig. 7.29b), gate dielectric layers (including tunnel oxide, charge

Micron Ex. 1014, p. 308
Micron v. YMTC
IPR2025-00119

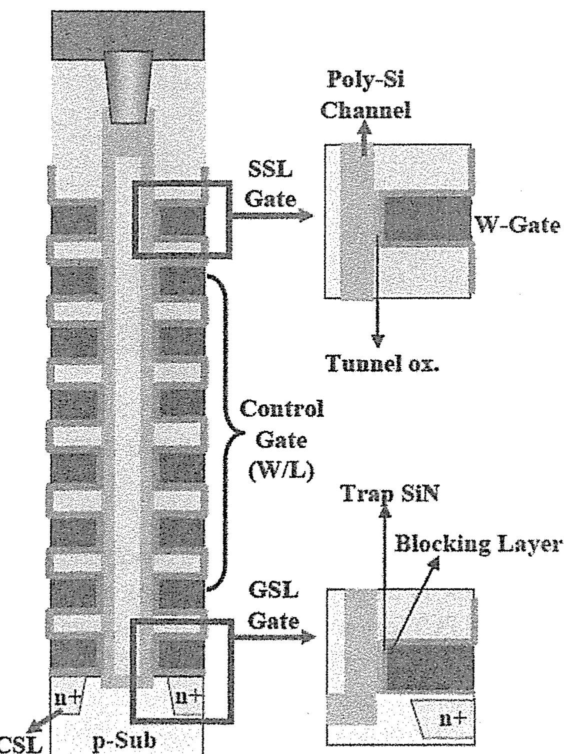

FIGURE 7.27 Schematic structures of TCAT flash cell string. Details of selection transistors are shown.

trap SiN and blocking dielectric) and gate metal are deposited in the conventional order (Fig. 7.29c). This is the gate last process, not "gate first" process as for BiCS flash [13]. The conventional gate last process is one of the advantages of a TCAT flash cell. And then, separation of each gate node is followed by etch processes (Fig. 7.29d).

The TEM cross-sectional view of the unit cell in Fig. 7.30a shows a damascened tungsten W metal gate SONOS structure in the vertical NAND flash cell string [19]. The electric field induced between the adjacent cells programmed in different state accelerates the charge losses by charge spreading mechanism at the hot temperature storage (HTS) test [37]. However, as shown in Fig. 7.30b,c [38], the TCAT structure of the gate last process has a biconcave structure which contributes to prevent from lateral charge losses.

An equivalent circuit of TCAT cell and cross-sectional SEM image are shown in Fig. 7.31 [19,39,40]. This configuration has 24 stacked WL layers, two dummy WL (DWL) of Dummy 0/1, and two string select gate layers of SSL and GSL. The string is selected by a bit line and an upper select gate (SSL). The control gates (WLs) and SSL/GSL are connected to the metal layers at stair-like gate structure (Fig. 7.28f). The bottom of memory string is connected to the common source line (CSL) diffusion formed by a CSL implant on the silicon substrate.

Micron Ex. 1014, p. 309
Micron v. YMTC
IPR2025-00119

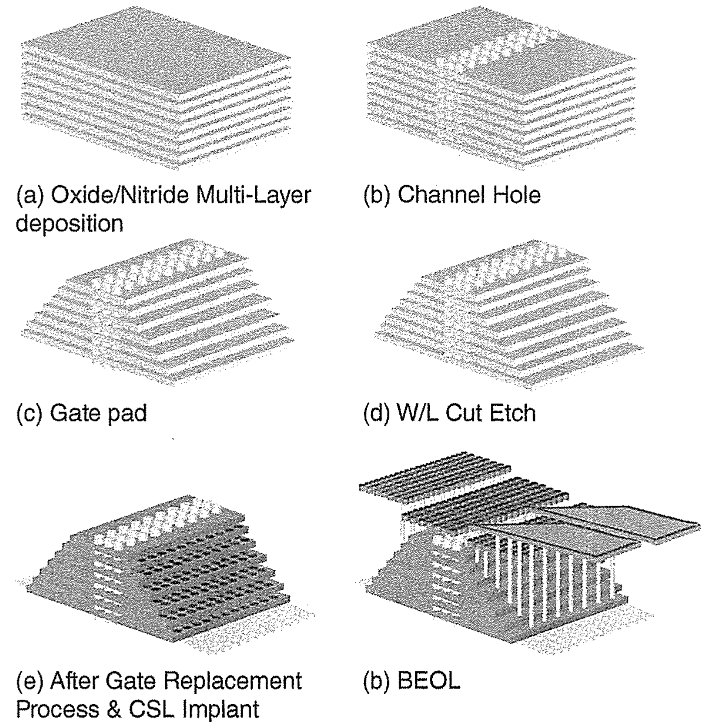

FIGURE 7.28 Process sequence of TCAT flash memory.

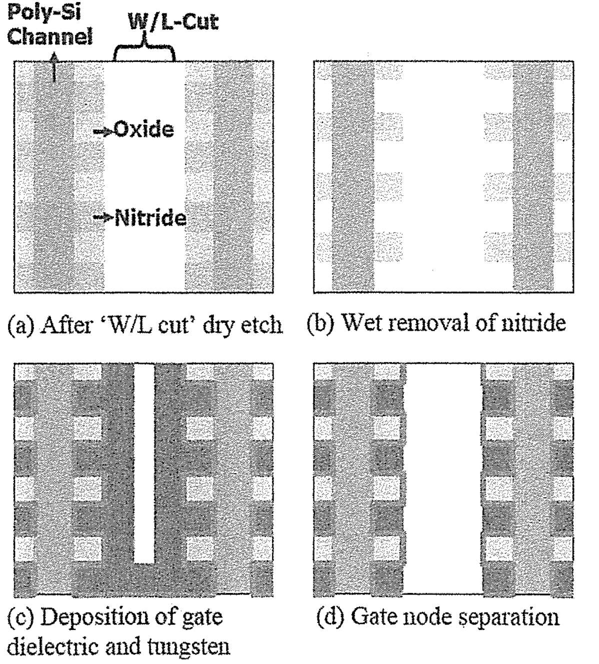

FIGURE 7.29 Concept of the process flow with "gate replacement."

Micron Ex. 1014, p. 310
Micron v. YMTC
IPR2025-00119

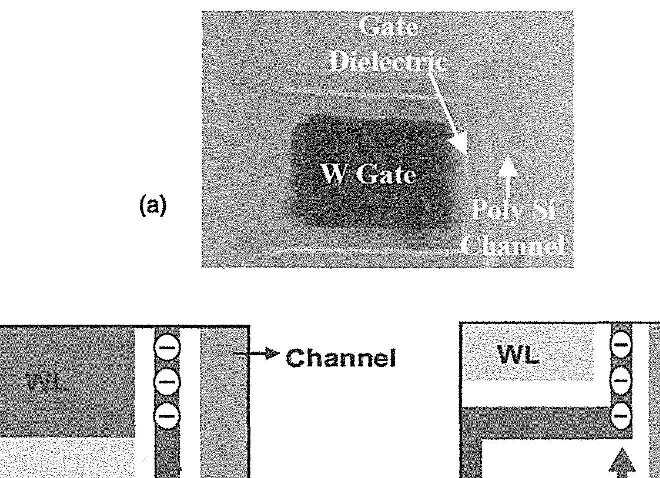

FIGURE 7.30 (a) Cross-sectional SEM images of a cell in the vertical NAND string of TCAT flash memory. Trap layer structure of (b) BiCS and (c) TCAT.

7.3.2 Electrical Characteristics

An important feature of TCAT NAND flash memory is the bulk erase operation. As shown in the schematic structure of Fig. 7.27, the channel poly plug in TCAT flash structure is directly connected to the Si substrate (p-sub), not the n+ common source

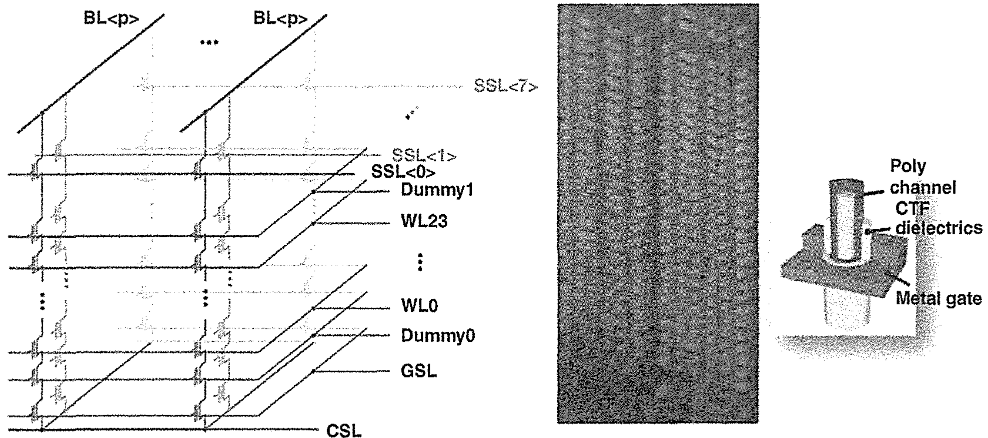

FIGURE 7.31 Schematic diagram and cross-sectional view of a 3D V-NAND array (TCAT flash memory array).

Micron Ex. 1014, p. 311
Micron v. YMTC
IPR2025-00119

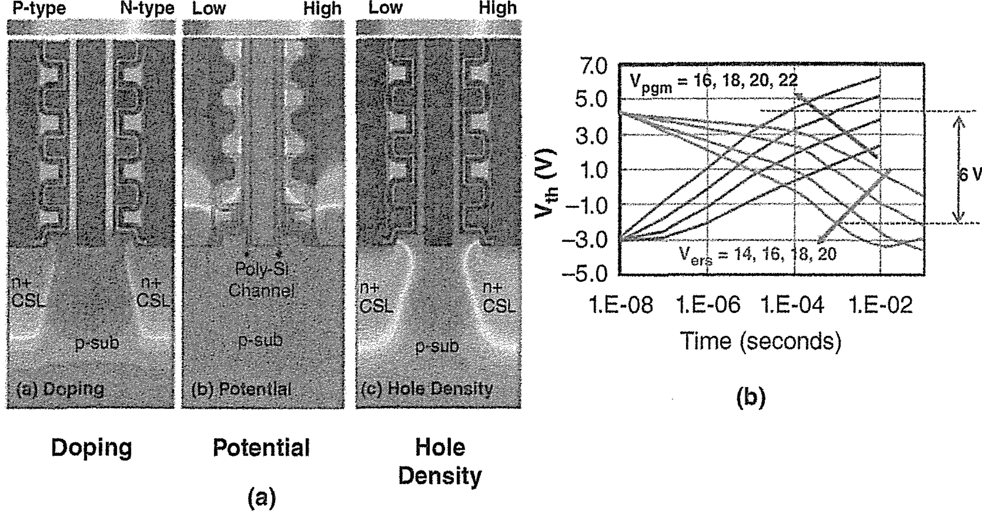

FIGURE 7.32 (a) Simulated profiles of doping, potential, and hole density during a bulk-erase operation of TCAT flash memory cells. (b) Program and erase characteristics.

diffusion layer as in the BiCS flash cell. Therefore, conventional bulk erase operation can be performed as described in the simulated profiles of Fig. 7.32a. Thanks to the bulk erase operation, the major peripheral circuits do not require to be changed from conventional 2D NAND flash memory to implement a TCAT NAND flash product [39, 40]. Figure 7.32b shows the program and erase (P/E) characteristics of the memory cell transistor [38]. A wide V_{th} window of ~6 V is obtained.

Figure 7.33 shows (a) program/erase (P/E) cycling endurance characteristics and (b) data retention characteristics. The V_t shift by 1K and 10K P/E cycling is kept less than 0.5 V and 1.5 V, respectively, which are small enough for mass production. And also, data retention characteristics show the wide V_t window even after 10 years of

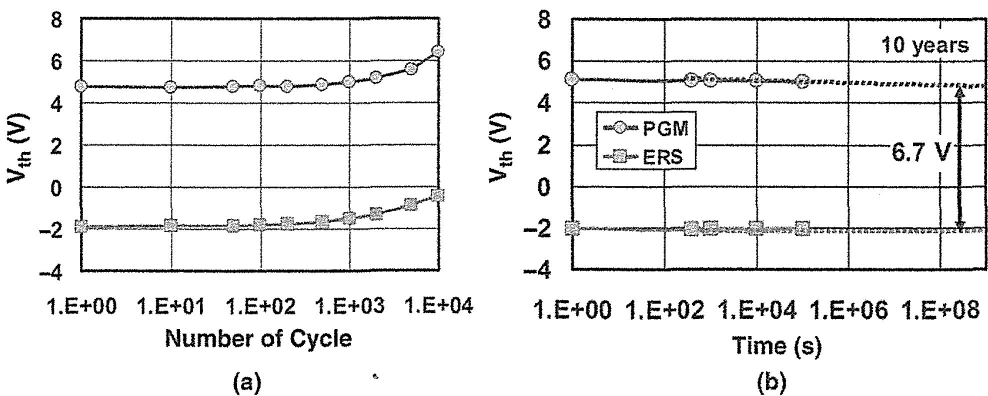

FIGURE 7.33 (a) Program/erase cycling endurance characteristics of TCAT cell. (b) Long-term data retention characteristics of a TCAT cell.

Micron Ex. 1014, p. 312
Micron v. YMTC
IPR2025-00119

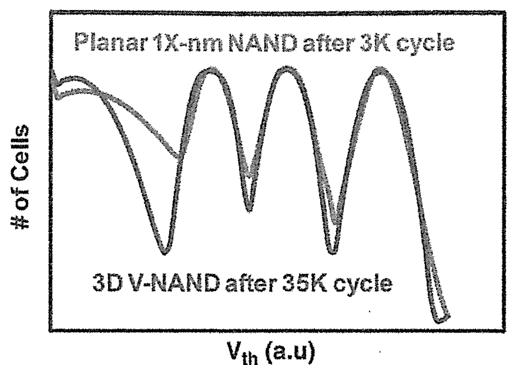

FIGURE 7.34 (a) Comparison of measured V_{th} distributions of planar 1X-nm NAND after 3K cycles and 3D V-NAND after 35K cycles.

lifetime. From these results, the performance and reliability of the TCAT cell proved to be appropriate for multilevel cell (MLC) operation.

Figure 7.34 shows a 2-bit/cell (MLC) V_{th} distribution of the 3D V-NAND (same as TCAT) after 35K program-erase cycles compared with that of a planar (2D) 1X-nm NAND after 3K cycles [39, 40]. The 3D V-NAND has a very excellent MLC V_{th} distribution, compared to that of the 1X-nm NAND, even with the tenfold greater number of program/erase cycles.

7.3.3 128-Gb MLC V-NAND Flash Memory

Based on the TCAT cell [19, 38, 41], the first three-dimensional NAND flash product with the V-NAND cell was implemented [39, 40]. Figure 7.35 shows the die micrograph of the 128-Gb MLC (2-bit/cell) 3D V-NAND flash memory device as the first generation of the V-NAND cell array technology. This memory chip has 24 stacked WL layers and consists of two planes each containing 64-Gb arrays (2732 of 3-MB blocks with 8-KB pages). The shared-WL-block scheme for the row circuit and the one-side page buffer for the column circuit are applied as in planar 2D NAND devices to reduce area. This organization helps to obtain small 133-mm^2 chip size with 80% cell array efficiency and 0.96 Gb/mm^2, which is the highest density ever reported.

The NAND string has 24 WL layers, two dummy word-line (DWL) layers, and two string select gate layers. And a BL is shared by the eight V-NAND strings, as shown in Fig. 7.31. Since there are 64K BLs, the size of a block is 3 MB (8 KB $\times$ 8 $\times$ 2 $\times$ 24).

Figure 7.36 shows the cell architecture diagram with decoders. This architecture is similar to that of a planar 2D NAND flash memory, except for the SSL decoders which select a target SSL to operate. This is because the 3D V-NAND has the same program and erase operations as 2D NAND flash, which are based on the FN tunneling mechanism. In particular, the bulk erase feature can provide better characteristics such as higher erase speed, lower power, and more reliability, compared with other 3D NAND cells based on the hole generation by the GIDL mechanism. So, conventional

Micron Ex. 1014, p. 313
Micron v. YMTC
IPR2025-00119

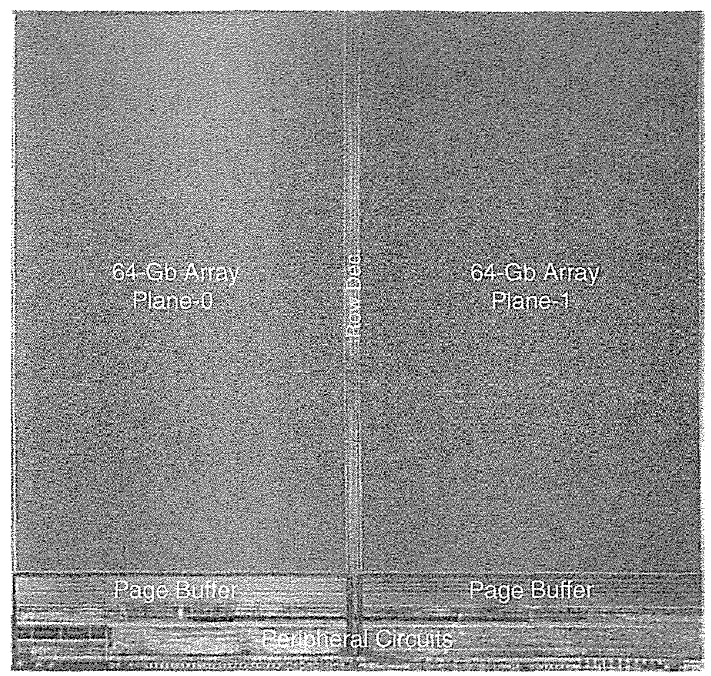

Bits per cell	2
Density	128 Gb
Technology	Three-dimensional vertical NAND, 3-metal layer
Organization	8KB x 384 pages x 5464 blocks x 8 strings
Program performance	50 MB/s for embedded application 36 MB/s for enterprise SSD application
Data interface speed	667 Mbps@Mono, 533 Mbps@8-stack
Power Supply	V_{cc} = 3.3 V / V_{ccq} = 1.8 V

FIGURE 7.35 Die micrograph and main feature of 128-Gb 2-bit/cell 3D V-NAND flash. Die size is 133 mm^2.

operations used in a planar 2D NAND can also be applied to the 3D V-NAND with simple modifications.

This chip has over 2.5 billion channel holes. This configuration can be seen in Fig. 7.31, which shows a simplified schematic diagram, an SEM image of the fabricated V-NAND array, and a cross-sectional diagram of a unit cell. In order to ensure high performance, a damascened metal-gate structure was adopted. And, as a basic cell structure, the surrounding gate (gate all-around structure) charge trap flash (CTF) cell (SONOS-type cell) is used with advanced barrier engineering material in a damascened metal-gate structure.

The chip accomplishes 50-MB/s write throughput with 3K endurance for typical embedded applications. Also, extended endurance of 35K is achieved with 36 MB/s of write throughput for data center and enterprise SSD applications.

Micron Ex. 1014, p. 314
Micron v. YMTC
IPR2025-00119

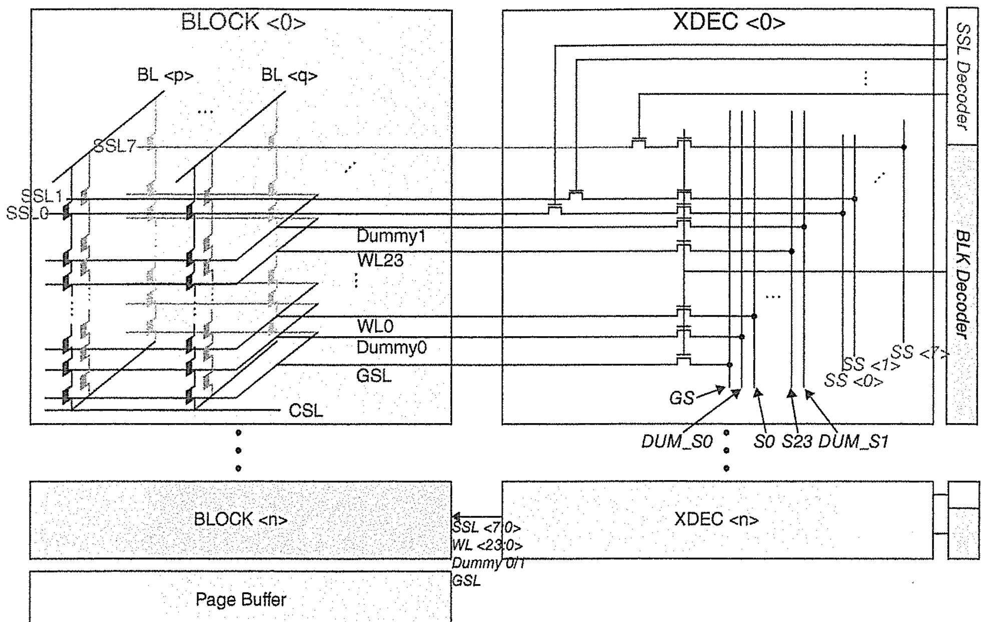

FIGURE 7.36 Block and X-decoder schematic diagram of 3D V-NAND flash memory.

7.3.4 128-Gb TLC V-NAND Flash Memory

The second generation three-dimensional V-NAND flash product with the 32 stacked cells was presented in ISSCC 2015 [42]. Figure 7.37 shows (a) the die micrograph of the 128-Gb TLC (3-bit/cell) 3D V-NAND flash memory device and (b) bit density. The die size is surprisingly reduced from the previous 133 mm^2 of 128-Gb MLC with 24 stacked WLs [39, 40] to 68.9 mm^2 of 128-Gb TLC with 32 stacked WLs [42]. This die size is smaller than 15-nm 64-Gb MLC 2D NAND flash memory of 75 mm^2, which was presented in the same conference [43], even higher density of 128 Gb.

In order to reduce die size, a new bit-line architecture was developed. In the new bit-line architecture, two bit lines are placed for one channel hole, as shown in Fig. 7.38b. Thanks to the new bit-line architecture, a two-cell plane could be changed to a one-cell plane. And also, a one-side page buffer, a shared block decoding scheme, and an MIM capacitor are adopted. Bit density is increased to 93% and exceeds over magnetic HDD (hard disk drive), as shown in Fig. 7.37b. A plane contains 2732 main blocks and additional 64 spare blocks. Each block has 6 MB in size with 384 16-KB pages. A device summary is shown in Fig. 7.39.

A new high-speed program (HSP) algorithm for TLC V-NAND was also developed. In a 2D FG cell, a three-step reprogram scheme (see Section 4.3 and 4.4) has been widely used for TLC programming to decrease the effect of floating-gate capacitive coupling interference (see Section 5.3). However, in a 3D V-NAND cell, floating-gate capacitive coupling interference is negligible due to the charge trap cell. Therefore, page programming algorithm could be simplified to the single program

Micron Ex. 1014, p. 315
Micron v. YMTC
IPR2025-00119

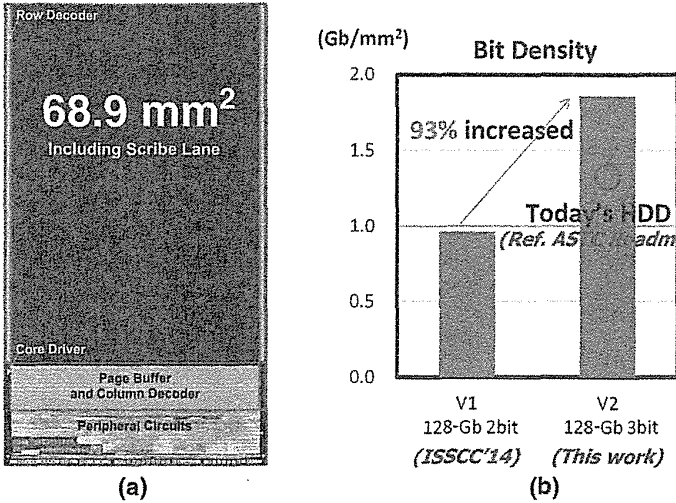

FIGURE 7.37 Die micrograph and bit density of 128-Gb 3-bit/cell 3D V-NAND flash. Small die size of 68.9 mm^2 can be achieved by using a 32-cell stacked V-NAND process, TLC (3 bit/cell), and 1-plane architecture. Bit density is increased 93% from former 128-Gb 2-bit/cell 3D V-NAND flash.

step of HSP (high speed program), as shown in Fig. 7.40. A page buffer receives three pages of data before 3b/cell programming operation, and it completes programming in a single sequence.

By using HSP, it is possible to improve programming performance and reduce programming power consumption, as shown in Fig. 7.41. The page program time of tPROG can be 200% faster than a typical planar 1X-nm 2D TLC NAND flash with the conventional reprogram algorithm, as shown in Fig. 7.41a. And also, power consumption during programming can be reduced 40%, as shown in Fig. 7.41b.

Even in fast page programming speed, memory cell V_t distribution is good enough to guarantee the reliability of product, as shown in Fig. 7.42. The V_t distribution is shown for initial and 5K P/E cycle cases. P/E cycling is performed at the ambient temperature of 55°C. After 5K P/E cycles, the cell V_t distribution is still good. Fast

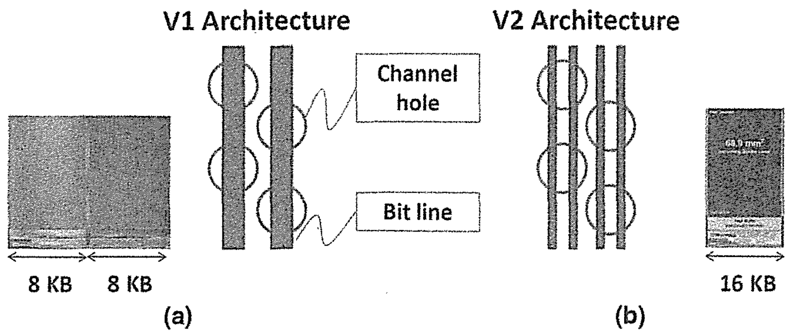

FIGURE 7.38 Bit-line architecture. Two bit lines in a channel hole pitch.

Micron Ex. 1014, p. 316
Micron v. YMTC
IPR2025-00119

Density	128 Gb
Bit per Cell	3
Chip Size	68.9 mm^2
Technology	Second generation V-NAND with 32 stacked WL layers
Organization	16 KB/Page, 384 Pages/Block, 2732 Blocks
I/O Bandwidth	Max. 1 GB/s
tBERS	3.5 ms (Typ.)
tPROG	700 μs
tR_4K	45 μs

FIGURE 7.39 Device summary of a 128-Gb 3-bit/cell 3D V-NAND flash.

tPROG of 700 μs and good endurance of over 5K P/E cycles make it suitable for both client and data-center SSD applications.

7.4 SMArT (STACKED MEMORY ARRAY TRANSISTOR)

7.4.1 Structural Advantage of SMArT

The SMArT (stacked memory array transistor) cell was presented as shown in Fig. 7.43 [29]. The SMArT cell has a similar structure and process with BiCS and TCAT cells. The fabrication process of charge storage ONO and metal gate is different from BiCS and TCAT. Figure 7.44 shows the structure comparison of BiCS, TCAT,

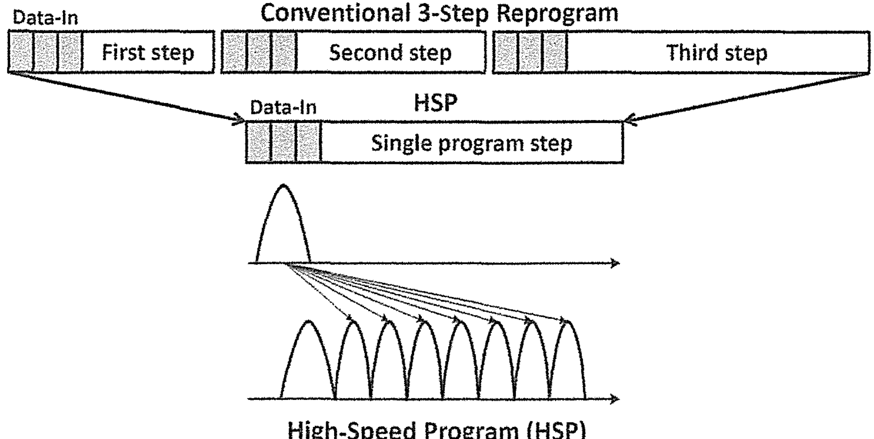

FIGURE 7.40 High-speed program (HSP) scheme. The single program step of HSP can be used in V-NAND cell because cell-to-cell interference is small in a charge trap cell.

Micron Ex. 1014, p. 317
Micron v. YMTC
IPR2025-00119

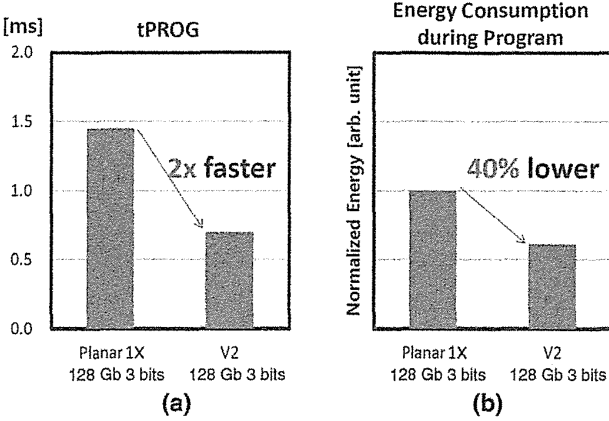

FIGURE 7.41 The program time and energy consumption during programming. Program time could be improved 200% (×2), and energy consumption can be reduced 40%.

and SMArT [44]. BiCS cell uses a poly-Si as word lines (WL), which is fabricated by SiO2/poly-Si multi-stacked layers, and does not use the WL replacement process by tungsten (W) metal as a low-resistance word line. Therefore, WL resistance of BiCS is higher than tungsten metal WL of TCAT and SMArT cell. However, the stacked height of SiO2/poly-Si multi-stacked layers can be lower than that of the W replacement process due to no ONO deposition in W replacement process. In the TCAT cell, WL resistance is much lower than that of the poly-Si WL of BiCS cell. However, the stacked height becomes high due to ONO deposition in the W replacement process. The SMArT cell can achieve both low stack height and low WL resistance, because of no ONO deposition in the W replacement process, as shown in Fig. 7.44. The ONO films are deposited before the W replacement process.

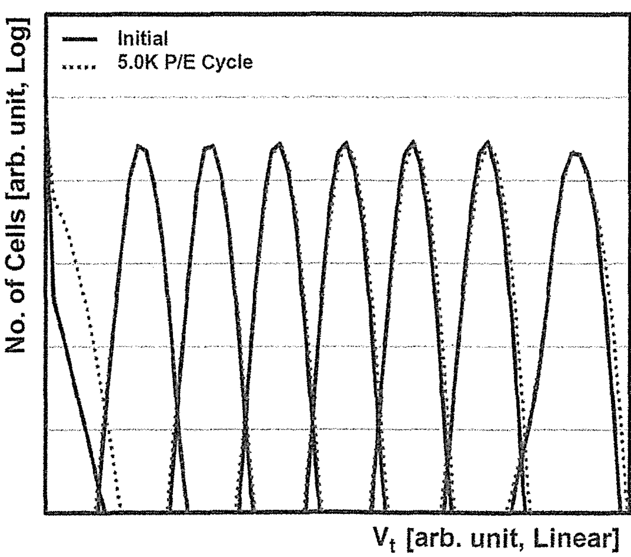

FIGURE 7.42 Threshold voltage distribution of a 128-Gb 3-bit/cell 3D V-NAND flash.

Micron Ex. 1014, p. 318
Micron v. YMTC
IPR2025-00119

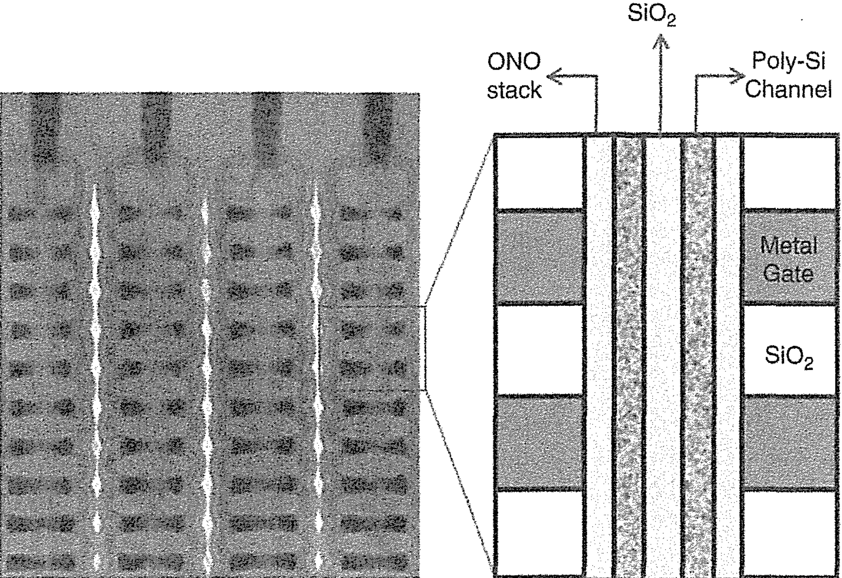

FIGURE 7.43 TEM cross-sectional image of SMArT (stacked memory array transistor) cell string and schematic drawing of a SMArT unit cell.

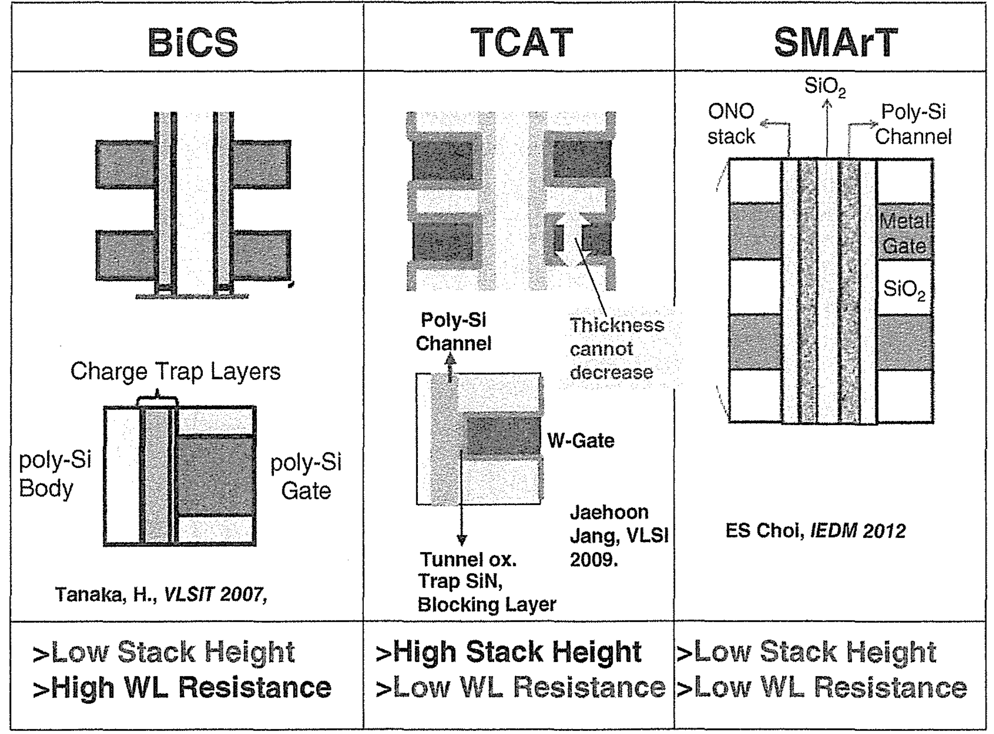

FIGURE 7.44 Comparison of SONOS 3D cells of BiCS, TCAT (V-NAND), and SMArT. First appearance in "Semiconductor Storage 2014", Nikkei Business Publications, Inc., 2013/07/31.

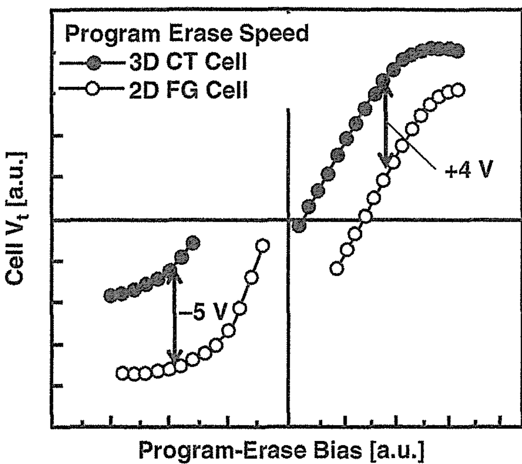

FIGURE 7.45 Comparison of program-erase characteristics of 2D 2y-nm node FG cell and 3D CTD SMArT cell.

Low stack height is very important for 3D NAND flash, because an aspect ratio of the multi-stack etching process can be reduced. Low aspect ratio and low stack height are the key challenge of 3D NAND flash fabrication, and it will be serious in the case of increasing number of stacked layers, as described in Section 8.7. The stack height is minimized by using the SMArT cell process (inserting ONO layer in the plug) with low resistive tungsten (W). Low WL resistance is fabricated by the gate replacement process. Then the SMArT cell has the "gate-last" process, providing better reliability.

7.4.2 Electrical Characteristics

Program and erase (P/E) speed of 3D charge trap (CT) SMArT cell is compared with 2D FG cell in Fig. 7.45 [29]. The program speed of 3D CT cell is much faster than 2D FG cell, but the erase speed is much slower in spite of the field enhancement effect of the surrounding-gate structure (gate all-around structure). Despite the smaller program/erase window, the NAND cell operation window is quite sufficient to MLC and TLC, because the program saturation V_t of a 3D CT cell is much larger than that of a 2D floating-gate cell, as shown in Fig. 7.45.

Figure 7.46 shows the cell-to-cell interference (floating-gate capacitive coupling interference) of a 2D floating-gate cell and a 3D SMArT cell [29]. As expected in the charge-trap-type (SONOS-type) cell of a 3D SMArT cell, the cell-to-cell interference is negligibly small in comparison with a 2D floating-gate cell. This means that the major scaling limiter of the cell-to-cell interference in 2D cell, described in Chapter 5, is not the problem in 3D charge trap (CT) cell.

The V_t distributions before and after program/erase cycling endurance of a 3D SMArT cell are shown in Fig. 7.47, compared with a two-dimensional (2D) 2y-nm generation floating-gate cell [29]. In a 2D 2y-nm generation cell, the V_t distribution width becomes wider after 3K or 5K program/erase cycling. However, in (a) 3D SMArT cell, the cell V_t distribution does not become wider up to 5K cycles. This

Micron Ex. 1014, p. 320
Micron v. YMTC
IPR2025-00119

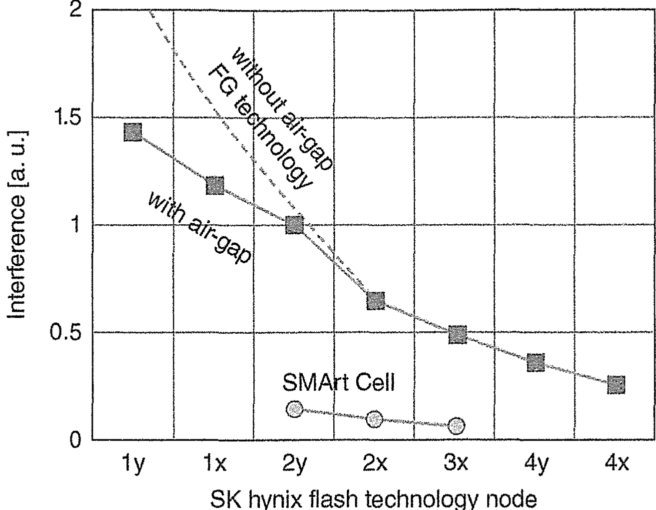

FIGURE 7.46 Comparison of total interference of a 2D FG cell and a 3D SMArT cell.

difference is known to be originated from the thin tunneling oxide of the charge trap cell where the interface traps are less generated than the floating-gate cell with thicker tunnel oxide.

7.5 VG-NAND (VERTICAL GATE NAND CELL)

7.5.1 Structure and Fabrication Process of VG-NAND

The vertical gate NAND (VG-NAND) flash array with horizontal multi-active layers had been proposed [20]. Figure 7.48 shows the structure and schematics of the VG-NAND array.

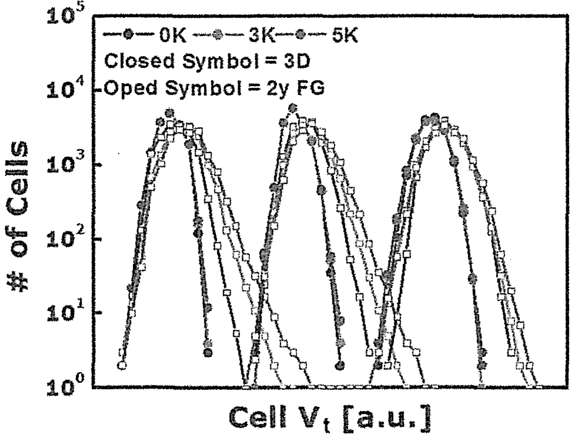

FIGURE 7.47 Comparison of V_t widening during program/erase cycling.

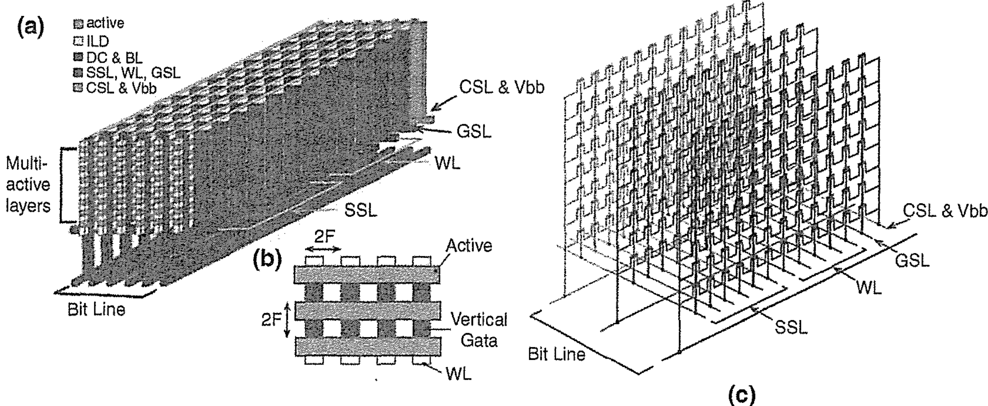

FIGURE 7.48 (a) Structure of vertical gate (VG)-NAND. (b) Top-down view of a VG-NAND showing $4*F^2$ cell size/layer. (c) Schematics of VG-NAND array with source and body tied to CSL (common source line). Each BL contains multi-actives, common vertical gate, and vertical plugs between multi-actives.

The VG-NAND flash has horizontal multilayer active strings and vertical gates (VG) for SSL, WL, and GSL. A charge trap layer is located between the active layer and the vertical gate, forming dual gate structure. Active layers are connected to a bit line (BL) and a source line (CSL) at the end of NAND strung. In the proposed array [20], word line (WL) and a BL are formed at the beginning of fabrication before the cell array, making an interconnect between WL, BL, and decoder easier. However, WL and BL can also be formed after making a memory cell array as a conventional 2D NAND flash memory cell. The source and active body (V_{bb}) are electrically connected to CSL (common source line) for enabling body erase operation. A positive bias is applied to CSL during erase. Array schematic of each layer is identical to the planar 2D NAND flash, except for SSL, as shown in Fig. 7.48c. VG-NAND requires 6 SSLs for 8 active layers and 8 SSLs for 16 active layers. Required number of SSL is expressed by

$$(\text{Number of SSL}) = 2 * \log_2(\text{Number of active layers})$$

A reason for the multi-SSLs is to select data from a chosen layer out of multilayers since VG-NAND cell uses common BL and common WL between multi-active layers. Figure 7.49 represents SSL schematics of VG-NAND with eight active layers and its operation table for a specific layer selection during read and program. A transistor with shade always turns on regardless of applied voltage on SSL while a transistor without shade only turns on under applied proper voltage.

Figure 7.50 describes a process sequence of VG-NAND cell. A process sequence is based on simple patterning and plugging. BL with $n+$ poly-Si is fabricated first, and then $n+$ poly-Si WL is formed on top of it (Fig. 7.50(1)). Multi-active layers with p-type poly-Si are formed with n-type ion implants for SSL layer selection, and alternated interlayer dielectrics are inserted between active layers. Then patterning is

Micron Ex. 1014, p. 322
Micron v. YMTC
IPR2025-00119

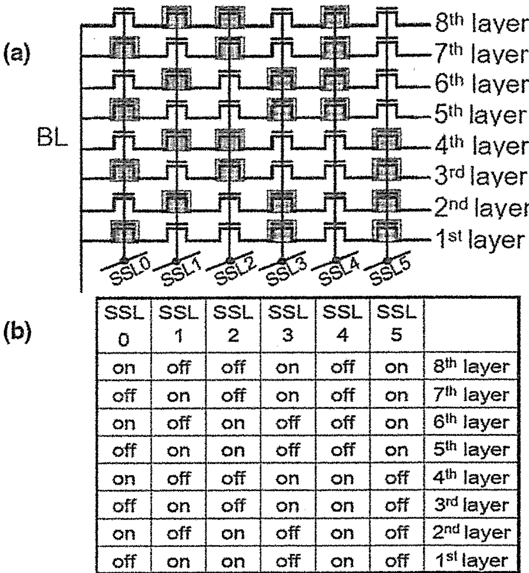

SSL 0	SSL 1	SSL 2	SSL 3	SSL 4	SSL 5	
on	off	off	on	off	on	8th layer
off	on	off	on	off	on	7th layer
on	off	on	off	off	on	6th layer
off	on	on	off	off	on	5th layer
on	off	off	on	on	off	4th layer
off	on	off	on	on	off	3rd layer
on	off	on	off	on	off	2nd layer
off	on	on	off	on	off	1st layer

FIGURE 7.49 (a) Schematics of SSL including depletion and enhancement transistors (b) operation table of SSL for a layer selection during read and program.

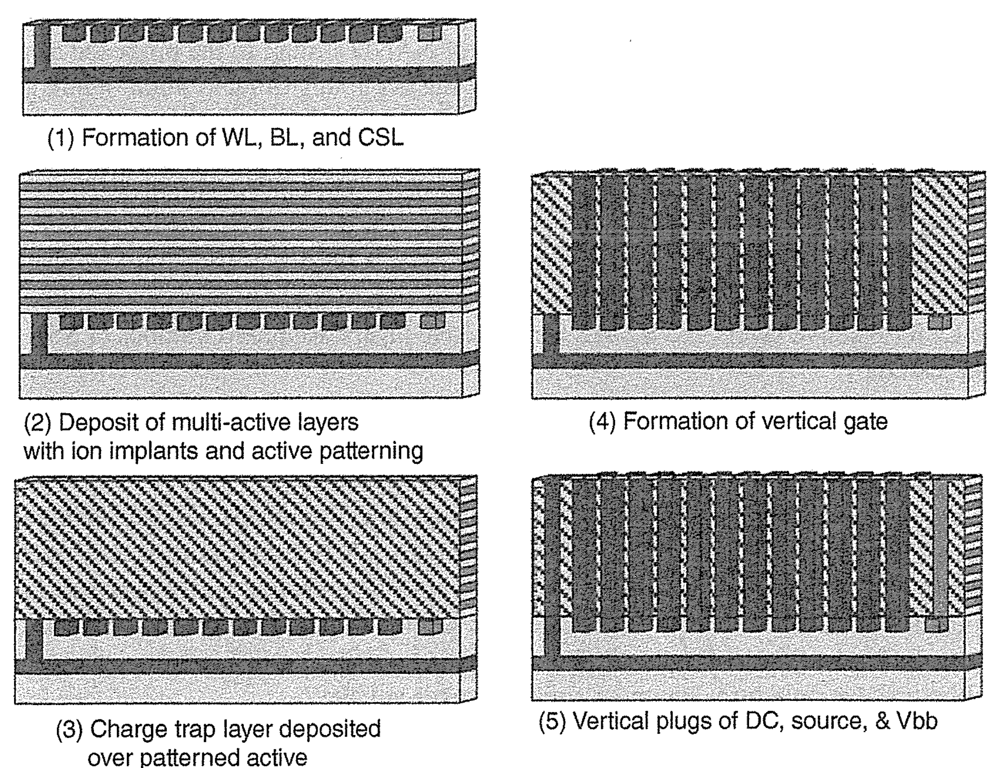

FIGURE 7.50 Process flow of VG-NAND flash array Integration based on simple patterning and plugging.

Micron Ex. 1014, p. 323
Micron v. YMTC
IPR2025-00119

carried on the multi-active layers (Fig. 7.50 (2)), and charge trap layers (ONO) are deposited over the patterned actives (Fig. 7.50 (3)). Consecutively, VG is formed by high aspect-ratio and high selective RIE, and connected to WL (Fig. 7.50 (4)). And as a final step, vertical plugs of DC and source-V_{bb} are connected to BL and CSL after contact ion implants (Fig. 7.50 (5)). N+ doped source and *p*-type active are electrically tied to CSL.

There are several challenges in VG-NAND for considering mass production. One is a VG patterning of high aspect and high selective RIE. As shown in Fig. 7.50 (4), a VG patterning has to remove WL poly silicon at the bottom of space between WLs and between active layers. This patterning has a very high aspect ratio (>30 @ 16 layers) etching with high selectivity for VG pattern material (SiO_2/SiN or resist).

The other challenge is the increased cost by the SSL formation. As described above, a large occupied area of SSL and many process steps of SSL formation are needed to fabricate the VG-NAND cell. The SSL occupied area is increased in accordance with an increasing number of stacked active layers. The effective cell size including the SSL area is getting larger due to large SSL occupied area. And, for each active layer, ion implantation process and mask lithography steps are needed to make an *n*-type channel. These process steps are also increased in accordance with an increasing number of stacked active layers.

In order to minimize the SSL area, several new schemes were proposed, such as the surrounding-gate transistor SSL scheme [45], the LSM (layer selection by multilevel scheme) with multi-state SSL V_t and multi-bias SSL [46], the island-gate SSL scheme [47–51], and so on.

As one example, Fig. 7.51 shows the island-gate SSL scheme of a VG NAND. Each channel layer is separately decoded by one island-gate SSL device. In one unit (contains $2*N$ channel layers, where N is number of stacked memory layers), all channel layers are grouped together for each memory layer and are connected to the metal-3 global BL through the "staircase" BL contacts formed at the BL pad region. All island-gate SSLs are connected by the interconnection of CONT/ML1/VIA1/ML2 toward SSL decoder. A common source line (CSL) is used to share the source of all memory layers. Figure 7.51b illustrates the detail layout in the case of $N = 4$. All $2*N$ (= 8) channel BLs are grouped into one unit, sharing the same BL pad. In the BL pad, "staircase" contacts are fabricated, where each contact corresponds to one memory layer, as shown in the inset. The staircase CONTs are then connected by ML3 BLs toward the page buffer for memory sensing. Each channel BL has own island-gate SSL for the selection/decoding, where SSL devices are all connected by ML2 lines (parallel to WL's) toward SSL decoder.

7.5.2 Electrical Characteristics

I_d–V_g characteristics of a VG-NAND cell is shown in Fig. 7.52 [20]. The conventional program and body-erase schemes have been performed. The V_t window of about 3.7 V is obtained. In the VG-NAND cell structure, a double gate is located on both sides of the active layer. Then gate controllability to channel is worse than the surrounding

Micron Ex. 1014, p. 324
Micron v. YMTC
IPR2025-00119

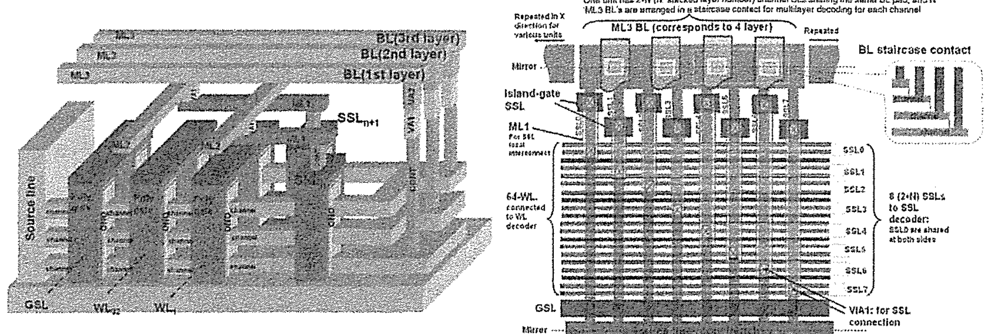

FIGURE 7.51 (a) Schematic diagram of a 3D VG NAND. WLs of the vertical layers are shared together. Every channel bit line is separately decoded by one island-gate SSL device. In one unit (containing 2∗*N* channel BLs), all channel BLs are grouped together for each layer and are connected to the metal 3 BL through the staircase BL contacts formed at the BL pad region. All island-gate SSL devices are connected by the interconnection of CONT/ML1/VIA1/ML2 routings toward the SSL decoder. A common source (CSL) is used to share the source planes of all memory layers. (b) Layout schematic for *N* (stack number) = 4. All 2∗*N* (= 8) channel BLs are grouped into one unit, sharing the same BL pad. In the BL pad, a staircase contact is fabricated, where each contact corresponds to one memory layer, as shown in the inset. The staircase CONT is connected by ML3 BLs toward page buffer for memory sensing. Each channel BL has its own island-gate SSL for the selection. The SSLs are connected through CONT/ML1/VIA1/ML2 toward the SSL decoder. A common source is fabricated to connect source lines of all memory layers.

gate cell such as BiCS, TCAT, and SMArT cells. The subthreshold slope would not be enhanced in case the of scaling cells due to using a thinner channel poly silicon layer as scaling.

Figure 7.53a shows the program/erase cycling endurance characteristics of a VG-NAND cell [20]. The window narrowing can be observed up to 1K cycles of

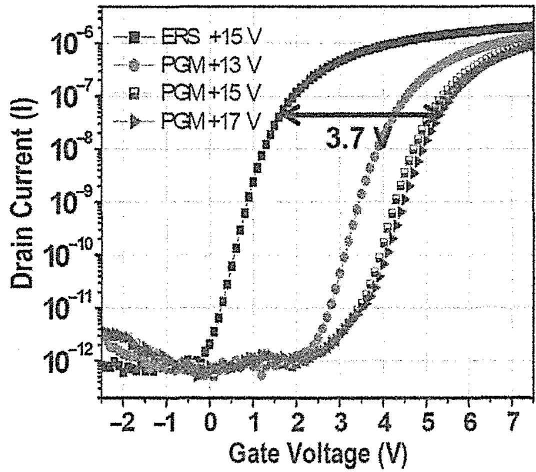

FIGURE 7.52 Program and body-erase window of a VG-NAND cell.

Micron Ex. 1014, p. 325
Micron v. YMTC
IPR2025-00119

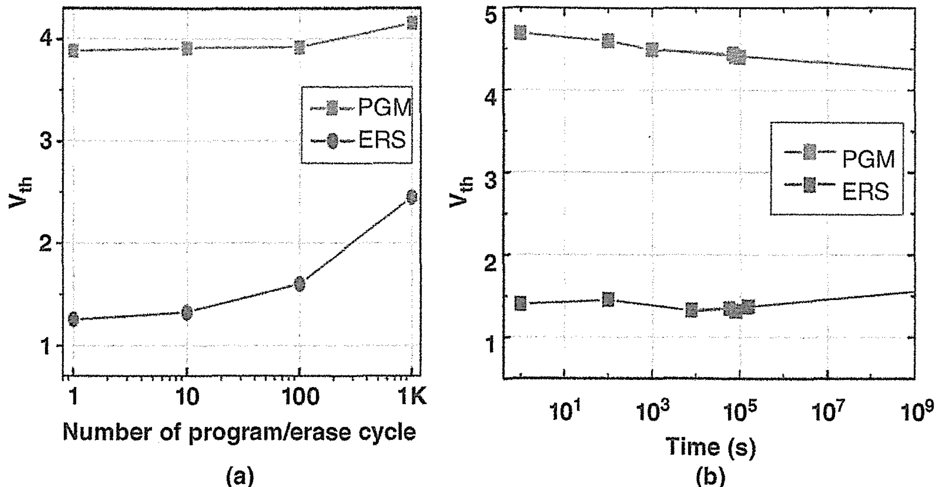

FIGURE 7.53 (a) Program and erase cycling endurance. (b) Data retention characteristics of a VG-NAND cell.

program/erase. Data retention characteristics at room temperature show the 10-year data retention capability in Fig. 7.53b.

In VG-NAND, a new interference mode had been reported [22, 47]. It comes from the channel potential interference in the proximity in the Z-direction (vertical direction; thickness of the buried oxide between stacked active channel layers), namely "Z-interference." Figure 7.54 shows that the interference in cell C may exceed 450 mV after programming the vertical adjacent cell (cell A) when the buried oxide thickness is scaled below 20 nm. Therefore, the Z-interference limits the Z-direction scaling. The thickness of buried oxide should be greater than 30 nm to avoid serious Z-interference.

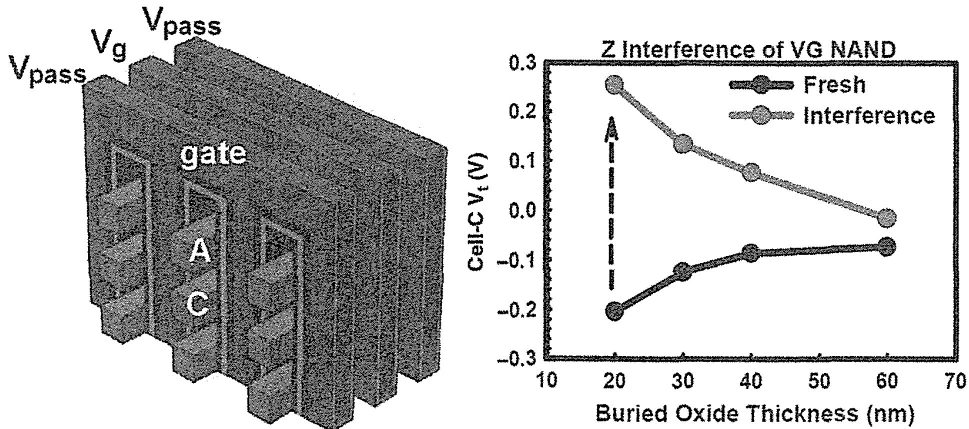

FIGURE 7.54 "Z interference" of VG-NAND when buried oxide thickness (F_Z) is scaled. In this calculation, $F = 60$ nm and $V_{pass} = 7$ V are used. Cell A is programmed with $e^- = 2E19$ cm^{-3} while cell C is the measured Z interference. When buried oxide thickness is only 20 nm, the Z interference may exceed 450 mV.

Micron Ex. 1014, p. 326
Micron v. YMTC
IPR2025-00119

7.6 DUAL CONTROL GATE—SURROUNDING FLOATING GATE CELL (DC-SF CELL)

7.6.1 Concern for Charge Trap 3D Cell

There has been tremendous attention on three-dimensional (3D) NAND flash memory [10, 13–23]. Most 3D NAND cells use a SONOS/TANOS device structure with a charge trap nitride as a storage layer. However, it is well known that these structures with a charge trap nitride layer have suffered from inherent problems, such as low erase speed, poor retention characteristics, and charge spreading issues [37] between cells along the charge trap nitride layer. The charge spreading problem in 3D charge trap cell is illustrated in Fig. 7.55a. The stored charges in Si nitride move toward the neighbor cells through a connected nitride layer, because the charge trap nitride layer is physically connected from top to bottom CGs in 3D SONOS/TANOS NAND flash. As a result, this would cause degradation of data-retention characteristics and poor V_t distribution of cell state in the 3D SONOS cell. As these problems are related to a charge trap nitride, the floating-gate-type 3D NAND flash is required to be used instead of charge trap nitride. However, applying a conventional two-dimensional (2D) floating-gate structure without schematic change is not suitable for 3D NAND flash because the lateral space occupation of the floating gate is large, resulting in larger cell size.

Here, a dual control gate with a surrounding floating-gate (DC-SF) cell for 3D NAND flash memory had been proposed [24–26]. This structure allowed us to apply a floating gate to a 3D stacked cell structure with minimal cell size and high coupling ratio. The DC-SF cell and 3D SONOS cell [10, 13–17] are compared in a vertical schematic as shown in Fig. 7.55. The surrounding FG in the DC-SF cell is completely isolated by IPD and tunnel oxide as shown in Fig. 7.55b. This implies that significant improvement of data retention is expected for the DC-SF cell due to the absence of a physical leakage path.

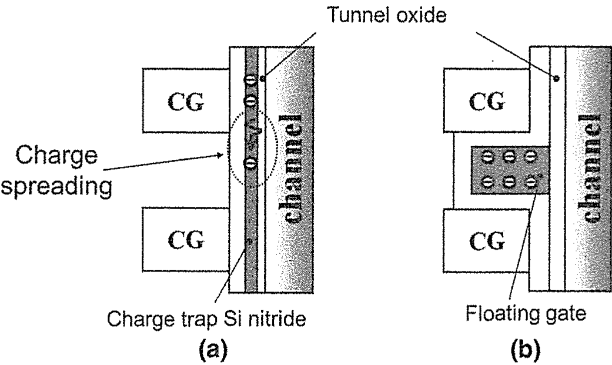

FIGURE 7.55 Comparison of 3D NAND flash cell structures. (a) SONOS cell (BiCS, etc.). (b) DC-SF cell. In the case of a SONOS cell, charge spreading problem is caused by a connected charge trap Si nitride layer.

Micron Ex. 1014, p. 327
Micron v. YMTC
IPR2025-00119

7.6.2 DC-SF NAND Flash Cells

A. Concept. Figure 7.56 shows the cross-sectional schematic of the DC-SF NAND flash cell. A surrounding FG is located in between the two control gates (CGs), which is a new approach for 3D NAND flash memory. The detailed schematic of the cell structure is illustrated in Fig. 7.56b. The surrounding FG is covered by inter-poly dielectric (IPD) and tunnel oxide. Therefore, two CGs are vertically capacitive coupled with FG. The tunnel oxide is only formed in between the channel poly and FG, while IPD is added on the side-wall of the CG, resulting in thicker dielectric layer formed between the channel poly and CG. This means that during program and erase, the charges can tunnel only through the tunnel oxide between the channel poly and FG without any tunneling between the channel poly and CGs.

There are several significant advantages of the DC-SF structure. The first advantage is that the floating gate, which is a proven and predictable technology in 2D NAND flash memory, can be used as a charge storage node so that many issues related to charge trap (SONOS and TANOS) cell can be eliminated. The second is the significant improvement in the coupling ratio because a new concept of functionality is implemented to 3D structure—one surrounding FG is controlled by two neighboring control gates. As a result, enlargement of the surface area between FG and two CGs can be achieved. Therefore, it can be attributed to low bias cell operation for program and erase. The third is to shrink the unit cell size in the horizontal direction, because FG is not positioned between the CG and channel poly in a horizontal direction, but is positioned in between two CGs in a vertical direction, implying that it is suitable for

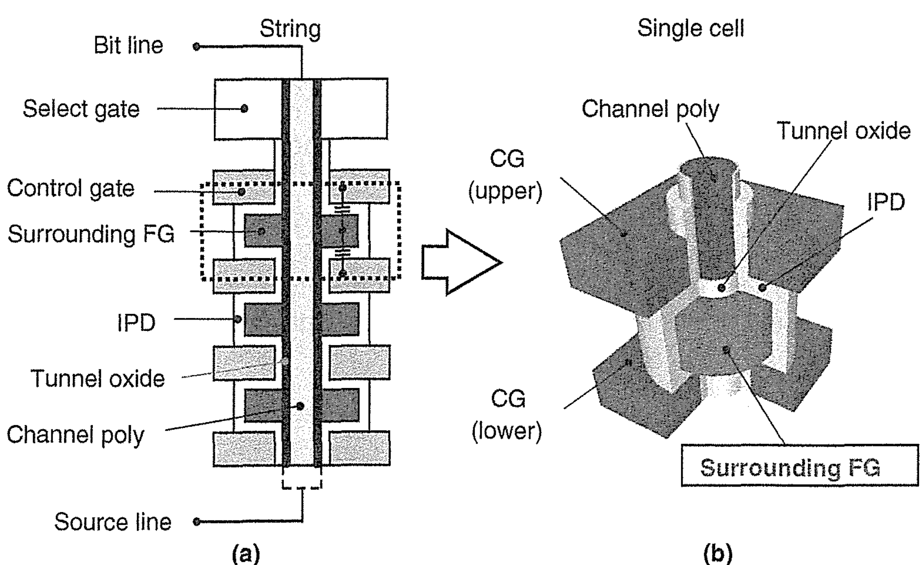

FIGURE 7.56 (a) Cross-sectional schematic of the DC-SF (dual control gate–surrounding floating gate) NAND flash cell. Two control gate (CGs) are vertically capacitive coupled with a floating gate (FG). (b) Bird's-eye view of the DC-SF NAND flash cell. The surrounding FG is capacitive, coupled with both upper and lower CGs.

Micron Ex. 1014, p. 328
Micron v. YMTC
IPR2025-00119

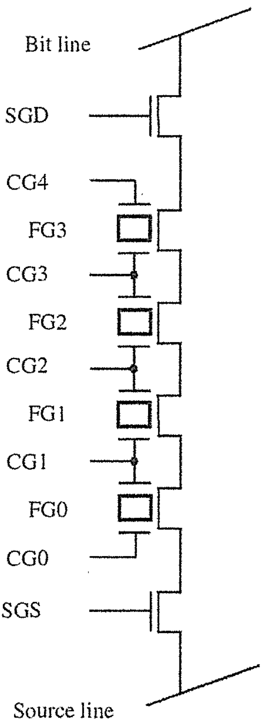

FIGURE 7.57 Equivalent circuit of the DC-SF NAND cell string.

fabrication of 3D NAND flash structure. The fourth is very small FG–FG coupling interference, because a CG positioned in two FGs plays a role of the electrical shield. Therefore, there is negligible capacitive coupled capacitance in between FGs. As a result, the DC-SF cell allows wide program/erase (P/E) window and low bias cell operation for 3D NAND flash device. The equivalent circuit of DC-SF cell string is given in Fig. 7.57. The single cell consists of one FG and two CGs.

B. Coupling Ratio. Figure 7.58 shows the top and cross-sectional view of the DC-SF cell. The capacitive coupled capacitance of the FG is estimated by two different formulas in the DC-SF structure. In the vertical direction of the FG, the coupled capacitance between the FG and two CGs (C_{IPD}) is determined by parallel plate capacitance, as shown in Eq. (7.1).

$$C_{\mathrm{IPD}} = \frac{2\varepsilon_r\varepsilon_0\pi(a_3^2 - a_2^2)}{d} \tag{7.1}$$

$$C_{\mathrm{Tox}} = \frac{2\pi\varepsilon_r\varepsilon_0 h}{\ln(a_2/a_1)} \tag{7.2}$$

On the other hand, the capacitive-coupled capacitance of the FG with tunnel oxide (C_{Tox}) in the horizontal direction is extracted by coaxial cable capacitance as shown in Eq. (7.2), because the FG is covered on the cylindrical channel poly. The calculation

Micron Ex. 1014, p. 329
Micron v. YMTC
IPR2025-00119

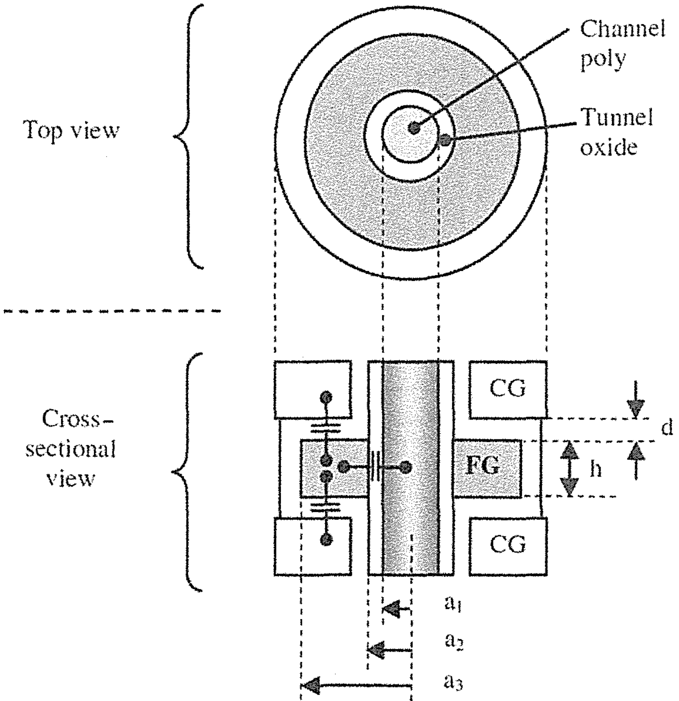

FIGURE 7.58 Floating-gate capacitance of the DC-SF cell.

of coupling ratio is plotted as a function of the FG width, FG height, and the radius of channel poly in case of $T_{ox} = 8$ nm and $T_{IPD} = 12$ nm thick, as shown in Fig. 7.59. The high coupling ratio of 0.68 can be obtained, for example, in the structure of $a_1 =$ 20 nm, $a_2 = 28$ nm, $a_3 = 68$ nm, $h = 40$ nm, and $d = 12$ nm; that is, FG width = $(a_3 - a_2) = 40$ nm, FG height = $h = 40$ nm, and radius of channel = $a_1 = 20$ nm.

The coupling ratio decreases with decreasing FG width $(a_3 - a_2)$, as shown in Fig. 7.59a, because the capacitor area of FG and CG decreases. On the contrary, the coupling ratio increases as the FG height (Fig. 7.59b) and radius of the channel (Fig. 7.59c) poly decrease, implying that the cell size in the horizontal direction can be reduced by increasing the coupling ratio in this structure. This result indicates that a high coupling ratio of about 0.7 can be maintained even though the cell size decreases, because the coupled capacitance of FG is compensated in both directions. Though the conventional planar 2D NAND flash memory suffers from low coupling ratio as the cell size decreases, the DC-SF cell structure has an advantage of maintaining a high coupling ratio even at the smaller cell size. With this structure, the coupling ratio of about 0.7 can be achieved.

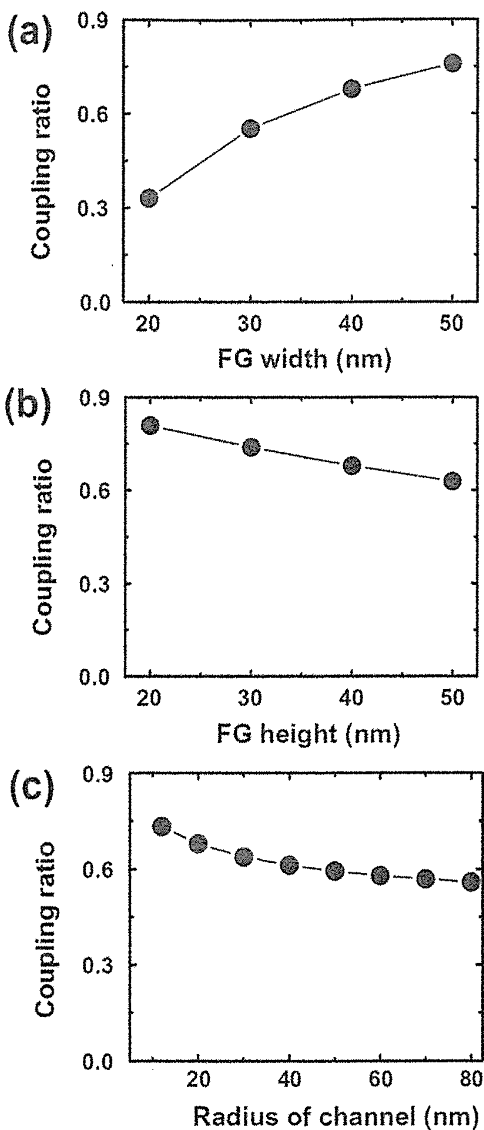

FIGURE 7.59 Coupling ratio of the DC-SF cell in case of T_{ox} = 8 nm and T_{IPD} = 12 nm. (a) Coupling ratio of the DC-SF cell as a function of FG width ($a_3 - a_2$) (FG height: 40 nm and radius of channel poly: 20 nm). (b) Coupling ratio of the DC-SF cell as a function of FG height (h) (FG width, 40 nm; radius of channel poly, 20 nm). (c) Coupling ratio of DC-SF cell as a function of radius of channel poly (a_1) (FG height, 40 nm; FG width, 40 nm).

C. Device Fabrication. The process sequence of the DC-SF cell is shown in Fig. 7.60. First, in situ thermal CVD SiO_2 and poly Si are deposited in sequence to make multi-stacked layers. Thus, holes are formed by etch process through the entire SiO_2/poly-Si stacked layers (Fig. 7.60a). To make a space for IPD and FG, oxide recess is carried out in the horizontal direction (Fig. 7.60b). IPD deposition is followed (Fig. 7.60c), and the space is filled with FG poly-Si deposition overall

Micron Ex. 1014, p. 331
Micron v. YMTC
IPR2025-00119

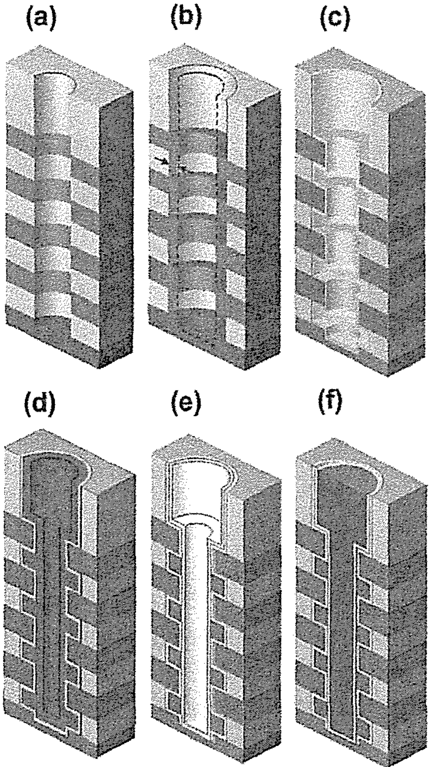

FIGURE 7.60 Process sequence of a DC-SF NAND flash cell. (a) Oxide/poly deposition and hole formation by etch process. (b) Oxide recess is carried out to make a space for IPD and FG. (c) IPD deposition. (d) FG poly-Si deposition. (e) Isotropic etch of FG and tunnel-oxide deposition. (f) Channel poly deposition.

inside the holes (Fig. 7.60d). To define complete FGs in the hole, the isotropic etch process of FG is performed. FGs of poly-Si are separated into each recess position. Tunnel oxide is deposited (Fig. 7.60e), and then the first channel poly-Si is deposited to cover tunnel oxide, and then the first channel poly-Si and tunnel oxide at bottom of holes are removed by RIE. And then the second channel poly-Si is deposited to fill hole, as shown in Fig. 7.60f. The second channel poly-Si is electrically connected to substrate. The cross-sectional TEM image of the DC-SF cell arrays is shown in Fig. 7.61a. It can be clearly seen that the surrounding FGs and CGs are well fabricated along the channel, as shown in Fig. 7.61b.

7.6.3 Results and Discussions

The operation conditions of the DC-SF cell are listed in Table 7.2. For the erase operation, an erase bias of −11 V is applied to all the CGs. Cell V_t values decrease to negative. In the program and read condition, FG2 between CG2 and CG3 is selected. The program bias (V_{pgm}: 15 V) is applied to both CG2 and CG3 simultaneously. Two different V_{pass} biases are used to prevent the program disturb. In the neighboring word

Micron Ex. 1014, p. 332
Micron v. YMTC
IPR2025-00119

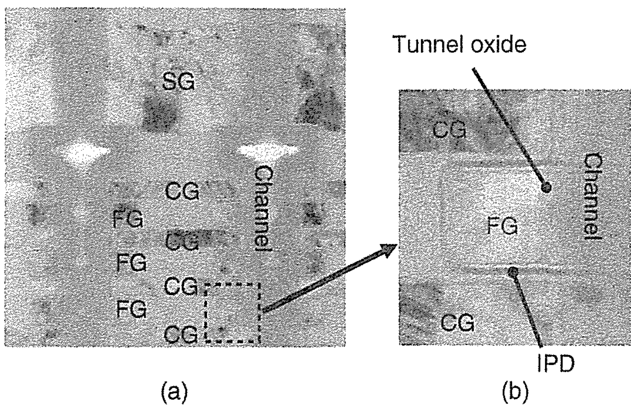

FIGURE 7.61 (a) TEM image of the DC-SF NAND cell string. FGs and CGs are stacked. (b) Detail TEM image of the single cell, showing the FG and two CGs with tunnel oxide and IPD on the channel.

line of CG1 and CG4, a lower V_{pass} bias of 2 V is applied. And the normal V_{pass} bias of 4 V is applied to the other CGs during programming. The potentials of FG1 and FG3 are compensated by a lower bias of 2 V in order to prevent program disturb. For the read operation, zero bias is applied to both CG2 and CG3 with a read pass bias (V_{read}) of 4 V to the other CGs. As can be seen in Table 7.2, all the operation biases are significantly lower than those of conventional 3D NAND flash memory based on charge trap nitride. This is due to the well-designed cell structure of the DC-SF and high coupling ratio.

The I_d–V_g characteristics of the DC-SF cell is plotted with different erase times in Fig. 7.62. The figure shows that cell V_t decreases as the erase time increases, implying that the erase cell operates effectively. As a result, a wide program/erase window of about 9.2 V is obtained.

Figure 7.63a shows the program characteristics. It shows that the DC-SF cell is well programmed even at a low program bias of 15 V. The coupling ratio of this cell

TABLE 7.2 Operation conditions for the DC-SF NAND cells[a]

Bias	Erase (V)	Program (V)	Read (V)
BL	0	0/Vcc	1
SGD	4.5	4.5	4.5
CG4	V_{erase}:−11	V_{pass2}:2	V_{read}:4
CG3	V_{erase}:−11	V_{pgm}:15	0
CG2	V_{erase}:−11	V_{pgm}:15	0
CG1	V_{erase}:−11	V_{pass2}:2	V_{read}:4
CG0	V_{erase}:−11	V_{pass1}:4	V_{read}:4
SGS	4.5	0	4.5
SL	0	Vcc	0

[a]FG2 between CG2 and CG3 is selected in program and read.

Micron Ex. 1014, p. 333
Micron v. YMTC
IPR2025-00119

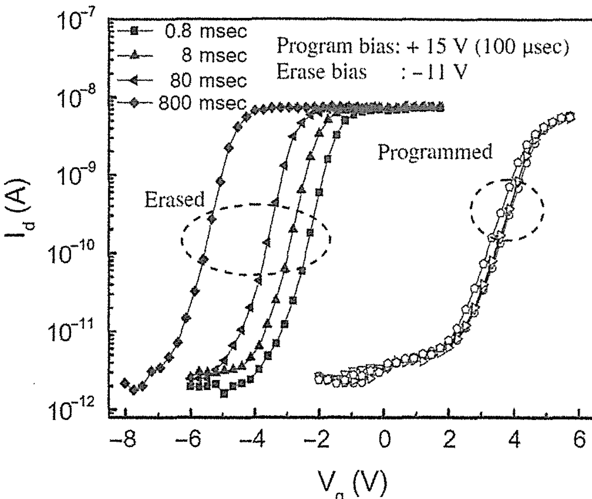

FIGURE 7.62 The I_d–V_g characteristics of the DC-SF NAND flash cell. V_g is VCG2 (= VCG3) bias. V_{read} for unselected control gate are VCG0 = VCG1 = VCG4 = 4 V. And bit-line voltage is V_d = 1 V.

is estimated to 0.71. Figure 7.63b shows the erase characteristics. The DC-SF cell can be erased well at low erase bias of -11 V for 1 ms. These operation voltages are significantly lower than those of conventional 3D SONOS NAND flash memory structure and planar 2D NAND flash cell. This implies that cell operation in the DC-SF structure is considerably effective because of a high coupling ratio.

The FG–FG coupling interference (floating-gate capacitive coupling interference) between a programmed cell and an adjacent cell was studied, as shown in Fig. 7.64. The ΔV_t of the adjacent cell has been measured as a function of programmed cell V_t from 2.0 to 3.6 V. Very small capacitive coupling interference of 12 mV/V is observed due to CG electric shield effect between FGs. And the FG–FG couplings

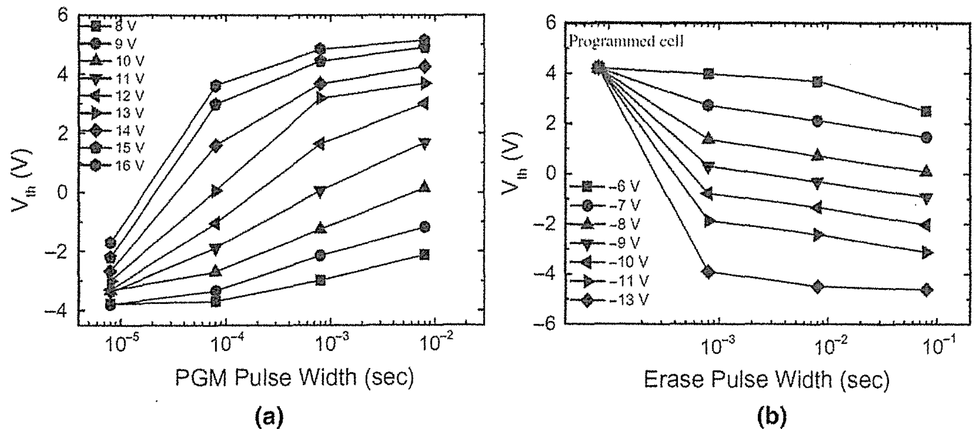

FIGURE 7.63 (a) The program and (b) erase characteristics of the DC-SF NAND flash cells.

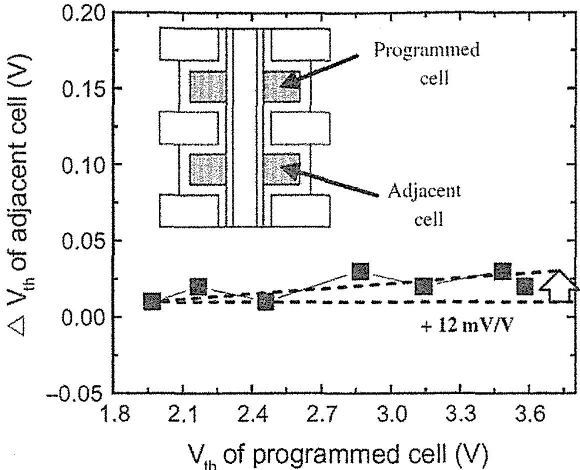

FIGURE 7.64 The interference characteristics between FG and FG (V_{th} difference of the adjacent FG versus V_{th} of the programmed cell). Very small FG–FG coupling interference value of 12 mV/V is obtained.

of x-direction (along WL) and y-direction (along BL) for one side are estimated to 1.1% and 0.7% of total FG capacitance, respectively, based on scaled cell size as shown in Fig. 7.67c. Then total FG–FG coupling of x- and y-directions is 3.6%. It is much smaller value in comparison with the conventional 2D FG cell. With this small FG–FG interference result, it is expected that V_t distribution setting could be acceptable for multilevel cell (MLC) or triple-level cell (TLC) as shown in Fig. 7.65.

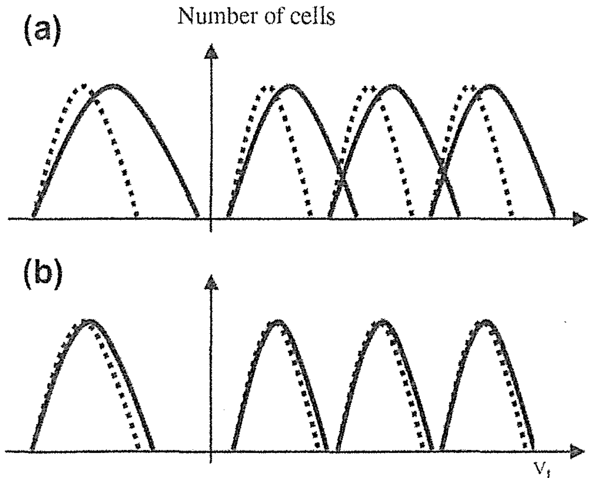

FIGURE 7.65 Cell threshold voltage (V_t) setting comparison between: (a) conventional planar FG cell with large FG–FG coupling interference and (b) DC-SF cell with small FG–FG coupling interference. The DC-SF cell has a wider V_t setting margin due to negligible FG–FG coupling.

Micron Ex. 1014, p. 335
Micron v. YMTC
IPR2025-00119

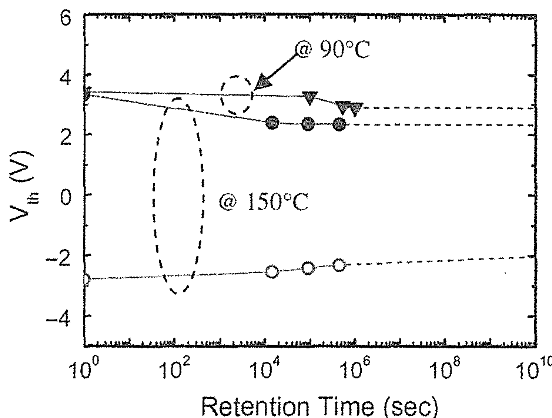

FIGURE 7.66 The data-retention characteristics of the DC-SF NAND flash cells.

Figure 7.66 shows the data-retention characteristics at two different temperatures (90°C and 150°C). For the high-temperature condition, the program and erase charge losses are 0.9 V and 0.2 V for 126 h, respectively.

7.6.4 Scaling Capability

In order to evaluate the scaling capability of the DC-SF cell, the effective cell size of the DC-SF structure and conventional 3D SONOS had been compared, as shown in Fig. 7.67. The assumption of physical unit cell size is that x- and y-pitch of BiCS [10, 13–17]/TCAT [19] are 100 and 160 nm, respectively. On the other hand, the x- and y-pitch of the DC-SF cell are 130 and 190 nm. The physical cell size of the DC-SF cell is larger than that of BiCS/TCAT, because space margin between FG and slit edge (gate edge) is needed. The feature size here is assumed to be 40 nm for both DC-SF and BiCS/TCAT. And, in this design rule, the high coupling ratio of 0.60 can still be obtained in the structure of a_1 = 15 nm, a_2 = 23 nm, a_3 = 50 nm, h = 30 nm, and d = 12 nm; that is, FG width = $(a_3 - a_2)$ = 27 nm, FG height = h = 30 nm, and radius of channel = a_1 = 15 nm. Even if the physical cell size of the DC-SF cell is larger than that of conventional BiCS/TCAT, the effective cell size of the DC-SF can be comparable with BiCS/TCAT, because multilevel cells (2 bits/cell, 3 bits/cell, and 4 bits/cell) are available due to wide cell V_t window and negligible FG–FG coupling interference.

7.7 ADVANCED DC-SF CELL

7.7.1 Improvement on DC-SF Cell

Floating-gate (FG)-type DC-SF 3D NAND flash memory cell was proposed [24, 26], as shown in Fig. 7.56. (Section 7.6) to overcome the intrinsic disadvantages of the charge-trap-type 3D cell. However, in the DC-SF cell process [24, 26], there were

Micron Ex. 1014, p. 336
Micron v. YMTC
IPR2025-00119

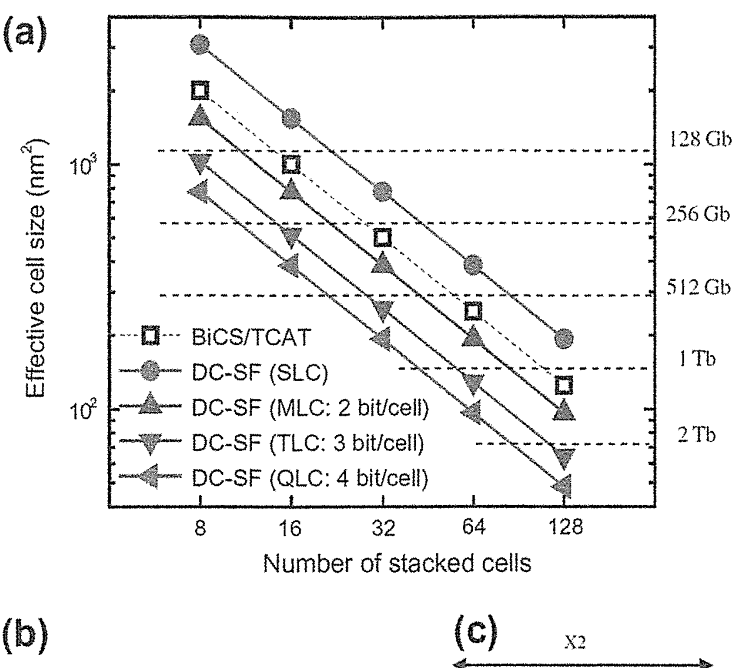

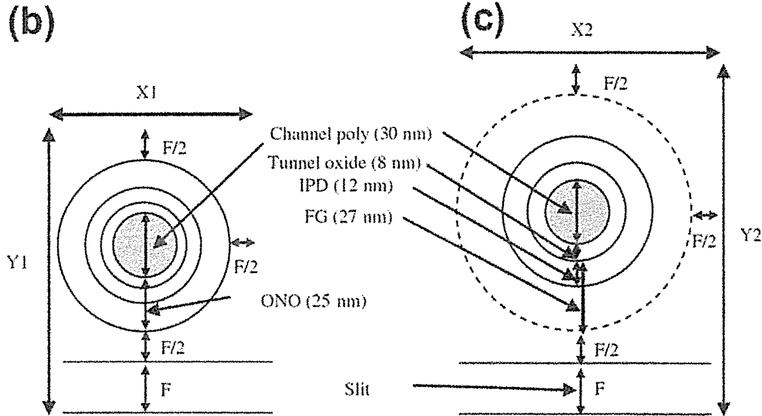

FIGURE 7.67 (a) Effective cell sizes for the DC-SF NAND flash cell. The DC-SF cell can be realized for 1 Tb with 3 bits/cell + 64 cells stacked, 2 Tb with 3 bits/cell + 128 cells stacked. (b) Assumption of cell size for BiCS ($F = 40$ nm, cell-to-cell distance: $F/2$, slit distance: F, $X1 * Y1 = 100 * 160\ \text{nm}^2$). (c) Assumption of cell size for DC-SF ($F = 40$ nm, cell-to-cell distance: $F/2$, slit distance: F, $X2 * Y2 = 130 * 190\ \text{nm}^2$).

still several critical problems, as shown in Fig. 7.68b, namely (1) high word-line resistance of the poly gate, (2) damage on IPD ONO by the FG separation process, and (3) field confinement at the FG edge during programming due to the horn shape FG. And also, read and program operations of the DC-SF cell had not been optimized yet, resulting in causing several disturb problems.

In Section 7.7, a novel metal control gate last process (MCGL process) [27, 28], new read scheme [25, 28], and new program schemes [28] for the DC-SF cell are introduced. Excellent performance and reliability of the DC-SF cell could be realized.

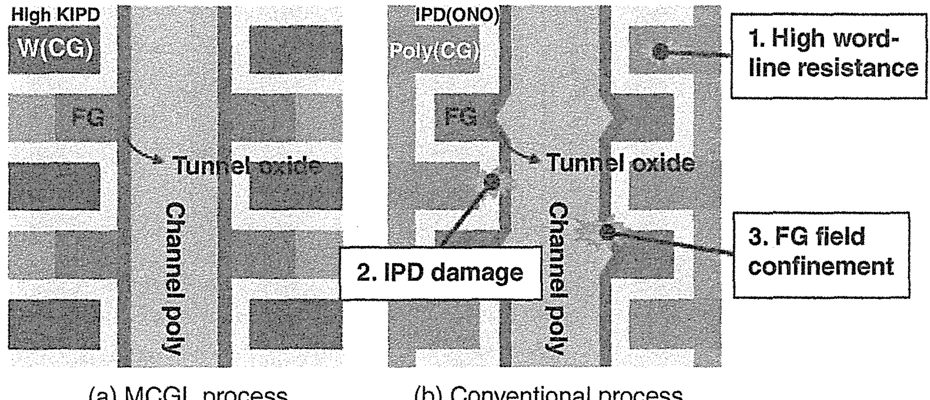

FIGURE 7.68 The DC-SF cell profile comparison. (a) MCGL (metal control gate last) process. (b) Conventional process. In (b) conventional process, there are several problems, such as (1) high word-line resistance, (2) IPD damage during FG separation process, and (3) FG field confinement due to the horn shape FG. The new MCGL process can solve all of these problems.

7.7.2 MCGL Process

The new MCGL (metal control gate last) process sequence of the DC-SF cell is described in Fig. 7.69 [27]. First, the multiple silicon oxide/nitride layers are deposited on N+/*p*-Si substrate. Next, the channel hole is patterned, and FGs are formed at oxide recess portion by isotropic poly etching (Fig. 7.69a). Tunnel oxide is deposited, and the channel contact hole is formed by etching through N+ layers to connect substrate and channel poly-Si directly (Fig. 7.69b). After channel poly-Si deposition, gates are patterned (Fig. 7.69c). Then stacked silicon nitride has recessed (Fig. 7.69d), and high-*k* IPD films are deposited on the FGs. After that, tungsten (W) film is deposited and separated to each stacked layers, as shown in Fig. 7.69e. Figure 7.70 shows the cross-sectional TEM image of the DC-SF cell arrays, fabricated by the MCGL process.

In this MCGL process, (1) low word-line resistance can be obtained by gate replacement process (SiN→W). And (2) IPD damage of FG separation process can be avoided due to IPD deposited after FG/channel-poly formation, in contrast with conventional process of ONO IPD before FG separation [24,26]. And also, (3) FG field confinement at FG edge during programming can be suppressed due to better FG shape by no IPD deposition before FG formation, as shown in Fig. 7.70b.

7.7.3 New Read Scheme

Conventional read operation of the DC-SF NAND flash string is to apply the read voltage V_R to two neighbor CGs of the selected FG, while $V_{\text{pass-read}}$ is applied to unselected CGs [24,26]. In order to investigate read operation issues in conventional read,

Micron Ex. 1014, p. 338
Micron v. YMTC
IPR2025-00119

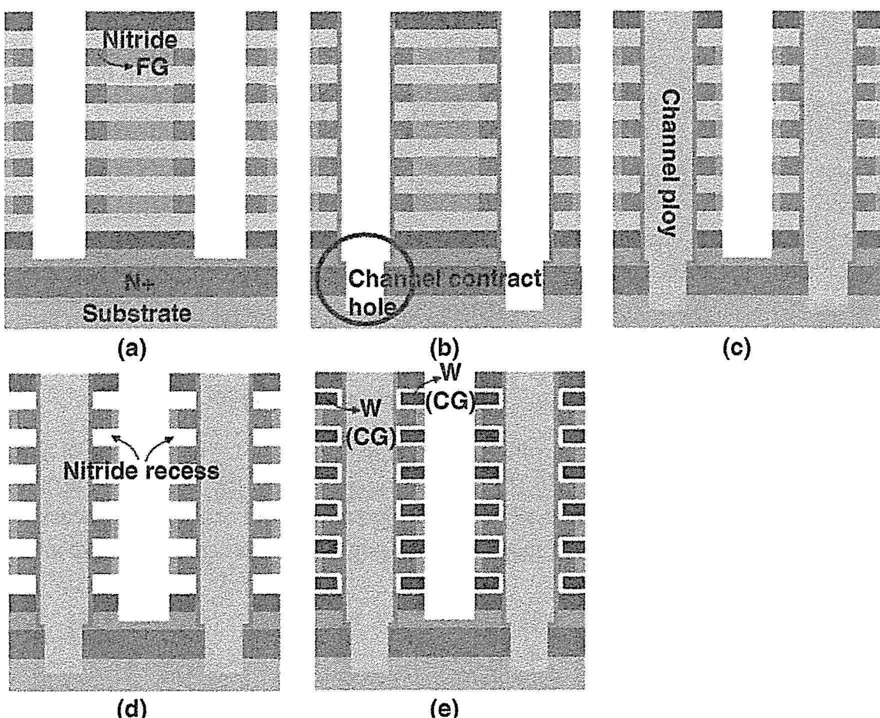

FIGURE 7.69 MCGL process sequence of the DC-SF NAND flash cell. (a) FG formation, (b) channel contact formation, (c) gate patterning, (d) nitride recess, (e) high-k IPD deposition and tungsten W (CG) formation.

the FG1 stored charge dependence has been investigated in several read conditions by TCAD simulation [25], as shown in Fig. 7.71.

Two unexpected characteristics are observed, as shown in Fig. 7.72. One is that selected cell V_t (FG0 and FG2 read) have shifted up when neighbor FG1 charge is negatively increased. This is because a transconductance is degraded due to increasing channel resistance under FG1, which stored negative charges, as shown in Fig. 7.73.

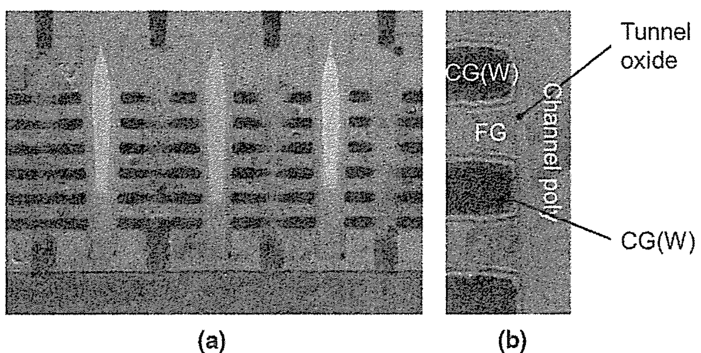

FIGURE 7.70 TEM image of (a) the MCGL process DC-SF cell array and (b) the FG/CG shape. The cell structure is showing a preferable vertical FG shape.

Micron Ex. 1014, p. 339
Micron v. YMTC
IPR2025-00119

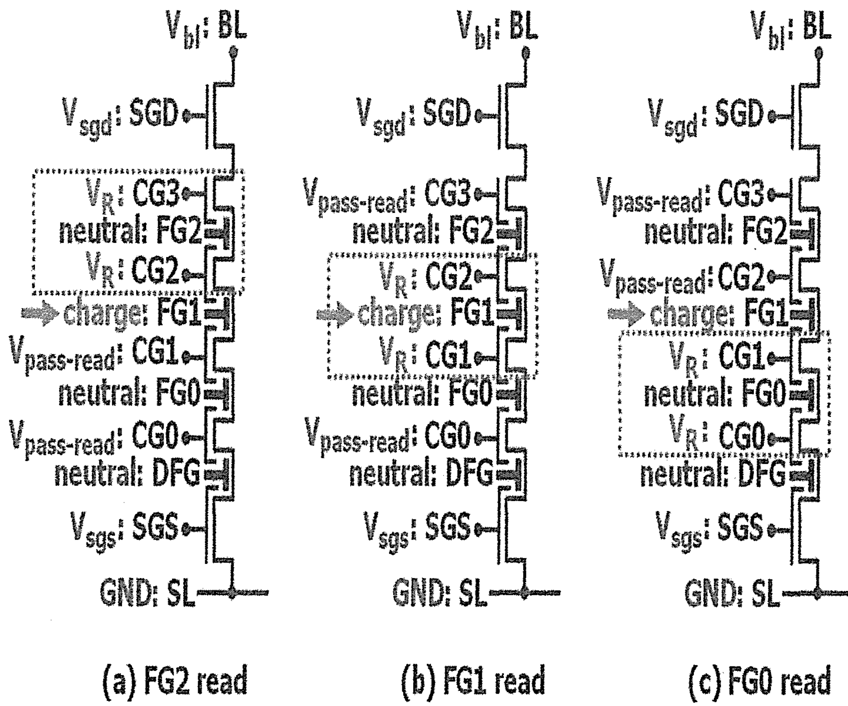

FIGURE 7.71 Conventional read operations. (a) FG2 read operation (CG2&3 VR), (b) FG1 read operation (CG1&2 VR), and (c) FG0 read operation (CG0&1 VR). Charges in FG1 are set to be various amounts to derive the FG charge dependence.

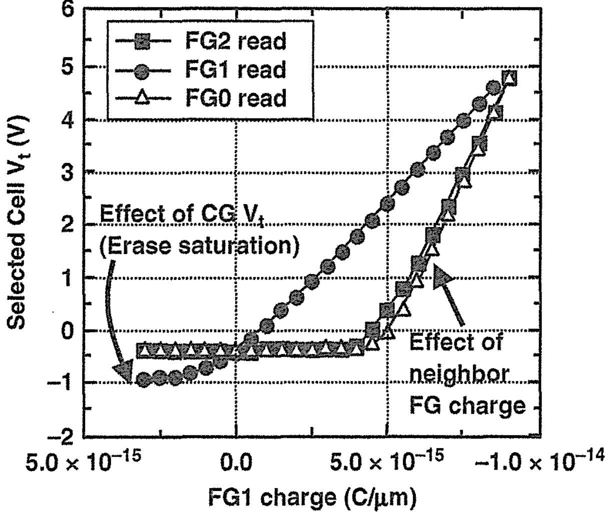

FIGURE 7.72 Simulated selected cell V_t of FG0, FG1, and FG2 read under various FG1 charges, as shown in Fig. 7.71.

Micron Ex. 1014, p. 340
Micron v. YMTC
IPR2025-00119

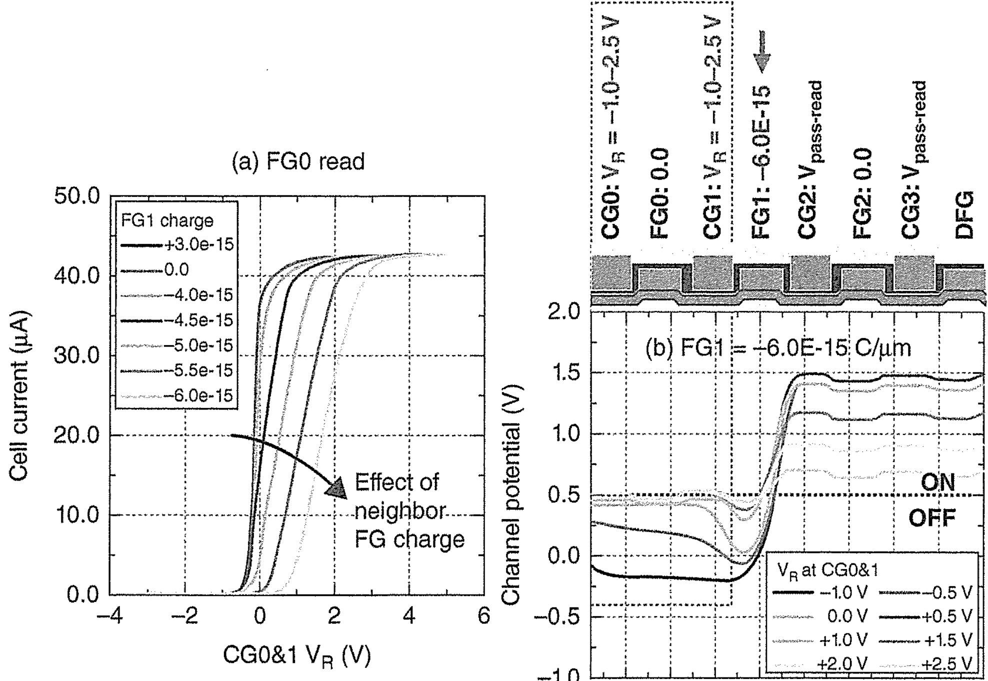

FIGURE 7.73 (a) Cell I_d–V_g of FG0 read under various FG1 charge. (b) Channel potential at FG1 = −6.0E-15 C/μm. When FG1 has a negative charge, the transconductance is degraded due to increasing channel resistance under FG1.

The selected cell V_t (FG0 or FG2) cannot be read correctly when FG1 is negatively charged ($>-5 \times 10^{-15}$C/μm).

The other is that selected cell V_t (FG1 read) saturates when selected FG1 charge is positively increased (erase saturation phenomena). This is because CG V_t limits the selected cell V_t, as shown in Fig. 7.74. Two neighbors CG1 and CG2 turn the channel "off" directly, even when FG1 is positively charged.

In order to derive a proper read operation, a simple capacitor network model is used, as shown in Fig. 7.75 [25].

Analytic expression of the FG1 potential is derived in Eq. (7.3). V_{FG1} is determined by the average bias of two neighbor CGs (V_{CG1} and V_{CG2}), stored charge (σ_{FG1}) in FG1, and the coupling ratio α as written in Eq. (7.4).

$$V_{\mathrm{FG1}} = \alpha \left(\frac{V_{\mathrm{CG1}} + V_{\mathrm{CG2}}}{2} - V_{\mathrm{T,FG1}} \right) \tag{7.3}$$

$$\alpha = \frac{2C_1}{2C_1 + C_2} \tag{7.4}$$

$$V_{T,\mathrm{FG1}} = -\frac{\sigma_{\mathrm{FG1}}}{2C_1} \tag{7.5}$$

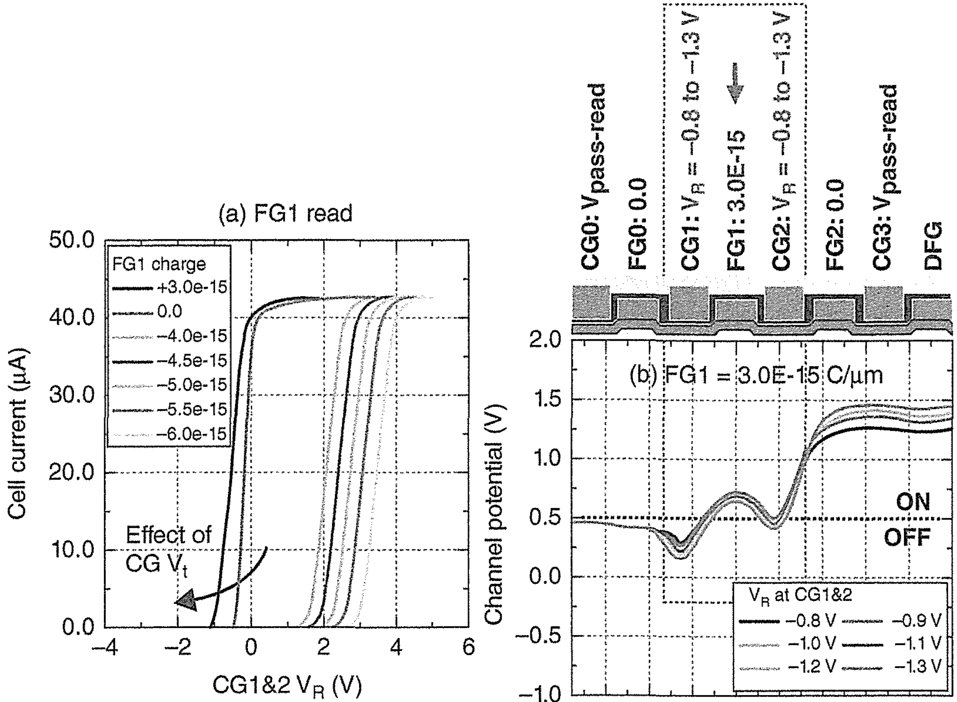

FIGURE 7.74 (a) Cell I_d–V_g of FG1 read under various FG1 charge. (b) Channel potential at FG1 = 3.0E-15 C/μm. The erase V_t saturation is caused by channel off state under CG1 and CG2.

The FG1 potential V_{FG1} during FG0 read operation can be described as Eq. (7.6) by substituting V_{CG1} and V_{CG2} with V_R and $V_{pass\text{-}read}$, respectively.

$$V_{FG1} = \alpha\left(\frac{V_R + V_{pass\text{-}read}}{2} - V_{T,FG1}\right) \quad (7.6)$$

Because V_R is predetermined value for cell read operation, the potential decrease of the FG1 due to stored negative charge ($\Delta V_{T,FG1} = -\sigma_{FG1}/2C_1$) have to be compensated by increasing $V_{pass\text{-}read}$ to keep the FG1 cell "ON" as pass transistor. Therefore, increasing $\Delta V_{pass\text{-}read}$ is determined quantitatively as written in Eq. (7.7). σ_{FG1_max} is the allowed maximum negative charge (allowed highest V_t).

$$\Delta V_{pass\text{-}read} = 2\Delta V_{T,FG1} = -\frac{\sigma_{FG1-max}}{C_1} \quad (7.7)$$

Equation (7.7) had confirmed $V_{pass\text{-}read}$ dependence in various FG1 charges (various $V_{T,FG1}$), as shown in Fig. 7.76. V_{pass_read2} have to increase 4 V to compensate a 2-V V_t increase of the neighbor FG1 cell. This strongly corresponds to Eq. (7.7).

Most of NAND devices are currently adopting multilevel cell (MLC) operation, which is using three read voltages (V_Rs) to identify each program levels, as shown

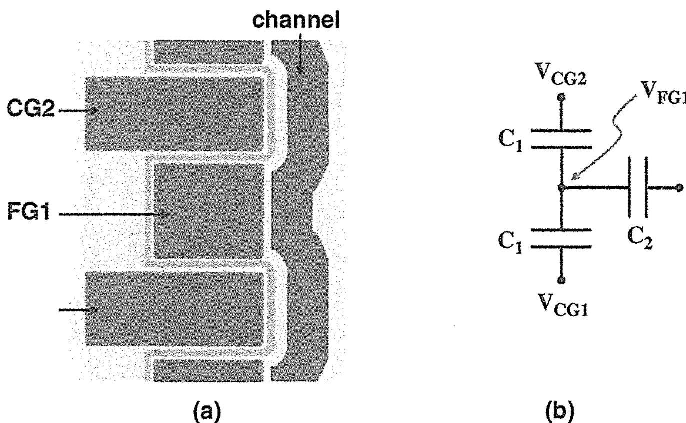

FIGURE 7.75 (a) Cross-sectional view of the DC-SF NAND unit cell. (b) Corresponding equivalent capacitor network.

in Fig. 7.77. For each V_R for PV1,2,3 read, $V_{\text{pass-read2}}$ and $V_{\text{pass-read1}}$ (see Fig. 7.76a) should be different voltages to compensate neighbor FG1 potential.

$V_{\text{pass-read2}}$ compensates V_R change and $\sigma_{\text{FG1_max}}$, as described in Eq. (7.8), which is derived the same way as Eq. (7.7).

$$\Delta V_{\text{pass-read2}} = -\Delta V_R - \frac{\sigma_{\text{FG-max}}}{C_1} \tag{7.8}$$

And also, in order to maintain that all unselected FG cells are "ON" even if the cells are in high V_t (PV3) as the worst case, $V_{\text{pass-read1}}$ has to be equal to V_R (Eq. (7.9)).

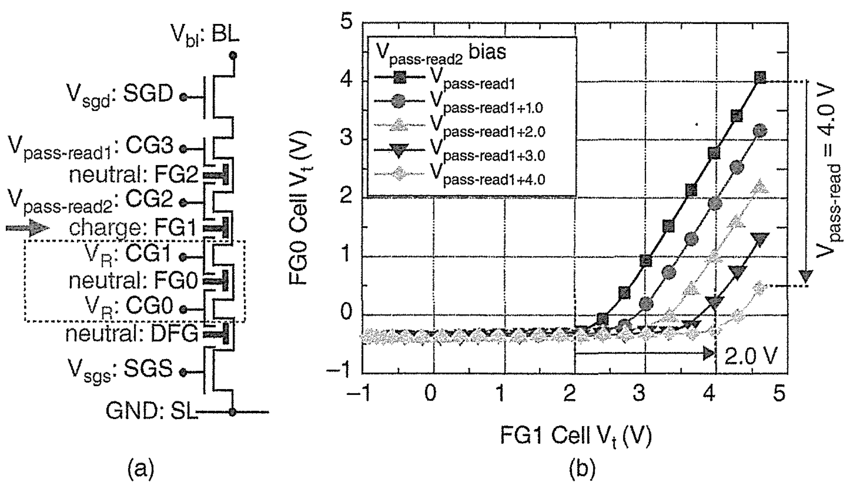

FIGURE 7.76 (a) FG0 read operation. (b) FG0 cell V_t under several $V_{\text{pass-read2}}$ conditions. $V_{\text{pass-read1}} = 5.0$ V.

Micron Ex. 1014, p. 343
Micron v. YMTC
IPR2025-00119

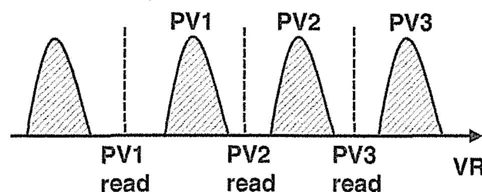

FIGURE 7.77 Multilevel cell (MLC) read operation.

This is because $V_R + V_{\text{pass-read2}}$ for FG1 should be equal to $V_{\text{pass-read2}} + V_{\text{pass-read1}}$ for FG2 (see Fig. 7.76a).

$$V_{\text{pass-read1}} = V_R \tag{7.9}$$

Figure 7.78 shows the new read condition of the MLC DC-SF NAND cell, which is from Eqs. (7.8) and (7.9). $V_{\text{pass-read2}}$ has to be decreased as V_R is increased; conversely, $V_{\text{pass-read1}}$ has to be increased as V_R is increased. And in region of $V_R =$ 0–1 V, $V_{\text{pass-read1}}$ is a used fixed voltage of 1.0 V, because the CG voltage has to turn channel "ON," as described in Fig. 7.74. The new multilevel read operation condition is summarized in Table 7.3.

7.7.4 New Programming Scheme

The programming scheme of the DC-SF cell has to be optimized to avoid program disturb problems. Figure 7.79 describes program disturb modes (inhibit modes) of DC-SF cell. There are two inhibit modes; mode (A), electron injection mode; and

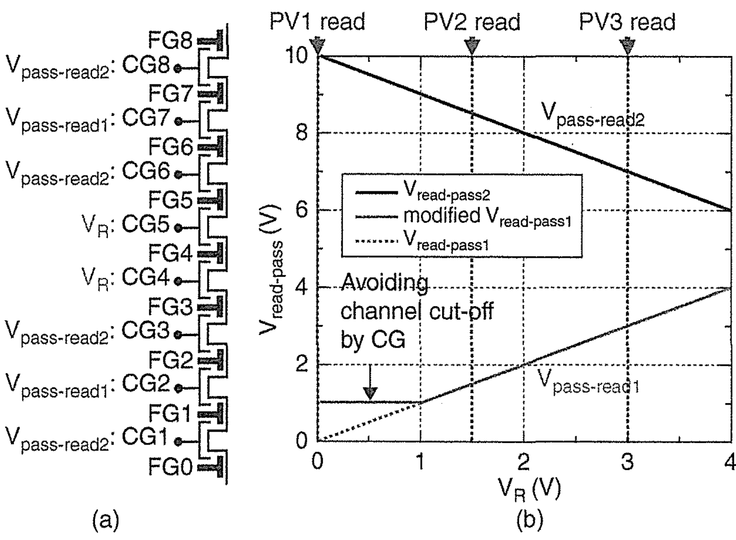

FIGURE 7.78 (a) New read operation of DC-SF NAND string. (b) $V_{\text{pass-read1\&2}}$ dependence on V_R, as shown in Eqs. (7.8) and (7.9).

Micron Ex. 1014, p. 344
Micron v. YMTC
IPR2025-00119

TABLE 7.3 The new read scheme of DC-SF NAND string

Electrode		PV1 read $V_R = 0.0$ V	PV2 read $V_R = 1.5$ V	PV3 read $V_R = 3.0$ V
CG8	$V_{\text{pass-read2}}$	10.0 V	8.5 V	7.0 V
CG7	$V_{\text{pass-read1}}$	1.0 V	1.5 V	3.0 V
CG6	$V_{\text{pass-read2}}$	10.0 V	8.5 V	7.0 V
CG5 CG4	V_R	0.0 V	1.5 V	3.0 V
CG3	$V_{\text{pass-read2}}$	10.0 V	8.5 V	7.0 V
CG2	$V_{\text{pass-read1}}$	1.0 V	1.5 V	3.0 V
CG1	$V_{\text{pass-read2}}$	10.0 V	8.5 V	7.0 V

mode (B), charge loss mode. Mode (A) is a conventional program inhibit mode, which has a weak electron injection stress, caused by a high field in tunnel oxide due to FG coupled with two CGs (e.g., V_{pass_n+2} and V_{pgm_n+1}). Mode (A) becomes severe in the case of the lower V_t (e.g., erase state) due to a high field of tunnel oxide. On the other hand, mode (B) is a new charge loss mode that is unique in the DC-SF cell. Electrons in FG are ejected to CG by a high field in IPD. Mode (B) become severe in the case of high cell V_t (e.g., PV3 state, such as $V_t = 4$ V) and low V_{pass_n-2}. In order to minimize program disturb, V_{pass_n-2} and V_{pass_n+2} have to be optimized.

Figure 7.80 shows the measurement results of mode (B), which is accelerated by thin IPD (oxide equivalent 12 nm thick). V_t is decreased as V_{pgm_n-1} is increased and as V_{pass_n-2} is decreased. From this data, the maximum allowed electric field in IPD is estimated to 8.3 MV/cm from conditions of $V_{\text{pgm}_n-1} = 15$ V, $V_{\text{pass}_n-2} = 5$ V, and $V_t = 4$ V.

Figure 7.81 shows the potential differences among FG/CG/substrate during programming ($V_{\text{pgm}} = 15$ V) in the case of (a) $V_t = -1$ V and (b) $V_t = 4$ V. The potential difference between FG and substrate (V_{fg_sub}) becomes large as V_{pass_n-2}, V_{pass_n+2} are increased. In (a) $V_t = -1$ V, V_{fg_sub} reaches to the mode (A) limitation (criteria) of 7 V at V_{pass_n-2}, $V_{\text{pass}_n+2} = 1$ V. Then, in (a) $V_t = -1$ V, V_{pass_n-2} and V_{pass_n+2}

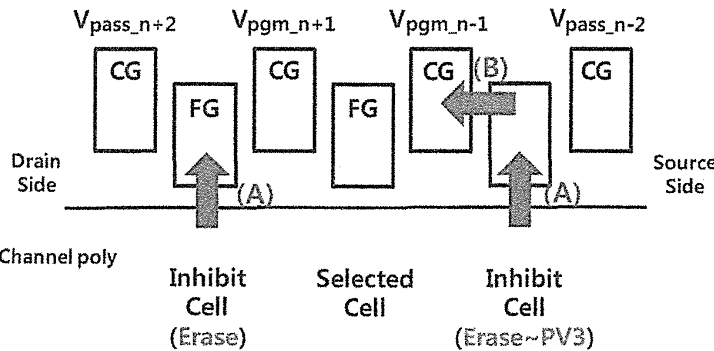

FIGURE 7.79 Two program inhibit modes of DC-SF cell. Mode (A), electron injection mode; weak electron injection from substrate to FG due to high field on tunnel oxide. Mode (B), charge loss mode; electron emission from FG to CG due to high field on IPD.

Micron Ex. 1014, p. 345
Micron v. YMTC
IPR2025-00119

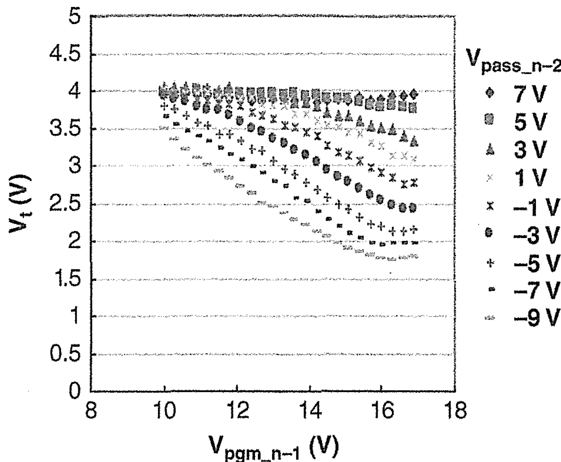

FIGURE 7.80 Measured charge loss of the mode (B) during programming of DC-SF cell. Charge loss (electron emission) from FG to CG is increased as increasing $V_{\text{pgm_n-1}}$ and decreasing $V_{\text{pass_n-2}}$.

have to be less than 1 V to keep $V_{\text{fg_sub}} < 7$ V. And in (b) $V_t = 4$ V, the potential difference between CG and FG ($V_{\text{cg1_fg}}$) reach the mode (B) limitation of 12.5 V at $V_{\text{pass_}n\text{-2}} = -2$ V. The limitation is determined by the maximum allowed electric field of 8.3 MV/cm in mode (B) in the case of IPD thickness = 15 nm. Then, in (b) $V_t = 4$ V, $V_{\text{pass_}n\text{-2}}$ has to be more than −2 V to keep $V_{\text{cg1_fg}} < 12$ V. Mode (B) is located only in source side inhibit cell (right-side inhibit cell in Fig. 7.79). Therefore, $V_{\text{pass_}n\text{-2}}$ has to be in the range of −2 V to 1 V, and $V_{\text{pass_}n+2}$ has to be less than 1 V, because the drain-side inhibit cell (left-side inhibit cell in Fig. 7.79) is only in the case of low V_t (erase state).

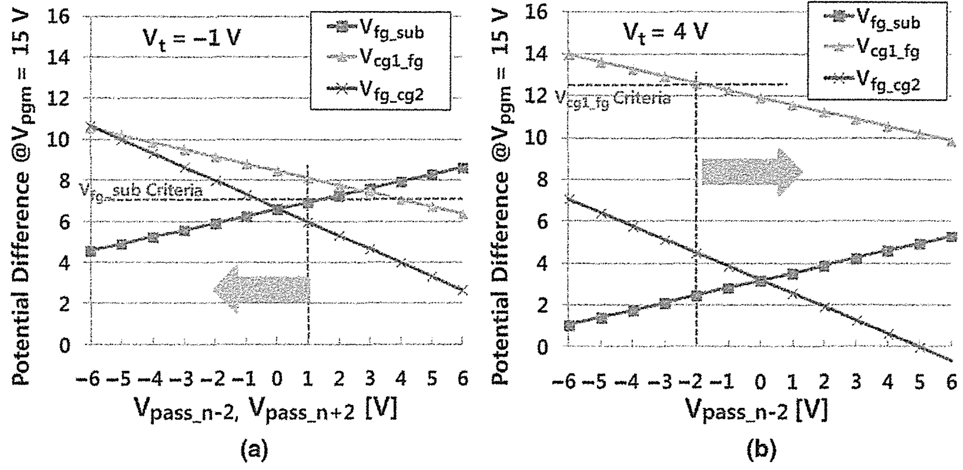

FIGURE 7.81 The potential difference among FG/CG/substrate during programming in the case of (a) $V_t = -1$ V and (b) $V_t = 4$ V. In (a) $V_t = -1$ V, maximum $V_{\text{pass_}n\text{-2}}/V_{\text{pass_}n+2}$ is determined to be 1 V by the criteria of mode (A). And, in (b) $V_t = 4$ V, minimum $V_{\text{pass_}n\text{-2}}/V_{\text{pass_}n+2}$ is determined to be −2 V by the criteria of mode (B).

Micron Ex. 1014, p. 346
Micron v. YMTC
IPR2025-00119

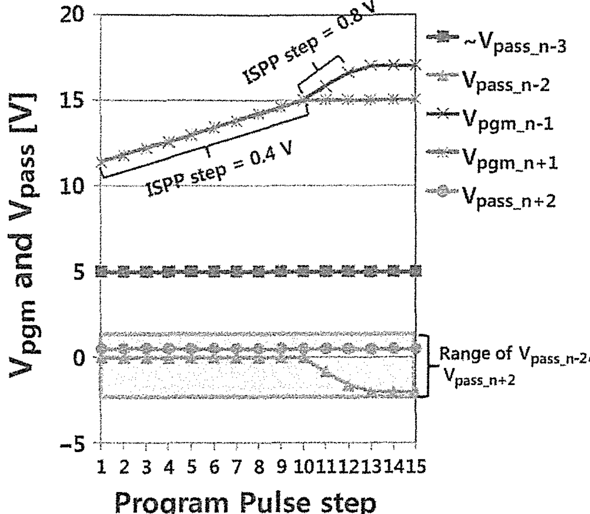

FIGURE 7.82 The proposed program scheme of the DC-SF cell.

Figure 7.82 shows one example of a new ISPP program scheme for the DC-SF cell. V_{pgm}s ($V_{pgm_n\text{-}1}$ and V_{pgm_n+1}) are incrementally stepped up (ISPP) using 0.4-V steps until reaching 15 V. And if more program pulses are needed, $V_{pgm_n\text{-}1}$ is stepped up using 0.8-V steps and V_{pass_n-2} has stepped down using −0.8-V steps in order to prevent mode (A) at the right-side inhibit cell in Fig. 7.79. V_{pgm_n+1} maintains 15 V, and then V_{pass_n+2} can be kept at a positive voltage of 0.5–1.0 V to transfer bit-line voltage (0 V) for programming cells.

The coupling ratio of DC-SF cell is sensitive with the channel diameters [26], which are normally large at top-side cells and small at bottom-side cells. Then, the programming voltage and inhibit voltage would need to be optimized by matching with the coupling ratio for each cell layer.

Figure 7.83 shows the program disturbance of neighbor cells. Almost no V_t shift is observed in neighbor cells because optimized V_{pass} for neighbor cell are used during programming.

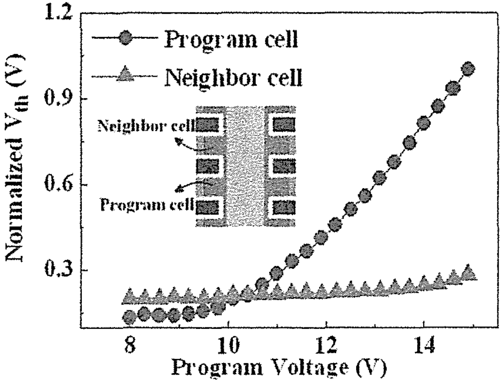

FIGURE 7.83 Program disturbance of neighbor cell. Low $V_{pass_n\text{-}2}$ = 1 V is used.

Micron Ex. 1014, p. 347
Micron v. YMTC
IPR2025-00119

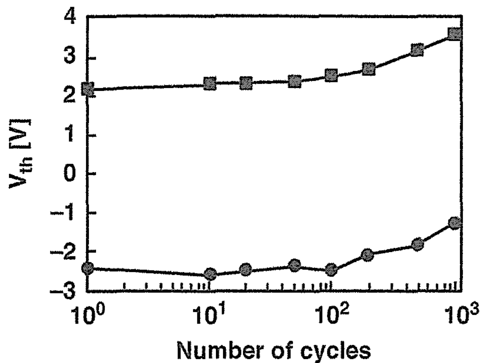

FIGURE 7.84 Program/erase cycling endurance characteristics of the DC-SF cell.

7.7.5 Reliability

Program/erase cycling endurance characteristics are shown in Fig. 7.84. The V_{th} shift after cycling is small, less than 1.3 V even after 1K cycles. Data retention characteristic is also evaluated. The PV3 V_{th} shift of 60 mV after 250°C 120 min is small, which is comparable with conventional planar 2D FG NAND flash characteristics. Therefore, any serious process damages on tunnel oxide and IPD in DC-SF cells have not been observed in the optimizing MCGL process.

Advanced DC-SF (dual control gate with surrounding floating gate) cell process and operation schemes had been introduced. In order to improve performance and reliability of the DC-SF cell, the new metal control gate last (MCGL) process had been developed. The MCGL process could realize a low resistive tungsten (W) metal word line, a low damage on tunnel oxide/IPD (inter-poly dielectric), and a preferable FG shape. Also, new read and program operation schemes had been developed. In the new read operation, the higher and lower $V_{pass\text{-}read}$ are alternately applied to unselected control gates (CGs) to compensate lowering FG potential to be a pass transistor. And in the new program scheme, the optimized V_{pass} are applied to neighbor WL of selected WL to prevent program disturb and charge loss through IPD. Thus, by using the MCGL process and the new read/program schemes, high performance and high reliability of the DC-SF cell could be realized for 3D NAND flash memories.

REFERENCES

[1] Masuoka, F.; Momodomi, M.; Iwata, Y.; Shirota, R. New ultra high density EPROM and flash EEPROM with NAND structure cell, *Electron Devices Meeting, 1987 International*, vol. 33, pp. 552–555, 1987.

[2] S. Aritome, 3D Flash Memories, International Memory Workshop 2011 (IMW 2011), short course.

[3] Jung, S.-M.; Jang, J.; Cho, W.; Cho, H.; Jeong, J.; Chang, Y.; Kim, J.; Rah, Y.; Son, Y.; Park, J.; Song, M.-S.; Kim, K.-H.; Lim, J.-S.; Kim, K. Three dimensionally stacked NAND flash memory technology using stacking single crystal Si layers on ILD and

Micron Ex. 1014, p. 348
Micron v. YMTC
IPR2025-00119

TANOS structure for beyond 30 nm node, *Electron Devices Meeting, 2006. IEDM '06. International*, pp. 1–4, 11–13 Dec. 2006.

[4] Park, K.-T.; Kim, D.; Hwang, S.; Kang, M.; Cho, H.; Jeong, Y.; Seo, Y.-l.; Jang, J.; Kim, H.-S.; Jung, S.-M.; Lee, Y.-T.; Kim, C.; Lee, W.-S., A 45 nm 4 Gb 3-dimensional double-stacked multi-level NAND flash memory with shared bitline structure, *Solid-State Circuits Conference, 2008. ISSCC 2008. Digest of Technical Papers. IEEE International*, pp. 510, 632, 3–7 Feb. 2008.

[5] Park, K.-T.; Kang, M.; Hwang, S.; Kim, D.; Cho, H.; Jeong, Y.; Seo, Y.-l.; Jang, J.; Kim, H.-S.; Lee, Y.-T.; Jung, S.-M.; Kim, C. A fully performance compatible 45 nm 4-gigabit three dimensional double-stacked multi-level NAND flash memory with shared bit-line structure, *Solid-State Circuits, IEEE Journal of*, vol. 44, no. 1, pp. 208, 216, Jan. 2009.

[6] Lai, E.-K.; Lue, H.-T.; Hsiao, Y.-H.; Hsieh, J.-Y.; Lu, C.-P.; Wang, S.-Y.; Yang, L.-W.; Yang, T.; Chen, K.-C.; Gong, J.; Hsieh, K.-Y.; Liu, R.; Lu, C.-Y. A multi-layer stackable thin-film transistor (TFT) NAND-type flash memory, *Electron Devices Meeting, 2006. IEDM '06. International*, pp. 1–4, 11–13 Dec. 2006.

[7] Endoh, T.; Kinoshita, K.; Tanigami, T.; Wada, Y.; Sato, K.; Yamada, K.; Yokoyama, T.; Takeuchi, N.; Tanaka, K.; Awaya, N.; Sakiyama, K.; Masuoka, F. Novel ultra high density flash memory with a stacked-surrounding gate transistor (S-SGT) structured cell, *Electron Devices Meeting, 2001. IEDM '01. Technical Digest International*, pp. 2.3.1–2.3.4, 2001.

[8] Endoh, T.; Kinoshita, K.; Tanigami, T.; Wada, Y.; Sato, K.; Yamada, K.; Yokoyama, T.; Takeuchi, N.; Tanaka, K.; Awaya, N.; Sakiyama, K.; Masuoka, F. Novel ultrahigh-density flash memory with a stacked-surrounding gate transistor (S-SGT) structured cell, *Electron Devices, IEEE Transactions on*, vol. 50, no. 4, pp. 945, 951, April 2003.

[9] F. Masuoka, Forbes Global, *Forbes Magazine*, New York, 24 June 2002, 26 pp.

[10] Tanaka, H.; Kido, M.; Yahashi, K.; Oomura, M.; Katsumata, R.; Kito, M.; Fukuzumi, Y.; Sato, M.; Nagata, Y.; Matsuoka, Y.; Iwata, Y.; Aochi, H.; Nitayama, A. Bit cost scalable technology with punch and plug process for ultra high density flash memory, *VLSI Symposium Technical Digest, 2007*, pp. 14–15.

[11] Nitayama, A.; Aochi, H., Bit cost scalable (BiCS) technology for future ultra high density memories, *VLSI Technology, Systems, and Applications (VLSI-TSA), 2013 International Symposium on*, pp. 1, 2, 22–24 April 2013.

[12] Nitayama, A.; Aochi, H. Bit cost scalable (BiCS) technology for future ultra high density storage memories, *VLSI Technology (VLSIT), 2013 Symposium on*, pp. T60, T61, 11–13 June 2013.

[13] Fukuzumi, Y.; Katsumata, R.; Kito, M.; Kido, M.; Sato, M.; Tanaka, H.; Nagata, Y.; Matsuoka, Y.; Iwata, Y.; Aochi, H.; Nitayama, A. Optimal integration and characteristics of vertical array devices for ultra-high density, bit-cost scalable flash memory, *IEEE IEDM Technical Digest*, pp. 449–452, 2007.

[14] Komori, Y.; Kido, M.; Katsumata, R.; Fukuzumi, Y.; Tanaka, H.; Nagata, Y.; Ishiduki, M.; Aochi, H., Nitayama, A., Disturbless flash memory due to high boost efficiency on BiCS structure and optimal memory film stack for ultra high density storage device, *IEEE IEDM Technical Digest*, pp. 851–854, 2008.

[15] Katsumata, R.; Kito, M.; Fukuzumi, Y.; Kido, M.; Tanaka, H.; Komori, Y.; Ishiduki, M.; Matsunami, J.; Fujiwara, T.; Nagata, Y.; Zhang, L.; Iwata, Y.; Kirisawa, R.; Aochi, H.,

Micron Ex. 1014, p. 349
Micron v. YMTC
IPR2025-00119

Nitayama, A. Pipe-shaped BiCS flash memory with 16 stacked layers and multi-level-cell operation for ultra high density storage devices, *VLSI Symposium Technical Digest, 2009*, pp. 136–137.

[16] Maeda, T.; Itagaki, K.; Hishida, T.; Katsumata, R.; Kito, M.; Fukuzumi, Y.; Kido, M.; Tanaka, H.; Komori, Y.; Ishiduki, M.; Matsunami, J.; Fujiwara, T.; Aochi, H.; Iwata, Y., Watanabe, Y., Multi-stacked 1G cell/layer pipe-shaped BiCS flash memory, *VLSI Symposium Technical Digest, 2009*, pp. 22–23.

[17] Ishiduki, M.; Fukuzumi, Y.; Katsumata, R.; Kito, M.; Kido, M.; Tanaka, H.; Komori, Y.; Nagata, Y.; Fujiwara, T.; Maeda, T.; Mikajiri, Y.; Oota, S.; Honda, M.; Iwata, Y.; Kirisawa, R.; Aochi, H., Nitayama, A., Optimal device structure for pipe-shaped BiCS flash memory for ultra high density storage device with excellent performance and reliability, *IEEE IEDM Technical Digest*, pp. 625–628, 2009.

[18] Kim, J.; Hong, A. J.; Ogawa, M.; Ma, S.; Song, E. B.; Lin, Y.-S.; Han, J.; Chung, U.-I.; Wang, K. L. Novel 3-D structure for ultra high density flash memory with VRAT (vertical-recess-array-transistor) and PIPE (planarized integration on the same plane), *VLSI Symposium Technical Digest, 2008*, pp. 122–123.

[19] Jang, J. H.; Kim, H.-S.; Cho, W.; Cho, H.; Kim, J.; Shim, S. I.; Jang, Y.; Jeong, J.-H.; Son, B.-K.; Kim, D. W.; Kim, K.; Shim, J.-J.; Lim, J. S.; Kim, K.-H.; Yi, S. Y.; Lim, J.-Y.; Chung, D.; Moon, H.-C.; Hwang, S.; Lee, J.-W.; Son, Y.-H.; Chung, U.-I., Lee, W.-S. Vertical cell array using TCAT (terabit cell array transistor) technology for ultra high density NAND flash memory, *VLSI Symposium Technical Digest, 2009*, pp. 192–193.

[20] Kim, W. J.; Choi, S.; Sung, J.; Lee, T.; Park, C.; Ko, H.; Jung, J.; Yoo, I., and Park, Y., Multi-layered vertical gate NAND flash overcoming stacking limit for terabit density storage, *VLSI Symposium Technical Digest, 2009*, pp. 188–189.

[21] Kim, J.; Hong, A. J.; Sung, M. K.; Song, E. B.; Park, J. H.; Han, J.; Choi, S.; Jang, D.; Moon, J.-T.; Wang, K. L. Novel vertical-stacked-array-transistor (VSAT) for ultra-high-density and cost-effective NAND flash memory devices and SSD (solid state drive), *VLSI Technology, 2009 Symposium on*, pp. 186, 187, 16–18 June 2009.

[22] Hsiao, Y.-H.; Lue, H.-T.; Hsu, T.-H.; Hsieh, K.-Y.; Lu, C.-Y., A critical examination of 3D stackable NAND flash memory architectures by simulation study of the scaling capability, *IMW, 2010*, pp. 142–145, 2010.

[23] Hsu, T.-H.; Lue, H.-T.; Hsieh, C.-C.; Lai, E.-K.; Lu, C.-P.; Hong, S.-P.; Wu, M.-T.; Hsu, F. H.; Lien, N. Z.; Hsieh, J.-Y.; Yang, L.-W.; Yang, T.; Chen, K.-C.; Hsieh, K.-Y.; Liu, R.; Lu, C.-Y. Study of sub-30 nm thin film transistor (TFT) charge-trapping (CT) devices for 3D NAND flash application, *IEEE IEDM Technical Digest*, pp. 629–632, 2009.

[24] Whang, S. J.; Lee, K. H.; Shin, D. G.; Kim, B. Y.; Kim, M. S.; Bin, J. H.; Han, J. H.; Kim, S. J.; Lee, B. M.; Jung, Y. K.; Cho, S. Y.; Shin, C. H.; Yoo, H. S.; Choi, S. M.; Hong, K.; Aritome, S.; Park, S. K., Hong, S. J. Novel 3-dimensional dual control-gate with surrounding floating-gate (DC-SF) NAND flash cell for 1tb file storage application, *IEEE IEDM Technical Digest*, pp. 668–671, 2010.

[25] Yoo, H. S. ; Choi, E. S.; Joo, H. S.; Cho, G. S.; Park, S. K.; Aritome, S.; Lee, S. K.; Hong, S. J. New read scheme of variable $V_{pass\text{-}read}$ for dual control gate with surrounding floating gate (DC-SF) NAND flash cell, *Memory Workshop (IMW), 2011 3rd IEEE International*, pp. 1–4, 22–25 May 2011.

[26] Aritome, S.; Whang, S. J.; Lee, KiH.; Shin, D. G.; Kim, B. Y.; Kim, M. S.; Bin, J. H.; Han, J. H.; Kim, S. J.; Lee, B. M.; Jung, Y. K.; Cho, S. Y.; Shin, C. H.; Yoo, H. S.; Choi, S. M.; Hong, K.; Park S. K.; Hong, S. J. A novel three-dimensional dual control-gate with

Micron Ex. 1014, p. 350
Micron v. YMTC
IPR2025-00119

surrounding floating-gate (DC-SF) NAND flash cell original research article, *Solid-State Electronics*, vol. 79, pp. 166–171, Jan. 2013.

[27] Noh, Y.; Ahn, Y.; Yoo, H.; Han, B.; Chung, S.; Shim, K.; Lee, K.; Kwak, S.; Shin, S.; Choi, I.; Nam, S.; Cho, G.; Sheen, D.; Pyi, S.; Choi, J.; Park, S.; Kim, J.; Lee, S.; Aritome, S.; Hong, S.; Park, S. A new metal control gate last process (MCGL process) for high performance DC-SF (dual control gate with surrounding floating gate) 3D NAND flash memory, *VLSI Technology (VLSIT), 2012 Symposium on*, pp. 19–20, 12–14 June 2012.

[28] Aritome, S.; Noh, Y.; Yoo, H.; Choi, E. S.; Joo, H. S.; Ahn, Y.; Han, B.; Chung, S.; Shim, K.; Lee, K.; Kwak, S.; Shin, S.; Choi, I.; Nam, S.; Cho, G.; Sheen, D.; Pyi, S.; Choi, J.; Park, S.; Kim, J.; Lee, S.; Hong, S.; Park, S.; Kikkawa, T. Advanced DC-SF cell technology for 3-D NAND flash, *Electron Devices, IEEE Transactions on*, vol. 60, no. 4, pp. 1327–1333, April 2013.

[29] Choi, E.-S.; Park, S.-K., Device considerations for high density and highly reliable 3D NAND flash cell in near future, *Electron Devices Meeting (IEDM), 2012 IEEE International*, pp. 9.4.1–9.4.4, 10–13 Dec. 2012.

[30] Takato, H.; Sunouchi, K.; Okabe, N.; Nitayama, A.; Hieda, K.; Horiguchi, F.; Masuoka, F. High performance CMOS surrounding gate transistor (SGT) for ultra high density LSIs, *Electron Devices Meeting, 1988. IEDM '88. Technical Digest, International*, pp. 222, 225, 11–14 Dec. 1988.

[31] Pein, H.; Plummer, J. D. "A 3-D sidewall flash EPROM cell and memory array," *Electron Device Letters, IEEE*, vol. 14, no. 8, pp. 415, 417, Aug. 1993.

[32] Pein, H. B.; Plummer, J. D., Performance of the 3-D sidewall flash EPROM cell, *Electron Devices Meeting, 1993. IEDM '93. Technical Digest, International*, pp. 11, 14, 5–8 Dec. 1993.

[33] Pein, H.; Plummer, James D. Performance of the 3-D PENCIL flash EPROM cell and memory array, *Electron Devices, IEEE Transactions on*, vol. 42, no. 11, pp. 1982, 1991, Nov. 1995.

[34] Hsu, T.-H.; Lue, H.-T.; King, Y.-C.; Hsiao, Y.-H.; Lai, S.-C.; Hsieh, K.-Y.; Liu, R.; Lu, C.-Y. Physical model of field enhancement and edge effects of FinFET charge-trapping NAND flash devices, *Electron Devices, IEEE Transactions on*, vol. 56, no. 6, pp. 1235, 1242, June 2009.

[35] Congedo, G.; Arreghini, A.; Liu, L.; Capogreco, E.; Lisoni, J. G.; Huet, K.; Toque-Tresonne, I.; Van Aerde, S.; Toledano-Luque, M.; Tan, C.-L.; Van denbosch, G.; Van Houdt, J. Analysis of performance/variability trade-off in Macaroni-type 3-D NAND memory, *Memory Workshop (IMW), 2014 IEEE 6th International*, pp. 1, 4, 18–21 May 2014.

[36] Toledano-Luque, M.; Degraeve, R.; Roussel, P. J.; Luong, V.; Tang, B.; Lisoni, J. G.; Tan, C.-L.; Arreghini, A.; Van denbosch, G.; Groeseneken, G.; Van Houdt, J. Statistical spectroscopy of switching traps in deeply scaled vertical poly-Si channel for 3D memories, *Electron Devices Meeting (IEDM), 2013 IEEE International*, pp. 21.3.1, 21.3.4, 9–11 Dec. 2013.

[37] Kang, C. S.; Choi, J.; Sim, J.; Lee, C.; Shin, Y.; Park, J.; Sel, J.; Jeon, S.; Park, Y.; Kim, K. Effects of lateral charge spreading on the reliability of TANOS(TaN/AlO/SiN/Oxide/Si) NAND flash memory, *IRPS*, pp. 167–169, 2007.

[38] Cho, W.-s.; Shim, S. I.; Jang, J.; Cho, H.-s.; You, B.-K.; Son, B.-K.; Kim, K.-h.; Shim, J.-J.; Park, C.-m.; Lim, J.-s.; Kim, K.-H.; Chung, D.-w.; Lim, J.-Y.; Moon, H.-C.;

Micron Ex. 1014, p. 351
Micron v. YMTC
IPR2025-00119

Hwang, S.-m.; Lim, H.-s.; Kim, H.-S.; Choi, J.; Chung, C. Highly reliable vertical NAND technology with biconcave shaped storage layer and leakage controllable offset structure, *VLSI Technology (VLSIT), 2010 Symposium on*, pp. 173, 174, 15–17 June 2010.

[39] Park, K.-T.; Han, J.-m.; Kim, D.; Nam, S.; Choi, K.; Kim, M.-S.; Kwak, P.; Lee, D.; Choi, Y.-H.; Kang, K.-M.; Choi, M.-H.; Kwak, D.-H.; Park, H.-w.; Shim, S.-w.; Yoon, H.-J.; Kim, D.; Park, S.-w.; Lee, K.; Ko, K.; Shim, D.-K.; Ahn, Y.-L.; Park, J.; Ryu, J.; Kim, D.; Yun, K.; Kwon, J.; Shin, S.; Youn, D.; Kim, W.-T.; Kim, T.; Kim, S.-J.; Seo, S.; Kim, H.-G.; Byeon, D.-S.; Yang, H.-J.; Kim, M.; Kim, M.-S.; Yeon, J.; Jang, J.; Kim, H.-S.; Lee, W.; Song, D.; Lee, S.; Kyung, K.-H.; Choi, J.-H., 19.5 Three-dimensional 128 Gb MLC vertical NAND flash-memory with 24-WL stacked layers and 50 MB/s high-speed programming, *Solid-State Circuits Conference Digest of Technical Papers (ISSCC), 2014 IEEE International*, pp. 334, 335, 9–13 Feb. 2014.

[40] Park, K.-T.; Nam, S.; Kim, D.; Kwak, P.; Lee, D.; Choi, Y.-H.; Choi, M.-H.; Kwak, D.-H.; Kim, D.-H.; Kim, M.-S.; Park, H.-W.; Shim, S.-W.; Kang, K.-M.; Park, S.-W.; Lee, K.; Yoon, H.-J.; Ko, K.; Shim, D.-K.; Ahn, Y.-L.; Ryu, J.; Kim, D.; Yun, K.; Kwon, J.; Shin, S.; Byeon, D.-S.; Choi, K.; Han, J.-M.; Kyung, K.-H.; Choi, J.-H.; Kim, K. Three-dimensional 128 Gb MLC vertical nand flash memory with 24-WL stacked layers and 50 MB/s high-speed programming, *Solid-State Circuits, IEEE Journal of*, vol. 50, no. 1, pp. 204, 213, Jan. 2015.

[41] Choi, J.; Seol, K. S., 3D approaches for non-volatile memory, *VLSI Technology (VLSIT), 2011 Symposium on*, pp. 178, 179, 14–16 June 2011.

[42] Im, J.-w., Jeong, W.-P.; Kim, D.-H.; Nam, S.-W.; Shim, D.-K.; Choi, M.-H.; Yoon, H.-J.; Kim, D.-H.; Kim, Y.-S.; Park, H.-W.; Kwak, D.-H.; Park, S.-W.; Yoon, S.-M.; Hahn, W.-G.; Ryu, J.-H.; Shim, S.-W.; Kang, K.-T.; Choi, S.-H.; Ihm, J.-D.; Min, Y.-S.; Kim, I.-M.; Lee, D.-S.; Cho, J.-H.; Kwon, O.-S.; Lee, J.-S.; Kim, M.-S.; Joo, S.-H.; Jang, J.-H.; Hwang, S.-W.; Byeon, D.-S.; Yang, H.-J.; Park, K.-T.; Kyung, K.-H.; Choi, J.-H. A 128 Gb 3b/cell V-NAND flash memory with 1Gb/s I/O rate, *Solid-State Circuits Conference Digest of Technical Papers (ISSCC), 2015 IEEE International*, pp. 23–25 Feb. 2015.

[43] Sako, M.; Watanabe, Y.; Nakajima, T.; Sato, J.; Muraoka, K.; Fujiu, M.; Kono, F.; Nakagawa, M.; Masuda, M.; Kato, K.; Terada, Y.; Shimizu, Y.; Honma, M.; Imamoto, A.; Araya, T.; Konno, H.; Okanaga, T.; Fujimura, T.; Wang, X.; Muramoto, M.; Kamoshida, M.; Kohno, M.; Suzuki, Y.; Hashiguchi, T.; Kobayashi, T.; Yamaoka, M.; Yamashita, R. A low-power 64 Gb MLC NAND-flash memory in 15 nm CMOS technology, *Solid-State Circuits Conference Digest of Technical Papers (ISSCC), 2015 IEEE International*, pp. 23–25, Feb. 2015.

[44] Aritome, S. 3D NAND flash memory—full-scale production from 2015, *Semiconductor Storage 2014*, Nikkei Business Publications (in Japanese), pp. 34–45.

[45] Choi, E.-S.; Yoo, N. S.; Joo, H.-S.; Cho, G.-S.; Park, S.-K.; Lee, S.-K. A novel 3D cell array architecture for terra-bit NAND flash memory, *Memory Workshop (IMW), 2011 3rd IEEE International*, pp. 1, 4, 22–25 May 2011.

[46] Kim, W.; Seo, J. Y.; Kim, Y.; Park, S. H.; Lee, S. H.; Baek, M. H.; Lee, J.-H.; Park, B.-G. Channel-stacked NAND flash memory with layer selection by multi-level operation (LSM), *Electron Devices Meeting (IEDM), 2013 IEEE International*, pp. 3.8.1, 3.8.4, 9–11 Dec. 2013.

[47] Lue, H. T.; Hsu, T.-H.; Hsiao, Y.-H.; Hong, S. P.; Wu, M. T.; Hsu, F. H.; Lien, N. Z.; Wang, S.-Y.; Hsieh, J.-Y.; Yang, L.-W.; Yang, T.; Chen, K.-C.; Hsieh, K.-Y.; Lu, C.-Y. A

Micron Ex. 1014, p. 352
Micron v. YMTC
IPR2025-00119

highly scalable 8-layer 3D vertical-gate (VG) TFT NAND flash using junction-free buried channel BE-SONOS device, *VLSI Technology (VLSIT), 2010 Symposium on*, pp. 131, 132, 15–17 June 2010.

[48] Chang, K.-P.; Lue, H.-T.; Chen, C.-P.; Chen, C.-F.; Chen, Y.-R.; Hsiao, Y.-H.; Hsieh, C.-C.; Shih, Y.-H.; Yang, T.; Chen, K.-C.; Hung, C.-H.; Lu, C.-Y. Memory architecture of 3D vertical gate (3DVG) NAND flash using plural island-gate SSL decoding method and study of it's program inhibit characteristics, *Memory Workshop (IMW), 2012 4th IEEE International*, pp. 1, 4, 20–23 May 2012.

[49] Chen, C.-P.; Lue, H.-T.; Chang, K.-P.; Hsiao, Y.-H.; Hsieh, C.-C.; Chen, S.-H.; Shih, Y.-H.; Hsieh, K.-Y.; Yang, T.; Chen, K.-C.; Lu, C.-Y. A highly pitch scalable 3D vertical gate (VG) NAND flash decoded by a novel self-aligned independently controlled double gate (IDG) string select transistor (SSL), *VLSI Technology (VLSIT), 2012 Symposium on*, pp. 91, 92, 12–14 June 2012.

[50] Hung, C.-H.; Lue, H.-T.; Hung, S.-N.; Hsieh, C.-C.; Chang, K.-P.; Chen, T.-W.; Huang, S.-L.; Chen, T. S.; Chang, C.-S.; Yeh, W.-W.; Hsiao, Y.-H.; Chen, C.-F.; Huang, S.-C.; Chen, Y.-R.; Lee, G.-R.; Hu, C.-W.; Chen, S.-H.; Chiu, C.-J.; Shih, Y.-H.; Lu, C.-Y., Design innovations to optimize the 3D stackable vertical gate (VG) NAND flash, *Electron Devices Meeting (IEDM), 2012 IEEE International*, pp. 10.1.1, 10.1.4, 10–13 Dec. 2012.

[51] Chen, S.-H.; Lue, H.-T.; Shih, Y.-H.; Chen, C.-F.; Hsu, T.-H.; Chen, Y.-R.; Hsiao, Y.-H.; Huang, S.-C.; Chang, K.-P.; Hsieh, C.-C.; Lee, G.-R.; Chuang, A.; Hu, C.-W.; Chiu, C.-J.; Lin, L. Y.; Lee, H.-J.; Tsai, F.-N.; Yang, C.-C.; Yang, T.; Lu, C.-Y. A highly scalable 8-layer vertical gate 3D NAND with split-page bit line layout and efficient binary-sum MiLC (minimal incremental layer cost) staircase contacts, *Electron Devices Meeting (IEDM), 2012 IEEE International*, pp. 2.3.1, 2.3.4, 10–13 Dec. 2012.

Micron Ex. 1014, p. 353
Micron v. YMTC
IPR2025-00119

8

CHALLENGES OF THREE-DIMENSIONAL NAND FLASH MEMORY

8.1 INTRODUCTION

In Chapter 7, several types of three-dimensional (3D) NAND flash memory cells were introduced. In this chapter, challenges of 3D NAND flash memory are discussed.

First, several types of 3D NAND cells are compared in pros and cons of cell structure, process, and memory cell operation in Section 8.2.

The common challenge items of 3D NAND cells are discussed in Sections 8.3–8.9 to clarify key issues of achieving a lower cost, a better performance, and a reasonable reliability.

Many 3D NAND cells are use a SONOS (Silicon(Gate)–Oxide–Nitride–Oxide–Silicon (substrate)) charge storage structure. The data retention characteristic of SONOS cell has problems of quick charge loss and large V_t shift in retention bake because of charge detrapping through thinner tunnel oxide. In Section 8.3, data retention issues are discussed.

The program disturb mechanisms of 3D NAND cells are much different from that of 2D NAND cells, because cell structure and array architecture are totally changed. The analysis results of program disturb in 3D NAND cells are presented in Section 8.4.

WL capacitance is much increased in the stacked word-line (WL) structure in the 3D NAND cell of BiCS, TCAT (V-NAND), and SMArT, because a plane structure of WL has a large parasitic capacitance. However, WL resistance is decreased due to

Nand Flash Memory Technologies, First Edition. Seiichi Aritome.
© 2016 The Institute of Electrical and Electronics Engineers, Inc. Published 2016 by John Wiley & Sons, Inc.

Micron Ex. 1014, p. 354
Micron v. YMTC
IPR2025-00119

wide WL width. The word-line RC (resistance–capacitance) delay in 3D NAND cell is described in Section 8.5.

The cell current is much decreased in the 3D NAND cell, because channel material is changed from crystal Si (substrate Si) to poly-Si. In Section 8.6, cell current issues in the 3D NAND cell are discussed with channel conduction mechanism, V_G dependence, RTN, back-side trap effect in macaroni channel, and laser anneal process.

In order to reduce bit cost in 3D NAND cell, it is very important to increase the number of stacked cells. In Section 8.7, serious problems of high aspect ratio process and small cell current are discussed in the case of increasing number of stacked cells. And some possible solutions will be presented.

The new structure of the peripheral circuit under cell array is described in Section 8.8. And then, the power consumption issue is presented in Section 8.9.

Finally, the future trend of the 3D NAND cell is discussed in Section 8.10. The lower bit cost can be realized by aggressively increasing number of stacked cells. This will have a big impact on the mass-storage market, such as SSD (solid–state drive) for a consumer and enterprise server for the future.

8.2 COMPARISON OF 3D NAND CELLS

In this chapter, several types of 3D NAND flash memory cells are compared. Figure 8.1 shows the comparison of major 3D NAND flash memory cells, in terms of cell structure, fabrication processes, and operations. For cells, channel structure is

		BICS / P-BiCS	TCAT (V-NAND)	SMArT	VG-NAND	DC-SF
Cell	Channel	Vertical	Vertical	Vertical	Horizontal	Vertical
	Gate Structure	Surrounding (GAA)	Surrounding (GAA)	Surrounding (GAA)	Dual	Surrounding (GAA)
	Charge Storage	SONOS	SONOS (TANOS)	SONOS (TANOS)	SONOS (TANOS)	FG
Process	Stacked Layer	SiO2/ Poly	SiO2/ SiN	SiO2/ SiN	SiO2/ Poly	SiO2/ SiN
	Gate Process	Gate First	Gate Last	Gate Last	Gate Last	Gate Last
	Key Process	Channel Hole RIE	WL Separation	WL Separation	VG Patterning	WL Separation FG Process
Operation	Program	FN	FN	FN	FN	FN
	Erase	FN	FN	FN	FN	FN
	Program Disturb	SG/Dummy-WL Control	SG/Dummy-WL Control	SG/Dummy-WL Control	Z-disturb	Vpass Window
	Erase Speed	Slow	Slow	Slow	Slow	Fair
	P/E cycling	Good	Good	Good	Fair	Fair
	Data Retention	Detrapping / Charge spreading	Detrapping / Charge spreading	Detrapping / Charge spreading	Detrapping / Charge spreading	Detrapping / SILC
	Key	WL RC delay			Layer Selection Scheme	

FIGURE 8.1 Comparison table of major 3D NAND cells for cell structure, process, and operation.

Micron Ex. 1014, p. 355
Micron v. YMTC
IPR2025-00119

categorized into "vertical" or "horizontal." Most 3D cells have a "vertical" channel that is fabricated by channel plug through multi-stacked gate layers. And "vertical" channels have the "surrounding (GAA; gate all around)" gate structure. The "surrounding" gate structure has a better performance of cell current and cutoff current than "dual" gate structure because of a better controllability of channel potential by gate electrode. And also, the surrounding gate SONOS cell should have a better erase performance due to suppressing the electron back tunneling from control gate by a field relaxation in block oxide.

For processes, in the etching (RIE) viewpoint for a stacked layer, a stacked layer of SiO_2/SiN is easier to set in the RIE condition than that of SiO_2/poly(-Si) because of the similar etching condition of dielectric SiO_2 and SiN. However, in the case of SiO_2/SiN, the gate replacement process from SiN to metal tungsten (W) is needed, as shown in Section 7.3. The tungsten (W) word line has to be separated for each word line ("WL separation"). This is a key process in TCAT (V-NAND), SMArT, and DC-SF cells. For the gate process, The "gate last" process has an advantage that can use the same fabrication order of a gate dielectric film as fabrication order of 2D cell. This means that the gate dielectrics are fabricated in order of tunnel oxide, charge storage SiN, blocking dielectric, and gate tungsten (W). In the case of "gate first," the fabrication order becomes the opposite of blocking dielectric, charge storage SiN, tunnel oxide, and then channel poly-Si. The legacy process of 2D cannot be used in the "gate first" process case.

For operations, the mechanism of program and erase operation is basically the same in all 3D cells, however, erase performance is different between charge trap cells (SONOS(TANOS)) and floating gate (FG) cells. SONOS (TANOS) cells have slower erase than floating gate (FG) cells, even electric field enhancement occurs in tunnel oxide during erase. The program disturb conditions and characteristics of 3D cells are greatly changed from that of 2D cells, as described in detail in Section 8.4. The program/erase cycling performance of SONOS cells is inherently better than that of FG cells; however, data retention of SONOS cells is worse than that of FG cells because of initial data loss, as described in Section 8.3.

The effective memory cell size of several 3D NAND cells is calculated and compared, based on assumptions of Fig. 8.2 and Fig. 8.3 [1]. In SONOS or TANOS 3D cells, thickness of gate dielectric ONO (tono) is assumed to have the fixed value of 20-nm thickness. And the size difference of the channel hole between top and bottom in BiCS/TCAT/SMArT/DC-SF is the fixed value of 10 nm (D), regardless of the number of stacked cells. And the size difference of channel poly of VG-NAND between top and bottom is also a fixed value of 10 nm (D). Minimum width (min W) of hole size of BiCS/TCAT/SMArT/DC-SF at bottom or minimum channel poly-Si space at bottom are the fixed value of 20 nm. In DC-SF cells, the width of floating gate (W_{fg}) of 27 nm is added to obtain a sufficient coupling ratio.

Based on these assumptions, effective cell sizes of each cell type were calculated. Cell size, size of X- and Y-direction, physical cell size, and effective cell size of each cell are shown in Fig. 8.3. In VG-NAND cells, the area of source-side select gate is added 3% of cell size, and the area of drain-side select gate is added 3% for each stacked layer to select the channel layer (see Section 7.5).

Micron Ex. 1014, p. 356
Micron v. YMTC
IPR2025-00119

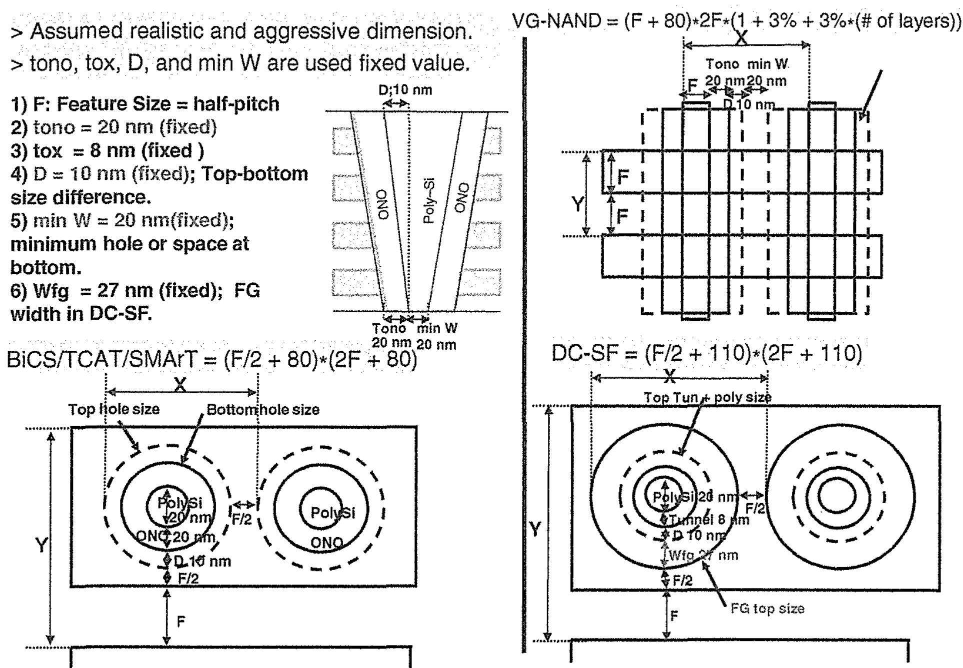

FIGURE 8.2 Assumption of 3D NAND flash memory cell size calculation (1).

Figure 8.4 shows the scaling trend of effective memory cell size in 16 stacked 3D NAND memory cells in comparison with 2D planar FG (P-FG) cells. It can be seen that 3D NAND memory cells cannot be effectively scaled down as feature size is scaled down, in comparison with P-FG MLC (planar FG MLC cells). It means that the increasing number of stacked cells is the only reasonable way to reduce the effective memory cell size in 3D cells.

	Planar-FG	P-BICS/TCAT/SMArT	VG-NAND	DC-SF
Cell Size	1.25*X*Y (= 5F2)	X*Y	X*Y*(1 + 3% + 3%*(# of stacked layer))	X*Y
X [BL pith]	2F	F/2 + 2*t_{ono} + 2*D + min W	F + 2*t_{ono} + 2*D + min W	F/2 + 2*t_{ox} + 2*D + min W + 2*Wfg
Y [WL pitch]	2F	2F + 2*t_{ono} + 2*D + min W	2F	2F + 2*t_{ox} + 2*D + min W + 2*Wfg
Physical Cell Size [nm2] @F = 40 nm	8000	16000	9600	24700
Effective Cell Size @F = 40 nm,16stacked	-------	1000	906	1544 (SLC), 772(MLC)

- 3D memory cell size is strongly limited by tono, D, and minW, which are independent on Feature size, F.

1) F: Feature Size = half-pitch
2) t_{ono} = 20 nm (fixed)
3) tox = 8 nm (fixed)
4) D = 10 nm (fixed); Top-bottom size difference.
5) min W= 20 nm(fixed); minimum hole or space at bottom.
6) Wfg = 27 nm (fixed); FG width in DC-SF.

FIGURE 8.3 Assumption of 3D NAND flash memory cell size calculation (2).

Micron Ex. 1014, p. 357
Micron v. YMTC
IPR2025-00119

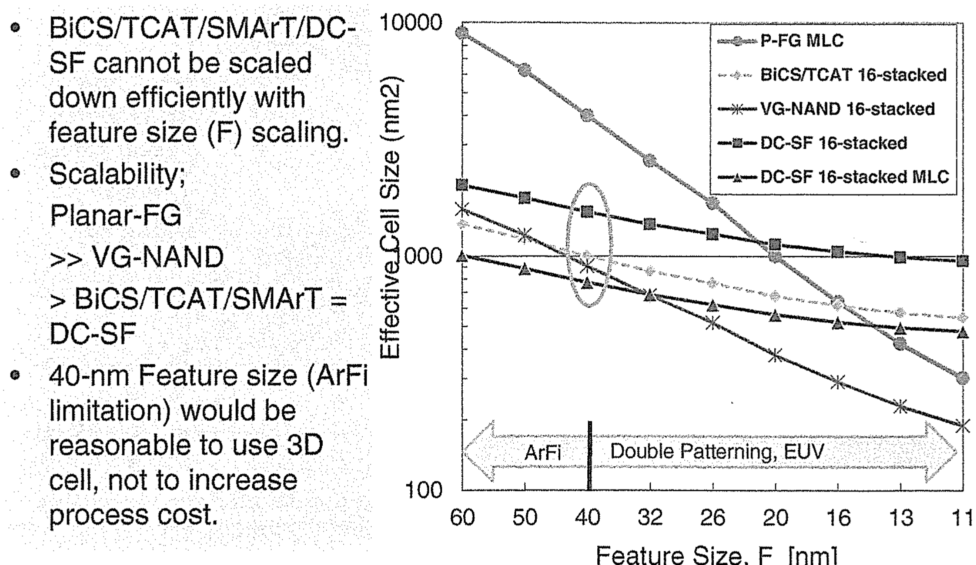

FIGURE 8.4 Scalability of 3D NAND flash memory cell.

Figure 8.5 shows the transition scenario from 2D planar FG NAND cells to 3D NAND cells. The effective cell size of a 1Y-nm 2D cell is nearly equal to that of 16 stacked 3D NAND of BiCS or TCAT or DC-SF cells. This means that a transition from 2D cells to 3D cells is possible from 1Y-nm generation 2D NAND cells if more than 16 stacked 3D NAND cells are used. In fact, 3D NAND flash production was started in 2013 by using 24 stacked cells, and it was extended to 32 stacked cells in 2014, and 48 stacked cells in 2015.

8.3 DATA RETENTION

8.3.1 Quick Initial Charge Loss

The data retention characteristic of a 3D SONOS cell is much different from that of a conventional 2D FG cell. In general knowledge for 2D cells, the 2D SONOS cell shows a larger V_t shift in a retention bake than the 2D FG cell because of a quick charge detrapping through thinner tunnel oxide. Figure 8.6 shows the data retention characteristics after 3K program/erase cycles in both (a) a 3D SONOS SMArT cell and (b) a 2D 2y-nm generation FG cell [2]. The V_t distribution width of a 3D SONOS cell after a 3K cycle is very tight in comparison with that of 2D FG cells. However, after high temperature (HT) data retention bake, V_t distribution width become larger and a large V_t shift-down is observed. These data retention characteristics are similar to well-known data retention characteristics in a 2D SONOS cell (charge trap (CT) cell). In a 3D SONOS cell, the data retention characteristic is one of key challenges that have to be improved or managed.

The quick initial charge loss had been reported in a 2D SONOS cell [3]. Figure 8.7 shows the typical data retention test results for the 2D SONOS cell (a) with cut

Micron Ex. 1014, p. 358
Micron v. YMTC
IPR2025-00119

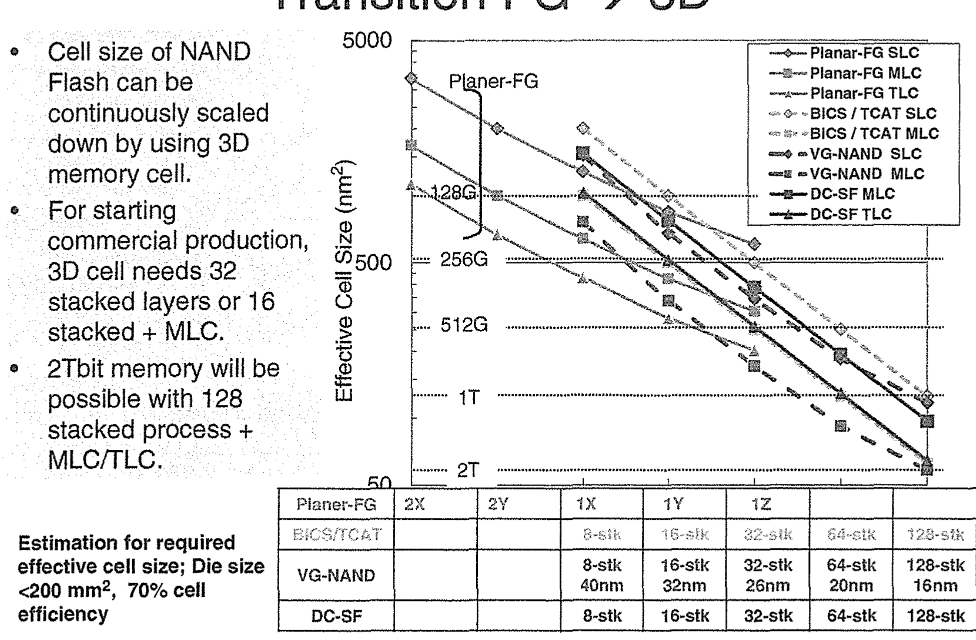

Planer-FG	2X	2Y	1X	1Y	1Z		
BICS/TCAT			8-stk	16-stk	32-stk	64-stk	128-stk
VG-NAND			8-stk 40nm	16-stk 32nm	32-stk 26nm	64-stk 20nm	128-stk 16nm
DC-SF			8-stk	16-stk	32-stk	64-stk	128-stk

FIGURE 8.5 Transition scenario from planar FG cell to 3D cell.

ONO and (b) without cut ONO [3]. All cells are first erased to $V_t < 0$ V and then programmed to $V_t > 3$ V, followed by immediate data retention measurements. In cells of $V_t > 4$ V, the quick initial charge loss are observed and quickly saturates to a 200 to 300-mV V_t shift within 1 s. Even in cells of $V_t = 3.4$ V, the quick charge loss of 100 to 200 mV within 1 sec are observed. The cells in both WL-etching processes cut ONO and non-cut ONO show similar behavior. This indicates that the quick initial

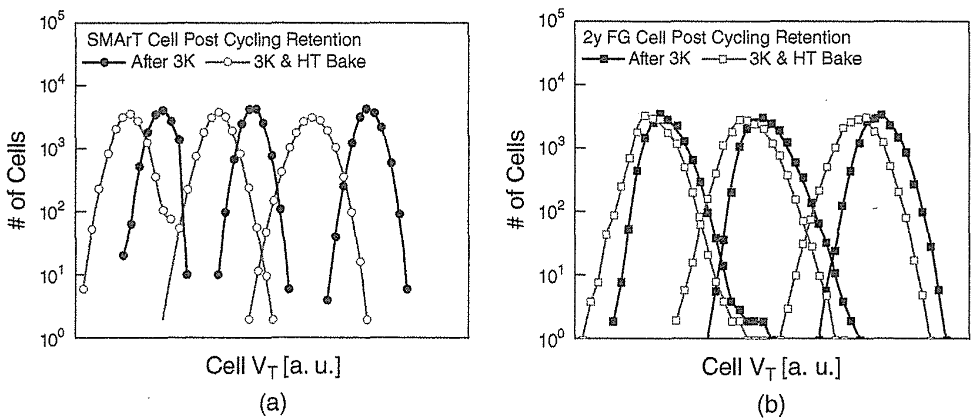

FIGURE 8.6 Cell V_{th} distribution of high temperature (HT) retention bake after P/E cycling of (a)3D SMArT Cell and (b) 2D 2y-nm node FG cell.

Micron Ex. 1014, p. 359
Micron v. YMTC
IPR2025-00119

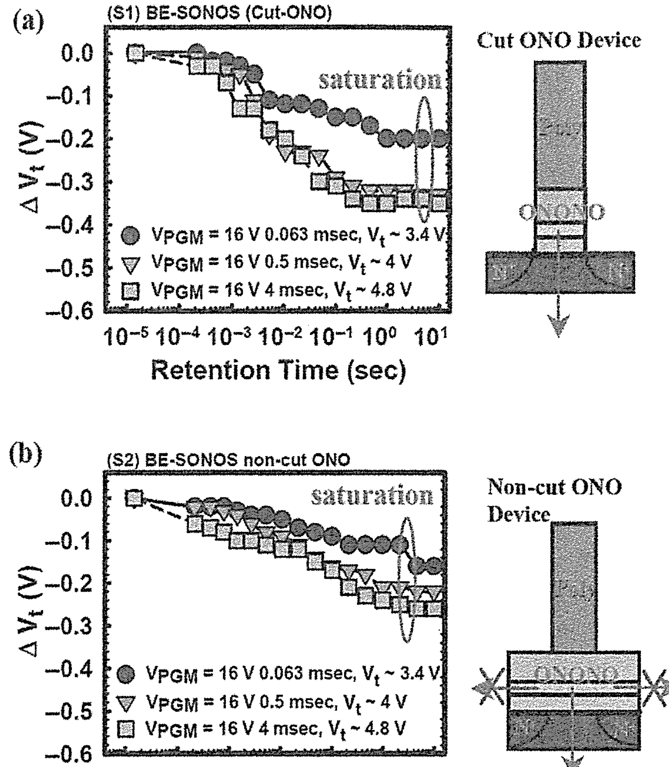

FIGURE 8.7 (a) Quick initial charge loss of 2D SONOS cell with cut ONO, under different program V_t conditions ($V_{t,\text{pgm}} = 3.4, 4, 4.8$ V). Higher programmed state V_t shows a larger charge loss that saturates in < 1 s to a few seconds. (b) Quick charge loss of 2D SONOS with non-cut ONO, under different program V_t conditions. Since the two devices show similar characteristics, the quick charge loss is not caused by charge lateral spreading, but rather through a vertical charge loss mechanism.

charge loss is not related to the charge lateral migration in SiN but to the charge loss through a vertical path.

This quick charge loss phenomenon increases the V_{th} distribution width of program states, and thus it makes damage on the reliability of the programmed data. To minimize the quick charge loss problem, the negative counter pulse scheme was introduced [4,5] in a 3D V-NAND device, as shown in Fig. 8.8. The negative gate voltage is applied to a selected word line just after program pulse (V_{pgm}), while applying V_{read} to unselected word lines to make self-boosting on the channel potential, as shown in Fig. 8.8a. The electron detrapping from charge storage SiN to channel is accelerated by the field between the negative gate voltage and the boosting channel potential. Therefore, during the program sequence, the programmed state's V_{th} distribution can be improved, as shown in Fig. 8.8b. Since this operation is performed in verify read operations, timing penalty for applying this scheme is small.

Micron Ex. 1014, p. 360
Micron v. YMTC
IPR2025-00119

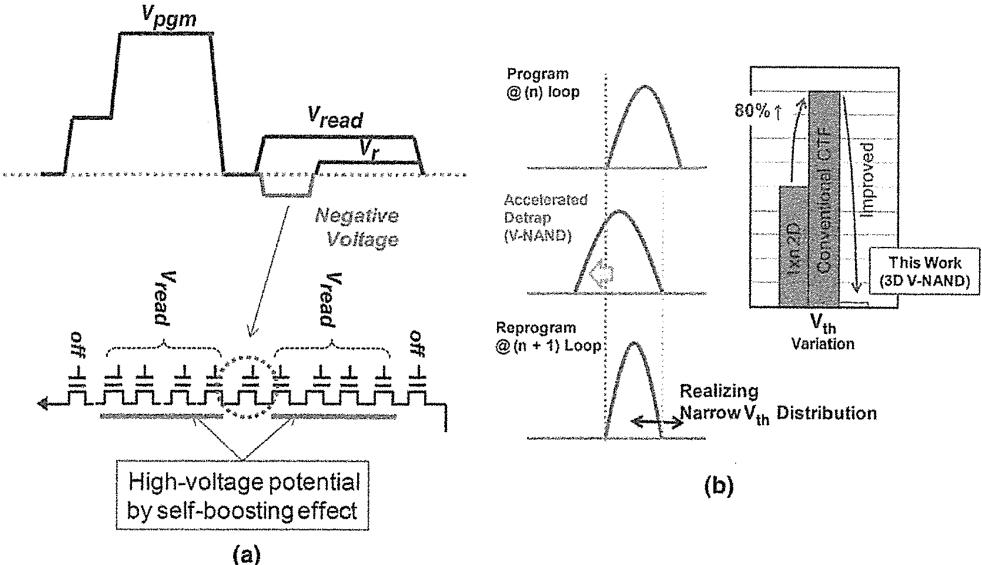

FIGURE 8.8 (a) Negative counter-pulse scheme. (b) Diagram of its mechanism and measured V_{th} variation.

8.3.2 Temperature Dependence

Another important data retention issue in a 3D SONOS cell is that a charge loss mechanism is changed over the temperature range in a regular acceleration test, in contrast with the same mechanism over test temperature in a conventional 2D FG cell, as shown in Fig. 8.9 [2]. In a 2D FG cell, V_t shift is a linear relationship with bake temperature. It means that the data loss mechanism is the same over acceleration bake temperature. However, in a 3D SONOS cell (SMArT cell), V_t shift is a nonlinear relationship with bake temperature. It suggests that the data loss mechanism is different between low temperature and high temperature. The data loss

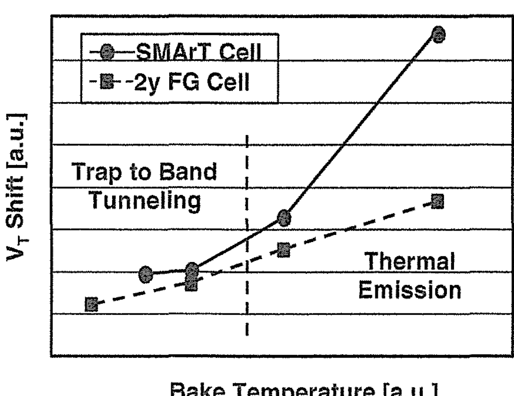

FIGURE 8.9 Temperature dependence of high temperature (HT) retention bake of SMArT cell, compared with 2D 2y-nm FG cell.

Micron Ex. 1014, p. 361
Micron v. YMTC
IPR2025-00119

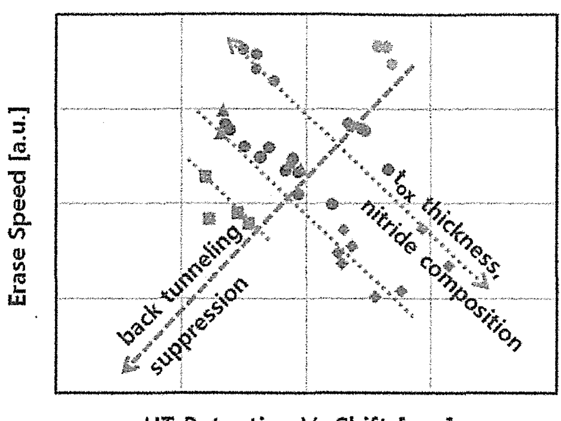

FIGURE 8.10 Trade-off relationship of erase speed and high temperature (HT) data retention V_t shift in a SMArT cell.

mechanisms are considered to be the band-to-band tunneling at low temperature (LT) and the thermal emission at high temperature (HT) [2]. Therefore, the lifetime of data retention cannot be estimated by a simple temperature acceleration test, which has been used as the most general in a 2D FG cell. It is considered that LT lifetime below 90°C has to be evaluated from extrapolation of a long time test in relative LT, at least 3-week V_t shift.

The data retention characteristic of a charge trap cell has trade-off relationship with the erase speed. The typical trade-off relationship between the erase speed and the charge loss at high temperature (HT) is shown in Fig. 8.10 [2]. The way to reduce HT charge loss without the slow erase is to suppress the conduction of the electron from gate to nitride (back tunneling). The suppression of back tunneling can be normally realized by using a large work-function metal gate (e.g., TaN/W) and physically thick Hi-k block dielectric film (e.g., Al_2O_3, or Hf-oxide).

8.4 PROGRAM DISTURB

8.4.1 New Program Disturb Modes

Program disturb phenomena and mechanisms of a 3D NAND cell are much different from that of a 2D NAND cell.

Figure 8.11a shows a schematic view of the cell array architecture of a 3D NAND cell [6, 7] in BiCS, TCAT/V-NAND, and SMArT cell. The NAND string (STR) is located at the intersection point of the drain selection transistor (DSL) and the bit line (BL). Word lines of each string (STR) are connected at a common point in the block, namely Fig. 8.11a shows one physical block. The different point from a 2D NAND cell is that N strings in one block are connected to the same bit line through different select transistors of DSL_1 to DSL_N. In the case of a 2D NAND cell, one string

Micron Ex. 1014, p. 362
Micron v. YMTC
IPR2025-00119

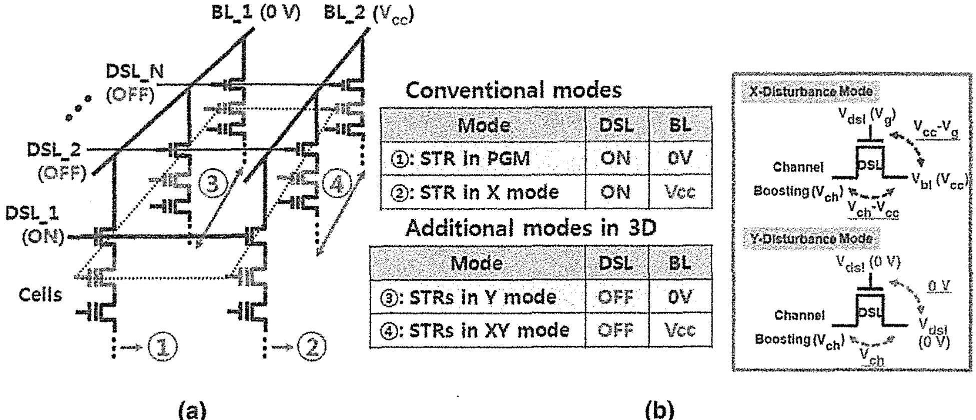

FIGURE 8.11 (a) Program disturbance modes of 3D NAND flash cell array. N strings are connected to the same bit line in the same block. (b) Comparison of program disturbance modes in a 3D NAND flash cell array. In a 3D NAND cell, two new modes of Y-mode and XY-mode are added.

in the block is connected to one bit line. This 3D NAND array architecture makes a new program disturb mode, as shown in Fig. 8.11b.

When DSL_1 is in the turn-on state (ON; selected), STRs along DSL_1 are in either programming (PGM) or program disturb X mode, depending on the BL bias, where "X mode" has BL in high bias of V_{cc}. Disturb X mode is the same as a conventional program disturb mode in a 2D NAND cell. However, in a 3D NAND cell, the remaining DSL_2 to DSL_N are in the turn-off state (OFF; unselected) so that STRs along DSL_2 to DSL_N are in either program disturb Y or program disturb XY mode, where "Y mode" has BL in 0 V and DSL in turn-off state, and "XY mode" has BL in high bias of V_{cc} and DSL in the turn-off state.

The XY mode is not more severe than the conventional X mode, because the boosting voltage in STR does not cause a leakage current through DSL due to DSL = OFF and BL = V_{cc}. However, the program disturb Y mode has much severer than conventional X mode, because the boosting voltage in STR may cause a leakage current through DSL due to BL = 0 V. In addition, DSL in a 3D NAND cell has the larger subthreshold slope than DSL in a 2D NAND cell. This means that DSL in a 3D NAND cell has large leakage current [2, 6]. Furthermore, in a 2D NAND cell, the leakage current through DSL does not occur in program disturb X mode because the V_t of a DSL transistor becomes high in the program disturb mode due to a strong body effect (strong back gate effect or source bias effect). However, in a 3D NAND cell, the leakage current of DSL cannot be easily suppressed because V_t of surrounding gate transistor of DSL does not become high due to a weak body-effect during program disturb conditions.

In order to suppress a program disturbance in a 3D NAND cell, several approaches to reduce leakage current through DSL were proposed [6]. They are (1) high V_t of DSL, (2) applying negative bias to DSL, and (3) inserting dummy word lines between DSL and edge word line. Both (1) and (2) can decrease a large leakage

Micron Ex. 1014, p. 363
Micron v. YMTC
IPR2025-00119

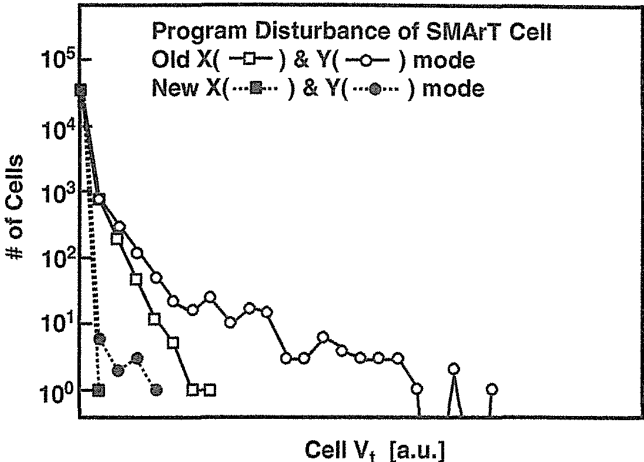

FIGURE 8.12 Suppression of program disturbance fail bit by applying the optimized program inhibit conditions.

current of DSL in a 3D cell. And (3) can control the potential drop from boosting voltage to the voltage applied on DSL, and (3) can also manage the hot carrier generation at edge word-line region by relaxing a high lateral electric field. Therefore, the dummy WL condition (bias, V_t setting, number of dummy WLs, etc.) have to be carefully designed. Figure 8.12 shows the improvement results of program disturb characteristics of X and Y mode by applying conditions of (1), (2), and (3) [2].

8.4.2 Analysis of Program Disturb

Detail mechanism of program disturb in 3D NAND cell had been analyzed [7].

The channel (CH) potential profile of each program disturb modes is calculated by TCAD simulation, as shown in Fig. 8.13a. The CH boosting level of each program disturb modes is determined by the different DSL leakage levels according to bias conditions of BL and DSL. Typically, the CH boosting level of Y mode is the lowest among three modes, and the CH boosting level of XY mode is same or lower than that of X mode. Figure 8.13b shows the measured incremental step pulse programming (ISPP) characteristics of both the program (PGM) mode and three program disturb modes. The CH boosting level of V_{ch} can be derived by the V_G different between the ISPP curves of three program disturb modes and that of the PGM mode. It is confirmed that the V_{ch} of the Y mode is smaller than that of other program disturb modes, which is consistent with the TCAD simulation results in Fig. 8.13a.

In actual array operation, all three program disturb modes occur simultaneously, and thus disturb fail bits appear by statistically complicated circumstance of neighbor cells. Figure 8.14 shows the simulation (model) and measurement (chip) results of the erase (ERS) cell V_t distribution in initial and after programming all pages in a block. The modeling parameters include the ISPP characteristics in Fig. 8.13b, CH boosting variations, RTN, and initial ERS cell V_t distribution. And the modeling parameters

Micron Ex. 1014, p. 364
Micron v. YMTC
IPR2025-00119

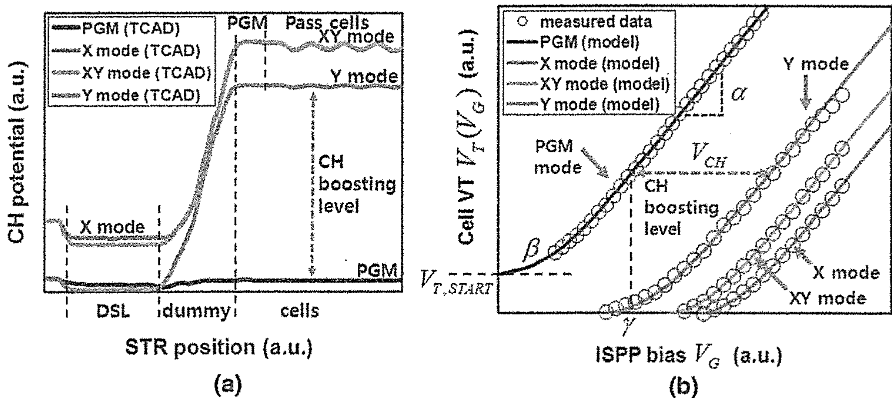

FIGURE 8.13 (a) Channel potential level during program boosting operation by TCAD simulation for X, XY, and Y mode. (b) Cell V_t shift in ISPP program operation of program (PGM) mode and three program disturb modes of X, XY, and Y mode.

were calibrated so that ERS cell V_t distribution after programming is consistent with measured data in cell array. It appears that many bits are over the read voltage (V_r) and then become failure bits.

The effects of three program disturb modes were analyzed by using this model.

In general, program disturb failure bits are caused in ISPP end bias, because cell V_t become highest by highest V_{pgm}, as shown in Fig. 8.13b. Therefore, the probability for a specific cell to be in each program disturb mode at a specific ISPP bias is calculated and shown in Fig. 8.15. In the case of conventional 2D cell, failure bits are caused in only X mode. However, in the case of a 3D cell, failure bits are caused in not only X mode but also two additional modes of Y and XY modes. The probability

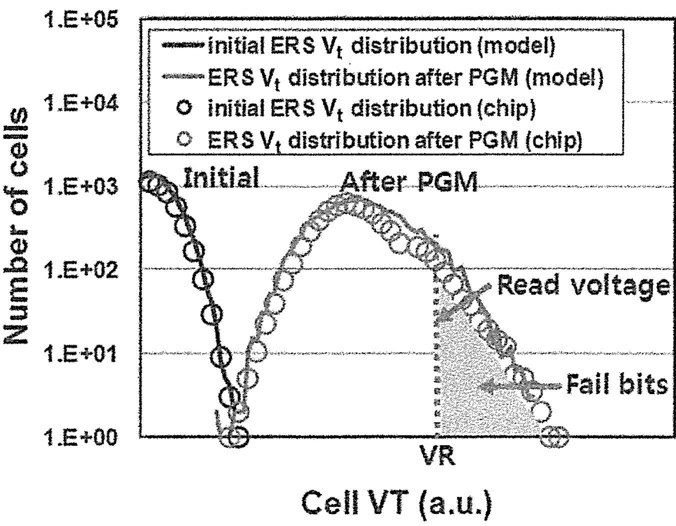

FIGURE 8.14 Change of the erase (ERS) V_t distribution after program operation (PGM).

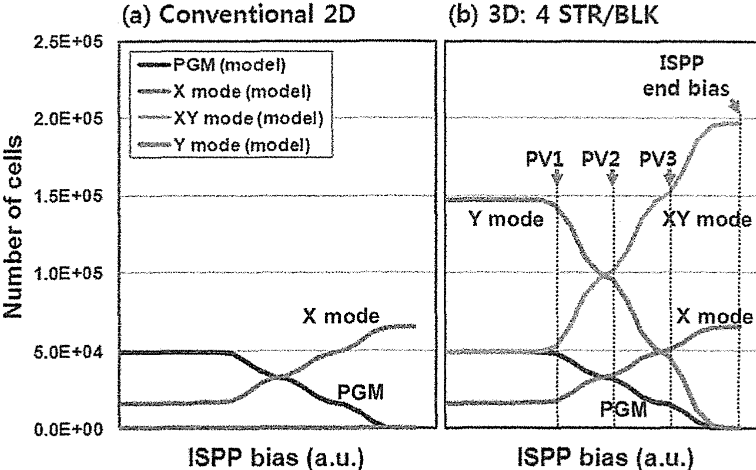

FIGURE 8.15 Probability (number of cells) of each program disturbance mode with increasing ISPP bias.

for a cell in Y mode, which has the lowest CH boosting level, constantly decreases with increasing ISPP bias so that there are a few cells in Y mode at ISPP end bias. However, the portion of cells in XY mode, which has lower CH boosting level than X mode, increases constantly so that there are three times more cells in XY mode than those in X mode at ISPP end bias.

Figure 8.16 shows the effects of Y mode on the ERS cell V_t distribution after programming all pages in a block. The CH boosting level of Y mode is intentionally lowered from the reference level while that of other two modes is fixed on the reference

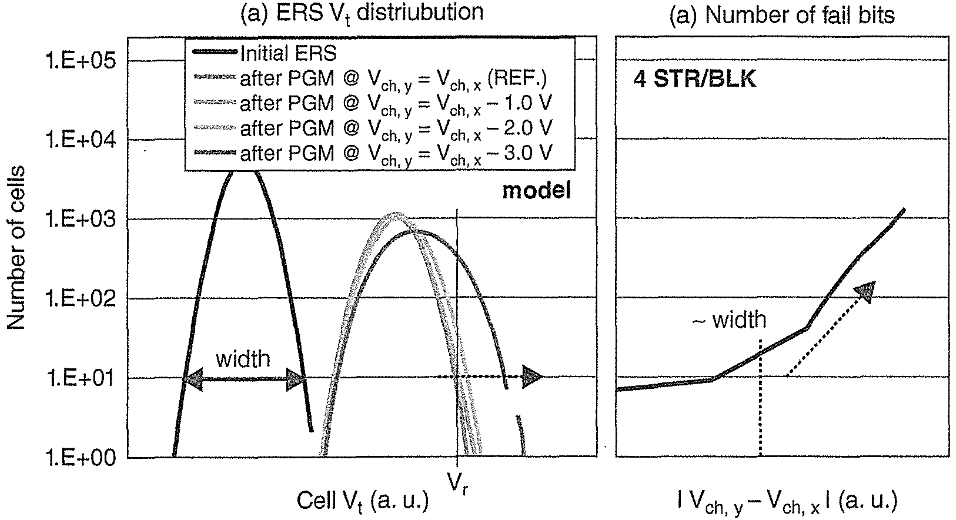

FIGURE 8.16 Effects of Y mode on the erase (ERS) V_t distribution after programming (PGM).

Micron Ex. 1014, p. 366
Micron v. YMTC
IPR2025-00119

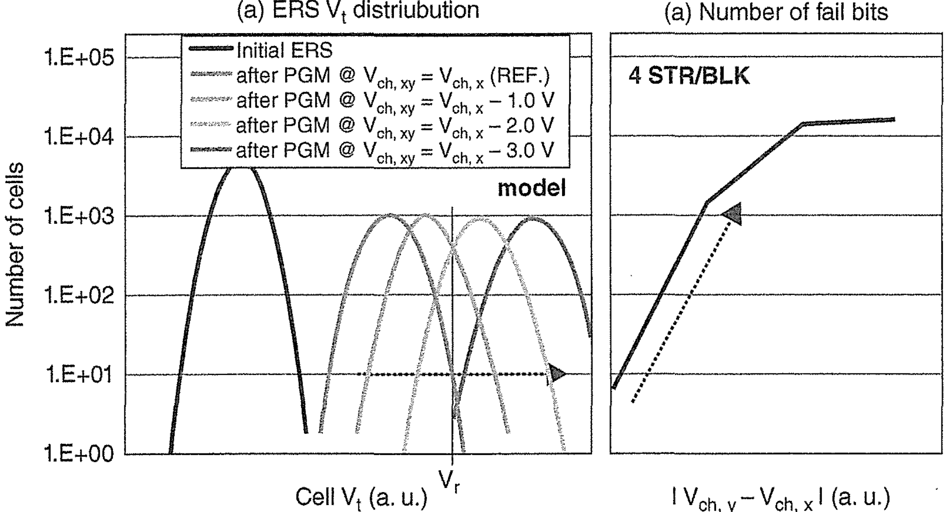

FIGURE 8.17 Effects of XY mode on the erase (ERS) V_t distribution after programming (PGM).

level. It was found that the right-side tail of the ERS cell V_t distribution following programming begins to move up to the positive direction when the difference in CH boosting level between Y mode and other two modes are over 2.0 V. This means that the fail bits (right-side tail bits) originate from Y mode disturb cells in high stress at the end of ISPP, even if these Y mode cells have very low probability of occurrence at the end of ISPP in actual array operation.

Figure 8.17 shows the effects of XY mode on the ERS cell V_t distribution after programing all pages in a block. The CH boosting level of XY mode is intentionally lowered from the reference level while that of other two modes is fixed on the reference level. It was found that the peak of the ERS cell V_t distribution following programming increases in exact proportion to the difference of CH boosting level between XY mode and other two modes. This means that the fail bits originate from XY mode disturb cells in high probability at the end of ISPP.

In order to decrease an effective cell size, the number of STRs per one physical block (BLK) is increased due to decreasing the number of wide gate space in block boundary. Therefore, it is important to estimate the change in the ERS cell V_t distribution following programming as the number of STRs per one physical BLK changes. Figure 8.18 shows the effects of the number of STRs per one physical BLK on the ERS cell V_t distribution after programming. The number of STRs in a physical BLK is intentionally increased from 1 STR/BLK, which is the conventional 2D case, to 16 STR/BLK. It was found that the peak of ERS state V_t distribution following programming increases logarithmically as the number of STRs increases. This is because the number of XY mode stress increases in the exact proportion to number of STRs in a physical BLK. Thus, the resultant fail bits come from the repeated application of ISPP end bias.

Micron Ex. 1014, p. 367
Micron v. YMTC
IPR2025-00119

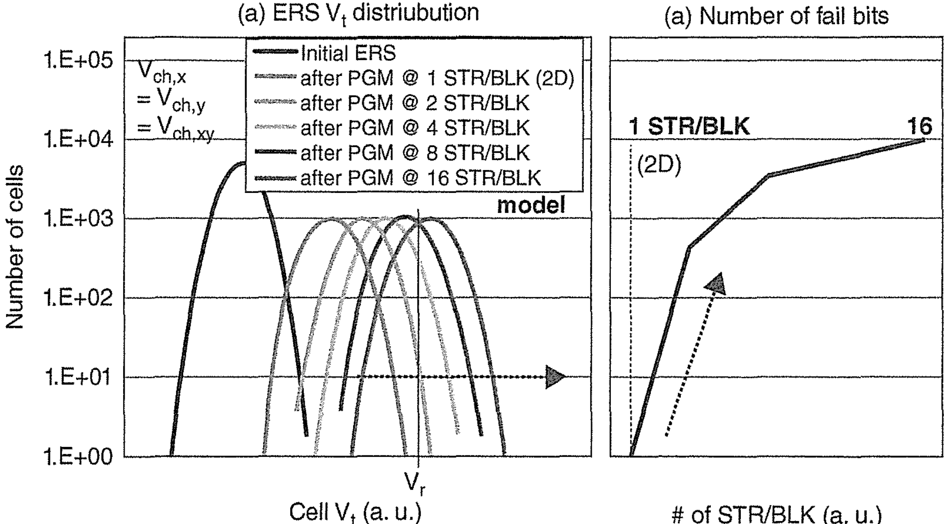

FIGURE 8.18 Effects of cell architecture (number of NAND string in block) on the erase (ERS) V_t distribution after programming (PGM).

Figure 8.19 shows the CH potential profile of cell STR under one of the program disturb modes. There are two major leakage current paths. One is the diffusion current from the bit line (BL) through the DSL. The other is the generation of electron–hole pairs in the area of dummy word lines, where potential drop occurs. The mechanism of electron–hole generation would be trap-assisted generation in a poly silicon channel or in band-to-band tunneling (BTBT) [2, 6]. Therefore, it is important to minimize these currents in order to maintain high CH boosting level of each program disturb mode.

When a STR is under one of the program disturb modes, there is a considerable CH potential drop in the relatively narrow region of dummy WLs, which in turn

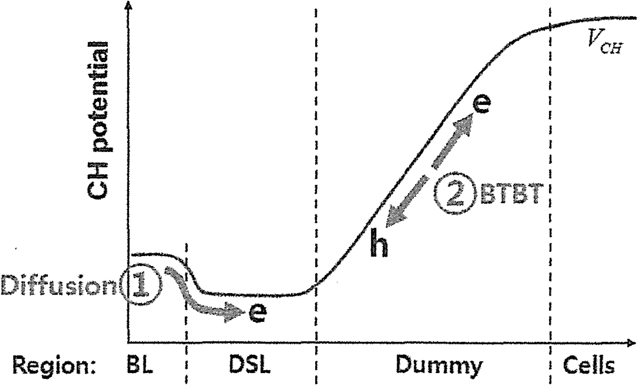

FIGURE 8.19 Two leakage paths that determine the CH boosting level. One is the diffusion current from the bit line (BL) through the DSL. The other is the generation of electron–hole pairs in the area of dummy word lines, where potential drop occurs.

Micron Ex. 1014, p. 368
Micron v. YMTC
IPR2025-00119

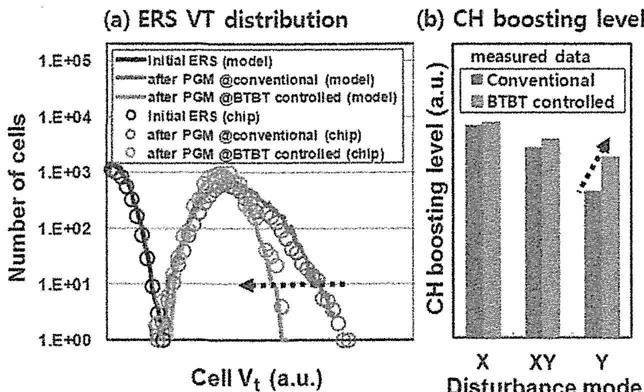

FIGURE 8.20 Effects of the BTBT (band-to-band tunneling) controlled program (PGM) operation. The BTBT-controlled program operation (applying a proper dummy WL scheme) can improve the channel (CH) boosting level and then can improve program disturb characteristics.

generates the electron and hole current. Therefore, it is very important to minimize the electric field in the dummy WL region by applying appropriate bias on dummy WLs together with targeting their V_t. Figure 8.20b shows the measured CH boosting level of conventional case and with applying a proper dummy WL scheme (potential and BTBT controlled). The CH boosting level of X, XY, and Y mode are improved up to 20% due to minimization of electron and hole pair generation in the dummy WL region. Figure 8.20a shows measured ERS cell V_t distribution after program in the array under a proper dummy WL scheme. The failure bits in the right-side tail are well suppressed as a result of a high CH boosting level of the Y mode. Moreover, modeling results are consistent with measured data in array.

8.5 WORD-LINE RC DELAY

The RC (resistance–capacitance) delay of word line has to be minimized for high-speed operation of read and program. In general, the guideline of the RC value is around 1 μs. It means that the time of ramp up and down of word line is about 3 μs (= 3RC), which has less impact on read and program performance. In order to minimize the RC value in 2D cells, the low-resistance materials (CoSi, TiSi, W, etc.) are applied on word line because word-line capacitance cannot be easily reduced due to fixed structure.

In stacked word-line (WL) structure in 3D NAND cells, such as BiCS, TCAT (V-NAND), and SMArT, a WL capacitance is greatly increased from 2D cells. This is because a plane structure of WL in 3D cells has a large parasitic capacitance, while a line structure in a 2D cell has a relatively small parasitic capacitance. Figure 8.21a shows the stacked WL structure of the 3D NAND cell along with resistor and capacitor models [4,5]. Figure 8.21b shows the WL resistance and capacitance of 3D cells in comparison with those of planar 2D NAND cells [4,5]. From comparison of 2D and

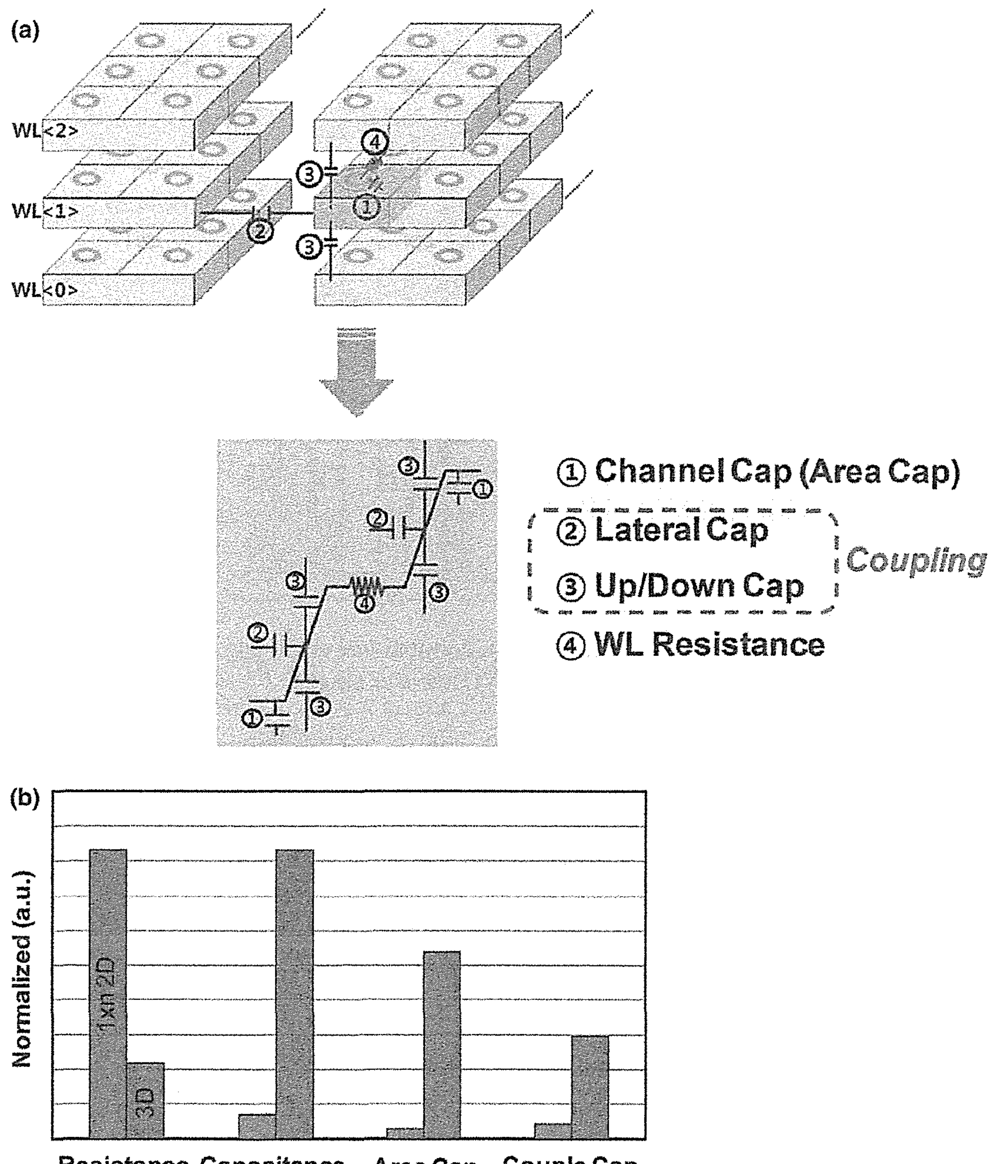

FIGURE 8.21 Word-line (WL) resistance and capacitance. (a) Model of 3D NAND cell (V-NAND array). (b) Comparison with a 2D planar cell.

3D cells in Fig. 8.21b, the RC delay of 3D cell is estimated to be around twice larger than that of 2D cells (resistance, 1/4; capacitance, 8 times). In order to reduce the WL RC delay in future 3D cells, the low-*k* dielectric or air gap between WLs would be effective, as shown in Fig. 8.22.

In 3D cells, the coupling capacitance between WLs is more than four times larger than that in a planar 2D cell, as shown in Fig. 8.21b. Because of this coupling, a large glitch is caused in the neighboring WLs during program and read operations, and it results in causing an unexpected disturbance problem. In order to resolve the problem,

Micron Ex. 1014, p. 370
Micron v. YMTC
IPR2025-00119

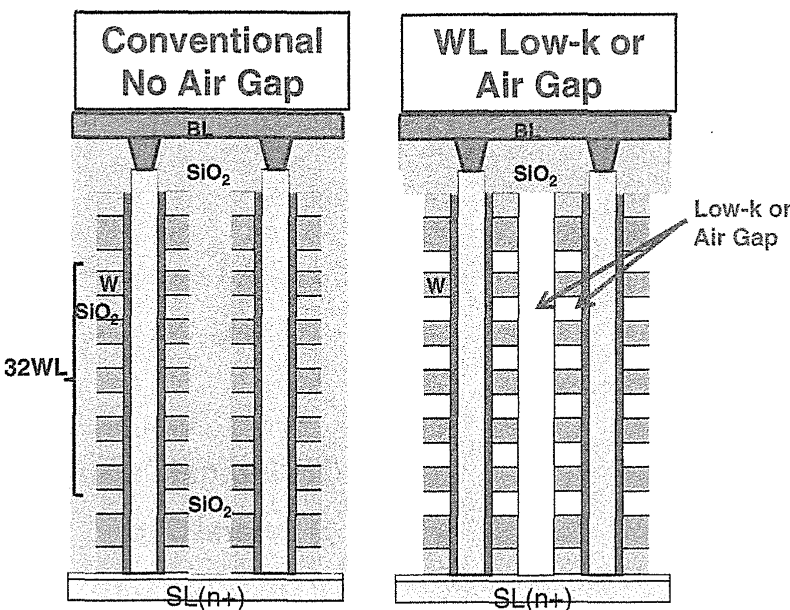

FIGURE 8.22 Schematic 3D cell structures of conventional no air gap and WL low-*k* or air gap. Word-line RC delay can be improved by WL low-*k* or air gap.

two schemes of a glitch-canceling discharge scheme and a pre-offset control scheme were proposed for the program operation [4,5]. In the first scheme, a coupling signal glitch is canceled by a WL discharge circuitry as described in Fig. 8.23a. Since core circuit signals operate in a very predictable and deterministic way, a glitch-canceling discharge scheme could be achieved by precise timing and amount control of the

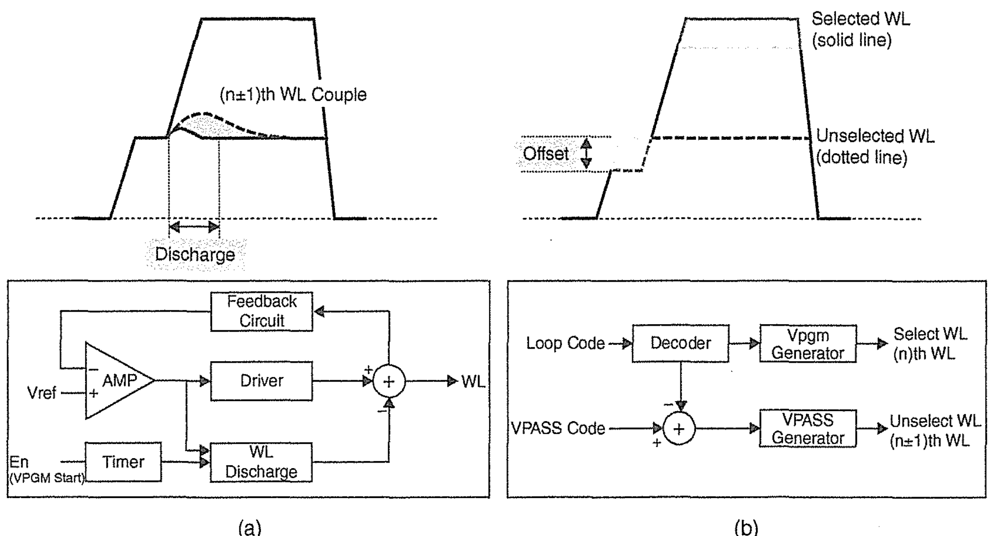

FIGURE 8.23 Bias and block diagrams of (a) a glitch-canceling discharge scheme and (b) a pre-offset control scheme.

Micron Ex. 1014, p. 371
Micron v. YMTC
IPR2025-00119

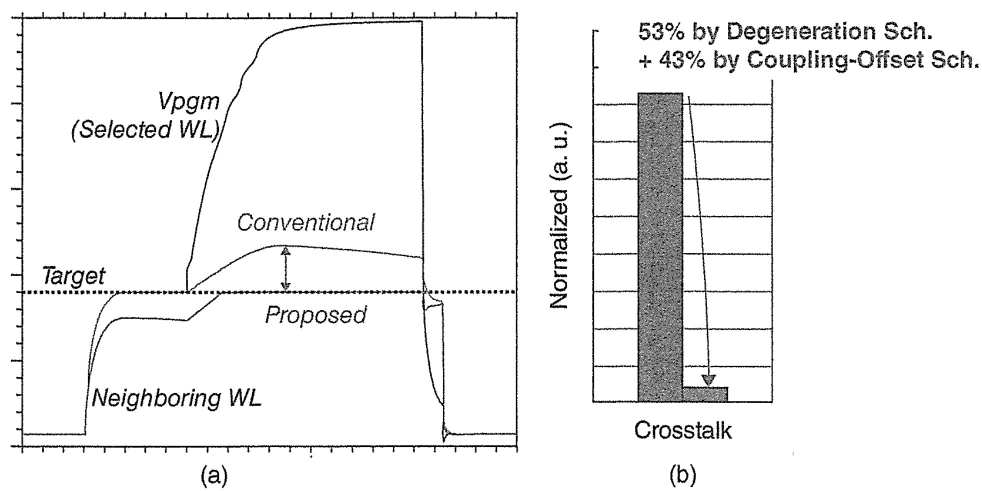

FIGURE 8.24 Simulated waveform of a word-line (WL) signal in a 3D V-NAND array with a glitch-canceling discharge scheme and a pre-offset control scheme.

discharge circuitry. In the pre-offset control scheme, the amount of the coupling glitch is predicted based on the target voltage of the aggressor WL. Then, the target voltage level of the neighbor victim WL could be adjusted according to the prediction, as shown in Fig. 8.23b. Figure 8.24 shows the worst-case simulation result of the proposed two schemes [4,5]. The aggressor WL is the selected WL, while the victim WL is the adjacent unselected WLs. As shown in the figure, the coupling glitch was significantly reduced by using the proposed schemes, which in turn results in eliminating the disturbance caused by WL-to-WL crosstalk.

8.6 CELL CURRENT FLUCTUATION

8.6.1 Conduction Mechanism

The 3D NAND flash cell has a concern to have the larger fluctuation in cell current than the 2D NAND flash cell, because the 3D cell has a different process and structure, such as a poly-Si channel, charge trap cell (thinner tunnel oxide), and tunnel oxide by deposition process. Before developing 3D NAND flash memory, there had been many reports, for example in reference 8, that conduction mechanism and modeling for poly-Si channel was investigated in the planar thin film transistors (TFTs). To understand characteristics of the 3D NAND cell, the very thin poly-silicon (77–185 Å) transistors had been investigated as TFTs [9]. The result showed that the transfer characteristics such as ON current and mobility are enhanced by large grain of poly-Si channel even if it is very thin poly-Si thickness. The 3D cell with a vertical and cylindrical poly-Si channel had been also investigated [10–18]. The variation and fluctuations of conduction property was reported [10–18].

Micron Ex. 1014, p. 372
Micron v. YMTC
IPR2025-00119

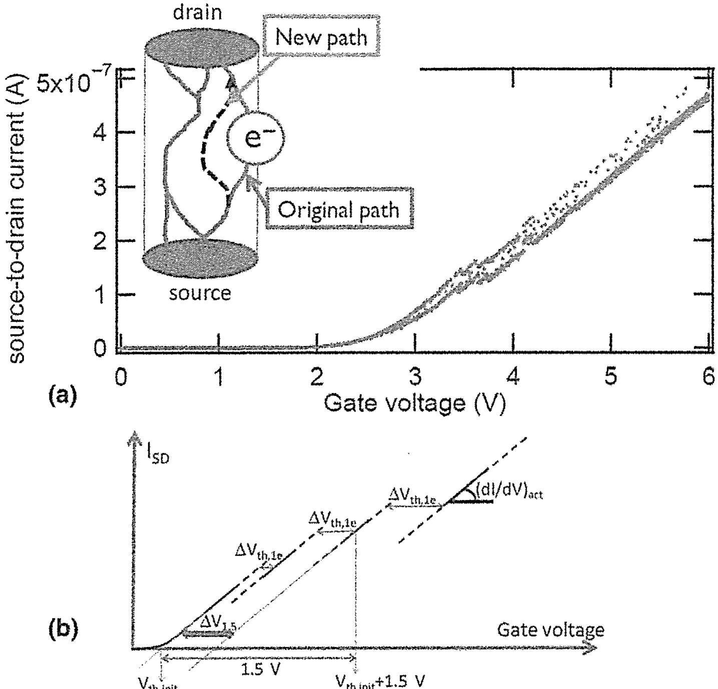

FIGURE 8.25 (a) A selected example of a I_{SD}–V_G characteristic measured with $V_D = 0.1$ V and 1-mV resolution (6000 dots are individual measurement points). This example clearly shows how the curve consists of a discrete number of well-defined curves, each corresponding to a different configuration of percolation paths from source to drain. Trapping of individual electrons (partially) blocks a conduction path as schematically drawn in the inset. A net negative charging is observed with increasing V_G. (b) Schematic reproduction of the I_{SD}–V_G characteristic in (a) with definitions. (i) $\Delta V_{th,1e}$ is the V_{th} shift caused by the trapping of one electron. Three different shifts are indicated. (ii) $(dI/dV)_{act}$ is the transconductance of the linear parts of the curve. (iii) $\Delta V_{1.5}$ is the total $V_{th\text{-shift}}$ between the $V_G = V_{th,init}$ and $V_G = V_{th,init} + 1.5$ V. It is a measure of the charging component in the I_{SD}–V_G curve.

A statistical evaluation of current–voltage characteristics in cylindrical (macaroni) and vertical poly-Si channels transistor had been studied the poly-Si conduction properties and defects [10].

A methodology is unique to extract all components that control the conduction in the poly-Si channel from simple I_{SD}–V_G characteristics. Figure 8.25a shows a 25°C I_{SD}–V_G characteristic up to $V_G = 6$ V measured with a 1-mV V_G resolution. The I_{SD}–V_G curve shows several current drops or shifts to higher V_G in the region of $V_G > V_{th}$. This phenomenon does not appear in transistors on a single-crystalline-Si substrate. The curve is made up of several well-defined curves, each corresponding to a particular current path configuration as illustrated schematically in the inset of Fig. 8.25a. One trap located close to a current path captures a single electron, and the path is partially blocked and then I_{SD} is shifted up. At increasing V_G, the I_{SD}–V_G curves shift to a higher voltage many times, indicating a negative charging by electrons into a poly-Si channel. The V_{th} jumps (I_{SD} shifts up) corresponding to

Micron Ex. 1014, p. 373
Micron v. YMTC
IPR2025-00119

individual electron charging, $\Delta V_{\mathrm{th},1e}$, as defined in Fig. 8.25b, definition (i), can be measured on many devices. The $\Delta V_{\mathrm{th},1e}$ has an exponential distribution and can be fully characterized for a high $\Delta V_{\mathrm{th},1e}$ tail. Because of the charging at increasing V_G, the I_{SD}–V_G curve is stretched out. The actual transconductance in the current paths, $(dI/dV)_{\mathrm{act}}$, is defined as the slope of the linear parts of the I–V corresponding to a fixed charge configuration, definition (ii) in Fig. 8.25b. The charging component is defined in Fig. 8.25b, definition (iii), by using $\Delta V_{1.5}$ to determine the total V_{th} shift for applied V_G between $V_{\mathrm{th,init}}$ and $V_{\mathrm{th,init}} + 1.5$ V. This shift $\Delta V_{1.5}$ can be as large as 0.8 V and depends strongly on the material and the temperature.

Three channel materials of microcrystalline-Si (μc-Si), poly-Si (p-Si), and large grain poly-Si (lgp-Si) were used in single vertical poly-Si channel transistor. The distributions of $\Delta V_{\mathrm{th},1e}$, $\Delta V_{1.5}$, and $(dI/dV)_{\mathrm{act}}$ taken at four temperatures (25°C, 60°C, 100°C, 130°C) and for the three channel materials are presented in Fig. 8.26 [10]. The conduction mechanism can be interpreted by using $\Delta V_{1.5}$ for the charging component and $(dI/dV)_{\mathrm{act}}$ for current path conduction.

In μc-Si shown in (1a)–(4a), a large charging component ($\Delta V_{1.5}$) at 25°C is observed, as shown in Fig. 8.26 (2a). The charging components ($\Delta V_{1.5}$) at higher temperature are largely decreased. It suggests that the conduction is mainly dependent on shallow energy level traps, which can be easily discharged with limited thermal energy. A temperature dependence of $(dI/dV)_{\mathrm{act}}$ in Fig. 8.26 (3a) shows the temperature-activated thermionic emission of electrons over defect-induced barriers, as schematically illustrated in Fig. 8.26 (4a). Reduction or passivation of the traps with hydrogen would be the main challenge for the μc-Si channel.

In p-Si shown in (1b)–(4b), the charging component ($\Delta V_{1.5}$) is not only smaller than $\Delta V_{1.5}$ of μc-Si but also its temperature dependence is reduced, as shown in Fig. 8.26 (2b). No significant difference between 25°C and 60°C is observed. Moreover, between 25°C and 60°C, the $\Delta V_{\mathrm{th},1e}$ distribution drastically reduces and narrows (Fig. 8.26 (1b)). It suggests a redistribution of the percolating current paths. At 25°C the current is confined to a small number of paths that are very sensitive to single electron trapping in shallow states, but above 60°C the current flow becomes more uniform. The temperature dependence of $(dI/dV)_{\mathrm{act}}$ of p-Si is identical to μc-Si, and current path is controlled by thermionic emission over defect-induced barriers, as shown in Fig. 8.26 (4b). The impact of temperature on $\Delta V_{1.5}$ in the range 60°C–130°C is very small, as shown in Fig. 8.26 (2b). This indicates that it is more difficult for energetically deeper traps to discharge thermally.

In lgp-Si shown in (1c)–(4c), the large charging component ($\Delta V_{1.5}$) with small temperature dependence (Fig. 8.26 (2c)) indicates a high density of deep traps. The value of $(dI/dV)_{\mathrm{act}}$ is much larger than that of μc-Si and p-Si, as shown in Fig. 8.26 (3c). This is very important to obtain a large cell current for a 3D NAND flash. However, the spread of $(dI/dV)_{\mathrm{act}}$ is very large in comparison to that of μc-Si and p-Si, as shown in Fig. 8.26 (3c). And there is only a weak temperature dependence. This can be explained by wider current paths in large Si-grains, as illustrated in Fig. 8.26 (4c). The grain boundaries would not act as current barriers, but only as trapping centers with mainly deep energy traps. The large poly-Si grain size causes a large device-to-device variability resulting in a broad spread of both $(dI/dV)_{\mathrm{act}}$ and

Micron Ex. 1014, p. 374
Micron v. YMTC
IPR2025-00119

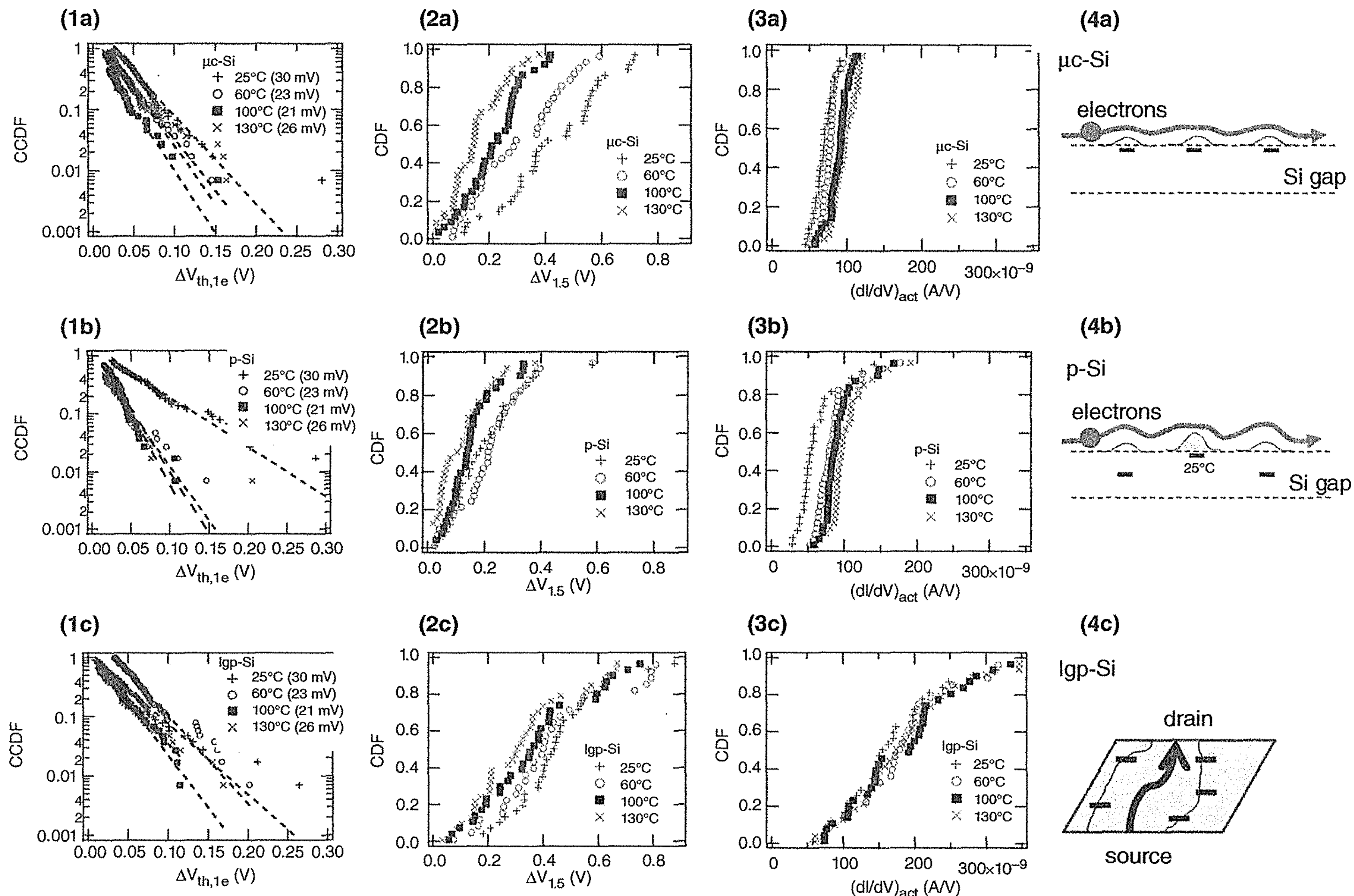

FIGURE 8.26 $\Delta V_{th,1e}$, $\Delta V_{1.5}$, $(dI/dV)_{act}$ of three channel materials of μc-Si (micro-crystalline-Si), p-Si (poly-Si), and lgp-Si large-grain poly-Si). (1) Distributions of $\Delta V_{th,1e}$ for different temperatures and materials. For p-Si (1b) a large difference between 25°C and the other T values indicates a thorough redistribution of current paths. (2) Distributions of the charging component quantified by $\Delta V_{1.5}$. Lowest charging is for p-Si. Largest T-dependence is for μc-Si, indicating shallow states. (3) Distribution of the actual transconductance $(dI/dV)_{act}$. Large spread for lpg-Si indicates few grain boundaries. Very narrow spread in μc-Si indicates the most uniform current flow. (4) Schematic drawing of the conduction model for each of the studied poly-Si options. (4a) and (4b) are band diagram schemes. (4c) is a simplified 2D plot of the surface current in the cylindrical transistor.

Micron Ex. 1014, p. 375
Micron v. YMTC
IPR2025-00119

$\Delta V_{1.5}$. Improving variability is the main challenge for lpg-Si implementation in a vertical stacked device.

In summary on channel material analysis, the large-grain poly-Si has higher mobility and higher transconductance than microcrystalline-Si and poly-Si; however, variability of a large-grain poly-Si is larger (worse) than that of microcrystalline-Si and poly-Si due to the wider current path in the large poly-Si grain.

More detailed analysis had been performed by using the same methodology and the same channel materials [11]. The values of $\Delta V_{\mathrm{TH,single}}$'s ($= \Delta V_{\mathrm{th},1e}$'s) caused by trapping of single electron in poly-Si (see Fig. 8.25b) is significantly larger than those expected from the charge sheet approximation ($\eta_0 \sim q/C_{\mathrm{OX}} = 1.2$ mV). The detected values of $\Delta V_{\mathrm{TH,single}}$ can reach magnitudes as large as hundreds of times the η_0 value. This implies that the conduction between source and drain is concentrated in a limited number of percolation paths, which can be blocked by trapped electrons [19], as described in the sketch in Fig. 8.25(a). As also observed on deeply scaled planar FETs and FinFETs, the $\Delta V_{\mathrm{th,single}}$ distribution follows to the first approximation an exponential distribution, related to the probability of finding a trap at a given distance from the critical point in a percolation path [20]. The average values $\eta = \Delta V_{\mathrm{th,single}}$ tend to increase with increasing grain size, as shown in Fig. 8.27a. With an increasing diameter of channel, a reduction of the tail of $\Delta V_{\mathrm{th,single}}$ distribution is observed due to the increased number of percolation paths reducing the relative impact of single traps, as shown in Fig. 8.27b.

The I_{READ} ($= I_{\mathrm{SD}}$) distribution for lgp-Si stretches out to larger values, but lower I_{READ} tail converges with the lower tail of poly-Si or μc-Si at extremely low percentiles, as shown in Fig. 8.28a [11]. Therefore, even if a large average grain size is used for a channel, the microcrystalline-Si structures remain in a low percentage of less than a few percent, resulting in a similar lower tail of I_{READ} to μc-Si and p-Si. Long N2 annealing slightly shifts the reading current at higher values due to the increase of the average transconductance, as shown in Fig. 8.28b. The lower tail of

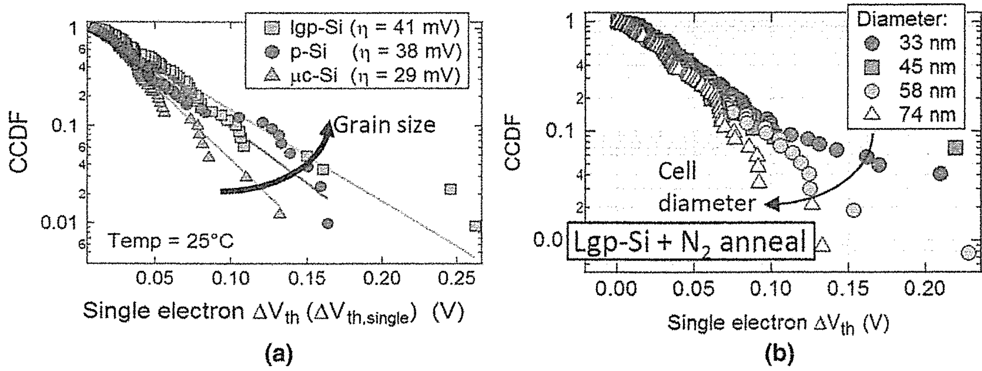

FIGURE 8.27 (a) Complementary cumulative distributions (CCDF = 1-CDF) of threshold voltage shifts $\Delta V_{\mathrm{th,single}}$ caused by single electron trapping (see Fig. 8.25) for different poly-Si materials. CCDFs follow an exponential distribution with the average values η given in the inset. (b) A weak reduction of the impact per trap on the $\Delta V_{\mathrm{th,single}}$ is observed by increasing the cell diameter.

Micron Ex. 1014, p. 376
Micron v. YMTC
IPR2025-00119

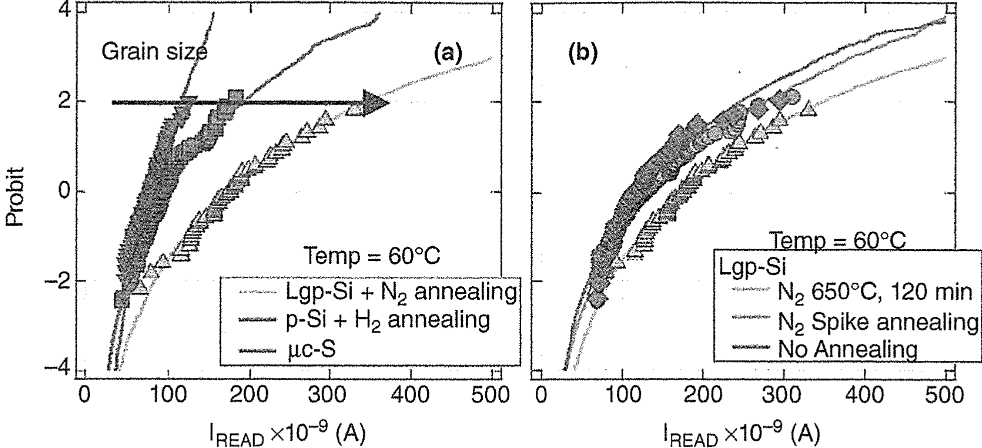

FIGURE 8.28 (a) The highest I_{READ} values are registered for lgp-Si. Interestingly, at low percentiles, the predicted currents converge. (b) Long N2 annealing slightly shifts the reading current at higher values.

I_{READ} in lgp-Si seems to be in sufficient percentage to have an impact on actual read operation in 3D NAND device. It would be a potential issue in a 3D NAND cell.

8.6.2 V_G Dependence

The switching traps were characterized to see their physical properties. A statistical analysis in different channel poly-Si was performed in comparison with monocrystalline planar nFETs. It was confirmed that a significant part of the switching traps were in the poly-Si channel [12].

Figure 8.29 shows two examples of one trap switching with a typical RTN signal in lower V_G of below V_{th}, and one trap switching with a sharply defined switching voltage of $V_{G,switching}$ in higher V_G of above V_{th}, more than 3.5 V in this case [12]. As Fig. 8.30a shows, a large density of switching traps was observed close to V_{th} (band #1)

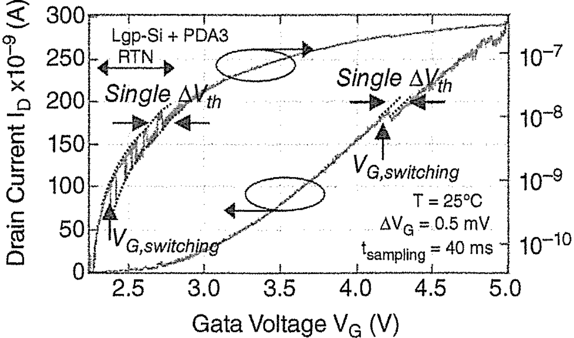

FIGURE 8.29 Random telegraph noise (RTN) and abrupt current drops are clearly observed during the I_D–V_G tracing when high V_G resolution and short sampling time are used. Drain voltage was fixed at 100 mV.

Micron Ex. 1014, p. 377
Micron v. YMTC
IPR2025-00119

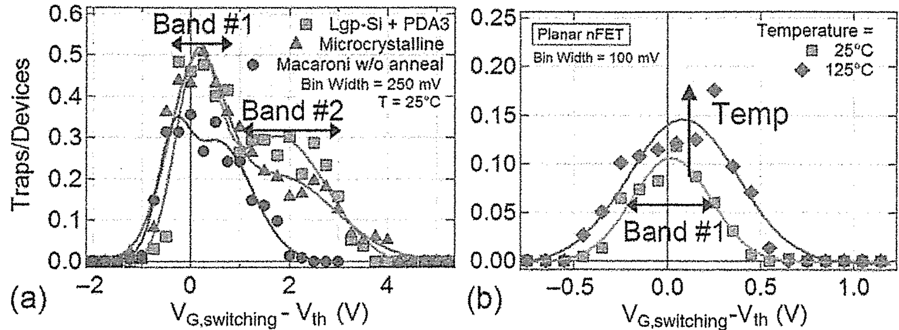

FIGURE 8.30 (a) Independently of the polysilicon option, two distinctive bands appear at the spectra of the number of switching traps normalized by the number of tested devices. (b) For the monocrystalline planar reference, only one band is visible, already indicating that traps switching at higher V_G are polysilicon related.

with a prominent shoulder (band #2) at higher V_G for all the poly-Si processes. Figure 8.30b shows the trap spectrum for monocrystalline planar nFETs obtained in the same procedure. According to the model presented in Fig. 8.31, band #1 is due to the charging of the interface traps and the poly-Si channel traps that shift below the Fermi level E_F when the gate voltage V_G is swept up to V_{th}. For the monocrystalline planar nFETs, the trap spectrum increases with higher temperature (Fig. 8.30b) and is associated with interface traps which are strongly thermally activated. On the other hand, opposite behavior with temperature is observed for poly-silicon channel. The switching traps are reduced at higher temperature. Therefore, it is considered that an important portion of traps are in the poly-Si bulk.

On the other hand, for $V_G > V_{th}$ as shown in Fig 8.31b, the Fermi level E_F in the channel remains at a fixed level, and only the defects that lie within a few kT from E_F can cause I_D fluctuations (band #2). Taking into account that this band was not detected in the reference monocrystalline planar nFETs as shown in Fig. 8.30b, it was concluded that the traps of band #2 are exclusively inside the poly-Si channel.

For the macaroni structure channel, the lowest density of switching traps is observed, as shown in Fig. 8.30a, even though they present the highest interface trap

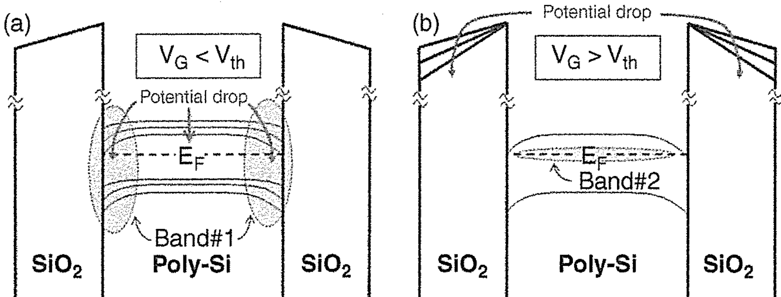

FIGURE 8.31 (a) For $V_G < V_{th}$, the Fermi level E_F sweeps the poly-band gap, progressively charging defects at the interface and in the polysilicon bulk. (b) Afterwards, the E_F in the channel is pinned and only the traps aligned with E_F can cause RTN events.

Micron Ex. 1014, p. 378
Micron v. YMTC
IPR2025-00119

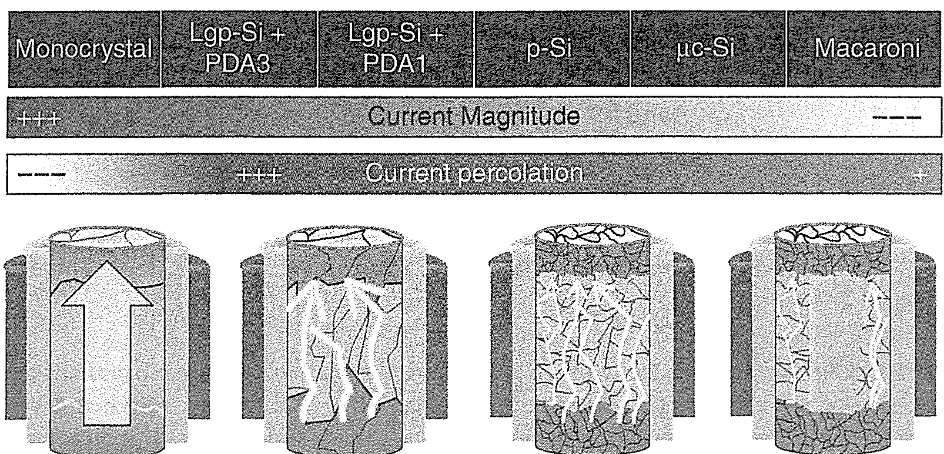

FIGURE 8.32 Higher current is achieved by enlarging the polysilicon grain size, at the expense of increasing the impact of single traps.

density. This is a direct consequence of the level of percolating conduction path in the channel as sketched in Fig. 8.32. The impact of a single electron-trapping/detrapping event on V_{th} increases with increasing grain size (Fig. 8.27a), intensifying the probability of detecting giant current fluctuations. In the ideal case of a single crystal channel nFET, uniform conduction will be restored and the impact of single electron trapping/detrapping events will be drastically reduced.

In the analysis above, the current drop or shift occurs in ON current region ($V_G > V_{th}$) in poly-Si channel, as shown in Figs. 8.25–8.30. This phenomenon could not be observed in monocrystalline planar nFET and 2D floating-gate NAND flash cells. In 3D NAND flash, the current drop or shift in ON current region ($V_G > V_{th}$) would have a strong impact on cell current fluctuations. This is because unselected cells, which are connected to selected cells in series, operate under the ON current region ($V_G > V_{th}$). If unselected cells have a current drop or shift, a cell current could cause the fluctuations.

However, the analysis above was done in a single vertical poly-Si channel transistor. It is not clear so far whether the current shift (V_t shift, such as $\Delta V_{th,1e}$) is caused by a large current flow or by a bias condition of applied $V_G(> V_{th})$. If the current shift is caused by large current flow, this phenomenon would not be a serious issue, because smaller current flows in actual read operation due to series resistance in NAND string. However, if the current shift is caused by bias condition ($V_G > V_{th}$), this phenomenon would have a very serious impact on cell current fluctuation. This is because the current fluctuation of unselected cells has a direct impact on a read current in 3D NAND cells. This does not happen in 2D cells. Therefore, this phenomenon would be a new potential issue in 3D NAND cells.

8.6.3 Random Telegraph Noise (RTN)

It was also reported that the cell current of 3D NAND cell greatly fluctuated by a trap inside a poly-Si channel [14].

Micron Ex. 1014, p. 379
Micron v. YMTC
IPR2025-00119

The channel poly-Si is made of silicon grain with different crystalline orientations. Traps at a grain boundary induce cell threshold voltage (V_t) fluctuations that are dependent on their location variations [8,21]. The charge transfer characteristics (ON current) of a planar thin film transistor (TFT) with a poly-Si channel are dominated not by poly-Si thickness but by the grain size of poly-Si [9]. And in the case of the same thickness of a poly-Si channel, the thinner poly-Si channel has better subthreshold characteristics without degradation of ON current and reliabilities. The average grain size integrated is larger than 100 nm in the report [9], however, SEM images show many types of defects, such as micro-subgrain, stacking fault, or multi-twin inside one grain that induces traps sites.

It had been reported that the variation of cell threshold voltage induced by a poly-Si trap was caused by two intrinsic mechanisms of random trap fluctuation (RTF) and random telegraph noise (RTN) [14].

The channel poly-Si had been modeled as a silicon material with high trap density distributed uniformly inside the channel. The trap distribution is evaluated by fine tuning the I_{BL}–V_{WL} curve of a 3D cell with a temperature range of −20°C to 85°C, as shown in Fig. 8.33a [14]. As reported in references 8 and 21, the large trap tail at the band edge was confirmed by the positive current dependence with temperature. The trap density at mid-gap, in the 1–5 × 10^{18}-cm^{-3} range, was derived by V_t and subthreshold slope temperature dependence. The same temperature dependence of the silicon mobility with an effective mobility calibrated to 130 cm^2·V^{-1}·s^{-1} had been used [8]. The cell V_t fluctuations are simulated by defining one trap at one location in space and energy. Thus the energy distribution is separated into a single energy level, as shown in Fig. 8.33b [14]; and for each energy level, at each location, the charge distribution follows a Poisson distribution with a coefficient corresponding to the continuous trap number. The benefit of this approach is not needed for the calibration parameters. The trap distribution is already calibrated from the I_{BL}–V_{WL} curves. As shown in Fig. 8.33a, this model had an excellent agreement with the measurement of the V_t distribution of a 3D NAND cell array with RTF that is described above [14].

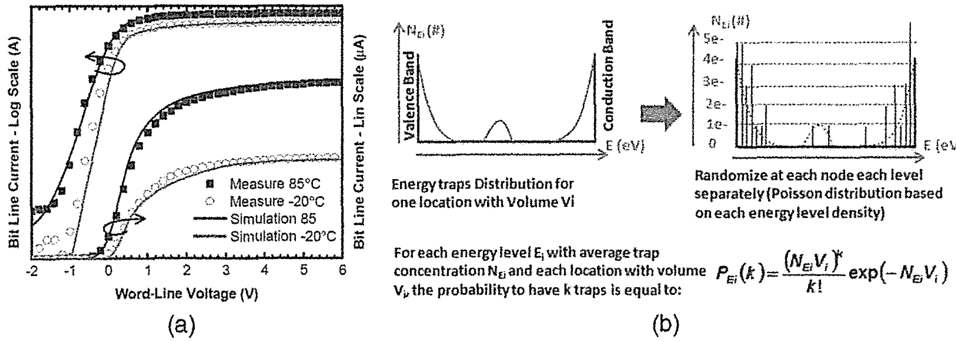

FIGURE 8.33 (a) Measured and simulated cell current at −20°C and 85°C (linear and logarithmic scale). The measured cell is in the median of the array distribution. (b) RTF modeling strategy. The model assumes a poisson distribution from the traps density concentration used for calibrating of (a). No other parameters need to be assumed.

Micron Ex. 1014, p. 380
Micron v. YMTC
IPR2025-00119

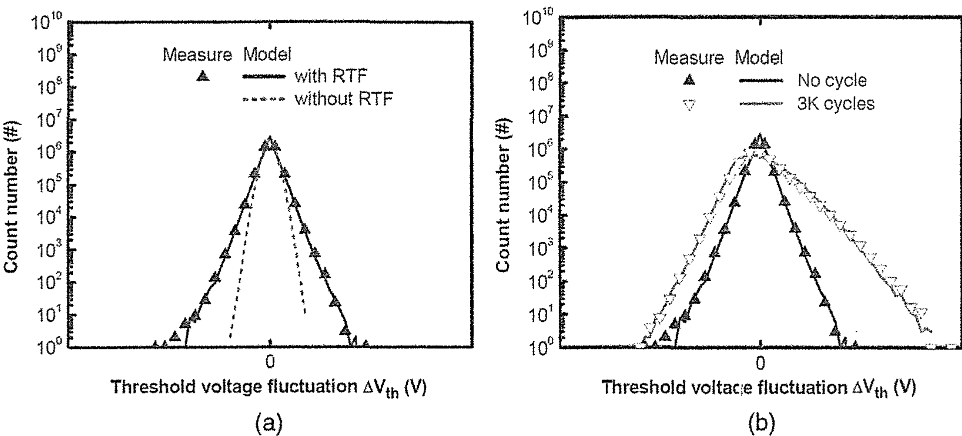

FIGURE 8.34 (a) Measured RTN after no cycles, and simulated RTN with and without RTF. (b) Measured and modeled RTN after no and 3K cycles.

Figure 8.34a shows a measured RTN distribution [14]. For each cell, RTN is evaluated by measuring V_t 200 times and compared to the average cell value [22]. Even if the channel of a 3D NAND cell is undoped poly-Si, RTN distribution presents an exponential tail, similar to 2D NAND cells [22, 23]. The exponential tail has been confirmed due to the presence of traps inside the poly-Si channel. The RTF must be considered when modeling RTN in a 3D NAND structure, as shown in Fig. 8.34a.

As the RTN traps occupancy follows Fermi statistics, their occupancy probability depends on the trap energy level. Thus RTN traps above (below) the Fermi level will be mainly empty (filled) inducing a positive (negative) tail. The probability distribution of the traps at ΔE_T can be evaluated based on the exponential tail coefficient of a single charge. The total RTN distribution is extracted from the sum of the V_t shift for each individual RTN trap. Thus, the total traps distribution is the convolution of the probability distribution over all the possible energy level, considering that for each energy level the trap number inside one cell follows a Poisson distribution [24].

Measurements had been modeled using this approach, as shown in Fig. 8.34b [14]. From RTN data of no cycle and 3K cycles, energy level of generated trap had been extracted. The majority of the switching traps in no cycle are close to the Fermi level. However, after 3K cycles, the RTN traps are generated at more than 0.2 eV above the Fermi level. The cycling induces the creation of switching traps enhancing the positive RTN tail. This can be explained by the degradation induced by the programming step [23, 25].

There are several other reports for RTN of 3D NAND cells [15–18, 26]. Figures 8.35a and 8.35b show the normalized noise power densities ($S_{\mathrm{id}}/I_{\mathrm{BL}}{}^2$) of 2D 32-nm FG cell and 3D stacked NAND cell, respectively [15]. The 3D stack devices show much higher normalized noise power densities ($S_{\mathrm{id}}/I_{\mathrm{BL}}{}^2$) compared to that of 2D 32-nm FG NAND devices because of more traps in poly-Si channel. Differently from the 2D FG NAND cell, 3D stacked devices show the higher $S_{\mathrm{id}}/I_{\mathrm{BL}}{}^2$ of the program state in the SS (subthreshold swing) region than that of erase state, because effective channel length decreases in program state due to higher channel V_{th} than

Micron Ex. 1014, p. 381
Micron v. YMTC
IPR2025-00119

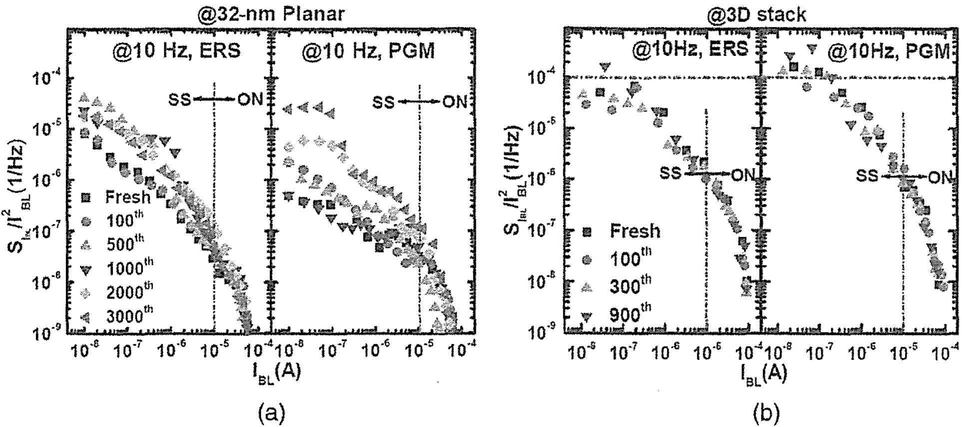

FIGURE 8.35 (a) Normalized noise power spectral density (S_{id}/I_{BL}^2) of 32-nm FG NAND flash memory device at 10 Hz with P/E cycling stress. "SS" represents subthreshold region. (b) S_{id}/I_{BL}^2 of 3D stacked NAND flash memory device at 10 Hz with P/E cycling stress.

V_{th} in gate space region (source/drain region). When cell are erased, the V_{th} in the channel is comparable to that of the gate space region.

8.6.4 Back-Side Trap in Macaroni Channel

The cell current of vertical "macaroni" poly-Si channel is fluctuated by back-side traps, which are located in the interface between the back-insulator and the poly-Si channel, as shown in Fig. 8.36 [27].

The current path was simulated in an erased cell ($V_{th} = -2$ V) and a programmed cell ($V_{th} = 1$ V, 4.5 V), as shown in Fig. 8.37. It was found that the current path of the programmed cell was formed at the back-side of channel poly-Si (Fig. 8.37b and c). On the contrary, the current path of the erased cell was formed at the front-side of channel poly-Si (Fig. 8.37a). From these results, it is recognized that the back-side

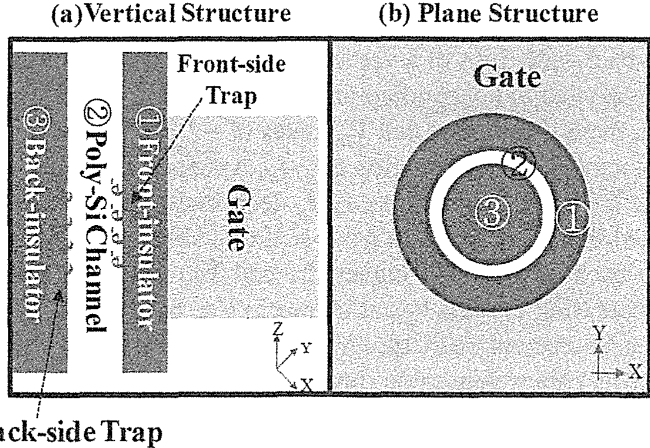

FIGURE 8.36 The schematic pictures for (a) vertical and (b) plane V-NAND structures.

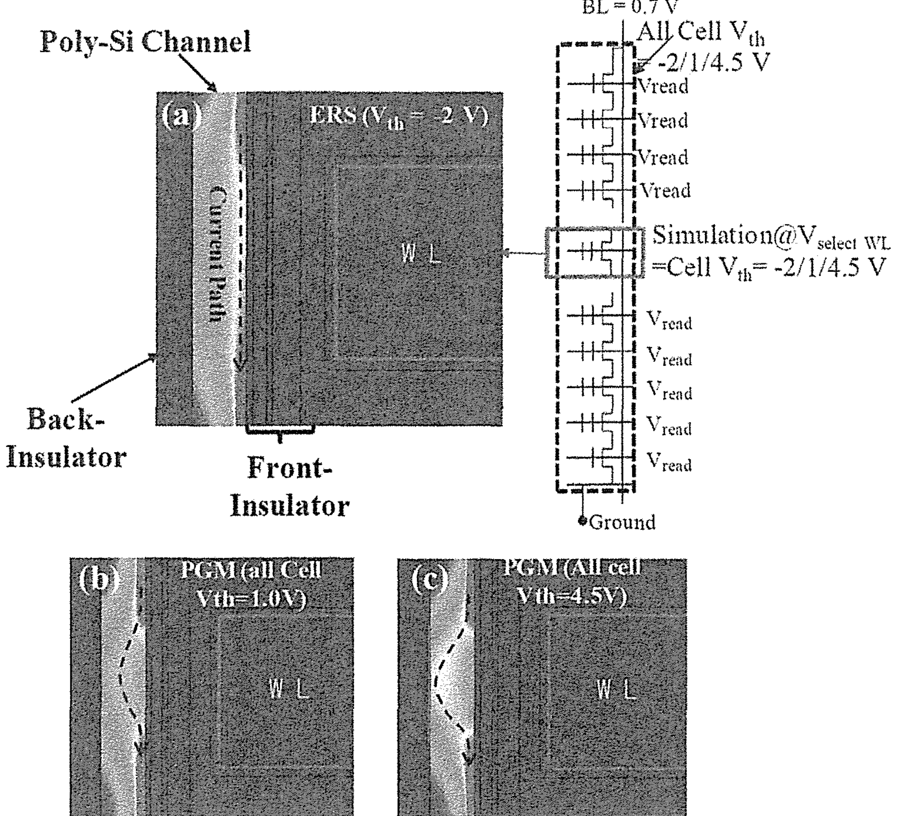

FIGURE 8.37 The simulation results for current path of select WL in V-NAND for (a) $V_{\text{select WL}}$ = cell $V_{\text{th}} = -2$ V, (b) $V_{\text{select WL}}$ = cell $V_{\text{th}} = 1$ V, and (c) $V_{\text{select WL}}$ = cell $V_{\text{th}} =$ 4.5 V, respectively.

traps have to be characterized. In general, back-side traps can be analyzed in the back-gate structure [28]. However, the vertical "macaroni" structure does not have a back gate. Then, a new characterization method was proposed [32]. It enables us to investigate the back-side traps of a vertical "macaroni" poly-Si channel by using the RTN measurement method depending on cell V_{th} states.

In Fig. 8.38, the RTN of three cell V_{th} states of −2 V/1 V/4 V shows the different distributions of total current fluctuation $\Delta I_d/I_d$. As expected in the simulation results of Fig. 8.37, total current fluctuation $\Delta I_d/I_d$ decreases as the cell V_{th} increases. This can be explained that the effect of a front-side trap should be smaller as the current path moves to back-side for the higher the cell V_{th}. The total current fluctuation decreases by increasing the cell V_{th}, as shown in Fig. 8.38.

The location of current path for the cell V_{th} states can be clearly confirmed through measuring capture/emission time of RTN as the gate bias increases. For the erase state, the capture time ($= \tau_1$) decreases as WL voltage (gate voltage) increases. Conversely, for the program state, the capture time increases as WL voltage increases, as shown in Fig. 8.39. This is because the capturing probability of traps is opposite

Micron Ex. 1014, p. 383
Micron v. YMTC
IPR2025-00119

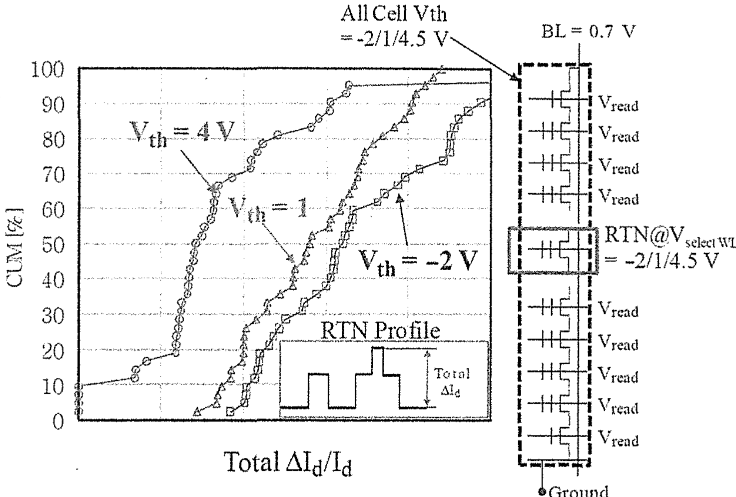

FIGURE 8.38 The cumulative curves of current fluctuation (= total $\Delta I_d/I_d$) at the same current (I_d = 100 nA) according to cell states of 40 cells. Inset shows the schematic picture of RTN profile.

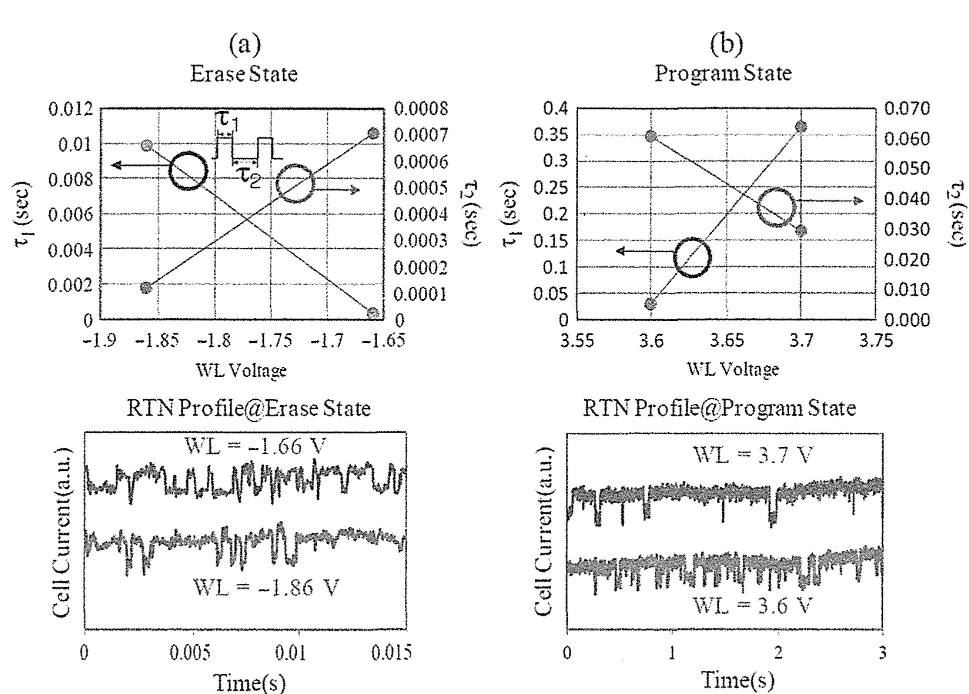

FIGURE 8.39 The RTN profile and change capturing time (τ_1) and emission time (τ_2) as the increasing gate voltage for (a) erase state and (b) program state.

Micron Ex. 1014, p. 384
Micron v. YMTC
IPR2025-00119

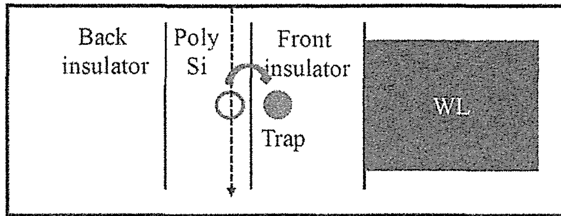

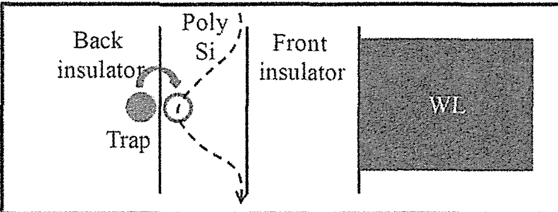

FIGURE 8.40 The schematic pictures for capturing/emission as increasing gate bias. (a) The capturing of electron decreases the current at front insulator (b) The emission of electron increases the current at back insulator.

at the front-insulator and the back-insulator as WL voltage increases, as illustrated in Fig. 8.40.

Figure 8.41 show the RTN distributions for (a) erase cell $V_{th} = -2$ V and (b) program cell $V_{th} = 4.5$ V before and after 10K P/E cycles. The RTN of (b) program cell is not changed according to P/E cycles. However, in the case of (a) erase cell $V_{th} = -2$ V, the RTN increased after P/E cycles, which means that generated traps after P/E cycles just affected the front-side interface, as shown in Fig. 8.41c.

8.6.5 Laser Thermal Anneal

It had been reported that the laser thermal anneal could improve a quality of channel poly-Si [29,30].

Figure 8.42a shows the equivalent grain size diameter (D_{EQ}) before and after anneals [30]. The larger grains are induced by furnace anneal (FA) as compared to poly before anneal, and the largest grains are obtained with the laser thermal anneal (LTA). Figure 8.42b shows the interface trap density, which is extracted by a charge pumping measurement. It is clear that LTA greatly reduces interface defects in the FA case. This indicates that LTA can obtain not only the larger grain size, but also a better channel–oxide interface and less defective grain boundaries.

The statistical distribution of I_D and subthreshold swing (STS) is shown in Fig. 8.43 for gate-only O (oxide-only) devices [30]. This electrical evaluation is done by sweeping the gate up to 5 V, while keeping 1 V at the drain. A clear improvement in both I_D and STS is observed in LTA devices, leading to up to 10 times higher I_D, 3 times steeper STS, and tighter distributions than the poly-Si case. A clear correlation of the LTA dose with STS and I_D is also confirmed in Fig. 8.43. An LTA value of

Micron Ex. 1014, p. 385
Micron v. YMTC
IPR2025-00119

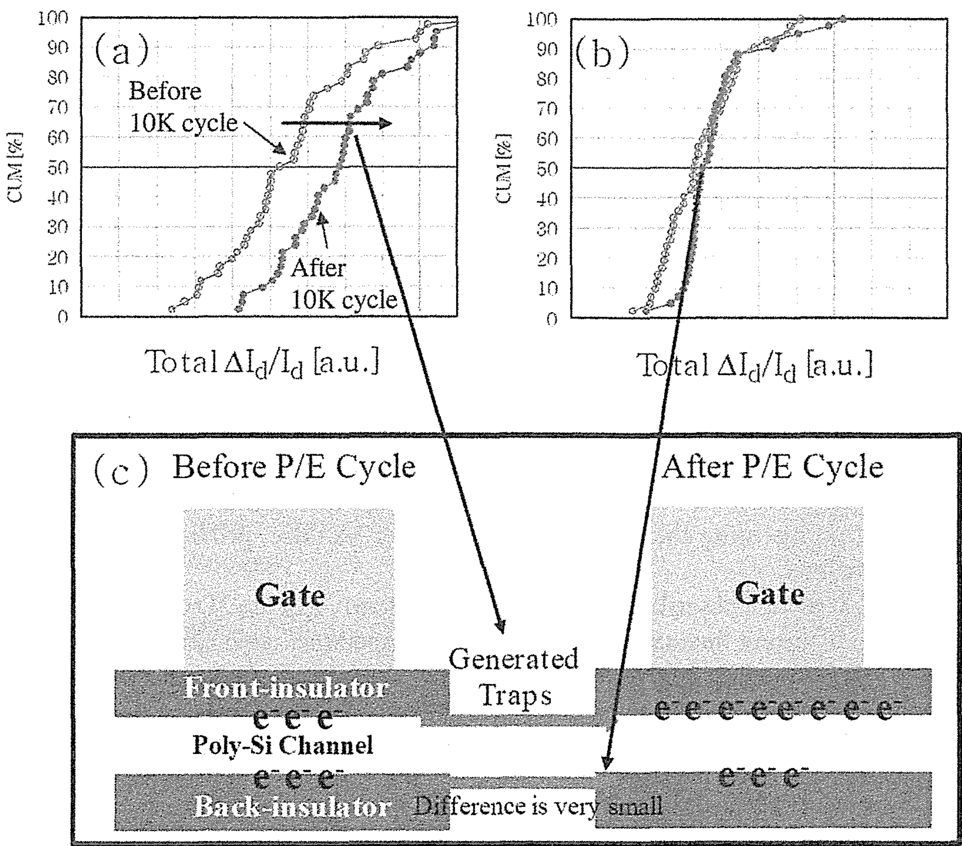

FIGURE 8.41 The RTN distributions before and after 10K P/E cycles at (a) $V_{th} = -2$ V, (b) $V_{th} = 4.5$ V. (c) The location differences of traps before and after 10K P/E cycle. Traps were generated between poly-Si and front-insulator by P/E cycling.

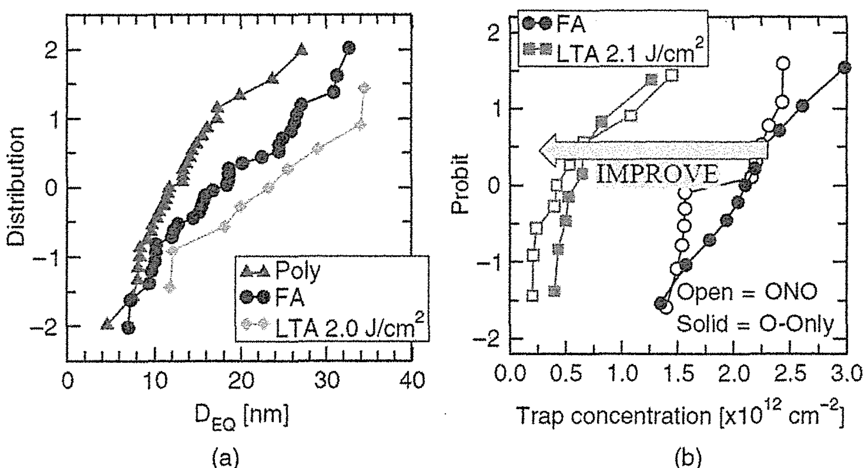

FIGURE 8.42 (a) Equivalent grain size diameter (D_{EQ}) is larger in furnace anneal (FA) and laser thermal anneal (LTA). (b) Trap concentration measured by charge pumping method. LTA clearly reduce interface traps both in O-only (oxide-only) and in ONO.

Micron Ex. 1014, p. 386
Micron v. YMTC
IPR2025-00119

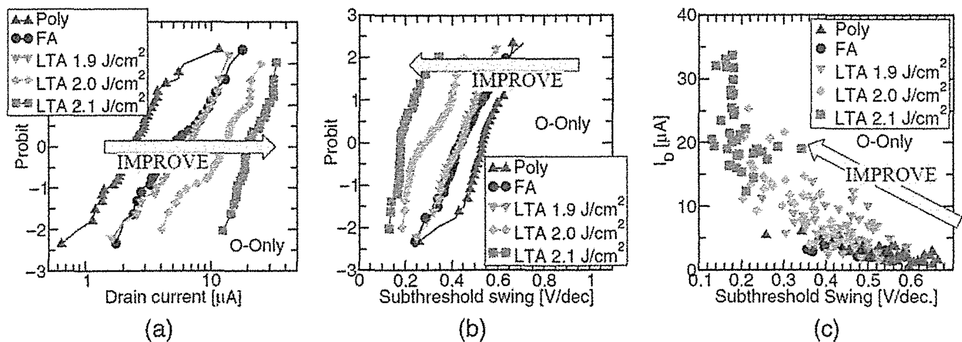

FIGURE 8.43 I_D–V_G curves analysis for O-only (oxide-only) devices. (a) ID distribution, (b) subthreshold swing (STS) distribution, (c) I_D-STS trade-off plot. Clear improvements in absolute value and spread can be observed. Clear correlation between I_D and STS also observed.

2.1 J/cm^2, representing the maximum applicable LTA dose, provides also the best electrical results.

In several reports described above, we can see clearly that the 3D cells have several issues of cell current fluctuations, such as large temperature dependence (Fig. 8.33a), large RTN, the cycling degradation of RTN, back-side trap effect, and so on. These issues have to be managed by the process improvements and operation optimizations to realize higher density and higher reliability of 3D NAND flash memory in the future.

8.7 NUMBER OF STACKED CELLS

In order to reduce the effective cell size, the number of stacked cells has to be increased in 3D NAND cells, as described in Section 8.2. However, if the number of stacked cells is increased, several serious problems are caused, as shown in Fig. 8.44.

The first one is a difficulty in stacked etching of plug hole and gate patterning. Aspect ratio will be more than 30 in over 32 cells stacked. As a realistic solution on this issue, the stacked process may be divided into several groups to avoid high aspect ratio (multi-stacked process). For example, 128 stacked cells are divided into 4 times (×4) 32 stacked cells, as shown in Fig. 8.44. It has to be considered the balance issue that the stacked process cost increases to 4 times, but density become 4 times.

The second one is a small cell current issue in poly-Si channel (see Section 8.6), as shown in Fig. 8.44 and Fig. 8.45 [2]. In the conventional sensing scheme in NAND flash, a sensing current (trip current) is around 60–80 nA/cell in the subthreshold region of a cell transistor. It is considered that more than 200-nA/cell saturation current in the worst case is required to have an enough sensing margin. However, as shown in Fig. 8.45, the cell current is greatly reduced to just ~20% of FG cell even at the 24 WLs (cells) stacked. And cell current is continuously decreased as the number of stacked cells is increased. The low current sensing scheme and/or the material development to enhance the cell current/mobility of the poly-Si channel have to be considered.

Micron Ex. 1014, p. 387
Micron v. YMTC
IPR2025-00119

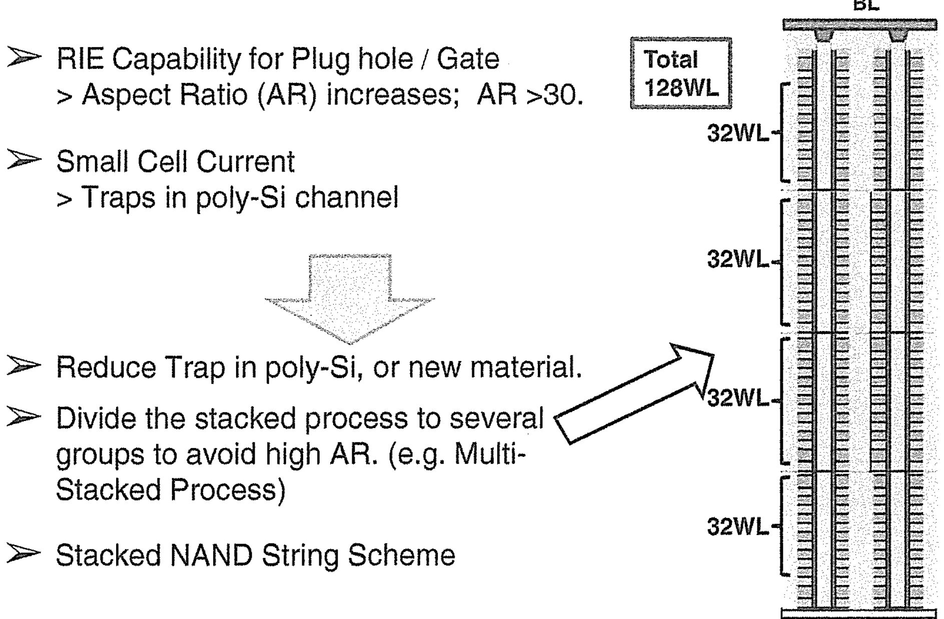

FIGURE 8.44 Problems and solutions for increasing the number of stacked layers in 3D NAND flash memory.

In order to solve the problems related to an increasing number of stacked cells, new array architecture would be a solution for future 3D NAND cells. As an example, the stacked NAND string scheme had been proposed, as shown in Fig. 8.46 [31]. The NAND strings of vertical channel 3D cell (BiCS, TCAT, SMArT) are vertically stacked. Bit lines or source lines are fabricated between the NAND strings. This

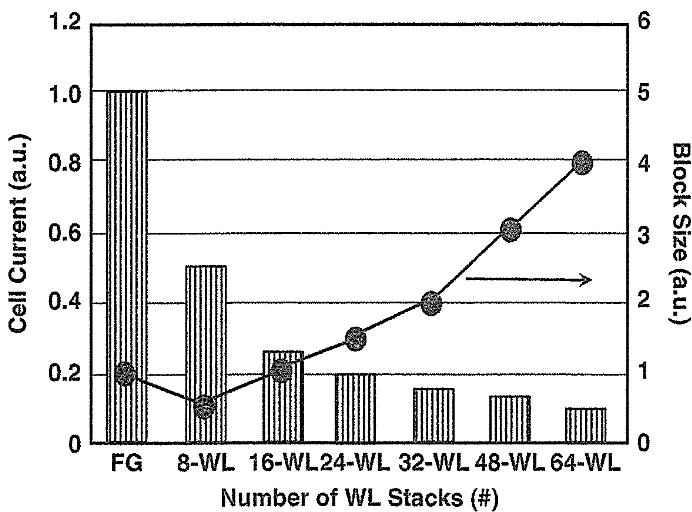

FIGURE 8.45 Trend of cell current and block size as number of WL (word-line) stacks.

Micron Ex. 1014, p. 388
Micron v. YMTC
IPR2025-00119

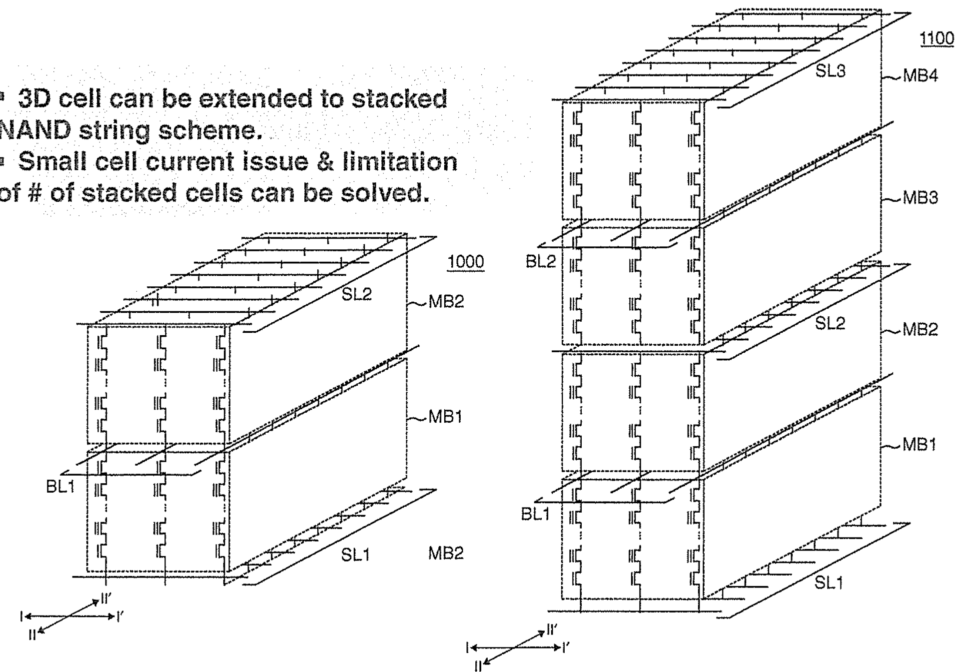

FIGURE 8.46 The stacked NAND string scheme.

architecture can solve the problems of both high aspect ratio etching issue and small cell current issue at the same time.

8.8 PERIPHERAL CIRCUIT UNDER CELL ARRAY

In the first and second generations of 3D NAND flash memory products shown in Fig. 7.35 and Fig. 7.37 in Chapter 7, the peripheral circuit and core circuit (page buffer and row decoder/WL-driver) are located outside of the cell array area, following the conventional 2D chip layout as described in Fig. 8.47a. However, the memory cell of 3D NAND flash has a vertically stacked cell structure. The channel and source/drain of memory cell transistors are not formed on Si substrate, but are formed in a deposited poly-Si. And the channel poly-Si and source/drain of memory cell are not required to connect to Si substrate basically. If the channel poly-Si is not connected to substrate, Si substrate in cell array area is not used for any circuit and device. Therefore, in future 3D NAND products, it will be possible to place some circuit or device on Si substrate in (under) a cell array area, in order to reduce the chip size (i.e., to reduce a bit cost).

Figure 8.47b shows an image that the peripheral circuit and core circuit are formed on Si substrate under a cell array. The cell efficiency of conventional chip layout is normally from 70% to 85%. If the peripheral circuit and core circuit can be formed on Si substrate under cell array, the cell efficiency can be expected to improve to around 95%. The memory chip size can be drastically reduced 10% to 25%, so that the bit cost can be reduced 10% to 25%.

Micron Ex. 1014, p. 389
Micron v. YMTC
IPR2025-00119

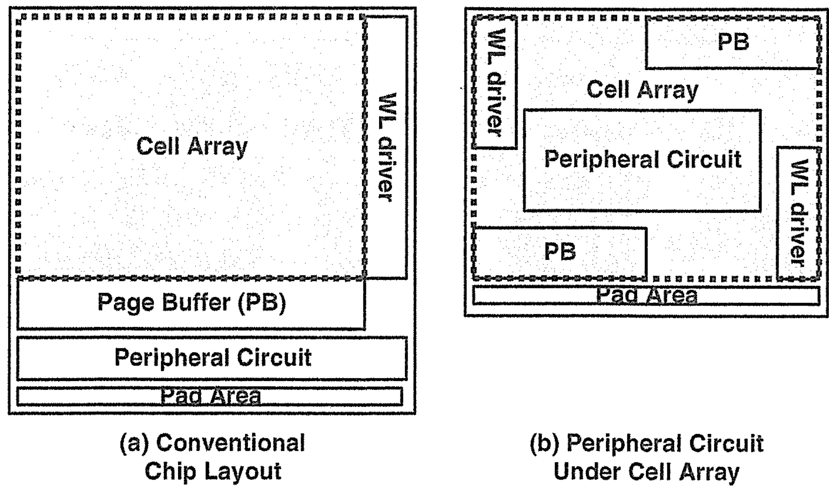

FIGURE 8.47 The memory chip layout image of (a) conventional 3D NAND flash memory and (b) 3D NAND flash memory with the peripheral circuit under cell array.

Figure 8.48 shows the cross-sectional view of (a) a conventional chip layout and (b) a peripheral circuit under a cell array. In (a) conventional chip layout, the page buffer of the core circuit and the peripheral circuit are located outside of the cell array area. However, in (b) the peripheral circuit under a cell array, the core circuit (including page buffer and word-line driver) and the peripheral circuit are located under the cell array area. The metal layers connect the memory cell with a core circuit and a peripheral circuit at the edge of a cell array, as shown in Fig. 8.48b.

In order to realize the peripheral circuit under a cell array, several issues have to be solved. The most important one is that the low-resistance metal layers are required under the cell. For a stable operation of peripheral circuit and core circuit, the low-resistance metal layers are required for the power supply lines (V_{cc}), ground line (V_{ss}), critical signal line, and so on. Normally, the Cu metal layer is used for this purpose in conventional 2D NAND flash memory chips. However, in the case of the peripheral circuit under a cell array, high-temperature processes (>800°C) of 3D memory cell fabrication have a serious damage on the low resistance metal layer (e.g., Cu layer). Therefore, the temperature of 3D cell fabrication has to be greatly decreased, or the high-temperature process immunity of a low-resistance metal layer is required to realize a peripheral circuit under a cell.

8.9 POWER CONSUMPTION

Low power consumption is one of the important requirements for NAND flash storage applications, such as SSD (solid-state drive). In particular, the high-end applications such as datacenters and enterprise SSDs strongly require the low power consumption during high-speed operation.

Micron Ex. 1014, p. 390
Micron v. YMTC
IPR2025-00119

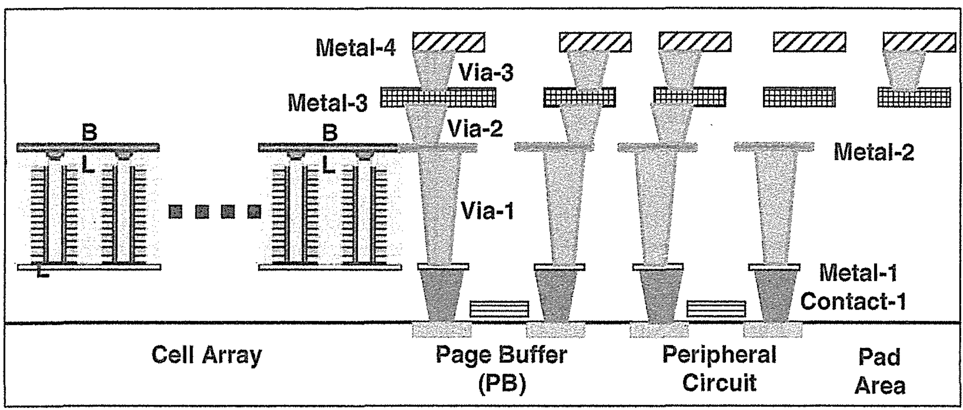

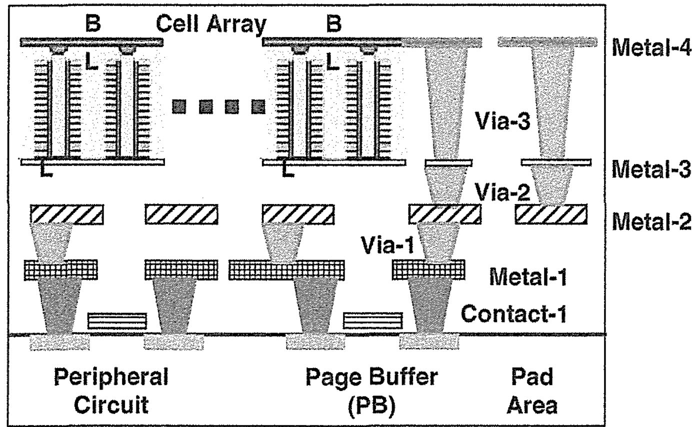

FIGURE 8.48 Cross-sectional image of 3D NAND flash memory in (a) conventional 3D NAND flash memory of cell array, core circuit and peripheral circuit and (b) 3D NAND flash memory with the peripheral circuit under cell array.

Figure 8.49a shows the power breakdown of a typical SSD system in four-way interleaving program operation [4, 5]. The NAND power accounts for about 47% of the entire SSD power, and this portion increases with more way interleaving, as shown in Fig. 8.49b. Figure 8.49c shows that the normalized NAND temperature increases with the increased number of way interleaving in programming. Then, in order not to exceed the temperature limit even with the eight-way interleaving, an SSD is often configured to intentionally reduce its performance and the operation temperature.

The first three-dimensional NAND flash product of the 128-Gb MLC (2-bit/cell) 3D V-NAND flash memory device had used the external high voltage of 12 V, which is available in the SSD board instead of the internal one generated from on-chip pumps to reduce the power without any sacrifice in performance, as shown in Fig. 8.50a [4,5]. When the external high voltage is used, a level detector is implemented so that when

Micron Ex. 1014, p. 391
Micron v. YMTC
IPR2025-00119

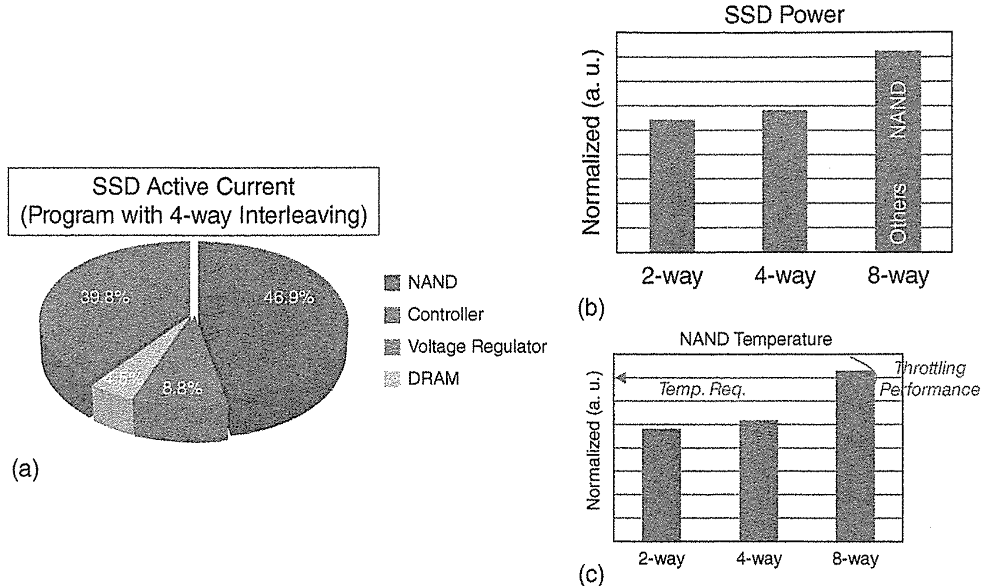

FIGURE 8.49 Diagrams of (a) NAND system power configuration in a four-way program operation. (b) NAND power accounts in SSD. (c) Temperature and way-throttling in an eight-way operation.

the high-voltage level is decreased below a threshold, it discharges internal nodes completely and safely. This operation protects the circuit from malfunctioning even with the unstable high voltage source or in the case of sudden power off. Figure 8.50b shows the simulation result of a level detector.

Figure 8.51 shows a measured active power of the 3D V-NAND at each operation of read, program, and erase. Compared with the consumption without using the external high-voltage scheme, about 50% of the energy consumption was reduced.

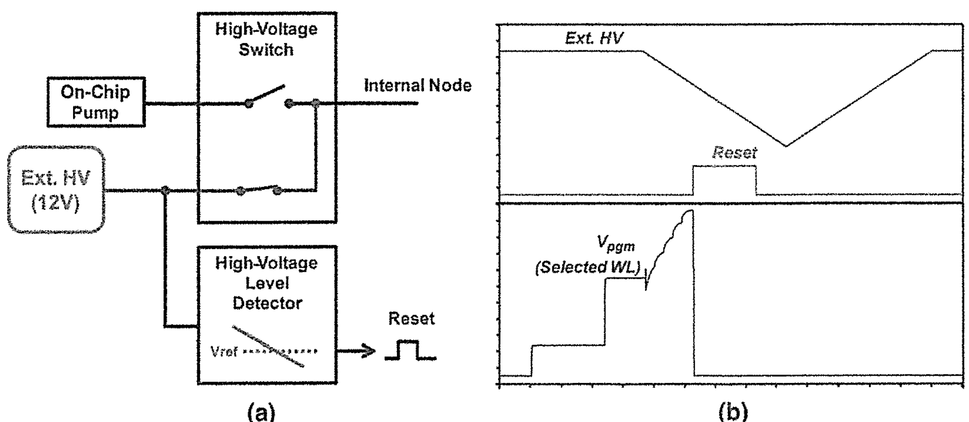

FIGURE 8.50 (a) External high-voltage-supply scheme of 12 V and (b) its simulated waveform.

Micron Ex. 1014, p. 392
Micron v. YMTC
IPR2025-00119

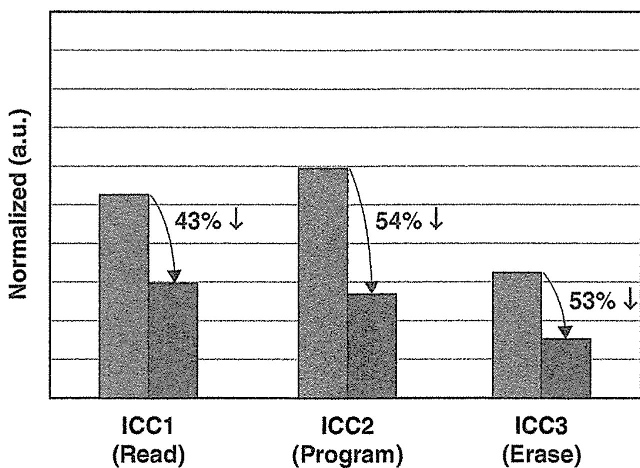

FIGURE 8.51 Measured active power dissipation using an external high-voltage-supply scheme.

As a result, it is possible to use eight-way full interleaving operation without the throttling, thereby increasing the overall SSD performance.

8.10 FUTURE TREND OF 3D NAND FLASH MEMORY

The future trend of 3D NAND flash memory is discussed.

Production of 3D NAND flash memory was started in August 2013. The architecture of the 3D cell was 24 stacked cells MLC (2b/cell) V-NAND as the first generation of 3D NAND [4,5], as shown in Fig. 8.52. The charge trap (CT) cell with a vertical channel was selected for production because the fabrication process of the vertical channel CT cell is simpler than that of other 3D cells. The second generation of 32 stacked cells TLC (3b/cell) V-NAND was released in 2014 [32]. In the following generation, a number of stacked cell will be intensively increased to reduce an effective memory cell size in the coming years, as shown in Fig. 8.52 and Fig. 3.1 in Chapter 3 [1,33]. The bit cost will be greatly reduced. The scaling trend is showing that 1-terabit NAND flash memory will be realized by using more than 64 stacked cells in 2018.

The development items for each generation of 3D NAND flash are much different from that of 2D NAND flash. In the development of the 2D NAND flash, the design rule of the memory cell is scaled down by around ×0.8 scaling ratio in each generation. There were many items which had to be newly developed, such as lithography, patterning, process change for smaller cell, layout change in core circuit (sense amplifier/page buffer, word line driver, etc.), cell reliability adjustment, and so on. A long time and a big effort were needed to complete development for each generation. However, in a 3D cell, development items from generation to next generation will be much reduced because the design rule of a memory cell will not be changed so

Micron Ex. 1014, p. 393
Micron v. YMTC
IPR2025-00119

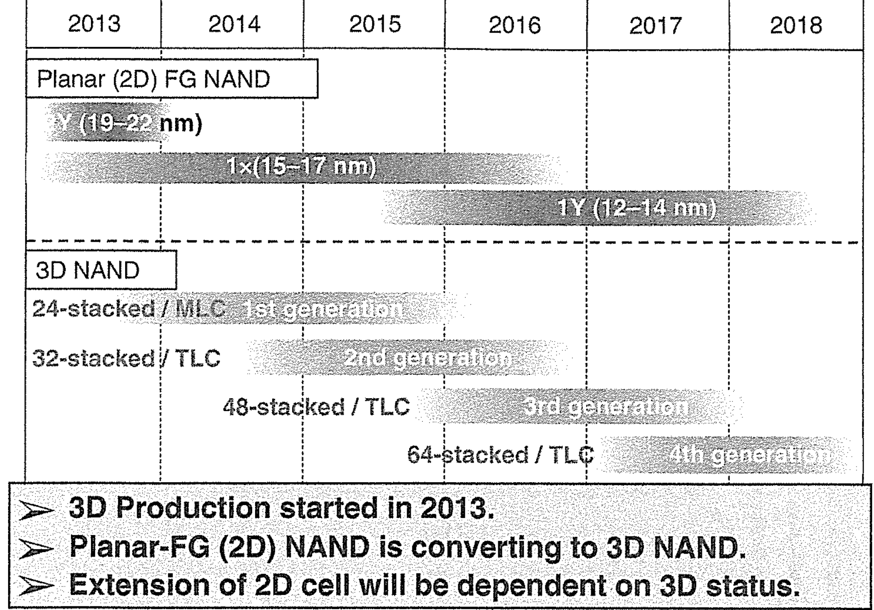

FIGURE 8.52 Transition from a planar 2D NAND cell to a 3D NAND cell.

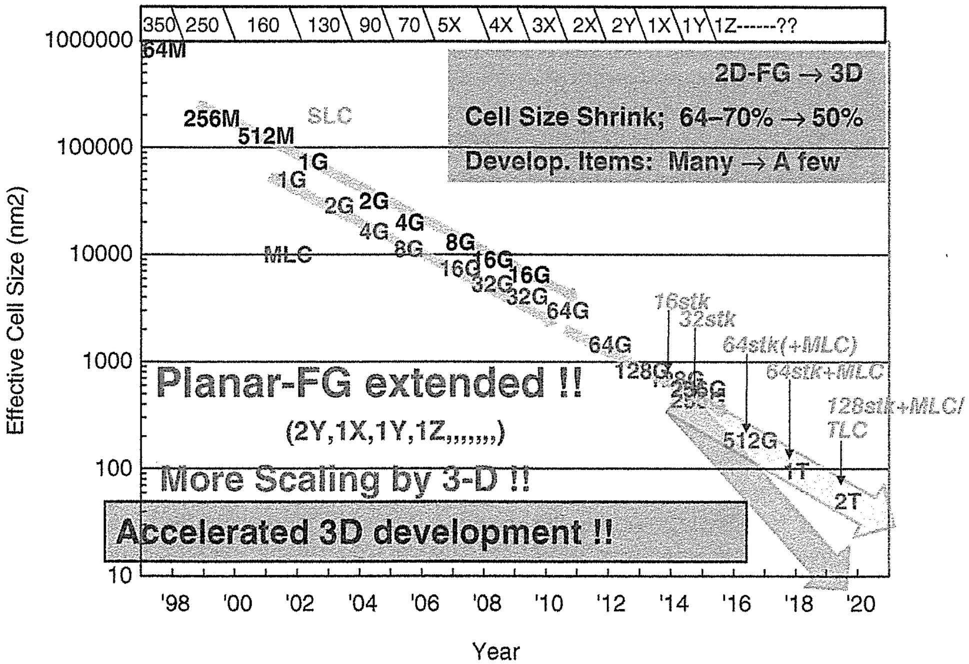

FIGURE 8.53 The case of the accelerated development of a 3D NAND flash memory cell.

Micron Ex. 1014, p. 394
Micron v. YMTC
IPR2025-00119

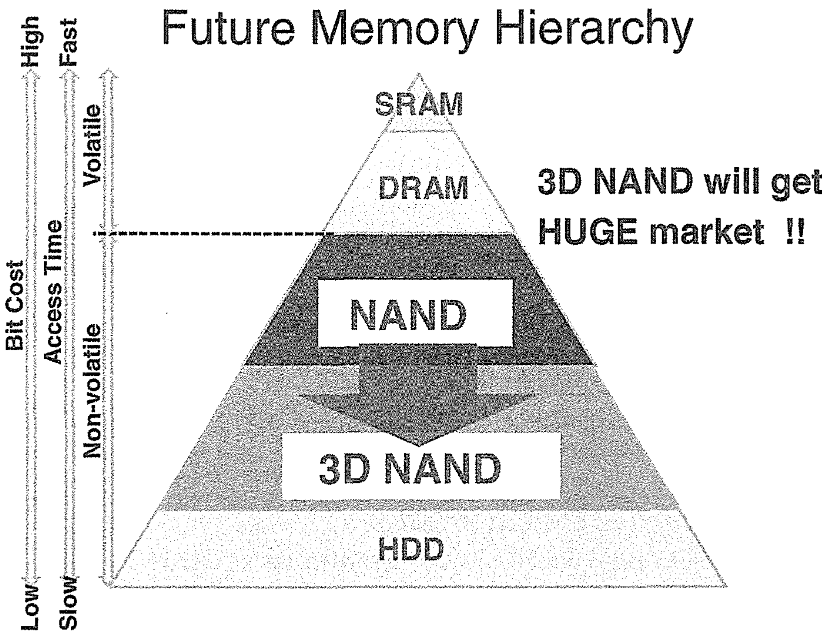

FIGURE 8.54 Future memory hierarchy with a three-dimensional NAND flash cell.

much. Many development items that are related to 2D memory cell scaling may not be developed in 3D flash development. Then, in 3D flash development, it should be focused on a small number of items that are related to process technologies for an increasing number of stacked cells, such as a plug etching, a gate etching, and so on. Therefore, the development speed of generation-by-generation of 3D NAND flash memory would be accelerated, as shown in Fig. 8.53.

The 3D NAND flash can continue to realize the lower bit cost by increasing the number of stacked cells, regardless of accelerating development or not. Then the magnetic memory, such as HDD, will be further replaced by the NAND flash-related product, including SSD (solid-state drive) for consumer and enterprise server, as shown in Fig. 8.54. The market size of SSD will be tremendously expanded in the near future.

REFERENCES

[1] Aritome, S. 3D Flash Memories, International Memory Workshop 2011 (IMW 2011), short course.

[2] Choi, E.-S.; Park, S.-K. Device considerations for high density and highly reliable 3D NAND flash cell in near future, *Electron Devices Meeting (IEDM), 2012 IEEE International*, pp. 9.4.1–9.4.4, 10–13 Dec. 2012.

[3] Chen, C.-P.; Lue, H.-T.; Hsieh, C.-C.; Chang, K.-P.; Hsieh, C.-C.; Lu, C.-Y. Study of fast initial charge loss and it's impact on the programmed states V_t distribution of charge-trapping NAND Flash, *Electron Devices Meeting (IEDM), 2010 IEEE International*, pp. 5.6.1, 5.6.4, 6–8 Dec. 2010.

[4] Park, K.-T.; Nam, S.; Kim, D.; Kwak, P.; LEE, D.; Choi, Y.-H.; Choi, M.-H.; Kwak, D.-H.; Kim, D.-H.; Kim, M.-S.; Park, H.-W.; Shim, S.-W.; Kang, K.-M.; Park, S.-W.; Lee, K.; Yoon, H.-J.; Ko, K.; Shim, D.-K.; Ahn, Y.-L.; Ryu, J.; Kim, D.; Yun, K.; Kwon, J.; Shin, S.; Byeon, D.-S.; Choi, K.; Han, J.-M.; Kyung, K.-H.; Choi, J.-H.; Kim, K. Three-dimensional 128 Gb MLC vertical nand flash memory with 24-WL stacked layers and 50 MB/s high-speed programming, *Solid-State Circuits, IEEE Journal of*, vol. PP, no. 99, pp. 1, 10, 2014.

[5] Park, K.-T.; Han, J.-m.; Kim, D.; Nam, S.; Choi, K.; Kim, M.-S.; Kwak, P.; Lee, D.; Choi, Y.-H.; Kang, K.-M.; Choi, M.-H.; Kwak, D.-H.; Park, H.-w.; Shim, S.-w.; Yoon, H.-J.; Kim, D.; Park, S.-w.; Lee, K.; Ko, K.; Shim, D.-K.; Ahn, Y.-L.; Park, J.; Ryu, J.; Kim, D.; Yun, K.; Kwon, J.; Shin, S.; Youn, D.; Kim, W.-T.; Kim, T.; Kim, S.-J.; Seo, S.; Kim, H.-G.; Byeon, D.-S.; Yang, H.-J.; Kim, M.; Kim, M.-S.; Yeon, J.; Jang, J.; Kim, H.-S.; Lee, W.; Song, D.; Lee, S.; Kyung, K.-H.; Choi, J.-H. 19.5 Three-dimensional 128 Gb MLC vertical NAND Flash-memory with 24-WL stacked layers and 50MB/s high-speed programming, *Solid-State Circuits Conference Digest of Technical Papers (ISSCC), 2014 IEEE International*, pp. 334, 335, 9–13 Feb. 2014.

[6] Shim, K.-S.; Choi, E.-S.; Jung, S.-W.; Kim, S.-H.; Yoo, H.-S.; Jeon, K.-S.; Joo, H.-S.; Oh, J.-S.; Jang, Y.-S.; Park, K.-J.; Choi, S.-M.; Lee, S.-B.; Koh, J.-D.; Lee, K.-H.; Lee, J.-Y.; Oh, S.-H.; Pyi, S.-H.; Cho, G.-S.; Park, S.-K.; Kim, J.-W.; Lee, S.-K.; Hong, S.-J. Inherent Issues and Challenges of Program Disturbance of 3D NAND Flash cell, *Memory Workshop (IMW), 2012 4th IEEE International*, pp. 1, 4, 20–23 May 2012.

[7] Yoo, H. S.; Choi, E.; Oh, J. S. ; Park, K. J.; Jung, S. W.; Kim, S.; Shim, K. S.; Joo, H. S.; Jung, S. W.; Jeon, K. S.; Seo, M. S.; Jang, Y. S. ; Lee, S. B.; Lee, J. Y.; Oh, S. H.; Cho, G. S.; Park, S.; Lee, S.; Hong, S. Modeling and optimization of the chip level program disturbance of 3D NAND flash memory, *Memory Workshop (IMW), 2013 5th IEEE International*, pp. 147, 150, 26–29 May 2013.

[8] Wong, M.; Chow, T.; Wong, C. C.; Zhang, D. A quasi two-dimensional conduction model for polycrystalline silicon thin-film transistor based on discrete grains, *Electron Devices, IEEE Transactions on*, vol. 55, no. 8, pp. 2148, 2156, Aug. 2008.

[9] Kim, B.; Lim, S.-H.; Kim, D. W.; Nakanishi, T.; Yang, S.; Ahn, J.-Y.; Choi, H. M.; Hwang, K.; Ko, Y.; Kang, C.-J. Investigation of ultra thin polycrystalline silicon channel for vertical NAND flash, *Reliability Physics Symposium (IRPS), 2011 IEEE International*, pp. 2E.4.1, 2E.4.4, 10–14 April 2011.

[10] Degraeve, R.; Toledano-Luque, M.; Suhane, A.; Van den Bosch, G.; Arreghini, A.; Tang, B.; Kaczer, B.; Roussel, P.; Kar, G.S.; Van Houdt, J.; Groeseneken, G. Statistical characterization of current paths in narrow poly-Si channels, *Electron Devices Meeting (IEDM), 2011 IEEE International*, pp. 12.4.1, 12.4.4, 5–7 Dec. 2011.

[11] Toledano-Luque, M.; Degraeve, R.; Kaczer, B.; Tang, B.; Roussel, P. J.; Weckx, P.; Franco, J.; Arreghini, A.; Suhane, A.; Kar, G.S.; Van den Bosch, G.; Groeseneken, G.; Van Houdt, J. Quantitative and predictive model of reading current variability in deeply scaled vertical poly-Si channel for 3D memories, *Electron Devices Meeting (IEDM), 2012 IEEE International*, pp. 9.2.1, 9.2.4, 10–13 Dec. 2012.

[12] Toledano-Luque, M.; Degraeve, R.; Roussel, P. J.; Luong, V.; Tang, B.; Lisoni, J. G.; Tan, C.-L.; Arreghini, A.; Van den Bosch, G.; Groeseneken, G.; Van Houdt, J. Statistical spectroscopy of switching traps in deeply scaled vertical poly-Si channel for 3D memories, *Electron Devices Meeting (IEDM), 2013 IEEE International*, pp. 21.3.1, 21.3.4, 9–11 Dec. 2013.

Micron Ex. 1014, p. 396
Micron v. YMTC
IPR2025-00119

[13] Degraeve, R.; Toledano-Luque, M.; Arreghini, A.; Tang, B.; Capogreco, E.; Lisoni, J.; Roussel, P.; Kaczer, B.; Van den Bosch, G.; Groeseneken, G.; Van Houdt, J. Characterizing grain size and defect energy distribution in vertical SONOS poly-Si channels by means of a resistive network model, *Electron Devices Meeting (IEDM), 2013 IEEE International*, pp. 21.2.1, 21.2.4, 9–11 Dec. 2013.

[14] Nowak, E.; Kim, J.-H.; Kwon, H. Y.; Kim, Y.-G.; Sim, J. S. ; Lim, S.-H.; Kim, D. S.; Lee, K.-H.; Park, Y.-K.; Choi, J.-H.; Chung, C. Intrinsic fluctuations in Vertical NAND flash memories, *VLSI Technology (VLSIT), 2012 Symposium on*, pp. 21, 22, 12–14 June 2012.

[15] Jeong, M.-K.; Joe, S.-M.; Jo, B.-S.; Kang, H.-J.; Bae, J.-H.; Han, K.-R.; Choi, E.; Cho, G.; Park, S.-K.; Park, B.-G.; Lee, J.-H. Characterization of traps in 3-D stacked NAND flash memory devices with tube-type poly-Si channel structure, *Electron Devices Meeting (IEDM), 2012 IEEE International*, pp. 9.3.1, 9.3.4, 10–13 Dec. 2012.

[16] Jeong, M.-K.; Joe, S.-M.; Seo, C.-S.; Han, K.-R.; Choi, E.; Park, S.-K.; Lee, J.-H. Analysis of Random Telegraph Noise and low frequency noise properties in 3-D stacked NAND flash memory with tube-type poly-Si channel structure, *VLSI Technology (VLSIT), 2012 Symposium on*, pp. 55, 56, 12–14 June 2012.

[17] Park, J. K.; Moon, D.-I.; Choi, Y.-K.; Lee, S.-H.; Lee, K.-H.; Pyi, S. H.; Cho, B. J. Origin of transient V_{th} shift after erase and its impact on 2D/3D structure charge trap flash memory cell operations, *Electron Devices Meeting (IEDM), 2012 IEEE International*, pp. 2.4.1, 2.4.4, 10–13 Dec. 2012.

[18] Jeong, M.-K.; Joe, S.-M.; Kang, H.-J.; Han, K.-R.; Cho, G.; Park, S.-K.; Park, B.-G.; Lee, J.-H. A new read method suppressing effect of random telegraph noise in NAND flash memory by using hysteretic characteristic, *VLSI Technology (VLSIT), 2013 Symposium on*, pp. T154, T155, 11–13 June 2013.

[19] Ghetti, A.; Compagnoni, C.M.; Spinelli, A.S.; Visconti, A. Comprehensive analysis of random telegraph noise instability and its scaling in deca–nanometer Flash memories, *IEEE Transactions on Electron Devices*, vol. 56, pp. 1746–1752, 2009.

[20] Franco, J.; Kaczer, B.; Toledano-Luque, M.; Roussel, P. J.; Mitard, J.; Ragnarsson, L.-A.; Witters, L.; Chiarella, T.; Togo, M.; Horiguchi, N.; Groeseneken, G.; Bukhori, M. F.; Grasser, T.; Asenov, A. Impact of single charged gate oxide defects on the performance and scaling of nanoscaled FETs, *Reliability Physics Symposium (IRPS), 2012 IEEE International*, pp. 5A.4.1, 5A.4.6, 15–19 April 2012.

[21] Kimura, M.; Inoue, S.; Shimoda, T.; Eguchi, T. Dependence of polycrystalline silicon thin-film transistor characteristics on the grain-boundary location, *Journal of Applied Physics*, vol. 89, no. 1, pp. 596, 600, Jan 2001.

[22] Kang, D.; Lee, S.; Park, H.-M.; Lee, D.-J.; Kim, J.; Seo, J.; Lee, C.; Song, C.; Lee, C.-S.; Shin, H.; Song, J.; Lee, H.; Choi, J.-H.; Jun, Y.-H. A new approach of NAND flash cell trap analysis using RTN characteristics, *VLSI Technology (VLSIT), 2011 Symposium on*, pp. 206, 207, 14–16 June 2011.

[23] Compagnoni, M. C.; Gusmeroli, R.; Spinelli, A. S.; Lacaita, A. L.; Bonanomi, M.; Visconti, A. Statistical model for random telegraph noise in flash memories, *Electron Devices, IEEE Transactions on*, vol. 55, no. 1, pp. 388, 395, Jan. 2008.

[24] Takeuchi, K.; Nagumo, T.; Yokogawa, S.; Imai, K.; Hayashi, Y. Single-charge-based modeling of transistor characteristics fluctuations based on statistical measurement of RTN amplitude, *VLSI Technology, 2009 Symposium on*, pp. 54, 55, 16–18 June 2009.

Micron Ex. 1014, p. 397
Micron v. YMTC
IPR2025-00119

[25] Nagumo, T.; Takeuchi, K.; Hase, T.; Hayashi, Y. Statistical characterization of trap position, energy, amplitude and time constants by RTN measurement of multiple individual traps, *Electron Devices Meeting (IEDM), 2010 IEEE International*, pp. 28.3.1, 28.3.4, 6–8 Dec. 2010.

[26] Kang, H.-J.; Jeong, M.-K.; Joe, S.-M.; Seo, J.-H.; Park, S.-K.; Jin, S. H.; Park, B.-G.; Lee, J.-H. Effect of traps on transient bit-line current behavior in word-line stacked nand flash memory with poly-Si body, *VLSI Technology (VLSI-Technology): Digest of Technical Papers, 2014 Symposium on*, pp. 1, 2, 9–12 June 2014.

[27] Kang, D., Lee, C., Hur, S., Song, D., and Choi, J.-H. A new approach for trap analysis of vertical NAND flash cell using RTN characteristics., *Electron Devices Meeting (IEDM), 2014 IEEE International*, pp. 367–370, Dec. 2014.

[28] Kimura, M.; Yoshino, T.; Harada, K. Complete extraction of trap densities in poly-Si thin-film transistors, *Electron Devices, IEEE Transactions on*, vol. 57, no. 12, pp. 3426, 3433, Dec. 2010.

[29] Congedo, G.; Arreghini, A.; Liu, L.; Capogreco, E.; Lisoni, J. G.; Huet, K.; Toque-Tresonne, I.; Van Aerde, S.; Toledano-Luque, M.; Tan, C.-L.; Van den Bosch, G.; Van Houdt, J. Analysis of performance/variability trade-off in Macaroni-type 3-D NAND memory, *Memory Workshop (IMW), 2014 IEEE 6th International*, pp. 1, 4, 18–21 May 2014.

[30] Lisoni, J. G.; Arreghini, A.; Congedo, G.; Toledano-Luque, M.; Toque-Tresonne, I.; Huet, K.; Capogreco, E.; Liu, L.; Tan, C.-L.; Degraeve, R.; Van den Bosch, G.; Van Houdt, J. Laser thermal anneal of polysilicon channel to boost 3D memory performance, *VLSI Technology (VLSI-Technology): Digest of Technical Papers, 2014 Symposium on*, pp. 1, 2, 9–12 June 2014.

[31] Aritome, S. US Patent 8,891,306.

[32] Im, J.-w.; Jeong, W.-P., Kim, D.-H., Nam, S.-W., Shim, D.-K., Choi, M.-H., Yoon, H.-J., Kim, D.-H., Kim, Y.-S., Park, H.-W., Kwak, D.-H., Park, S.-W., Yoon, S.-M., Hahn, W.-G., Ryu, J.-H., Shim, S.-W., Kang, K.-T., Choi, S.-H., Ihm, J.-D., Min, Y.-S., Kim, I.-M., Lee, D.-S., Cho, J.-H., Kwon, O.-S., Lee, J.-S., Kim, M.-S., Joo, S.-H., Jang, J.-H., Hwang, S.-W., Byeon, D.-S., Yang, H.-J., Park, K.-T., Kyung, K.-H., Choi, J.-H. A 128 Gb 3b/cell V-NAND Flash Memory with 1Gb/s I/O rate, *Solid-State Circuits Conference Digest of Technical Papers (ISSCC), 2015 IEEE International*, pp. 23–25 Feb. 2015.

[33] Aritome, S. Scaling challenges beyond 1X-nm DRAM and NAND flash, Joint Rump session in VLSI Symposium 2012.

Micron Ex. 1014, p. 398
Micron v. YMTC
IPR2025-00119

9

CONCLUSIONS

9.1 DISCUSSIONS AND CONCLUSIONS

The development of NAND flash memory started in 1987 in the R&D center of Toshiba Corporation [1]. The target market was the replacement of magnetic memory, such as HDD, and so on. [2]. For this target, the most important requirement to achieve was "low bit cost." A memory cell size has to be as small as possible to achieve low bit cost. In general, ideal "physical" two-dimensional memory cell size is $4{*}F^2$ (F: feature size), which is defined by 2∗F pitch for both x- and y-directions. The first NAND flash memory cells of 1-μm rule [3, 4] was $8{*}F^2$ cell size by using a wide x-direction pitch of 4 μm (4∗F) because LOCOS isolation width was 3 μm wide due to the limitation of the high-voltage operation. The LOCOS isolation width was limited by the punch-through of the bit-line junction and threshold voltage of the parasitic field LOCOS transistor, because a high voltage of ~22 V was applied to the junction and control gate during programming. In order to reduce the LOCOS isolation width, a new FTI (field-through-implantation) process had been developed [5] (Section 3.2). Very narrow LOCOS isolation width of 0.8 μm (2∗F in 0.4-μm feature size) could be realized. Memory cell size could be scaled down to $6{*}F^2$ by using a 3∗F bit-line pitch in the 0.4-μm rule.

For scaling down memory cell size further, the self-aligned shallow trench isolation cell (the SA-STI cell) had been developed [6] (Sections 3.3 and 3.4). The isolation width could be scaled down to F by using STI, and then the BL pitch could be reduced to ideal 2∗F in comparison with that of LOCOS cell of 3∗F bit-line pitch. Therefore,

Nand Flash Memory Technologies, First Edition. Seiichi Aritome.
© 2016 The Institute of Electrical and Electronics Engineers, Inc. Published 2016 by John Wiley & Sons, Inc.

Micron Ex. 1014, p. 399
Micron v. YMTC
IPR2025-00119

the cell size of NAND flash memory could be drastically shrunk to 66% (from $6*F^2$ to ideal $4*F^2$; F: feature size). The SA-STI cell process was applied to a NAND flash product with the structure of the SA-STI with an FG wing [7,8] (Section 3.3), because the aspect ratio of the stacked gate could be reduced by the FG wing structure. The SA-STI cell with an FG wing had been used from 0.25-μm generation to 0.12-μm generation. After that, the SA-STI cell without an FG wing had been used from 90-nm generation [6] (Section 3.4). The SA-STI cell has an excellent scalability. The cell size could decrease straightforward as feature-size decreased from 0.25 μm [6] to 1X nm [9] (Figs. 3.1 and 3.2 in Section 3.1). Therefore, the SA-STI cell structure and process have been used more than 10 years and 10 generations due to simple process and structure. Moreover, the SA-STI cell has another advantage, namely, an excellent reliability. The tunnel oxide has no degradation at the STI edge corner because of no sharp STI edge corner by fabricating a floating gate with STI patterning.

The cell size of NAND flash became ideal $4*F^2$ by the SA-STI cell. The feature size (F) is normally determined by the capability of the lithography tool. At present, the most advanced lithography tool is the ArF immersion (ArFi) stepper. Minimum feature size is 38–40 nm. Then the scaling of feature size (F) was limited by 38–40 nm. In order to accelerate to scale down the NAND flash memory cell size further, the double patterning process had started to be used from the 3X-nm generation. The sidewall spacer was used as a patterning mask in the conventional double patterning process. Thanks to double patterning, feature size could be scaled down from 38–40 nm to 19–20 nm. Furthermore, quadruple (×4) patterning had been used beyond 20 nm [9]. Feature size (F) could be scaled down to 10 nm by using ArFi.

As shown in the ITRS roadmap (http://www.itrs.net/), from around the year 2005, the NAND flash memory became a so-called "process driver" device, which has led to the scaling and development of lithography/patterning for minimum device dimension (line/space pitch), by replacing DRAM. This is because the NAND flash memory cell can be easily scaled down as scaling a minimum device dimension, without any electrical, operational, and reliability limitations due to the contribution of key technologies of the SA-STI cell and the uniform program/erase scheme. Therefore, the development of NAND flash memory has had a great impact on leading fine pitch patterning technologies, such as ArF immersion lithography, double patterning, quadruple patterning, and so on.

The multilevel cell is another important technology to reduce "effective" memory cell size without F scaling. In the multilevel cell, V_t distribution width has to be tightly controlled to have enough RWM (read window margin) [10] to prevent from read failure. Several advanced operations for multilevel cells were presented in Chapter 4 to obtain a tight V_t distribution as well as high reliability and performance. The multilevel cells NAND flash product of MLC (2 bits/cell), TLC (3 bits/cell), and QLC (4 bits/cell) are using these advanced operations and architectures, such as ISPP program, bit-by-bit verify, two-step verify scheme, pseudo-pass scheme in page program (Section 4.2), the advanced page program sequence, ABL architecture (Section 4.3), moving read algorithm (Section 4.7), and so on.

The memory cell size of the SA-STI cell could be intensively scaled down by using double and quadruple patterning. However, the SA-STI cell has been facing serious

physical limitations, such as floating-gate capacitive coupling interference, electron injection spread, RTN, high field limitation, patterning limitation, and so on. The scaling challenge and limitations were discussed in Chapter 5. Read window margin (RWM) was quantitatively analyzed, and then the solutions to overcome scaling limitations were clarified [10] (Section 5.2). It was concluded that 1Y- to 1Z-nm (13- to 10-nm) SA-STI cells could be realized by using the 60% air-gap process.

The other important requirement for NAND flash is "high reliability." At a term of starting NAND flash development, the program/erase schemes were intensively discussed by an internal development team in order to select a proper scheme. It was not clear how program/erase scheme had an impact on reliability. Then, the reliability of the NAND flash cell was analyzed in several program/erase (P/E) schemes, such as the CHE (channel hot-electron) program scheme [1], the nonuniform P/E scheme [11, 12], and the uniform P/E scheme [13–15] to decide the proper P/E scheme.

The P/E cycling endurance and data retention characteristics were evaluated and analyzed in the two P/E schemes [13, 16] (Sections 6.2 and 6.3). It had been clarified that the uniform P/E scheme, which is used in the NAND flash, had appropriate reliability in comparison with other schemes [13, 16, 17]. And also, the read disturb characteristics had been analyzed in the cells that were subjected to P/E cycling endurance stress [15, 17] (Section 6.4). It had been clarified that the uniform P/E scheme had the better read disturb characteristics because SILC (stress-induced leakage current) could be suppressed by the bipolarity FN (Fowler–Nodheim) program scheme. As a result, the uniform P/E scheme was decided for NAND flash operation.

The uniform P/E scheme had another important advantage. The uniform P/E scheme can realize very low power consumption for programming a large number of memory cells simultaneously (page program). Therefore the programming speed per byte can be quite fast (~100 Mbyte/s). Due to high reliability and fast programming, the uniform program/erase scheme became de facto standard technology. All of the NAND suppliers (Toshiba/SanDisk, Samsung, Micron/Intel, SK Hynix) have used the uniform P/E scheme for all NAND flash products over 20 years.

In 2007, the new three-dimentional (3D) NAND flash cell of BiCS (bit cost scalable technology) was proposed [18] in order to further scale down the memory cell size of NAND flash. The 3D cells have a vertically stacked structure by the new concept of stacked gate layers. Then effective cell size can be reduced without the scaling feature size of F. After proposal of BiCS, many types of 3D cells were proposed. In Chapter 7, major 3D cells were reviewed and compared. Many of them, including BiCS, TCAT (V-NAND), SMArT, and VG-NAND, are using the SONOS charge trap (CT) cell with SiN charge trap layer. However, the SONOS cell has two serious problems of a slow erase (erase V_t saturation) and a poor data retention. To overcome these SONOS problems, the FG (floating-gate) 3D NAND cell of the DC-SF cell (dual control-gate–surrounding floating-gate cell) was proposed [19, 20] (Sections 7.6 and 7.7). Due to replacing a charge trap cell with a FG cell, the problem related with 3D SONOS could be perfectly solved.

Production of the 3D NAND cell was started in 2013. The 24 stacked cells MLC (2b/cell) V-NAND was the first generation of 3D NAND [21]. The charge trap (CT) cell with a vertical channel was used because of its simple fabrication process. The

Micron Ex. 1014, p. 401
Micron v. YMTC
IPR2025-00119

second generation of 32 stacked cells TLC (3b/cell) V-NAND was released in 2014 [22]. In the following generation, the number of stacked cells will be greatly increased to reduce an effective memory cell size and a bit cost in the coming years. The scaling trend is showing that 1 terabit of NAND flash memory will be realized by using more than 64 stacked cells in 2018.

However, in order to further proceed to the higher-density 3D NAND flash memory, several problems that still remain have to be solved. The challenges of 3D NAND flash memory were discussed in Chapter 8. For 3D NAND cell scaling, it is very important to increase the number of stacked cells without increasing the process cost. The small cell current problem and high-aspect RIE process will be critical. The stacked NAND string scheme [23] or the divided stack process would be one of the solutions for future 3D NAND flash memory.

9.2 PERSPECTIVE

From the production start of NAND flash memory in 1992, the worldwide NAND market has been tremendously expanded due to the boom of a digital camera, USB drive, MP3 player, smartphone, tablet-PC, and SSD (solid-state drive). The overall NAND market is expected to hit $35 billion in 2015. NAND flash memory has created new large volume markets and industries of consumer, computer, mass-storage, and enterprise server. This trend is still so rapidly growing in the world.

The reasons why the NAND flash memory was accepted to the emerging applications were a low bit cost, high reliability, high performance (fast programming), and low power consumption. To achieve these requirements, over 25 years, many indispensable technologies have been developed and implemented to NAND flash products as a de facto standard [24], as described in this book. In order to continue this trend, NAND flash memory has to continuously satisfy market requirements. The most important requirement is the low bit cost. A bit cost of NAND flash memory has to be further reduced. Therefore, the scaling of an effective memory cell size is essential.

The 2D NAND flash has continued mass production by using a 15-nm technology in 2015 (Fig. 8.52). The next generation of 12- to 14-nm technology would come into production on 2016. And the following generation, which is probably close to 10-nm technology, would be possible to implement, as shown in Chapter 5. However, even in 12- to 14-nm technology, it will be tough to realize due to serious scaling limitation. The operation or system solutions will be key technologies to manage a scaling limitation. And the minimum feature size (F) will not exceed over 9.5–10 nm, because it is a limitation of ArFi quadruple patterning. If F is over 9.5–10 nm, process cost greatly increases.

Production of 3D NAND had already started; however, 2D NAND flash will not quickly disappear in the market, because 2D NAND flash is widely accepted in the market and also has a big infrastructure for production. Then 2D NAND flash will continue in production parallel with 3D NAND flash for more than 5 years.

Micron Ex. 1014, p. 402
Micron v. YMTC
IPR2025-00119

For the 3D NAND flash, the increasing number of stacked cells is very important to realize the smaller effective cell size. If the number of stacked cells is increased to 128 cells, a 2-terabit NAND flash memory product is expected. A critical challenge to increase the number of stacked cells is the extremely high aspect ratio process. The multi-stacked process, which has the divided stacked layers (Fig. 8.44 in Chapter 8), can solve this issue. If the multi-stacked process is realized, the scaling pace of the effective cell size would be much accelerated, as 50% shrinkage of effective cell size for each generation in contrast to 64–70% shrinkage in 2D planar FG cell, as described in Section 8.10 (see Fig. 8.53).

On the other hand, a small cell current is also a serious issue in increasing the number of stacked cells. As one of the solutions, the stacked NAND string scheme, as shown in Fig. 8.46 in Chapter 8, can solve this issue as well as an issue of high aspect ratio process. If the stacked NAND string scheme is successfully developed, low bit cost and high-performance 3D NAND flash memory can be realized.

The low power consumption is other important requirement for NAND flash memory. The power consumption of storage memory has been greatly reduced by using NAND flash memory, compared with magnetic memory of HDD. In the data center, SSD based on NAND flash memory can reduce the power consumption of an enterprise server, replaced HDD, because of low power operation in NAND flash memory as well as low cooling power. The NAND flash is successfully contributing to the ecological environment of the earth in the present and for the future.

REFERENCES

[1] Masuoka, F. Momodomi, M.; Iwata, Y.; Shirota, R. New ultra high density EPROM and flash EEPROM with NAND structure cell, *Electron Devices Meeting, 1987 International,* vol. 33, pp. 552– 555, 1987

[2] Masuoka, F. Flash memory makes a big leap, *Kogyo Chosakai*, vol. 1, pp. 1–172, 1992 (in Japanese).

[3] Itoh, Y.; Momodomi, M.; Shirota, R.; Iwata, Y.; Nakayama, R.; Kirisawa, R.; Tanaka, T.; Toita, K.; Inoue, S.; Masuoka, F. An experimental 4 Mb CMOS EEPROM with a NAND structured cell, *Solid-State Circuits Conference, 1989. Digest of Technical Papers. 36th ISSCC, 1989 IEEE International,* pp. 134–135, 15–17 Feb. 1989.

[4] Momodomi, M.; Iwata, Y.; Tanaka, T.; Itoh, Y.; Shirota, R.; Masuoka, F. A high density NAND EEPROM with block-page programming for microcomputer applications, *Custom Integrated Circuits Conference, 1989, Proceedings of the IEEE 1989*, pp. 10.1/1–10.1/4, 15–18 May 1989.

[5] Aritome, S.; Hatakeyama, I.; Endoh, T.; Yamaguchi, T.; Shuto, S.; Iizuka, H.; Maruyama, T.; Watanabe, H.; Hemink, G.; Sakui, K.; Tanaka, T.; Momodomi, M., Shirota, R. An advanced NAND-structure cell technology for reliable 3.3V 64 Mb electrically erasable and programmable read only memories (EEPROMs), *Japanese Journal of Applied Physics*, vol. 33, (1994) pp. 524–528, part 1, no. 1B, Jan. 1994.

[6] Aritome, S.; Satoh, S.; Maruyama, T.; Watanabe, H.; Shuto, S.; Hemink, G. J.; Shirota, R.; Watanabe, S.; Masuoka, F. A 0.67 μm^2 self-aligned shallow trench isolation cell

Micron Ex. 1014, p. 403
Micron v. YMTC
IPR2025-00119

(SA-STI cell) for 3 V-only 256 Mbit NAND EEPROMs, *Electron Devices Meeting, 1994. IEDM '94. Technical Digest, International*, pp. 61–64, 11–14 Dec. 1994.

[7] Shimizu, K.; Narita, K.; Watanabe, H.; Kamiya, E.; Takeuchi, Y.; Yaegashi, T.; Aritome, S.; Watanabe, T. A novel high-density $5F^2$ NAND STI cell technology suitable for 256 Mbit and 1 Gbit flash memories, *Electron Devices Meeting, 1997. IEDM '97. Technical Digest, International*, pp. 271–274, 7–10 Dec. 1997.

[8] Takeuchi, Y.; Shimizu, K.; Narita, K.; Kamiya, E.; Yaegashi, T.; Amemiya, K.; Aritome, S. A self-aligned STI process integration for low cost and highly reliable 1 Gbit flash memories, *VLSI Technology, 1998. Digest of Technical Papers. 1998 Symposium on*, pp. 102–103, 9–11 June 1998.

[9] Hwang, J.; Seo, J.; Lee, Y.; Park, S.; Leem, J.; Kim, J.; Hong, T.; Jeong, S.; Lee, K.; Heo, H.; Lee, H.; Jang, P.; Park, K.; Lee, M.; Baik, S.; Kim, J.; Kkang, H.; Jang, M.; Lee, J.; Cho, G.; Lee, J.; Lee, B.; Jang, H.; Park, S.; Kim, J.; Lee, S., Aritome, S.; Hong, S.; Park, S. A middle-1X nm NAND flash memory cell (M1X-NAND) with highly manufacturable integration Technologies, *Electron Devices Meeting (IEDM), 2011 IEEE International*, pp. 199–202, Dec. 2011.

[10] Aritome, S.; Kikkawa, T. Scaling Challenge of Self-Aligned STI cell (SA-STI cell) for NAND Flash Memories, *Solid-State Electronics*, 82, 54–62, 2013.

[11] Shirota, R., Itoh, Y., Nakayama, R., Momodomi, M., Inoue, S., Kirisawa, R., Iwata, Y., Chiba, M., Masuoka, F. New NAND cell for ultra high density 5V-only EEPROMs, *Digest of Technical Papers—Symposium on VLSI Technology*, 1988, pp. 33–34.

[12] Momodomi, M.; Kirisawa, R.; Nakayama, R.; Aritome, S.; Endoh, T.; Itoh, Y.; Iwata, Y.; Oodaira, H.; Tanaka, T.; Chiba, M.; Shirota, R.; Masuoka, F. New device technologies for 5 V-only 4 Mb EEPROM with NAND structure cell, *Electron Devices Meeting, 1988. IEDM '88. Technical Digest, International*, pp. 412–415, 1988.

[13] Aritome, S.; Kirisawa, R.; Endoh, T.; Nakayama, R.; Shirota, R.; Sakui, K.; Ohuchi, K.; Masuoka, F. Extended data retention characteristics after more than 10^4 write and erase cycles in EEPROMs, *International Reliability Physics Symposium, 1990. 28th Annual Proceedings*, pp. 259–264, 1990.

[14] Kirisawa, R.; Aritome, S.; Nakayama, R.; Endoh, T.; Shirota, R.; Masuoka, F. A NAND structured cell with a new programming technology for highly reliable 5 V-only flash EEPROM, *1990 Symposium on VLSI Technology, 1990. Digest of Technical Papers*. pp. 129–130, 1990.

[15] Aritome, S.; Shirota, R.; Kirisawa, R.; Endoh, T.; Nakayama, R.; Sakui, K.; Masuoka, F. A reliable bi-polarity write/erase technology in flash EEPROMs, *International Electron Devices Meeting, 1990. IEDM '90. Technical Digest, 1990*, pp. 111–114, 1990.

[16] Aritome, S.; Shirota, R.; Sakui, K.; Masuoka, F. Data retention characteristics of flash memory cells after write and erase cycling, *IEICE Transaction Electronics*, vol. E77-C, no. 8, pp. 1287–1295, Aug. 1994.

[17] Aritome, S.; Shirota, R.; Hemink, G.; Endoh, T.; Masuoka, F. Reliability issues of flash memory cells, *Proceedings of the IEEE*, vol. 81, no. 5, pp. 776–788, May 1993.

[18] Tanaka, H.; Kido, M.; Yahashi, K.; Oomura, M.; Katsumata, R.; Kito, M.; Fukuzumi, Y.; Sato, M.; Nagata, Y.; Matsuoka, Y.; Iwata, Y.; Aochi, H.; Nitayama, A. Bit cost scalable technology with punch and plug process for ultra high density flash memory, *VLSI Symposium Technical Digest, 2007*, pp. 14–15.

[19] Aritome, S.; Whang, S.J.; Lee, K.H.; Shin, D.G. Kim, B.Y.; Kim, M. S.; Bin, J.H.; Han, J.H.; Kim, S.J.; Lee, B.M.; Jung, Y.K.; Cho, S.Y.; Shin, C.H.; Yoo, H.S.; Choi,

Micron Ex. 1014, p. 404
Micron v. YMTC
IPR2025-00119

S.M.; Hong, K.; Park, S.K.; Hong, S.J. A novel three-dimensional dual control-gate with surrounding floating-gate (DC-SF) NAND flash cell, *Solid-State Electronics*, vol. 79, pp. 166–171, (2013).

[20] Aritome, S.; Noh, Y.; Yoo, H.; Choi, E.S.; Joo, H.S.; Ahn, Y.; Han, B.; Chung, S.; Shim, K.; Lee, K.; Kwak, S.; Shin, S.; Choi, I.; Nam, S.; Cho, G.; Sheen, D.; Pyi, S.; Choi, J.; Park, S.; Kim, J.; Lee, S.; Hong, S.; Park, S.; Kikkawa, T. Advanced DC-SF Cell Technology for 3-D NAND Flash, *Electron Devices, IEEE Transactions on*, vol. 60, no. 4, pp. 1327–1333, April 2013.

[21] Park, K.-T.; Nam, S.; Kim, D.; Kwak, P.; LEE, D.; Choi, Y.-H.; Choi, M.-H.; Kwak, D.-H.; Kim, D.-H.; Kim, M.-S.; Park, H.-W.; Shim, S.-W.; Kang, K.-M.; Park, S.-W.; Lee, K.; Yoon, H.-J.; Ko, K.; Shim, D.-K.; Ahn, Y.-L.; Ryu, J.; Kim, D.; Yun, K.; Kwon, J.; Shin, S.; Byeon, D.-S.; Choi, K.; Han, J.-M.; Kyung, K.-H.; Choi, J.-H.; Kim, K. Three-dimensional 128 Gb MLC vertical nand flash memory with 24-WL stacked layers and 50 MB/s high-speed programming, *Solid-State Circuits, IEEE Journal of*, vol. 50, no. 1, pp. 204, 213, Jan. 2015.

[22] Im, J.-w.; Jeong, W.-P.; Kim, D.-H.; Nam, S.-W.; Shim, D.-K.; Choi, M.-H.; Yoon, H.-J.; Kim, D.-H.; Kim, Y.-S.; Park, H.-W.; Kwak, D.-H.; Park, S.-W.; Yoon, S.-M.; Hahn, W.-G.; Ryu, J.-H.; Shim, S.-W. Kang, K.-T.; Choi, S.-H.; Ihm, J.-D.; Min, Y.-S.; Kim, I.-M.; Lee, D.-S.; Cho, J.-H.; Kwon, O.-S.; Lee, J.-S.; Kim, M.-S.; Joo, S.-H.; Jang, J.-H.; Hwang, S.-W.; Byeon, D.-S.; Yang, H.-J.; Park, K.-T.; Kyung, K.-H.; Choi, J.-H. A 128 Gb 3b/cell V-NAND flash memory with 1Gb/s I/O rate, *Solid-State Circuits Conference Digest of Technical Papers (ISSCC), 2015 IEEE International*, pp. 23–25 Feb. 2015.

[23] S. Aritome, US Patent 8,891,306.

[24] Aritome, S. NAND Flash Innovations, *Solid-State Circuits Magazine, IEEE*, vol. 5, no. 4, pp. 21, 29, fall 2013.

Micron Ex. 1014, p. 405
Micron v. YMTC
IPR2025-00119

INDEX

ABL architecture. *See* All-bit-line architecture
Advanced DC-SF cell
  charge loss mode with, 326f, 327f
  cross-sectional view of, 324f
  difference among FG/CG/substrate with, 327f
  effective cell sizes for, 318f
  equivalent capacitor network with, 324f
  improvement on, 317–18, 319f
  MCGL process for, 319, 320f, 329
  new programming scheme for, 325–28, 326f, 327f, 328f
  new read scheme for, 319–25, 321f, 322f, 323f, 324f, 325f, 326t
  profile comparison for, 319f
  program disturbance of neighbor cell, 328f
  program/erase cycling endurance characteristics of, 329f
  program inhibit modes of, 326f
  program scheme of, 328f
  reliability of, 329, 329f
Advanced LOCOS cell, 40–42
  operation of, 42, 42t
  process technology of, 42t
  scaling in, 40f, 41–42, 41f, 42t
Advanced NAND flash device technologies
  dummy word line scheme in, 77–82, 78f, 79f, 80t, 81f, 82f, 83f
  p-type floating gate, 82–88, 84f, 85f, 86f, 87f, 88f
Air gap, 149–53
  process flow of, 149, 150f
  program disturb with, 249
  STI, 152, 152f
  threshold voltage shift by FG interference with, 151, 151f
  word-line, 152, 152f
  word-line RC delay with, 352f
All-bit-line (ABL) architecture, 7
  floating-gate capacitive coupling interference in, 112, 112f
  memory core circuits of, 111–12, 111f
  page program sequence for MLC with, 111–13, 111f, 112f
  RWM with, 134

Nand Flash Memory Technologies, First Edition. Seiichi Aritome.
© 2016 The Institute of Electrical and Electronics Engineers, Inc. Published 2016 by John Wiley & Sons, Inc.

Micron Ex. 1014, p. 406
Micron v. YMTC
IPR2025-00119

Array architecture, 18, 19f
program and erase operation with, 24, 24f
read operation for, 22f
Arrhenius law of activation energy, 223
Arrhenius plot, 224f
Attack cell
inhibit, 256, 256f
negative V_t shift phenomena with, 254–58, 254f, 255f, 256f, 257f, 259f, 262f
program-inhibited test with, 254, 254f
program speed dependence of, 256
slow attack cell compared with fast, 257–58
victim cell V_t shift in, 256f

Background pattern dependency (BPD)
page program sequence with, 108
RWM with, 131, 132f, 134, 134f
V_t distribution width with, 94, 94f
Back-side trap in macaroni channel, cell current fluctuation with, 363–66, 363f, 364f, 365f, 366f, 367f
Band-to-band tunneling (BTBT)
channel coupling with, 249, 249f
electron emission with, 196
GIDL current as, 249
program disturb with, 345–50, 350f
schematic illustration of, 249f
self-boosting model with, 241, 243, 243f, 244f
BiCS (Bit cost scalable) technology, 7–8, 383
comparison of other 3D NAND cells with, 276t, 300f, 336–39, 336t, 338f, 339f, 340f
concept of, 275f, 276–78, 277f
cross-sectional SEM photo of, 277f
data retention characteristics of, 285f
effective memory cell size of, 337, 338f
electrical characteristics of, 279–85, 280f, 281f, 282f, 283f, 284f, 285f
erase operation for, 281f
fabrication process of, 278–79
edge of control gates in, 279, 279f
low process cost in, 278f
LPCVD TEOS film in, 279
"macaroni" body vertical transistor in, 282–83, 282f, 283f
pipe-shaped, 285–89, 286f, 287f, 288f, 289f
program disturb phenomena with, 343
program/erase characteristics of, 280f
scalability of, 339f
stacked cells with, 369
subthreshold swing in, 283, 283f
top-down view of, 277f
trap density at poly-silicon in, 282f
WL capacitance with, 335
word-line RC delay with, 350
Bipolarity program/erase, 4t
Bipolarity stress, 225f, 226, 226f, 227f
Bit-by-bit verify operations, 4t, 6f
data modification rule for, 99f
intelligent verify circuit schematic for, 98, 98f
program and erase V_t distributions with, 257, 258f
programmed V_{th} distribution using, 163, 163f
simulated waveform for, 99f
V_t distribution width for MLC in, 98–99, 98f, 99f
Bit cost scalable technology. *See* BiCS technology
Bit line (BL), VG-NAND flash with, 303–5, 304f
Boosting mode, 31–32, 32f
BPD. *See* Background pattern dependency
BTBT. *See* Band-to-band tunneling

Carrier separation technique
analysis of cell structured capacitor with, 260f
electron flow in, 260f
negative V_t shift phenomena with, 260–62, 260f, 261f
CBR. *See* Channel boosting ratio
Cell architecture
array, 18, 19f
cell string, 17, 18f
single, 17, 18f
Cell arrangement, for program-inhibited test, 254, 254f

Micron Ex. 1014, p. 407
Micron v. YMTC
IPR2025-00119

Cell array, peripheral circuit under, 370–71, 371f, 372f
Cell current fluctuation
  back-side trap in macaroni channel in, 363–66, 363f, 364f, 365f, 366f, 367f
  conduction mechanism in, 353–58, 354f, 356f, 357f, 358f
  cumulative curves of, 365f
  V_G dependence in, 358–60, 358f, 359f, 360f
  laser thermal anneal in, 366–68, 367f, 368f
  measured and simulated cell, 361f
  poly-Si channel with, 353–55, 358–64
  RTN with, 358, 358f, 360–63, 361f, 362f, 363f
  3D NAND flash cell with, 353–68, 354f, 356f–368f
Cell operation
  program and erase dynamics
    data retention degraded with, 197, 197f
    high electric field with, 171
    p-type floating gate cycling endurance with, 84–86, 85f, 86f
    threshold voltages calculation in, 30–31, 30f, 31f
    V_{tun} calculation in, 28–29, 29f
    tunnel current calculation in, 28
  program and erase operation, 21–28, 23f
    cell array program scheme with, 24, 24f
    DC-SF cell, 315f
    erase operation of, 26–27, 27f
    erase verify operation of, 27–28, 28f
    four schemes of, 21–23, 22f
    high program voltage with, 23, 24f
    incremental step pulse programming with, 25–26, 25f, 26f
    power consumption with, 23
    program verify operation with, 26
    read disturb with, 197, 198f
    SMArT and, 301, 301f
    tunnel oxide with, 198, 202, 202f, 212
  program boosting operation in, 31–33, 32f, 33f
  read operation
    array architecture in, 22f
    page read, 21, 22f
    single cell, 21, 21f
Cell string architecture, 17, 18f
Cell V_t setting, 34–35, 34f
  V_t distribution width for MLC in, 94–95, 94f, 95f, 96f
CG. *See* Control gate
Channel boosting ratio (CBR), 240, 240f
  channel potential determined by, 242
  self-boosting model with, 241, 242
Channel coupling
  BTBT with, 249, 249f
  program disturb with, 248–49, 249f, 250f
Channel edge coupling, scaling with FGC interference and, 145–48, 146f, 147f
Channel hot electron (CHE) injection, 22–23, 22f, 195
  data retention with, 228f, 229f
  FN tunneling compared to, 227f
  program and erase with, 196t
  read disturb characteristics with, 228f
  write/erase technology with, 227f
  write scheme with, 226
Channel leakage current, 241f
Channel structure, 276t
Channel voltage equation, 240f
Charge storage
  SONOS, 276t, 295, 335
    characteristics of, 279, 280f
    comparison of, 300f, 308f
    conventional device, 279, 315, 317
    data retention characteristic of, 339, 342
    metal gate SONOS structure, 289–90
    nano wire SONOS device, 281f
    problems with slow erase, 383
    program/erase cycling performance of, 337
    quick charge loss with, 341f
    SMArT with, 342
  SONOS/TANOS, 276, 308
CHE injection. *See* Channel hot electron injection
Chemical mechanical polishing (CMP), 48

Micron Ex. 1014, p. 408
Micron v. YMTC
IPR2025-00119

Common source line. *See* CSL
Conduction band profile, 164f
Control gate (CG), 17, 18f
fabrication margin of between FGs and, 170–71, 170f
P-BiCS, 286–87
P-BiCS branched, 288f
program/erase pulses applied to, 210, 211f
voltage during read disturb condition, 230
voltage waveform for programming NAND cell, 154f
Conventional LOCOS cell, 40, 40f
Conventional programming pulse, 97f
Coupling ratio, DC-SF NAND flash cells, 310–11, 311f, 312f
CSL (Common source line)
3D V-NAND flash memory with, 296f
TCAT with, 289–90, 291f, 292f, 293f
VG-NAND flash with, 303–5, 303f, 304f

Data retention
analysis of reliability in, 203–24, 211f, 212f, 213f, 215f–222f, 224f
characteristics of reliability in, 203–10, 203f–209f
DC-SF cell, 317f
distributed cycling test with, 222–24, 222f, 224f
in NAND flash product, 219–21, 220f, 221f
neighbor cells data pattern dependence with, 183
program and erase cycling endurance with, 200–203, 200f, 202f
program and erase scheme dependence with, 203–4, 203f, 204f, 205f
program and erase scheme with, 198–200, 199f
program/erase cycling degradation in, 197, 197f, 210–16, 211f, 212f, 213f, 215f
RBER with, 219–21, 220f, 221f
retention-time distribution with scaling, 176, 176f
scaling impact on, 183–85, 183f, 184f, 185f
SILC with, 216–19, 216f, 217f, 218f, 219f
SONOS with, 339, 342
TCAT with, 293f
temperature dependence with, 204–8, 206f, 207f
3D NAND flash cell and challenges in
quick initial charge loss, 339–42, 340f, 341f, 342f
temperature dependence, 342–43, 342f, 343f
tunnel-oxide thickness dependence with, 208–10, 208f, 209f
tunnel oxide thickness in, 228f
VG-NAND with, 307f
DC-SF cell. *See* Dual control gate—surrounding floating gate cell
DIBL (Drain-induced barrier lowering), 246–48, 247f
Digital still camera (DSC), 1–2
Direct coupling with channel, 145–48, 146f.147f
Distributed cycling test, 222–24
Arrhenius plot for, 224f
equivalent model for, 222f
schematics for, 222, 222f
Double patterning, 4t
Drain-current–gate-voltage curves, 212f
Drain-induced barrier lowering. *See* DIBL
Drain selection transistor (DSL), program disturb phenomena with, 343–45, 349, 349f
DSC. *See* Digital still camera
DSL. *See* Drain selection transistor
Dual control gate-surrounding floating gate cell (DC-SF cell)
advanced
charge loss mode with, 326f, 327f
cross-sectional view of, 324f
difference among FG/CG/substrate with, 327f
effective cell sizes for, 318f
equivalent capacitor network with, 324f
improvement on, 317–18, 319f
MCGL process for, 319, 320f, 329
new programming scheme for, 325–28, 326f, 327f, 328f

Micron Ex. 1014, p. 409
Micron v. YMTC
IPR2025-00119

new read scheme for, 319–25, 321f, 322f, 323f, 324f, 325f, 326t
profile comparison for, 319f
program disturbance of neighbor cell, 328f
program/erase cycling endurance characteristics of, 329f
program inhibit modes of, 326f
program scheme of, 328f
reliability of, 329, 329f
cell threshold voltage with, 316f
charge spreading problem with, 308f
comparison of other 3D NAND cells with, 276t
concern for charge trap 3D cell with, 308, 308f
cross-sectional schematic of, 309f
data-retention characteristics of, 317f
DC-SF NAND flash cells
concept, 309–10, 309f, 310f
coupling ratio, 310–11, 311f, 312f
device fabrication, 312–13, 313f, 314f
effective cell sizes for, 318f
effective memory cell size of, 337, 338f
equivalent circuit of, 310f
FG–FG coupling interference with, 315, 316f
floating-gate capacitance of, 311f
I_d–V_g characteristics of, 315f
operation conditions for, 314t
process sequence of, 313f
profile comparison for, 319f
program and erase characteristics of, 315f
results and discussions for, 313–17, 314t, 315f, 316f, 317f
scalability of, 339f
scaling capability with, 317, 318f
SONOS/TANOS device structure with, 308
TEM image of, 314f
Dummy word-line (DWL), 77–82, 82f, 290, 294
band-to-band electron/hole generation contour with, 81f
GIDL (gate-induced drain leakage) mechanism with, 79, 79f
layout view of, 78f
measured erased V_{th} of memory cells in, 83f
memory cell shielding from high-voltage with, 81–82
program disturb with, 77–78
read and erase condition for, 80t
scaling a NAND flash memory cell with, 78, 80

EASB. *See* Erase-area self-boosting scheme
ECC. *See* Error correction code
EEPROM (Electrically erasable and programmable read-only memory), 1
data retention with, 198
EIS. *See* Electron injection spread
Electrically erasable and programmable read-only memory. *See* EEPROM
Electric field distribution simulation, 173, 173f
Electric field in tunnel oxide (E_{tun}), 28
Electron current density, 236–37
Electron emission
BB-t mechanism of, 196
Fowler-Nordheim tunneling with, 196, 196f
Electron-emitted stress, 225f, 226, 226f, 227f
Electron flow, 260f
Electron-injected stress, 225f, 226, 226f
Electron injection spread (EIS)
methods of, CHE, 22–23, 22f, 195
data retention with, 228f, 229f
FN tunneling compared to, 227f
program and erase with, 196t
read disturb characteristics with, 228f
write/erase technology with, 227f
write scheme with, 226
methods of, Fowler-Nordheim tunneling, 7
CHE compared to, 227f
degradation mechanism of, 196, 196f, 198, 210
electron emission with, 196, 196f, 227f
electron injection with, 195, 196f, 227f

Micron Ex. 1014, p. 410
Micron v. YMTC
IPR2025-00119

Electron injection spread (EIS) (*Continued*)
high electric field for, 171
NAND string boosting model with, 241
SILC with, 226, 231f
uniform program and erase scheme with, 199, 201, 210, 229, 263
RWM with, 131, 132f, 133, 133f
scaling with
effect of lower doping in FG, 158–61, 159f, 160f, 161f
theory of, 153–58, 153f, 154f, 155f, 156f, 157f, 158
V_t distribution width with, 94, 94f
Erase (ERS)
effects of BTBT on, 350, 350f
effects of cell architecture on, 349f
effects of XY mode on, 348, 348f
effects of Y mode on, 347f
V_t distribution with, 345–46, 346f
Erase-area self-boosting scheme (EASB), 32, 33f
Erase operation, 26–27, 27f
Erase verify operation, 27–28, 28f
Erratic over-program, 250–52, 250f
neutral electron-assisted two-step tunneling with, 251
RBER with, 252f
root cause of, 251
schematic model of, 251f
stress-induced leakage current with, 252f
V_t distribution with, 250
Error correction code (ECC), pseudo-pass scheme with, 102
ERS. *See* Erase
E_{tun}. *See* Electric field in tunnel oxide

Failure bit counting (FBC), PPS compared to, 102–4
Failure time, in few-electron memory, 177, 177f
FBC. *See* Failure bit counting
FG. *See* Floating gate
FGC. *See* Floating-gate capacitive coupling
FH. *See* Field oxide height
FIBE. *See* Floating-gate induced barrier enhancement
Field oxide height (FH)
analysis of cell structured capacitor with, 260f, 261f
attack cell program with, 256, 256f, 257f
negative V_t shift phenomena with, 253–54, 253f, 255f, 256, 256f, 257f, 263–64
dependence of, 254, 255f
Field oxide of cell transistor, potential distribution of, 146–47, 146f
Field recess conditions, V_{th} shift dependence on, 147f
Field-through implantation process (FTI process), 43–44, 44f
isolation width with, 381
Field-through implantation (FTI) technique, 8, 40
Flash memory. *See also* NAND flash memory
applications of, 1–2
invention of, 1
Floating gate (FG), 17, 18f. *See also* Planar FG cell
capacitance of, 311f
capacitive coupling effect, 6
effect on EIS of lower doping in, 158–61, 159f, 160f, 161f
electron injection to, 22, 22f, 23, 79
electron phenomena with, 175–78, 176f, 177f
erase operation, electrostatic potential of memory cells with, 82f
fabrication margin of between CG and, 170–71, 170f
Fermi potential of, 230
hot holes injected into, 263
n-type, 84–86, 85f, 86f, 87f, 88
phosphorus-doped poly-Si, 82
planar, 338, 339f
p-type, 82–88, 84f, 85f, 86f, 87f, 88f
SA-STI cell using
characteristics of, 53–56, 54f, 55f, 56f, 57f
characteristics of peripheral devices, 56–59, 58f, 59f
device parameters of, 51t
fabrication process flow of, 50–53, 50f, 51f, 51t, 52f, 53f

Micron Ex. 1014, p. 411
Micron v. YMTC
IPR2025-00119

schematic cross-sectional view of, 52f
structure of, 48–49, 49f
scaling and number of electrons stored on, 175
stored electrons with scaling in, 153f
threshold voltage shift with, 151, 151f
voltage calculation, 142–43
$\sigma\Delta V_t$ calculation with phosphorus doping in, 160–61, 160f
Floating-gate capacitive coupling (FGC)
ABL architecture and interference for, 112, 112f
equations of interference with, 106, 107f
even/odd programming scheme with, 112f
FG–FG coupling interference, DC-SF cell, 315, 316f
original NAND architecture with worst case of, 106, 106f
programmed V_t distribution width with, 135–37, 136f, 137f
RWM with, 131, 132f, 133–37, 136f
scaling with interference from, 10
air gap and low-*k* material, 149–53, 150f, 151f, 152f
coupling with source/drain, 148–49, 148f, 149f, 150f
direct coupling with channel, 145–48, 146f.147f
measurement results on design-rule cell array, 144f
model of, 142–45, 142f, 144f, 145f
parasitic capacitance coupling with, 142f
V_t distribution width with, 94, 94f
Floating-gate induced barrier enhancement (FIBE), 148–49
FN tunneling. *See* Fowler-Nordheim tunneling
4 bits/cell. *See* QLC
Fowler-Nordheim (FN) tunneling, 7
CHE compared to, 227f
degradation mechanism of, 196, 196f, 198, 210
electron emission with, 196, 196f, 227f
electron injection with, 195, 196f, 227f
high electric field for, 171
NAND string boosting model with, 241
SILC with, 226, 231f
uniform program and erase scheme with, 199, 201, 210, 229, 263
FTI process. *See* Field-through implantation process
FTI technique. *See* Field-through implantation technique
Future memory hierarchy, 376f

Gate design rules, V_{th} reductions in, 173, 173f
Gate-induced drain leakage mechanism. *See* GIDL mechanism
Gate process, 276t
Gate space material, threshold voltage shift by FG interference with, 151, 151f
Gate structure, 276t
branched control, 288f
conventional two-dimensional floating, 308
damascened metal, 295
stair-like, 278, 290
surrounding, 301
vertical gate, 303, 303f
GIDL (Gate-induced drain leakage) mechanism, 79, 79f
memory reliability with, 242f, 244–46, 248, 249, 264f
program disturb with, 242f, 244–46, 248, 249
GSL
3D V-NAND flash memory with, 296f
TCAT with, 289–90, 292f
VG-NAND flash with, 303–5, 303f, 304f

High-field problem, 6
High-speed program (HSP), TLC V-NAND with, 296–97, 298f
High-speed programming, 6f, 7
High-voltage transistor (HV Tr), 21
Hot carrier injection mechanism
DIBL with, 246–48, 247f
GIDL mechanism with, 244–46, 248
program disturb with, 244–48, 244f, 245f, 246f, 247f
read disturb with, 235–37, 236f, 237f
schematic of boosting, 237, 237f
simulation of, 245f, 246f

Micron Ex. 1014, p. 412
Micron v. YMTC
IPR2025-00119

HSP. *See* High-speed program
HV Tr. *See* High-voltage transistor

Ideal memory cell size, 6
IEDM (International Electron Device Meeting), 1984 paper discussing flash memory at, 1, 2f
Incremental step pulse program (ISPP), 4t, 6f, 25–26, 248
  PGM and program disturb modes, 345, 346f
  program disturb phenomena with, 345–48, 346f, 347f
  programmed V_t distribution width with, 135–36
  program voltage waveform for, 25f
  RWM with, 135–36
  V_t distribution width for MLC in, 95–97, 97f
  threshold voltage distribution with and without, 26f
Inhibit-pulse waveforms, 242f
Intelligent verify circuit schematic, 98, 98f
Interfered cell, BL current *versus* WL voltage of, 150
International Electron Device Meeting. *See* IEDM
Inter-poly capacitance, 157
Interpoly dielectric (IPD), 17, 18f
Isolation technology, 43–46, 45f
  breakdown voltage of bit-line junction with, 43, 44f
  FTI process with, 43–44, 44f
  between neighboring bit lines, 43f
ISPP. *See* Incremental step pulse program
ITRS roadmap, 382

J/L current. *See* Junction leakage current
Junction leakage (J/L) current, 241

λ
  dependence on Na for fixed cell geometry, 168f
  equation for, 169
Laser thermal anneal (LTA), 366–68
  equivalent grain size diameter with, 367f
  poly-Si with, 366
  subthreshold swing distribution with, 368f
Leakage current density calculation, 216
Line edge roughness (LER), 179
Line-type word line (W/L) cut, 289
Local self-boosting scheme (LSB), 33f
  advanced programming with, 106–8, 107f, 110f
  FG–FG coupling interference with, 134, 135f, 137, 137f
LOCOS cell, 8, 10
  advanced, 40–42, 40f, 41f, 42t
  conventional, 40, 40f
  isolation technology, 42t, 43–46, 43f, 44f, 45f
  isolation width, 381
  program-boosting mechanism in, 239–40
  reliability, 46–48, 46f, 47f
Low bit cost, 6, 6f
  multilevel cell in development of, 93
  NAND flash memory, 37, 381
  SSDs, 376
  stacked cells for, 376
  TLC with, 113
Low-*k* material, 149–53, 150f, 151f, 152f
LPCVD TEOS film, 279
LSB. *See* Local self-boosting scheme
LSE structure, 214, 215f
LTA. *See* Laser thermal anneal

"Macaroni" body vertical transistor, 282–83, 282f, 283f
Macaroni channel devices, 283–84, 283f, 284f
  back-side trap in, 363–66, 363f, 364f, 365f, 366f, 367f
  cumulative curves of current fluctuation with, 365f
  RTN distributions with, 366, 367f
  schematic pictures for, 363f
    capturing/emission with, 366f
  simulation results for, 364f
MCGL (Metal control gate last) process
  advanced DC-SF cell with, 319, 320f, 329
  TEM image of, 320f
MLC. *See* Multilevel cell
MOSFET
  RTN in, 161, 162f
  variation in standard deviation of V_t for, 179f
Moving read algorithm, 122–23, 122f

Micron Ex. 1014, p. 413
Micron v. YMTC
IPR2025-00119

MSB program
advanced programming with, 106–9, 110f
FG–FG coupling interference with, 134–35, 135f, 137f, 140f
Multilevel cell (MLC), 6–7, 6f
advanced operation for, 93–123
cell size reduction for, 382
cell V_t setting in, 34–35, 34f
cost per bit in development of, 93
EASB with, 32
fabrication process of, 93
moving read algorithm for, 122–23, 122f
page program sequence, 10
ABL architecture with, 111–13, 111f, 112f
core architecture and page assignment with, 109f
original scheme, 104–7, 105f, 106f, 107f
parasitic effects of V_{th} distribution with, 108, 109f
program scheme 1, 107–8, 107f, 109f
program scheme 2, 108–11, 109f, 110f, 111f
worst-case cell-to-cell interference with, 110f
program operation for tight V_t distribution width for
bit-by-bit verify operations in, 98–99, 98f, 99f
cell V_t setting in, 94–95, 94f, 95f, 96f
incremental step pulse program (ISPP), 95–97, 97f
pseudo-pass scheme in page program in, 102–4, 102f, 103f, 104f
two-step verify scheme in, 99–102, 99f, 100f, 101f
QLC, 6, 115–19, 118f, 119f, 382
read operation with advanced DC-SF cell, 325f
reliability of SLC compared to, 93
RWM with, 382–83
structure of, 93
V_t distribution image of, 95, 95f
V_t distribution of four states for, 96f
three-level, 119–21, 120f, 121f
TLC, 6, 7
advanced operation for, 113–15, 113f, 114f, 115f, 116f–117f
bit cost with, 113
conventional page program sequence of, 113–14, 113f
new page program sequence of, 114, 114f
page program sequence, 10
V_t distribution image of, 95, 95f
V_t distributions of, 115, 116f–117f
TSP was applied to, 115, 115f, 118f
V-NAND flash memory, 296–98, 297f, 298f, 299f
V-NAND flash memory, 294–95
block and X-decoder schematic diagram of, 296f
main feature of, 295f

NAND flash memory
cell architecture, 17–18, 18f, 19f
development of, 381
first proposed, 1, 2f
history of, 4t–5t
low bit cost as requirement for, 37, 381
peripheral device architecture, 19–21, 20f
principle of, 17–35
program and erase schemes for, 196t
reliability of, 195–266
channel coupling with, 248–49, 249f, 250f
data retention characteristics with, 203–10, 203f–209f
data retention in NAND flash product, 219–21, 220f, 221f
detrapping and SILC with, 229–34, 230f, 231f, 232f, 233f
distributed cycling test with, 222–24, 222f, 224f
erratic over-program with, 250–52, 250f, 251f
hot carrier injection mechanism in, 235–37, 236f, 237f, 244–48, 244f–247f
model of self-boosting with, 238–44, 238f, 239f, 241f, 242f, 243f, 244f
multilevel cell compared to SLC with, 93
negative V_t shift phenomena with, 253–63, 253f–262f
program and erase cycling endurance with, 200–203, 200f, 202f

Micron Ex. 1014, p. 414
Micron v. YMTC
IPR2025-00119

NAND flash memory (*Continued*)
program and erase scheme with, 198–200, 199f
program disturb, 238–49, 238f, 239f, 241f–247f, 249f, 250f
program/erase cycling degradation with, 210–16, 211f, 212f, 213f, 215f
RBER in, 234, 234f, 235f
read disturb, 224–37, 224f–237f, 225t
SILC with, 216–19, 216f, 217f, 218f, 219f
summary of, 263–66, 264f, 265f
requirements for, 6, 6f
scaling for, 10, 129–86
target market of, 3f
technology road map for, 38f
three-dimensional, 7–8
NAND flash memory devices, 37–88. *See also* Three-dimensional NAND flash cell
advanced
dummy word line scheme in, 77–82, 78f, 79f, 80t, 81f, 82f, 83f
p-type floating gate, 82–88, 84f, 85f, 86f, 87f, 88f
LOCOS cell, 8, 10
advanced, 40–42, 40f, 41f, 42t
conventional, 40, 40f
isolation technology, 42t, 43–46, 43f, 44f, 45f
reliability, 46–48, 46f, 47f
planar FG cell
electrical characteristics of, 68–69, 68f, 69f
structure advantages of, 66–67, 67f, 68f
p-type floating gate, 82–88, 84f, 85f, 86f, 87f, 88f
SA-STI cell, 4t, 6, 6f
aspect ratio of, 68f
cross sections of, 67f
data retention with, 216–19, 217f, 218f, 219f
leakage current density calculation, 216
negative V_t shift phenomena with, 253
program and erase characteristics of, 64f
program/erase cycling endurance with, 216–19, 216f, 217f, 218f, 219f
RWM with, 131, 382–83
scaling with, 129, 130f, 381–82
structure along word line, 253
structure challenge in scaling, 170–71, 170f
subthreshold characteristics of, 64f
TDDB characteristics of tunnel oxide in, 65, 65f
SA-STI cell with FG wing
characteristics of, 53–56, 54f, 55f, 56f, 57f
characteristics of peripheral devices, 56–59, 58f, 59f
fabrication process flow of, 50–53, 50f, 51f, 51t, 52f, 53f
schematic view of, 49f
structure of, 48–49, 49f
SA-STI cell without FG wing
characteristics of, 64–66
coupling ratio as function of gate width of, 61f
cross-sectional view of, 60f
fabrication process flow of, 60–61, 62f
memory cell parameters of, 61t
structure of, 59–60, 60f, 61f, 61t
top view of, 60f
structure scaling of, 37, 38f
SWATT cell, 8, 10, 69–76
concept of, 70–71, 70f, 71f, 72f
electrical characteristics of, 74–76, 74f, 75f, 76f, 77f
fabrication process of, 71–74, 73f
N-ch (N-channel), 19, 20f
Negative V_t shift phenomena
attack cell in, 254–58, 254f, 255f, 256f, 257f, 259f, 262f
background with, 253–54, 253f, 254f
carrier separation in programming conditions, 260–62, 260f, 261f
experiment with, 253–54, 253f, 254f
model, 262–63, 262f
negative V_t shift, 254–56, 255f, 256f
program-inhibited test with, 254, 254f

Micron Ex. 1014, p. 415
Micron v. YMTC
IPR2025-00119

program speed and victim cell V_t dependence, 256–59, 257f, 258f, 259f
RWM with, 253
Neutral electron-assisted two-step tunneling, 251
New NOR-type flash P/E scheme, 22f, 23
Non-uniform P/E scheme, 22f
NOR-type flash P/E scheme, 22f, 23
N-type floating gate
cycling endurance of, 88
hole/electron erasing tunneling current distribution with, 87f
program/erase cycling endurance of, 84–86, 85f, 86f
N-type phosphorus-doped poly-Si floating gate, 82

1.5 bits/cell. *See* Three-level (1.5 bits/cell) NAND flash
128-Gb MLC V-NAND flash memory, 294–95
block and X-decoder schematic diagram of, 296f
CSL with, 296f
GSL with, 296f
main feature of, 295f
SSL with, 294, 296f
128-Gb TLC V-NAND flash memory, 296–98
bit-line architecture of, 296, 297f
device summary of, 298f
die micrograph and bit density of, 297f
energy consumption during programming with, 299f
high-speed program algorithm for, 296–97, 298f
threshold voltage distribution of, 299f
ONO. *See* Oxide–nitride–oxide
OTF. *See* Oxide trap fluctuations
Oxide gate space material, threshold voltage shift by FG interference with, 151, 151f
Oxide–nitride–oxide (ONO), 200
Oxide trap fluctuations (OTF), 180, 181f

Page programming, 4t, 6f
flowchart of, 102f
program performance of, 104f
pseudo-pass scheme in, 102–4, 102f, 103f, 104f
Page program sequence
ABL architecture with, 111–13, 111f, 112f
core architecture and page assignment with, 109f
MLC, 10
original scheme, 104–7, 105f, 106f, 107f
parasitic effects of V_{th} distribution with, 108, 109f
program scheme 1, 107–8, 107f, 109f
program scheme 2, 108–11, 109f, 110f, 111f
RWM with, 134, 135f
TLC, 10
conventional sequence, 113–14, 113f
new sequence, 114, 114f
TSP, 115, 115f, 118f
worst-case cell-to-cell interference with, 110f
Patterning limitation with scaling, 178–79, 178f, 179f
P-BiCS. *See* Pipe-shaped BiCS
PC. *See* Pipe-connection
P-ch (P-channel), 19–20, 20f
Peripheral circuit under cell array, 3D NAND flash cell, 370–71
cross-sectional image of, 372f
memory chip layout image of, 371f
Peripheral device architecture, 19–21, 20f
Peripheral transistors, 20, 20f
cross-sectional view of, 53f
P/E scheme. *See* Program/erase scheme
P-FG cells. *See* Planar FG cells
PGM. *See* Programming
Pipe-connection (PC), 285
Pipe-shaped BiCS (P-BiCS), 285–89, 289f
advantages of, 287f
branched control gate structure with, 288f
control gates with, 286–87
crosssectional view of, 286f
data retention characteristics of, 285f
fabrication process of, 286, 287f
row decoder configuration of, 287–89, 288f
schematic of, 286f

Micron Ex. 1014, p. 416
Micron v. YMTC
IPR2025-00119

Planar FG (P-FG) cells, 338, 339f
aspect ratio of, 68f
cell-to-cell interference with, 68f
cross sections of, 67f
electrical characteristics of, 68–69, 68f, 69f
program/erase characteristics of, 69f
structure advantages of, 66–67, 67f, 68f
Poly-Si channel
cell current fluctuation with
conduction mechanism in, 353–55
V_G dependence in, 358–60
RTN in, 360–64
laser thermal anneal with, 366
number of stacked cells with, 368, 369f
stacked cells with, 368
Power consumption
external high-voltage-supply scheme with, 373f, 374f
measured dissipation with, 374f
SSDs with, 371–74, 373f, 374f, 385
3D NAND flash cell, 371–74, 373f, 374f
PPS. *See* Pseudo-pass scheme
Process driver device, 382
Process-induced fluctuations, 180, 181f
Process node, threshold voltage shift as function of, 166f
Program and erase dynamics
data retention degraded with, 197, 197f
high electric field with, 171
p-type floating gate cycling endurance with, 84–86, 85f, 86f
threshold voltages calculation in, 30–31, 30f, 31f
V_{tun} calculation in, 28–29, 29f
tunnel current calculation in, 28
Program and erase operation
cell array program scheme with, 24, 24f
DC-SF cell, 315f
erase operation of, 26–27, 27f
erase verify operation of, 27–28, 28f
four schemes of, 21–23, 22f
high program voltage with, 23, 24f
incremental step pulse programming with, 25–26, 25f, 26f
power consumption with, 23
program verify operation with, 26
read disturb with, 197, 198f
SMArT and, 301, 301f
tunnel oxide with, 198, 202, 202f, 212
Program boosting operation, 31–33, 32f, 33f
Program disturb
air gap with, 249
analysis of, 345–50, 346f, 347f, 348f, 349f, 350f
BiCS with, 343
boosting mode in, 31–32, 32f
BTBT with, 345–50, 350f
channel coupling with, 248–49, 249f, 250f
defined, 31
DIBL with, 246–48, 247f
drain selection transistor with, 343–45, 349, 349f
dummy word line with, 77–78
GIDL mechanism with, 242f, 244–46, 248, 249
hot carrier injection mechanism with, 244–48, 244f, 245f, 246f, 247f
ISPP with, 345–48, 346f, 347f
model of self-boosting with, 238–44, 238f, 239f, 241f, 242f, 243f, 244f
new modes of, 343–45, 344f, 345f
V_{pass} mode in, 31, 32f
SMArT with, 343
TCAT with, 343
3D NAND flash cell challenges with, 343–50, 344f–350f
V-NAND with, 343
Program/erase cycling endurance
advanced DC-SF cell, 329f
analysis of reliability with, 203–24, 211f, 212f, 213f, 215f–222f, 224f
data retention characteristics with, 203–10, 203f–209f, 383
data retention in NAND flash product with, 219–21, 220f, 221f
degradation in, 197, 197f, 210–16, 211f, 212f, 213f, 215f
distributed cycling test with, 222–24, 222f, 224f
drain-current–gate-voltage curves for, 212f
endurance characteristics with, 200–203, 200f, 202f
program and erase scheme in, 198–200, 199f

Micron Ex. 1014, p. 417
Micron v. YMTC
IPR2025-00119

SILC with, 216–19, 216f, 217f, 218f, 219f
SONOS with, 337
TCAT with, 293f
threshold voltage shift in, 213–14, 213f
VG-NAND with, 307f
Program/erase (P/E) scheme, 7
FN tunneling with uniform, 199, 201, 210, 229, 263
NAND flash, 196t
new NOR-type flash, 22f, 23
non-uniform, 22f
NOR-type flash, 22f, 23, 196t
read disturb with dependence in, 224–29, 224f–229f, 225t
reliability and data retention with, 198–200, 199f
uniform, 22f, 383
Program-inhibited test, cell arrangement for, 254, 254f
Program interference phenomena, 171
Programming (PGM)
effects of BTBT on, 350, 350f
effects of cell architecture on, 349f
effects of XY mode on, 348f
effects of Y mode on, 347f
V_t distribution with, 345–46, 346f
Program pulse waveforms, 97f, 242f
Pseudo-pass scheme (PPS)
error correction code with, 102
FBC compared to, 102–4
flowchart of page program sequence with, 102f
in page program, V_t distribution width for MLC in, 102–4, 102f, 103f, 104f
program performance of, 104f
P-type floating gate, 82–88, 84f, 85f, 86f, 87f, 88f
advantage to, 83
cycling endurance of, 88, 88f
data retention characteristic of, 88, 88f
doping concentration in, 83–84
hole/electron erasing tunneling current distribution with, 87f
program/erase cycling endurance of, 84–86, 85f, 86f
transient deep-depletion in, 84, 84f
QLC (4 bits/cell), 6, 382
advanced operation for, 115–19, 118f, 119f
QSPT (Quadruple patterning) process, 178, 178f
Quick initial charge loss, 339–42, 340f, 341f, 342f

Random dopant fluctuations (RDF), 180, 181f
V_t variation with, 182–83
Random telegraph noise (RTN), 6
cell current fluctuation with, 358, 358f, 360–63, 361f, 362f, 363f
measured and simulated, 362f
Monte Carlo simulation in investigation of, 163, 163f
in MOSFET, 161, 162f
poly-Si channel with, 360–64
profile and change capturing time with, 365f
programmed V_t distribution width with, 135, 136f
RWM with, 131, 134, 135, 136f
scaling limit by, 10, 131, 134, 135, 136f
V_t distribution width with, 94, 94f
threshold voltage fluctuation due to, 162, 162f
traps between poly-Si and front-insulator with, 366, 367f
RBER (Raw bit error rate)
charge-loss, 221f
data retention performance with, 219–21, 220f, 221f
erratic over-programming with, 252f
of read disturb, 234, 234f, 235f
room-temperature retention time with, 220f
RC (Resistance-capacitance) delay
air gap with, 352f
bias and block diagrams of, 352f
BiCS with, 350
SMArT with, 350
TCAT with, 350
V-NAND with, 350
word-line, 253f, 350–53, 351f, 352f
RDF. *See* Random dopant fluctuations

Micron Ex. 1014, p. 418
Micron v. YMTC
IPR2025-00119

Read disturb
  control gate voltage during, 230
  detrapping and SILC with, 229–34, 230f, 231f, 232f, 233f
  electron current density with, 236–37
  hot carrier injection mechanism in, 235–37, 236f, 237f
  in NAND flash product, 234–35, 234f, 235f
  program and erase operation with, 197, 198f
  program/erase scheme dependence with, 224–29, 224f–229f, 225t
  RBER in, 234, 234f, 235f
  SA-STI cell without FG wing and, 66f
  SWATT cell and, 77f
Read operation
  array architecture in, 22f
  page read, 21, 22f
  single cell, 21, 21f
Read window margin (RWM), 68, 130–42
  ABL with, 134
  assumption for, 131–35, 131f, 131t, 132f, 133f, 134f, 135f
  BPD with, 131, 132f, 134, 134f
  calculation for, 132–35, 133f, 134f, 135f
  EIS with, 131, 132f, 133, 133f
  FGC with, 131, 132f, 133–37, 136f
  ISPP with, 134–36
  MLC with, 382–83
  negative V_t shift phenomena with, 253
  page program sequence with, 134, 135f
  programmed V_t distribution width with, 135–37, 136f, 137f
  RTN with, 131, 134, 135, 136f
  RWM V_t setting dependence, 140–41, 141f
  SA-STI cell with, 131, 382–83
  trend of, 139–40, 141f
  V_t window, 137–39, 138f, 139f, 140f
Reliability, 195–266
  advanced DC-SF cell, 329, 329f
  data retention
    analysis of, 203–24, 211f, 212f, 213f, 215f–222f, 224f
    characteristics of, 203–10, 203f–209f, 383
    distributed cycling test with, 222–24, 222f, 224f
    in NAND flash product, 219–21, 220f, 221f
    program and erase cycling endurance with, 200–203, 200f, 202f
    program and erase scheme dependence with, 203–4, 203f, 204f, 205f
    program and erase scheme with, 198–200, 199f
    program/erase cycling degradation, 210–16, 211f, 212f, 213f, 215f
    SILC with, 216–19, 216f, 217f, 218f, 219f
    temperature dependence with, 204–8, 206f, 207f
    tunnel-oxide thickness dependence with, 208–10, 208f, 209f
  erratic over-program with, 250–52, 250f, 251f
  high, 6f, 7
  multilevel cell compared to SLC with, 93
  negative V_t shift phenomena
    background with, 253–54, 253f, 254f
    carrier separation in programming conditions, 260–62, 260f, 261f
    experiment with, 253–54, 253f, 254f
    model, 262–63, 262f
    negative V_t shift, 254–56, 255f, 256f
    program-inhibited test with, 254, 254f
    program speed and victim cell V_t dependence, 256–59, 257f, 258f, 259f
    RWM with, 253
  program disturb
    channel coupling with, 248–49, 249f, 250f
    hot carrier injection mechanism with, 244–48, 244f, 245f, 246f, 247f
    model of self-boosting with, 238–44, 238f, 239f, 241f, 242f, 243f, 244f
  program/erase cycling endurance
    analysis of, 203–24, 211f, 212f, 213f, 215f–222f, 224f
    data retention characteristics with, 203–10, 203f–209f
    data retention in NAND flash product with, 219–21, 220f, 221f

Micron Ex. 1014, p. 419
Micron v. YMTC
IPR2025-00119

degradation, 197, 197f, 210–16, 211f, 212f, 213f, 215f
distributed cycling test with, 222–24, 222f, 224f
endurance characteristics with, 200–203, 200f, 202f
program and erase scheme in, 198–200, 199f
SILC with, 216–19, 216f, 217f, 218f, 219f
read disturb
detrapping and SILC with, 229–34, 230f, 231f, 232f, 233f
hot carrier injection mechanism in, 235–37, 236f, 237f
in NAND flash product, 234–35, 234f, 235f
program/erase scheme dependence with, 224–29, 224f–229f, 225t
RBER in, 234, 234f, 235f
summary of, 263–66, 264f, 265f
Resistance-capacitance delay. *See* RC delay
RIE condition, 337, 369f
Row decoder configuration, P-BiCS, 287–89, 288f
RTN. *See* Random telegraph noise
RWM. *See* Read window margin

SA-STI cell. *See* Self-aligned shallow trench isolation cell
Scalability
BiCS, 339f
DC-SF, 339f
SMArT, 339f
TCAT, 339f
Scaling. *See also* BiCS technology
advanced LOCOS cell, 40f, 41–42, 41f, 42t
cell structure challenge with, 170–71, 170f
challenge of NAND flash memory, 10, 129–86
charging process in few-electron memory with, 176
DC-SF cell with, 317, 318f
dopant atoms *versus* transistor size with, 182f
dummy word line in, 78, 80
electron phenomena with, 175–78, 176f, 177f
failure time in few-electron memory with, 177, 177f
FGC interference in, 10
air gap and low-*k* material, 149–53, 150f, 151f, 152f
coupling with source/drain, 148–49, 148f, 149f, 150f
direct coupling with channel, 145–48, 146f.147f
model of, 142–45, 142f, 144f, 145f
high-field limitation with, 171–75, 171f, 172f, 173f, 174f, 175f
impact on data retention, 183–85, 183f, 184f, 185f
inter-poly capacitance in, 157
NAND flash memory devices in structure, 37, 38f
patterning limitation with, 178–79, 178f, 179f
program electron injection spread in, 10
effect of lower doping in FG, 158–61, 159f, 160f, 161f
theory of, 153–58, 153f, 154f, 155f, 156f, 157f, 158
random telegraph signal noise in
in flash memory cells, 161–66
Monte Carlo simulation in investigation of, 163, 163f
scaling trend of, 166–70
read window margin in, 130–42
ABL with, 134
assumption for, 131–35, 131f, 131t, 132f, 133f, 134f, 135f
BPD with, 131, 132f, 134, 134f
calculation for, 132–35, 133f, 134f, 135f
EIS with, 131, 132f, 133, 133f
FGC with, 131, 132f, 133–37, 136f
ISPP with, 134–36
page program sequence with, 134, 135f
programmed V_t distribution width with, 135–37, 136f, 137f
RTN with, 131, 134, 135, 136f
RWM V_t setting dependence, 140–41, 141f
SA-STI cell with, 131

Micron Ex. 1014, p. 420
Micron v. YMTC
IPR2025-00119

Scaling (*Continued*)
trend of, 139–40, 141f
V_t window, 137–39, 138f, 139f, 140f
retention-time distribution with, 176, 176f
RTN and limit to, 10, 131, 134, 135, 136f
SA-STI cell with, 129, 130f, 381–82
self-boosting model with trend in, 244f
stored electrons in floating gate with, 153f
tunnel-oxide thickness in, 168
variation in, 179–83, 180f, 181f, 182f
word line high-field problem in, 174, 174f
Self-aligned shallow trench isolation cell (SA-STI cell), 4t, 6, 6f
aspect ratio of, 68f
cross sections of, 67f
data retention with, 216–19, 218f, 219f
in NAND flash cells, 217f
in NOR flash cell, 216, 216f
with FG wing
characteristics of, 53–56, 54f, 55f, 56f, 57f
characteristics of peripheral devices, 56–59, 58f, 59f
fabrication process flow of, 50–53, 50f, 51f, 51t, 52f, 53f
schematic view of, 49f
structure of, 48–49, 49f
without FG wing
characteristics of, 64–66
coupling ratio as function of gate width of, 61f
cross-sectional view of, 60f
fabrication process flow of, 60–61, 62f
memory cell parameters of, 61t
read disturb characteristics of, 66f
structure of, 59–60, 60f, 61f, 61t
top view of, 60f
leakage current density calculation, 216
negative V_t shift phenomena with, 253
program and erase characteristics of, 64f
program/erase cycling endurance with, 216–19, 216f, 217f, 218f, 219f
RWM with, 131, 382–83
scaling with, 129, 130f, 381–82
structure along word line, 253
structure challenge in scaling, 170–71, 170f
subthreshold characteristics of, 64f
TDDB characteristics of tunnel oxide in, 65, 65f
Self-boosting
program disturb with model of, 238–44, 244f
BB-t mechanism in, 241, 243, 243f
bias conditions in, 238f, 242f
CBR in, 241, 242
channel voltage equation in, 240f
coupling ratio calculation in, 238f
disturbed cell V_t as function of inhibit voltage in, 242–43, 243f
equivalent circuit for, 239f
inhibit voltage generation in, 238f
J/L current in, 241
V_{pass} and V_{pgm} waveforms in, 240, 241f
technology scaling trend in, 244f
transient channel potential in, 241
schemes
erase-area, 32, 33f
local, 32, 33f
program condition for, 171f
Shallow trench isolation (STI), 59, 61–63, 63f. *See also* Self-aligned shallow trench isolation cell
air gap, 152, 152f
cycling degradation with, 214
SWATT cell with, 70, 71
Sidewall transfer transistor cell (SWATT cell), 8, 10, 69–76
concept of, 70–71, 70f, 71f, 72f
coupling ratio as function of channel width for, 76f
electrical characteristics of
cell characteristics, 75, 75f, 76f
isolation, 74, 74f
electrical characteristics of reliability, 76, 77f
fabrication process of, 71–74, 73f
program and erase characteristics of, 75, 75f
program/erase cycling endurance characteristics of, 77f
read condition of, 71f

Micron Ex. 1014, p. 421
Micron v. YMTC
IPR2025-00119

read disturb characteristics of, 77f
schematic view and equivalent circuit of, 70f
SLC with, 70, 71
STI with, 70, 71
subthreshold characteristics of, 76f
threshold voltage distribution of, 72f
threshold voltage of parasitic field transistor in, 74f
SILC. *See* Stress-induced leakage current
Silicon(Gate)–Oxide–Nitride–Oxide–Silicon (substrate). *See* SONOS
Silicon nitride (SiN), 279
gate replacement with tungsten, 289
macaroni body vertical transistor with, 280f
select gate vertical transistor with, 280f
spacer, 151, 151f
Single bit cell (SLC), 6–7
die size per bit with, 121f
program speed with, 121f
reliability of multilevel cell compared to, 93
SWATT cell with, 70, 71
V_t distribution image of, 95, 95f
Single-cell architecture, 17, 18f
read operation for, 21, 21f
SiN spacer, threshold voltage shift by FG interference with, 151, 151f
Si/SiO2 interface, 211, 230
SLC. *See* Single bit cell
SMArT (Stacked memory array transistor), 383
comparison of other 3D NAND cells with, 276t, 300f, 336–39, 336t, 338f, 339f, 340f
comparison of total interference of, 302f
comparison of V_{th} widening with, 302f
effective memory cell size of, 337, 338f
electrical characteristics of, 301–2, 301f, 302f
program disturb phenomena with, 343
program-erase characteristics of, 301, 301f
scalability of, 339f
SONOS with, 342
stacked cells with, 369
structural advantage of, 298–301, 300f
TEM cross-sectional image of, 300f
WL capacitance with, 335
word-line RC delay with, 350
Solid-state disks. *See* SSDs
SONOS (Silicon(Gate)–Oxide–Nitride–Oxide– Silicon (substrate)), 276t, 295, 335
characteristics of, 279, 280f
comparison of, 300f, 308f
conventional device, 279, 315, 317
data retention characteristic of, 339, 342
metal gate SONOS structure, 289–90
nano wire SONOS device, 281f
problems with slow erase, 383
program/erase cycling performance of, 337
quick charge loss with, 341f
SMArT with, 342
SONOS/TANOS, 276, 308
SPT process, 178, 178f
SSDs (Solid-state disks), 7, 273
lower bit cost and, 376
power consumption with, 371–74, 373f, 374f, 385
SSE structure, 214, 215f
SSL
3D V-NAND flash memory with, 294, 296f
TCAT with, 289, 292f
VG-NAND flash with, 303–5, 303f, 304f, 306f
Stacked cells
BiCS with, 369
current issue in poly-Si channel with, 368
lower bit cost and, 376
NAND string scheme with, 370f
problems and solutions for, 368, 369f
SMArT with, 369
TCAT with, 369
3D NAND flash cell and number of, 368–70, 369f, 370f
trend of cell current and block size with, 369f
Stacked memory array transistor. *See* SMArT
Staircase programming pulse, 97f
Step-up program pulses, 96, 97f
STI. *See* Shallow trench isolation
Stop bit, 218, 218f

Micron Ex. 1014, p. 422
Micron v. YMTC
IPR2025-00119

Stress conditions, 225t
bipolarity stress, 225f, 226, 226f, 227f
electron-emitted stress, 225f, 226, 226f, 227f
electron-injected stress, 225f, 226, 226f
Stress-induced leakage current (SILC), 197, 197f, 198f
detrapping and, 229–34, 230f, 231f, 232f, 233f
equations for, 229–30
erratic over-program with, 252f
FN tunneling with, 226, 231f
program/erase scheme dependence with, 225–26, 226f
threshold voltage shift with, 229, 230f
tunnel oxide with, 219–20, 225–26, 226f, 229, 233f
after various write/erase cycling, 232, 232f
Subthreshold swing (STS), 283, 283f, 366, 368f
SWATT cell. *See* Sidewall transfer transistor cell

Tail bits, 218, 218f
program/erase cycle dependence of, 219, 219f
TCAD. *See* Technology computer-aided design
TCAT (Terabit cell array transistor), 383
comparison of other 3D NAND cells with, 276t, 300f, 336–39, 336t, 338f, 339f, 340f
cross-sectional SEM images of, 291f
CSL with, 289–90, 291f, 292f, 293f
data retention characteristics of, 293f
effective memory cell size of, 337, 338f
electrical characteristics of, 292–94, 293f, 294f
fabrication process for, 289–92, 290f, 291f, 292f
GSL with, 289–90, 292f
128-Gb MLC V-NAND flash memory, 294–95, 295f, 296f
128-Gb TLC V-NAND flash memory, 296–98, 297f, 298f, 299f
process sequence of, 291f
program disturb phenomena with, 343
program/erase cycling endurance characteristics of, 293f
scalability of, 339f
simulated profiles of doping for, 293f
SSL with, 289, 292f
stacked cells with, 369
structure of, 289–92, 291f, 292f
schematic structures, 290f
WL capacitance with, 335
word-line RC delay with, 350
Technology computer-aided design (TCAD), 241
simulation, 143, 146, 169, 184, 184f
Temperature dependence, 342–43, 342f, 343f
Terabit cell array transistor. *See* TCAT
Thin film transistors (TFTs), 353, 361
3 bits/cell. *See* TLC
3D NAND flash cells, 7–8
Three-dimensional NAND flash cell
advanced DC-SF cell
improvement on, 317–18, 319f
MCGL process for, 319, 320f, 329
new programming scheme for, 325–28, 326f, 327f, 328f
new read scheme for, 319–25, 321f, 322f, 323f, 324f, 325f, 326t
reliability of, 329, 329f
background of, 273–76, 274f, 275f, 276t
BiCS, 7–8, 383
comparison of other 3D NAND cells with, 276t, 300f, 336–39, 336t, 338f, 339f, 340f
concept of, 275f, 276–78, 277f
cross-sectional SEM photo of, 277f
data retention characteristics of, 285f
electrical characteristics of, 279–85, 280f, 281f, 282f, 283f, 284f, 285f
erase operation for, 281f
fabrication process of, 278–79, 278f, 279f
"macaroni" body vertical transistor in, 282–83, 282f, 283f
pipe-shaped, 285–89, 286f, 287f, 288f, 289f
program/erase characteristics of, 280f
subthreshold swing in, 283, 283f
top-down view of, 277f
trap density at poly-silicon in, 282f

Micron Ex. 1014, p. 423
Micron v. YMTC
IPR2025-00119

challenges of, 339–76
cell current fluctuation, 353–68, 354f, 356f–368f
data retention, 339–43, 340f, 341f, 342f
number of stacked cells in, 368–70, 369f, 370f
peripheral circuit under cell array in, 370–71, 371f, 372f
power consumption in, 371–74, 373f, 374f
program disturb, 343–50, 344f–350f
quick initial charge loss, 339–42, 340f, 341f, 342f
temperature dependence, 342–43, 342f, 343f
word-line RC delay, 253f, 350–53, 351f, 352f
comparison of major, 276t, 300f, 336–39, 336t, 338f, 339f, 340f
DC-SF cell
comparison of other 3D NAND cells with, 276t, 336–39, 336t, 338f, 339f, 340f
concept for, 309–10, 309f, 310f
concern for charge trap 3D cell with, 308, 308f
coupling ratio with, 310–11, 311f, 312f
DC-SF NAND flash cells, 309–13, 309f, 310f, 311f, 312f, 313f, 314f
device fabrication of, 312–13, 313f, 314f
results and discussions, 313–17, 314t, 315f, 316f, 317f
scaling capability, 317, 318f
future memory hierarchy with, 376f
future trend of, 374–76, 375f, 376f
history of, 274f
SMArT, 383
comparison of other 3D NAND cells with, 276t, 300f, 336–39, 336t, 338f, 339f, 340f
electrical characteristics of, 301–2, 301f, 302f
structural advantage of, 298–301, 300f
TCAT/V-NAND, 383
comparison of other 3D NAND cells with, 276t, 300f, 336–39, 336t, 338f, 339f, 340f
electrical characteristics of, 292–94, 293f, 294f
128-Gb MLC V-NAND flash memory, 294–95, 295f, 296f
128-Gb TLC V-NAND flash memory, 296–98, 297f, 298f, 299f
structure and fabrication process of, 289–92, 290f, 291f, 292f
transition from planar 2D NAND cell to, 375f
VG-NAND, 383
comparison of other 3D NAND cells with, 276t, 336–39, 336t, 338f, 339f, 340f
electrical characteristics of, 305–7, 306f, 307f
structure and fabrication process of, 302–5, 303f, 304f, 306f
Three-level (1.5 bits/cell) NAND flash
advanced operation for, 119–21, 120f, 121f
die size per bit with, 121f
program speed with, 121f
V_{th} distribution in, 121f
threshold distribution for, 120f
Three-Step Program (TSP), 115, 115f, 118f
Threshold voltage, 93
calculation, 30–31, 30f, 31f
comparison in devices with and without ISPP, 26f
DC-SF cell, 316f
fluctuation due to RTN, 162, 162f
of parasitic field transistor SWATT cell, 74f
program/erase cycling with shift in, 213–14, 213f
read disturb stress time with, 229–30, 230f
shift by FG interference, 151, 151f
SWATT cell with, 72f
TLC V-NAND and distribution of, 299f
TLC (3 bits/cell), 6, 7. *See also* 128-Gb TLC V-NAND flash memory
advanced operation for, 113–15, 113f, 114f, 115f, 116f–117f
bit cost with, 113

Micron Ex. 1014, p. 424
Micron v. YMTC
IPR2025-00119

TLC (3 bits/cell) (*Continued*)
- conventional page program sequence of, 113–14, 113f
- new page program sequence of, 114, 114f
- page program sequence, 10
- V_t distribution image of, 95, 95f
- V_t distributions of, 115, 116f–117f
- TSP was applied to, 115, 115f, 118f
- V-NAND flash memory, 296–98
  - bit-line architecture of, 296, 297f
  - device summary of, 298f
  - die micrograph and bit density of, 297f
  - energy consumption during programming with, 299f
  - high-speed program algorithm for, 296–97, 298f
  - threshold voltage distribution of, 299f

Transient channel potential, 241
Transient deep-depletion behavior, p-type floating gate with, 84, 84f
Trapezoidal programming pulse, 97f
TSP. *See* Three-Step Program
Tunnel oxide, 195–98
- of cell transistor, potential distribution of and, 146–47, 146f
- charge loss rate with, 217f
- data retention characteristics on, 208f
- data retention time as function of thickness in, 228f
- degradation with, 196, 196f, 210, 214, 219f, 265
- electron detrapping from, 205, 207, 210, 230, 231f, 264
- electron-emitted stress of, 227f
- endurance characteristics of memory cell with, 227f
- higher electric field in, 234, 265
- hole trappings in, 250, 251f
- program and erase operations with, 198, 202, 202f, 212
- programming voltages with, 199
- SILC with, 219–20, 225–26, 226f, 229, 233f
- stress conditions with, 225
- thickness dependence, 208–10, 208f, 209f

Two-step verify scheme, V_t distribution width for MLC in, 99–102, 99f, 100f, 101f

Uniform erase scheme, 199–201, 199f, 200f
Uniform P/E scheme, 22f, 383
Uniform program scheme, 199–201, 199f, 200f
Uniform write scheme, 199–201, 199f, 200f

Vertical gate NAND cell. *See* VG-NAND
Vertical-NAND. *See* V-NAND
V_G dependence, 358–60, 358f, 359f, 360f
VG-NAND (Vertical gate NAND cell), 383
- Bit line with, 303–5, 304f
- comparison of other 3D NAND cells with, 276t, 336–39, 336t, 338f, 339f, 340f
- CSL with, 303–5, 303f, 304f
- data retention characteristics of, 307f
- electrical characteristics of, 305–7, 306f, 307f
- GSL with, 303–5, 303f, 304f
- process flow of, 304f
- program and body-erase window of, 306f
- program and erase cycling endurance of, 307f
- schematic diagram of, 306f
- SSL with, 303–5, 303f, 304f, 306f
- structure and fabrication process of, 302–5, 303f, 304f, 306f
- top-down view of, 303f
- word line with, 303–5, 304f
- Z interference of, 307f

Victim cell, 172, 172f
- hot holes injected into FG of, 263
- inhibit, 254
- negative V_t shift phenomena with, 254–58, 254f, 255f, 256f, 257f, 259f, 262f
- programming of attack cell with, 254, 255f
- program speed and, 256–59, 257f, 258f, 259f
- V_t dependence with, 254–59, 255f, 257f, 258f, 259f

Micron Ex. 1014, p. 425
Micron v. YMTC
IPR2025-00119

V-NAND (Vertical-NAND), 383
comparison of other 3D NAND cells with, 276t, 336–39, 336t, 338f, 339f, 340f
cross-sectional view of, 292f
electrical characteristics of, 292–94, 293f, 294f
128-Gb MLC V-NAND flash memory, 294–95, 295f, 296f
128-Gb TLC V-NAND flash memory, 296–98, 297f, 298f, 299f
program disturb phenomena with, 343
schematic diagram of, 292f
structure and fabrication process of, 289–92, 290f, 291f, 292f
WL capacitance with, 335
word-line RC delay with, 350, 351f
Voltage drop across tunnel oxide (V_{tun}), 28–29, 29f
V_{pass} mode, 31, 32f
V_t. *See also* Negative Vt shift phenomena; ΔV_t spread
cell V_t setting in MLC, 34–35, 34f
distribution of four states, 96f
distribution width for MLC
bit-by-bit verify operations in, 98–99, 98f, 99f
cell V_t setting in, 94–95, 94f, 95f, 96f
ISPP in, 95–97, 97f
pseudo-pass scheme in page program in, 102–4, 102f, 103f, 104f
two-step verify scheme in, 99–102, 99f, 100f, 101f
distribution width for scaling with RWM
FGC in, 135–37, 136f, 137f
ISPP in, 135–36
RTN in, 135, 136f
distribution with erase, 345–46, 346f
distribution with PGM, 345–46, 346f
erratic over-program with distribution of, 250
program disturb with, 242–43, 243f
RDF, variation with, 182–83
RWM, V_t window, 137–39, 138f, 139f, 140f
RWM V_t setting dependence, 140–41, 141f
SWATT cell, distribution of, 72f
TLC in distributions of, 115, 116f–117f
variation in standard deviation with, 179f
$\sigma\Delta V_t$
equation for, 155
FG phosphorus doping in calculation of, 160–61, 160f
ΔV_t in calculation of, 156, 156f, 158f
ΔV_t spread, 154–55, 154f
cumulative probability distribution of, 165f
distributions for $V_{step} = 312$, 155, 155f
as function of $\sigma\Delta V_t$, 156, 156f, 158f
V_{tun}. *See also* Voltage drop across tunnel oxide
calculation in program and erase dynamics, 28–29, 29f

Well erase, 4t
WL. *See* Word line
W/L cut. *See* Line-type word line cut
Word line (WL)
air gap with, 152, 152f, 352f
BiCS with, 350
dummy, 290, 294
electric field between, 174–75, 175f
high-field problem, 174, 174f
RC, 253f, 350–53, 351f, 352f
SA-STI cell along, 253
simulated waveform of, 353f
SMArT with, 335, 350
TCAT with, 335, 350
trend of cell current and block size of stacks, 369f
VG-NAND flash with, 303–5, 304f, 335
V-NAND with, 350, 351f

Z interference, 307f

IEEE Press Series on Microelectronic Systems

The focus of the series is on all aspects of solid-state circuits and systems including the design, testing, and application of circuits and subsystems, as well as closely related topics in device technology and circuit theory. The series also focuses on scientific, technical and industrial applications, in addition to other activities that contribute to the moving the area of microelectronics forward.

R. Jacob Baker, *Series Editor*

1. *Nonvolatile Semiconductor Memory Technology: A Comprehensive Guide to Understanding and Using NVSM Devices*
   William D. Brown, Joe Brewer
2. *High-Performance System Design: Circuits and Logic*
   Vojin G. Oklobdzija
3. *Low-Voltage/Low-Power Integrated Circuits and Systems: Low-Voltage Mixed-Signal Circuits*
   Sanchez-Sinencio
4. *Advanced Electronic Packaging, Second Edition*
   Richard K. Ulrich and William D. Brown
5. *DRAM Circuit Design: Fundamental and High-Speed Topics*
   Brent Keith, R. Jacob Baker, Brian Johnson, Feng Lin
6. *CMOS: Mixed-Signal Circuit Design, Second Edition*
   R. Jacob Baker
7. *Nonvolatile Memory Technologies with Emphasis on Flash: A Comprehensive Guide to Understanding and Using NVM Devices*
   Joseph E. Brewer, Manzur Gill
8. *Reliability Wearout Mechanisms in Advanced CMOS Technologies*
   Alvin W. Strong, Ernest Y. Wu, Rolf-Peter Vollertsen, Jordi Sune, Giuseppe La Rosa, Timothy D. Sullivan, Stewart Rauch
9. *CMOS: Circuit Design, Layout, and Simulation, Third Edition*
   R. Jacob Baker
10. *Quantum Mechanics for Electrical Engineers*
    Dennis M. Sullivan
11. *Nanometer Frequency Synthesis Beyond Phase-Locked Loop*
    Liming Xiu
12. *Electrical, Electronics, and Digital Hardware Essentials for Scientists and Engineers*
    Ed Lipiansky
13. *Enhanced Phase-Locked Loop Structures for Power and Energy Applications*
    Masoud Karimi-Ghartemani
14. *From Frequency to Time-Averaged-Frequency: A Paradigm Shift in the Design of Electronic Systems*
    Liming Xiu
15. *NAND Flash Memory Technologies*
    Seiichi Aritome

Micron Ex. 1014, p. 427
Micron v. YMTC
IPR2025-00119

DATE DUE

JUL 15 2016			
MAY 28 2017			
			PRINTED IN U.S.A.

MARQUETTE UNIVERSITY
LIBRARIES

MARQUETTE UNIVERSITY LIBRARIES
3 5039 02427186 5

Examines the history, basic structure, and processes of NAND flash memory

NAND Flash Memory Technologies discusses basic and advanced NAND flash memory technologies, including the principle of NAND flash, memory cell technologies, multi-bits cell technologies, scaling challenges of memory cell, reliability, and 3-dimensional cell as the future technology. Chapter 1 describes the background and early history of NAND flash. The basic device structures and operations are described in Chapter 2. Next, the author discusses the memory cell technologies focused on scaling in Chapter 3, and introduces the advanced operations for multi-level cells in Chapter 4. The physical limitations for scaling are examined in Chapter 5 and Chapter 6 describes the reliability of NAND flash memory. Chapter 7 examines 3-dimensional (3D) NAND flash memory cells and discusses the pros and cons in structure, process, operations, scalability, and performance. In Chapter 8, challenges of 3D NAND flash memory are discussed. Finally, in Chapter 9 the author summarizes and describes the prospect of technologies and market for the future NAND flash memory.

- Offers a comprehensive overview of NAND flash memories, with insights into NAND history, technology, challenges, evolutions, and perspectives
- Describes new program disturb issues, data retention, power consumption, and possible solutions for the challenges of 3D NAND flash memory
- Valuable for those active in the field of flash memories and more generally non-volatile memory technologies.

NAND Flash Memory Technologies is a reference for engineers, researchers, and designers who are engaged in the development of NAND flash memory or SSD (Solid State Disk) and flash memory systems.

SEIICHI ARITOME was a Senior Research Fellow at SK Hynix Inc. in Icheon, Korea from 2009 to 2014. He has contributed to NAND flash memory technologies for over 27 years in several companies and nations. Dr. Aritome was a Program director at Powerchip Semiconductor Corp. in Hsinchu, Taiwan, a Senior Process Reliability Engineer at Micron Technology Inc. in Idaho, USA, and a Chief Specialist at Toshiba Corporation in Kawasaki, Japan. He received his PhD from the Graduate School of Advanced Sciences of Matter, Hiroshima University, Japan. Dr. Aritome is an IEEE Fellow and a member of the IEEE Electron Device Society.

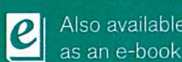
Also available as an e-book

Subscribe to our free Engineering eNewsletter at **wiley.com/enewsletters**

www.wiley.com/ieee

Cover image: Courtesy of the author

ISBN 978-1-119-13260-8

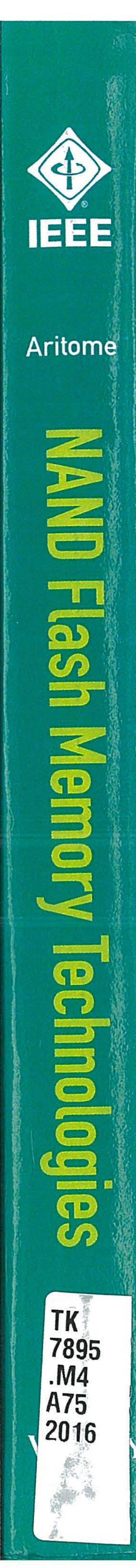
IEEE
Aritome
NAND Flash Memory Technologies
TK
7895
.M4
A75
2016